Université de Liège
Faculté des Sciences Appliquées

Numerical simulations of brittle and elasto-plastic fracture for thin structures subjected to dynamic loadings

Thèse présentée par

Gauthier BECKER
(Ingénieur Civil Electro-Mécanicien, Boursier du FRIA)

pour l'obtention du grade légal de
Docteur en Sciences de l'ingénieur
Année académique 2011-2012

Université de Liège - Computational & Multiscale Mechanics of Materials - Bât. B52/3
Chemin des Chevreuils 1, B-4000 Liège 1, Belgique
Tél +32-4-3669552 - Fax +32-4-3669217
Email : gauthier.becker@ulg.ac.be

Doctoral thesis publicly defended on Thursday 24th May 2012 in front of the thesis committee composed of:

- Jean-Philippe Ponthot, Professor, University of Liège, President
- Christophe Geuzaine, Professor, University of Liège
- Eric Béchet, Assistant professor, University of Liège
- Ludovic Noels, Assistant professor, University of Liège, Superviser
- Anne-Marie Habraken, Research Director FNRS, University of Liège
- Laurent Stainier, Professor, Ecole Centrale de Nantes (France)
- Jean-Yves Sener, Doctor, Materials & Systems for Safety & Security (MS3), Andenne
- Thomas Pardoen, Professor, Catholic University of Louvain
- Eric Wyart, Doctor, Cenaero, Gosselies
- Raùl Radovitzky, Professor, University of Cambridge Massachussetts (USA)

Abstract

The main purpose of this thesis is the development of a framework to model fracture initiation and propagation in thin bodies. This is achieved by the combination of two original models.

On one hand, (full) discontinuous Gakerkin formulations of Euler-Bernoulli beams as well as Kirchhoff-Love shells are established. These formulations allow modeling a thin structure with discontinuous elements, the continuity being ensured weakly by addition of interface terms. The first advantage of the recourse to a discontinuous method is an easy insertion of cohesive elements during the simulation without a modification of the mesh topology. In fact with a continuous method, the insertion of the cohesive elements at the beginning of the simulation leads to numerical issues and their insertion at onset of fracture requires a complex implementation to duplicate the nodes. By contrast, as interface elements are naturally present in a discontinuous formulation their substitution at fracture initiation is straightforward. The second advantage of the discontinuous Galerkin formulation is a simple parallel implementation obtained in this work by exploiting, the discontinuity of the mesh in an original manner. Finally, last advantage of the recourse to a discontinuous Galerkin method for thin bodies is to obtain a one field formulation. In fact, the $\mathcal{C}^1$ continuity is ensured weakly by interface terms without considering rotational degrees of freedom.

On the other hand, the through-the-thickness crack propagation is complicated by the implicit thickness model inherent to thin bodies formulations. Therefore we suggest an original cohesive model based on reduced stresses. Our model combines the different reduced stresses in such a way that the expected amount of energy is released during the crack process leading to a model which respects the energetic balance whatever the applied loadings.

The efficiency of the obtained framework is demonstrated through the simulation of several benchmarks whose results are in agreement with numerical and experimental data coming from the literature. Furthermore, the versatility of our framework is shown by simulating 2 very different fracture phenomena: the crack propagation for elastic as well as for elasto-plastic behavior and the fragmentation of brittle materials. This demonstrates that our framework is a powerful tool to study dynamics crack phenomena in thin structure problems involving a large number of degrees of freedom.

Résumé

L'objectif principal de cette thèse est le développement d'une technique permettant de modéliser l'initiation ainsi que la propagation d'une ou plusieurs fissures dans un corps mince. Cette technique combine deux modèles originaux.

D'une part, une formulation Galerkin (complètement) discontinue des poutres d'Euler-Bernoulli ainsi qu'une formulation Galerkin (complètement) discontinue des coques de type Kirchhoff-Love sont établies. Ces formulations permettent de modéliser une structure mince avec des éléments discontinus, la continuité étant assurée faiblement par l'addition de termes d'interface. Le premier avantage inhérent à l'utilisation d'une méthode Galerkin discontinue est une insertion aisée des éléments cohésifs au cours de la simulation et ce sans devoir modifier la topologie du maillage. En fait, dans le cas d'une méthode continue, des problèmes numériques apparaissent si l'insertion d'un élément cohésif est réalisée au début de la simulation et l'insertion au cours de la simulation rend l'implémentation complexe puisque les noeuds doivent être dupliqués dans le cas d'une méthode continue. Au contraire, comme les éléments d'interface sont naturellement présents dans une formulation discontinue la substitution de ces éléments d'interface par des éléments cohésifs à l'initialisation de la fracture est aisée. Le deuxième avantage d'une méthode Galerkin discontinue est qu'elle facilite l'implémentation en parallèle du schéma de résolution. Dans ce travail, celle-ci est obtenue en exploitant la discontinuité du maillage d'une manière originale. Enfin, dernier avantage dans le cas des corps minces d'une méthode Galerkin discontinue est l'obtention d'une formulation à un champ. En fait, comme la continuité C^1 est assurée faiblement grâce aux termes d'interface, il n'y a pas besoin de considérer des degrés de liberté en rotation.

D'autre part, la modélisation implicite de l'épaisseur, inhérente aux formulations des corps minces, complique la propagation d'une fissure à travers celle-ci. Dès lors, nous suggérons un modèle cohésif original basé sur les contraintes réduites. Notre modèle combine ces différentes contraintes réduites de manière à dissiper la bonne quantité d'énergie pendant le processus de fracture ce qui permet d'obtenir un modèle respectant le bilan d'énergie quelque soit le chargement appliqué.

L'efficacité de la technique proposée est démontrée á travers la simulation de différents exemples dont les résultats sont en accord avec les données numériques et expérimentales tirées de la littérature. De plus, deux phénomènes de fracture très différents (d'une part, la propagation de fissure dans un milieu élastique ou élasto-plastique et d'autre part, la fragmentation dans des matériaux fragiles) sont simulés pour démontrer la versatilité de la technique proposée. Cela démontre que cette dernière constitue un puissant outil pour étudier les

phénomènes dynamiques de fissuration dans les structures minces modélisées avec un maillage comportant un nombre important de degrés de liberté.

Preface

This thesis is the result of three years of research. As a preamble I would like to acknowledge each person who contributed to its success.

First my deepest gratitude goes to Professor Noels who supervised me during these three years. He found time in his overbooked schedule to enrich my intellectual skills by his advises (and I have to begrudge that he was always right) as well as his ideas. I greatly appreciated his unfailing support to my project as well as his involvement in the creation of a pleasant and stimulating working environment.

I owe special acknowledgment to the members of my committee. In particular, I acknowledge

- *Dr Habraken, Prof. Stainier, Prof. Ponthot and Dr Sener to their active participation to the annual meeting of my committee thesis. Your advises were precious for my researches.*

- *Prof. Geuzaine to his IT support and explanation on the core of Gmsh, the free software in which I have implemented my developments.*

- *Prof. Pardoen to his useful advises on ductile material behavior.*

It was also with a great pleasure that I regularly presented my work to Dr Sener and Mr Janssen, industrial partners of this thesis. I greatly appreciated your support and remarks during these three years. In particular I give thanks to Dr Sener and Dr Lacroix for the initiation of the research during my master thesis and for their suggestion to pursue in this field through a PhD. Furthermore, many thanks to Mr Janssen to let me use LS-DYNA. The use of an industrial finite element code was precious for the implementation of my method. I have also thought to the MS3 and GDTech teams for their friendly welcome and advises during all this work.

The financial support of the FNRS (via the FRIA fund) made possible this work.

I acknowledge the personnel of the "Applied sciences & mathematics" library and in particular Mr Borsus to get hold of some useful old papers from the cellar.

I was boosted by my colleagues who interrupted my days in a pleasant way at time table. Be sure that I will continue to eat a "Boulet frites" with you as long as possible.

Many thanks to my friends who probably never understood what I write in this thesis. It is not important because you were there for me when I need it.

Finally I acknowledge my parents and my (little) brother. My parents to their useful support during all my scholarship. Their advises and presence were (and are still) very precious. Many thanks to my brother for its Christmas gift without it, it will be impossible to finish to write this thesis without losing my mind.

Contents

Tables of notations & definitions

This works use several definitions and notations summarized below.

Definitions

Compact	A set is compact if every open cover of it is a finite subcover of the set
Compact closure	The closure of the set is a compact
Condition number	The condition number of a matrix A measures the stability and sensitivity of A to an error in the data. If the condition number of A is near 1, A is well conditionned.
Consistent	A numerical method is consistent if the strong form satisfies the equations of the method.
Cosserat plane	A Cosserat plane is a plane embedded in an Euclidean space with a deformation vector assigned at each points of it. The vector has the property to be invariant in length under rigid body motion and is not necessary along the normal of the surface.
Hyperelastic	A material model is hyperelastic if the stress tensor derives from a potential
Plate	Thin flat structure represented by a Cosserat plane (without no initial curvature)
Shell	Plate with an initial curvature
Stable	A numerical method is stable if a quantity related to the energy of the system remains constant or decreases over the time

Abbreviations

CG	Continuous Galerkin method
CZM	Cohesive zone model
DG	Discontinuous Galerkin method
DCB	Double clamped beam
dof	Degree of freedom
ECL	Extrinsic cohesive law
EFG	Element free Galerkin
FE	Finite element
LEFM	Linear elastic fracture mechanics
pdf	Probability density function
PMMA	Polymethylmethacrylate
RKPM	Reproducing kernel particle method
RVE	Representative volume element
SCB	Simply clamped beam
SPH	Smooth hydrodynamic particles
TSL	Traction separation law

Conventions

Consider x as a representation of a mathematical quantity (scalar, vector or tensor).

x	Italic letter: scalar quantity (0 order tensor with 1 component)
$\boldsymbol{x}$	Bold italic letter:1^{st} order tensor (vector)
$\mathbf{x}$	Bold letter: 2^{nd} order tensor (matrix)
$\underline{\boldsymbol{x}}$	Underlined bold italic letter: unknowns system vector
$\mathcal{X}$	Calligraphic italic letter: 4^{th} order tensor (81 components)
$\mathbb{X}$	Double lined letter: manifold
$x(y)$	Symbol followed by another one between brackets: x is depending on y. This is not, *a priori* , used to define a mathematical priority between operations
$\dot{x}$	Symbol overcome by a dot: 1^{st} total derivative of x with respect to time
$\ddot{x}$	Symbol overcome by two dots: 2^{nd} total derivative of x with respect to time
$x^{\mathbf{n}}$	The exponent is a bold roman letter: x is evaluated at the (pseudo-)time step **n**
x_0	x is expressed in the initial configuration
x_{iner}	x is expressed in the reference initial frame
x_α	The index is a Greek letter: α^{th} scalar component of a two-component vector $\boldsymbol{x}$ (formulated in the convected basis in the case of thin body kinematics)
x^α	The exponent is a Greek letter: α^{th} scalar component of a two-component vector $\boldsymbol{x}$ (formulated in the conjugated basis in the case of thin body kinematics)
$x_{\alpha\beta}$	Both indices are Greek letters: component $\alpha\beta$ of a two by two matrix **x** (formulated in the convected basis in the case of thin body kinematics)
$x^{\alpha\beta}$	Both exponents are Greek letters: component $\alpha\beta$ of a two by two matrix **x** (formulated in the conjugated basis in the case of thin body kinematics)
$x_{,\alpha}$	The index is a Greek letter preceded by a comma: partial derivative of x with respect to the α^{th} variable $\alpha \in [1\,;2]$ (formulated in the convected basis in the case of thin body kinematics)
$x^{,\alpha}$	The exponent is a Greek letter preceded by a comma: partial derivative of x with respect to the α^{th} variable $\alpha \in [1\,;2]$ (formulated in the conjugated basis in the case of thin body kinematics)
$x^{\boldsymbol{\xi}}$	The exponent is a bold greek letter: x is evaluated at node $\boldsymbol{\xi}$

x_i	The index is a roman letter: i$^{\text{th}}$ scalar component of a 3-component vector $\boldsymbol{x}$ (formulated in the convected basis in case of thin body formulations)
x^i	The exponent is a roman letter: i$^{\text{th}}$ scalar component of a 3-component vector $\boldsymbol{x}$ (formulated in the conjugated basis in case of thin body formulations)
$x_{,i}$	The index is a roman letter preceded by a comma: partial derivative of x with respect to the i^{th} variable $i \in [1;3]$ (formulated in the convected basis in the case of thin body kinematics)
$x^{,i}$	The exponent is a roman letter preceded by a comma: partial derivative of x with respect to the i^{th} variable $i \in [1;3]$ (formulated in the conjugated basis in the case of thin body kinematics)
x_{ij}	Both indices are roman letters: scalar component $i, j \in [1;3] \times [1;3]$ of matrix $\mathbf{x}$
$\mathcal{X}_{\alpha\beta\gamma\delta}$	All the indices are Greek letter: component $\alpha, \beta, \gamma, \delta \in [1;2] \times [1;2] \times [1;2] \times [1;2]$ of 4$^{\text{th}}$ order tensor $\mathcal{X}$ (formulated in the convected basis in the case of thin body kinematics)
$\mathcal{X}^{\alpha\beta\gamma\delta}$	All the indices are Greek letter: component $\alpha, \beta, \gamma, \delta \in [1;2] \times [1;2] \times [1;2] \times [1;2]$ of 4$^{\text{th}}$ order tensor $\mathcal{X}$ formulated in the conjugated basis in the case of thin body kinematics)
$\mathcal{X}_{ijkl}$	All the indices are roman letter: component $i, j, k, l \in [1;3] \times [1;3] \times [1;3] \times [1;3]$ of 4$^{\text{th}}$ order tensor $\mathcal{X}$ (formulated in the convected basis in the case of thin body kinematics)
$\overline{\mathrm{x}}$	Overlined letter: x is evaluated on the neutral axis of the thin bodies
$\widehat{\mathrm{x}}$	A wide hat above x: x is formulated in the basis of the interface (and not in the basis of the bulk element)

Mathematical operations

This work uses the Einstein notation (*i.e.* $\sum_{i}^{Z} x_i y_i$ is summarized by $x_i y_i$ with $Z = 2$ if the indices are Greek letters and $Z = 3$ if the indices are roman letters) unless otherwise stated. Consider x and y two mathematical quantities (scalar, vector or tensor),

$x_{,y} = \frac{\partial}{\partial y} x$	Partial derivative of x with respect of y
$\frac{d}{dy} x$	Total derivative of x with respect of y
$\|\|\boldsymbol{x}\|\|$	Euclidean norm of vector $\boldsymbol{x}$: $\|\|\boldsymbol{x}\|\| = \sqrt{x_i x_i}$
$\|\|\boldsymbol{x}\|\|_\infty$	Infinite norm of vector $\boldsymbol{x}$: $\|\|\boldsymbol{x}\|\|_\infty = \max_i x_i$
$\boldsymbol{x} \wedge \boldsymbol{y}$	Vector product between $\boldsymbol{x}$ and $\boldsymbol{y}$: $[\boldsymbol{x} \wedge \boldsymbol{y}]_i = \varepsilon_{ijk} x_j y_k$, with ε_{ijk} the Levi-Civita 3$^{\text{th}}$ order tensor
$\boldsymbol{x} \cdot \boldsymbol{y}$	Scalar product of $\boldsymbol{x}$ and $\boldsymbol{y}$: $\boldsymbol{x} \cdot \boldsymbol{y} = x_i y_i$
$\boldsymbol{x} \otimes \boldsymbol{y}$	Dyadic product of $\boldsymbol{x}$ and $\boldsymbol{y}$: $[\boldsymbol{x} \otimes \boldsymbol{y}]_{ij} = x_i y_j$
$\mathbf{x}^T$	Transpose of tensor $\mathbf{x}$: *e.g.* for a 2$^{\text{nd}}$ order tensor, $\left[\mathbf{x}^T\right]_{ij} = x_{ji}$
$\mathbf{x}^{-1}$	Invert tensor of $\mathbf{x}$: *e.g.* for a 2$^{\text{nd}}$ order tensor, $\left[\mathbf{x}^{-1}\right]_{ik} x_{kj} = \delta_{ij}$ with δ_{ij} the Kronecker delta
$\det \mathbf{x}$	Determinant of second order tensor
$\|x\|$	Absolute value of x: $\|x\| = x$ if $x \geq 0$ and $\|x\| = -x$ otherwise
$\mathrm{tr}\,\mathbf{x}$	Trace of a second order tensor $\mathbf{x}$
$\boldsymbol{x}\boldsymbol{y}$	Tensorial product of $\boldsymbol{x}$ and $\boldsymbol{y}$: *e.g.* for a second order tensor $\mathbf{x}$ and vector $\boldsymbol{y}$ product $[\mathbf{x}\boldsymbol{y}]_{ij} = x_{ik} y_k$ and for 2 second order tensors $[\mathbf{x}\mathbf{y}]_{ij} = x_{ik} y_{kj}$
$\mathbf{x} : \mathbf{y}$	Tensor contraction between a tensor $\mathbf{x}$ and a tensor $\mathbf{y}$: *e.g.* for two second order tensors $\mathbf{x} : \mathbf{y} = x_{ij} y_{ij}$
$\mathbf{x} : \mathcal{Y}$	Product between a matrix $\mathbf{x}$ and a 4$^{\text{th}}$ tensor $\mathcal{Y}$: $[\mathbf{x} : \mathcal{Y}]_{kl} = x_{ij} Y_{ijkl}$
$\mathcal{X} : \mathbf{y}$	Contraction between a 4$^{\text{th}}$ order tensor $\mathcal{X}$ and a second order $\mathbf{y}$: $[\mathcal{X} : \mathbf{y}]_{ij} = X_{ijkl} y_{kl}$
$\mathbb{A} \to \mathbb{B}$	Transformation which gives for each point of $\mathbb{A}$ a point of $\mathbb{B}$
$\mathbb{A} \times \mathbb{B} \to \mathbb{C}$	Transformation which gives for each point of $\mathbb{A}$ and $\mathbb{B}$, a point of $\mathbb{C}$
$[\![x]\!]$	Jump operator: $[\![x]\!] = (x^+ - x^-)$
$\langle x \rangle$	Mean operator: $\langle x \rangle = \frac{1}{2}(x^+ + x^-)$
$\left\|\left\|\sqrt{\mathcal{H}}\, a\right\|\right\|^2_{\mathbf{L}^2(l_e)}$	Abusive notation for $\int_{l_e} a \cdot \mathcal{H} \cdot a dl$, with $\mathcal{H}$ definite positive
$\left\|\left\|\sqrt{\mathcal{H}}\, a\right\|\right\|^2_{\mathbf{L}^2(s)}$	Abusive notation for $\frac{1}{2}\left\|\left\|\sqrt{\mathcal{H}}\, a\right\|\right\|^2_{\mathbf{L}^2(\partial l_e)}$
$\|\|\|\boldsymbol{u}\|\|\|$	Energetic norm defined for the weak discontinuous Galerkin form

$\ll$ x $\gg$	mathematical operator defined such as its value is null if x is negative and to x otherwise: $\ll x \gg = x$ if $x \geq 0$ and 0 otherwise

Variables

Scalar variables

α_F	Weighting factor of inertial forces for time integration algorithm of Hulbert-Chung
α_M	Weighting factor of external and internal forces for time integration algorithm of Hulbert-Chung
α_s	Boolean value to implement fracture criterion: $\alpha_s = 1$ if fracture and 0 otherwise
β	Fracture modes coupling parameter (*i.e.* $\beta = \frac{K_{IIc}}{K_{Ic}}$)
β_N	First Newmark parameter
β_i	i^{th} non dimensional stability parameters of the discontinuous Galerkin weak form of a thin body
B	Width of the damage localization band
c_d	Dilatational wave speed
γ	Second Newmark parameter
γ_s	Safety factor on the critical time step for explicit time integration
δ_{ij}	Kronecker symbol
Δ	Unidimensional cohesive opening displacement
Δ_c	Equivalent critical opening of crack lips
$\Delta_n^\star$	Normal effective opening of the cohesive law
$\Delta_t^\star$	Tangential effective opening of the cohesive law
$\Delta_{max}^\star$	Effective maximal opening of the cohesive law reached during the simulation
D	Damage variable
D_c	Critical damage value
D_f	Final damage value
Δt	Time step size
Δt_{crit}	Critical time step for explicit time integration
ε_{ijk}	Component $i, j, k \in [1\,;3] \times [1\,;3] \times [1\,;3]$ of Levi-Civita tensor
η_I	Coupling parameter between resultant cohesive efforts giving a mode I opening
η_{II}	Coupling parameter between resultant cohesive efforts giving a mode II opening
E	Young modulus
E_{tot}	Total energy
G	Energy dissipate by a fracture process
G_c	Fracture energy of the material
h	Thickness of a thin body
$h_{\min}$	Thickness coordinate of the lower skin of a thin body

$h_{\max}$	Thickness coordinate of the upper skin of a thin body
h_I^{eq}	Equivalent thickness for membrane/bending coupling of fracture mode I
h_{II}^{eq}	Equivalent thickness for in-plane shearing/torsion coupling of fracture mode II
$\overline{h}$	Hardening coefficient
h^s	Characteristic size of an element
I_p	Polar moment of mass inertia
I	Moment of inertia
j	Determinant of the deformation gradient with respect to the inertial frame
$\overline{j}$	Determinant of the deformation gradient with respect to the inertial frame evaluated on the neutral axis
J	Jacobian of the two-point deformation gradient
$\overline{J}$	Jacobian of the two-point deformation gradient evaluated on the neutral axis
J-integral	J-integral
K	Bulk modulus
K_{Ic}	Fracture toughness in mode I
K_{IIc}	Fracture toughness in mode II
λ	Undefined pressure
λ_h	Describes a change of shell thickness due to deformations
L	Length of the Euler-Bernoulli beam
l_e	Length of an element of an Euler-Bernoulli beam
μ	Shear modulus
μ_c	Frictional Coulomb coefficient
M	Nodal mass (scalar)
M_B	Bending moment of a beam
m	Nodal mass of the diagonalized mass matrix (scalar)
$\left\langle \tilde{m}^{22} \right\rangle_{\text{coh}}$	Bending contribution to the cohesive law
$\left\langle \tilde{m}^{21} \right\rangle_{\text{coh}}$	Torsion contribution to the cohesive law
M_{coh}	Unidimensional resultant bending cohesive stress
ν	Poisson ratio
ν_α	Inplane outward unit normal along α to a Cosserat plane
$\nu_{B\alpha}$	Inplane outward unit normal to a beam (used at interface element)
n	Number of nodes of a system
$\left\langle n^{22} \right\rangle_{\text{coh}}$	Tensile contribution to the cohesive law
$\left\langle n^{21} \right\rangle_{\text{coh}}$	Shearing contribution to the cohesive law
N_{coh}	Unidimensional resultant membrane cohesive stress
N	Shape function
N_B	Tensile effort of a beam

p	Pressure
p_B	Distributed load applied on a beam
ρ	Density
$\overline{\rho}$	Reduced density defined in the shell formulation
$\overline{\rho}_B$	Density by unit of surface
ρ_d	Spectral radius of the time integration algorithm of Hulbert-Chung
σ_{eff}	Effective stress used in the fracture criterion
σ_c	Strength used as fracture criterion in tension (*i.e.* fracture if $\sigma_{\text{eff}} > \sigma_c$ with $\sigma_{\text{eff}} \geq 0$)
σ_Y^0	Initial yield stress
σ_v	Von Mises yield stress
τ_c	Shearing strength used as fracture criterion in shearing (*i.e.* fracture if $\lvert\sigma_{\text{eff}}\rvert > \tau_c$)
t	Unidimensional cohesive traction
Tol	Tolerance of Newton-Raphson algorithm
U_{int}	Internal energy
V	Volume
V_B	shearing effort of a beam
w_g	Weight of Gauss point
W	Hyperelastic potential
W_{ext}	External work
W_{int}	Internal work
ξ^I	Coordinate of the shell in the reference frame, $I \in [1\,;\,3]$
Y	Damage energy release rate
Y_c	Threshold of deformation energy yielding damage

Vectors

$\boldsymbol{B}$	Body forces per unit volume
$\delta\boldsymbol{x}$	Kinematic admissible virtual displacement
$\Delta\boldsymbol{x}$	Positions increment during Newton-Raphson resolution
$\boldsymbol{\Delta}$	Cohesive displacement opening vector
$\boldsymbol{E}_I$	I^{th} Vector of the inertial (orthogonal) reference frame, $I \in [1\,;\,3]$
$\boldsymbol{F}_{ext}$	External forces
$\boldsymbol{F}_{inertial}$	Inertial forces
$\boldsymbol{F}_{int}$	Internal forces
$\boldsymbol{F}_{reac}$	Reaction forces
$\boldsymbol{g}_I$	I^{th} vector of the shell deformation gradient which corresponds by definition to the I^{th} vector of the convected frame, $I \in [1\,;\,3]$

$\boldsymbol{g}^I$	I^{th} vector of the conjugated frame to the convected frame, $I \in [1;3]$
$\boldsymbol{F}^{be}_{int\,n}$	Elementary internal membrane force vector of the Euler-Bernoulli beams formulation
$\boldsymbol{F}^{be}_{int\,b}$	Elementary internal bending force vector of the Euler-Bernoulli beams formulation
$\boldsymbol{F}^{bs}_{int\,cons\,n}$	Elementary consistent membrane internal force vector of the Euler-Bernoulli beams formulation
$\boldsymbol{F}^{bs}_{int\,comp\,n}$	Elementary compatibility membrane internal force vector of the Euler-Bernoulli beams formulation
$\boldsymbol{F}^{bs}_{int\,stab\,n}$	Elementary stability membrane internal force vector of the Euler-Bernoulli beams formulation
$\boldsymbol{F}^{bs}_{int\,cons\,m}$	Elementary consistent bending internal force vector of the Euler-Bernoulli beams formulation
$\boldsymbol{F}^{bs}_{int\,comp\,m}$	Elementary compatibility bending internal force vector of the Euler-Bernoulli beams formulation
$\boldsymbol{F}^{bs}_{int\,stab\,m}$	Elementary stability bending internal force vector of the Euler-Bernoulli beams formulation
$\boldsymbol{F}^{bs}_{int\,stab\,a}$	Elementary stability shearing internal force vector of the Euler-Bernoulli beams formulation
$\boldsymbol{F}^{bs}_{int\,coh\,n}$	Elementary cohesive membrane internal force vector of the Euler-Bernoulli beams formulation
$\boldsymbol{F}^{bs}_{int\,coh\,m}$	Elementary cohesive bending internal force vector of the Euler-Bernoulli beams formulation
$\boldsymbol{F}^{e}_{iner}$	Elementary inertial force vector of the Kirchhoff-Love shells formulation
$\boldsymbol{F}^{e}_{int\,n}$	Elementary internal membrane force vector of the Kirchhoff-Love shells formulation
$\boldsymbol{F}^{e}_{int\,b}$	Elementary internal bending force vector of the Kirchhoff-Love shells formulation
$\boldsymbol{F}^{s}_{int\,cons\,n}$	Elementary consistent membrane internal force vector of the Kirchhoff-Love shells formulation
$\boldsymbol{F}^{s}_{int\,comp\,n}$	Elementary compatibility membrane internal force vector of the Kirchhoff-Love shells formulation
$\boldsymbol{F}^{s}_{int\,stab\,n}$	Elementary stability membrane internal force vector of the Kirchhoff-Love shells formulation
$\boldsymbol{F}^{s}_{int\,cons\,m}$	Elementary consistent bending internal force vector of the Kirchhoff-Love shells formulation
$\boldsymbol{F}^{s}_{int\,comp\,m}$	Elementary compatibility bending internal force vector of the Kirchhoff-Love shells formulation
$\boldsymbol{F}^{s}_{int\,stab\,m}$	Elementary stability bending internal force vector of the Kirchhoff-Love shells formulation

$\boldsymbol{F}^{s}_{int\,stab\,a}$	Elementary stability shearing internal force vector of the Kirchhoff-Love shells formulation
$\boldsymbol{F}^{s}_{int\,coh\,n}$	Elementary cohesive membrane internal force vector of the Kirchhoff-Love shells formulation
$\boldsymbol{F}^{s}_{int\,coh\,m}$	Elementary cohesive bending internal force vector of the Kirchhoff-Love shells formulation
$\boldsymbol{l}$	Resultant across-the-thickness stress vector
$\boldsymbol{l}_B$	Resultant across-the-thickness stress vector of an Euler-Bernoulli beams
$\boldsymbol{m}^{\alpha}$	Reduced bending stress along axis α
$\tilde{\boldsymbol{m}}^{\alpha}$	Bending resultant stress along axis α
$\widehat{\tilde{\boldsymbol{m}}}^{\alpha}$	Bending resultant stress along axis α formulated in the basis of the interface
$\boldsymbol{m}^{\alpha}_{B}$	Bending resultant stress along axis α for Euler-Bernoulli beams
$\boldsymbol{n}^{\alpha}$	Reduced membrane stress along axis α
$\tilde{\boldsymbol{n}}^{\alpha}$	Membrane resultant stress along axis α
$\widehat{\tilde{\boldsymbol{n}}}^{\alpha}$	Membrane resultant stress along axis α formulated in the basis of the interface
$\boldsymbol{n}^{\alpha}_{B}$	Membrane resultant stress along axis α for Euler-Bernoulli beams
$\tilde{\boldsymbol{m}}^{\mathcal{A}}$	Resultant external torque
$\boldsymbol{n}^{\mathcal{A}}$	Resultant external surface traction
$\boldsymbol{\nu}$	Outward unit normal of the shell in the inertial frame
$\boldsymbol{\nu}_B$	Outward unit normal of the beam in the inertial frame
$\boldsymbol{t}$	Direction of the Cosserat surface
$\dot{\boldsymbol{w}}_{\boldsymbol{t}}$	Rotational inertia
$\boldsymbol{u}$	Small displacement field to the exact solution
$\boldsymbol{u}_h$	Small displacement field corresponding to the discretized solution of the problem
$\boldsymbol{T}$	Cohesive traction vector

Second order tensors

$\mathbf{C}$	Right Cauchy strain tensor
$\mathbf{C}^{e}$	Right elastic Cauchy strain tensor
$\boldsymbol{\varepsilon}$	Cauchy strain tensor (small strain)
$\mathbf{F}$	Deformation gradient
$\mathbf{I}$	Unity tensor (order 2)
$\mathbf{K}$	Stiffness matrix
$\boldsymbol{K}^{be}_{int\,n}$	Elementary internal membrane stiffness matrix

$\boldsymbol{K}^{be}_{int\,b}$	Elementary internal bending stiffness matrix
$\boldsymbol{K}^{bs}_{int\,consn}$	Elementary consistent membrane internal stiffness matrix
$\boldsymbol{K}^{bs}_{int\,compn}$	Elementary compatibility membrane internal stiffness matrix
$\boldsymbol{K}^{bs}_{int\,stabn}$	Elementary stability membrane internal stiffness matrix
$\boldsymbol{K}^{bs}_{int\,consm}$	Elementary consistent bending internal stiffness matrix
$\boldsymbol{K}^{bs}_{int\,compm}$	Elementary compatibility bending internal stiffness matrix
$\boldsymbol{K}^{bs}_{int\,stabm}$	Elementary stability bending internal stiffness matrix
$\boldsymbol{K}^{bs}_{int\,staba}$	Elementary stability shearing internal stiffness matrix
$\boldsymbol{K}^{bs}_{int\,cohn}$	Elementary membrane cohesive internal stiffness matrix
$\boldsymbol{K}^{bs}_{int\,cohm}$	Elementary bending cohesive internal stiffness matrix
$\boldsymbol{M}^{be}$	Elementary mass matrix of Euler Bernoulli beams
$\boldsymbol{\Phi}$	Deformation mapping
$\mathbf{P}$	First Piola-Kirchhoff stress tensor
$\mathbf{PK}$	Second Piola-Kirchhoff stress tensor
$\boldsymbol{\sigma}$	Cauchy stress tensor
$\tilde{\boldsymbol{\sigma}}$	Effective Cauchy stress tensor (for damage theory)
$\boldsymbol{\tau}$	Kirchhoff stress tensor
$\mathbf{T}$	Push-forward tensor is used to change the metric of shell
$\boldsymbol{\chi}$	Two-point deformation mapping

Fourth order tensors

$\mathcal{H}$	Hooke tensor
$\mathcal{C}$	Tangent modulus of the material law

Manifold

$\mathcal{A}$	Cosserat mid-plane surface of a shell
$\mathcal{C}^0$	Manifold of continuous mathematical functions
$\mathcal{C}^1$	Manifold of continuous mathematical functions with a continuous first derivative
$\mathcal{C}^2$	Manifold of continuous mathematical functions with both first and second derivatives continuous
$\mathbf{L}^2$	Lebesgue space of dimension 2
$GL_+(3,\mathbb{R})$	The invertible Lie group of dimension 3 with a positive Jacobian
$\mathbb{R}$	Mathematical manifold of real numbers
S^2	The unit sphere manifold
$\mathcal{S}$	Volume representing a shell in the reference frame
$\mathcal{S}_0$	Volume representing the reference configuration of a shell in the reference frame

Chapter 1

Introduction

Use of raw materials is streamlined by environmental and economic reasons. Indeed, the recent worldwide awareness of environment conservation leads to limit the quantity of raw materials used in different goods. In fact, if less material is used their extraction as well as their carriage impacts decrease their environmental cost. Furthermore, the takeoff on financial markets of raw materials prices reinforces this point as industrialists tend to produce with the smallest factory price. An obvious consequence of this reduction of raw material is the thinner design of some components. For example, pressurized gas cylinders or safety barriers are designed with a smaller thickness than in the past. However it is important to ensure their safe mechanical behavior in case of problems. Indeed a gas cylinder has to support an amount of overpressure and a safety barrier has to hold a car impacting it, motivating the development of numerical tools predicting the fracture of thin bodies.

The complexity of crack mechanics limits the recourse to analytical models to very simple situations, which leads during the last three decades to the development of some numerical methods. The scope of the present thesis comes within this context and contributes in this field. In particular, it focuses on the dynamic crack initiation and propagation in large problems (*i.e.* problems involving a large number of degrees of freedom) with a special care to pressurized components.

Toward this end, we present first in the Chapter 2 a review of the different methods developed in computational mechanics to model crack initiation and evolution. We show that the actual popular technique XFEM is well suited to model a quasi-static crack propagation in the context of linear elastic fracture mechanics. Nevertheless, its applicability in dynamics is still challenging especially for large problems. Besides, for this specific case, a new method combing cohesive zone method (CZM) and the discontinuous Galerkin (DG) formulation has been recently presented. This combination suggested by J. Mergheim *et al.* [157] and R. Radovitzky *et al.* [228, 211] allows avoiding the usual drawbacks of the cohesive element insertion (as lengthy discussed in Chapter 2) to model the crack initiation and propagation in a manner that is well designed for a parallel implementation. In fact, industrial components require models with a lot of degrees of freedom, especially in the case of tearing, as a very thin mesh is needed to well capture the crack path. Thus the recourse to parallel implementation is mandatory, on one hand, to reduce the computational time and, on the other hand,

to avoid memory issues. Nevertheless, this framework is presented in the literature for 3D elements only. Since the problems investigated in this work concern thin bodies, we formulate an original adaption to thin structure formulations. Indeed, modeling thin structures with 3D elements leads to an excessive number of degrees of freedom motivating the development of special formulations for thin bodies. However, such a full-DG formulation is lacking in the literature. Therefore in a first time, we develop a full-DG formulation for non linear thin structures. Once this formulation obtained, we can simulate the continuum part of the deformation with discontinuous elements and in a second time, we develop an original cohesive law adapted to thin structures to model a crack. Afterward, the study of the crack initiation and propagation is performed by a combination of the full-DG formulation with an extrinsic cohesive law. Such a law models, on phenomenological basis, the work of separation required to separate the crack lips. It is called extrinsic as it is used to model only the fracture process by opposition to intrinsic cohesive laws which also model the continuous deformations.

These developments are first realized in the case of linear Euler-Bernoulli beams in the Chapter 3. In fact, the particular case of beams allows performing several simplifications leading to a more understandable formulation that can be developed in an easier way. We start from the Euler-Bernoulli beam theory to develop a space discontinuous discretization of the beam. This discretization is based on the previous works of G. Engel *et al.* [91] where they presented a space continuous method but where the DG method is used to ensure weakly the $\mathcal{C}^1$ continuity (*i.e.* the continuity of the slope). Such a method has the advantage to be a one-field formulation (*i.e.* the nodal unknowns are only the spatial displacements). Starting from this formulation, we add interface terms to guarantee weakly the continuity of displacements and thus to have a full-DG formulation of the problem. We show that a consistent and stable discontinuous formulation can be obtained using the DG method, which ensures weakly the continuity at interfaces between elements, by adding some interface integral terms in the formulation. Furthermore, we illustrate the numerical properties of our original formulation through a numerical benchmark. We demonstrate that our formulation provides results as accurate as other methods coming from the literature. Afterward as the thickness is implicitly modeled in a thin bodies formulation, we develop an original cohesive law based on the resultant tension and bending stresses of the beam and we demonstrate that our model respects the energetic balance by dissipating the expected amount of energy during crack propagation.

The Chapter 4 suggests an original extension to Kirchhoff-Love shells formulation of our full-DG formulation presented in Chapter 3 for beams. This original shell formulation is shown to have numerical properties of consistency, stability and of optimal convergence rate in two different norms. Furthermore, we prove through several numerical benchmarks of continuum mechanics that this novel full-DG shell formulation provides results as accurate as other (continuous) methods coming from the literature. These examples include large deformations and plasticity to demonstrate with success the ability of our method in these conditions. As previously mentioned, a parallel implementation is needed to perform industrial problems and we present a novel original parallel implementation of the method, which is proved to be highly scalable on numerical examples. This implementation is performed in an open source software Gmsh [105], written in C++, allowing for the treatment of large problems.

Afterward, the Chapter 5 shows how the cohesive model developed for beams in Chapter 3 can be generalized to shells. The combination of this cohesive law with the full-DG formulation of shells presented in Chapter 4 provides a versatile and powerful framework to study dynamic crack initiation and propagation in thin bodies. Toward this end, we show through several numerical benchmarks that our framework is able to model crack propagation in notched specimen, as well as fragmentation due to acceleration. In particular, a model of the blast of a notched pressurized cylinder is presented. In this example, the deformations lead to plasticity before the propagation of the crack. It is shown, by comparison with experimental data coming from the literature that our framework can predict this crack propagation with the correct crack speed only if the elasto-plastic behavior is included in the formulation.

Finally, as perspective to this thesis we provide the basis to extend the DG/ECL framework to the ductile fracture in Chapter 6. We keep the same approach and we suggest modeling the damage in the constitutive behavior. A cohesive element can be inserted to model the apparition of a crack when a criterion based on a critical damage value. This concept is illustrated through an example demonstrating that the obtained results are qualitative although some improvements will be necessary to obtain quantitative ones.

Chapter 2

Computational fracture mechanics: review & contributions

The outcomes of this thesis are based on the combination of two main concepts: the Cohesive Zone Model (CZM) and the Discontinuous Galerkin (DG) method. Both concepts were developed independently during three decades before their recent combination to solve fracture mechanics problems by several authors as J. Mergheim *et al.* [157], R. Radovitzky *et al.* [211, 228, 137] or M. Prechtel *et al.* [210] for 3D problems. The cohesive zone method is used to model the fracture work inherent to new crack surface initiation. Therefore, this method can be coupled with the Finite Element (FE) method to model crack initiation or propagation at interface of elements in an appealing way. Unfortunately, the introduction of cohesive elements is an issue with Continuous Galerkin (CG) formulations as it has to introduce a discontinuity in a continuous mesh. Some ideas have been developed but the recourse to DG methods is very appealing in this case as it allows taking into account discontinuities in the unknowns fields. The continuity is then ensured weakly by interface terms. These ones can be used advantageously to insert the cohesive elements leading to a very simple and elegant implementation of the CZM.

Furthermore, DG/CZM framework is not the only way to compute fracture phenomena and other methods, as Linear Elastic Fracture Mechanics, meshless methods or enrichment methods (EFEM, XFEM), are also developed in the literature. Therefore, we summarize all these methods (with more developments for the chosen approaches) to justify the relevance of the development of a totally original DG/CZM framework for thin bodies formulation under dynamic loading. Finally, the perspectives of this review will be exploited in the next chapters to develop such a framework in an original way.

2.1 Linear Elastic Fracture Mechanics and its extension to the non linear range

The origin of fracture mechanics analysis comes from the determination of different fracture quantities (stress intensity factors, fracture energy release or J-integral) under linear elas-

tic assumption. This one is restrictive but is a good starting point for materials and geometries leading to a confined plastic zone at the crack tip. This method considers an initial crack and therefore cannot model a fracture initiation. taill The most commonly used criterion to

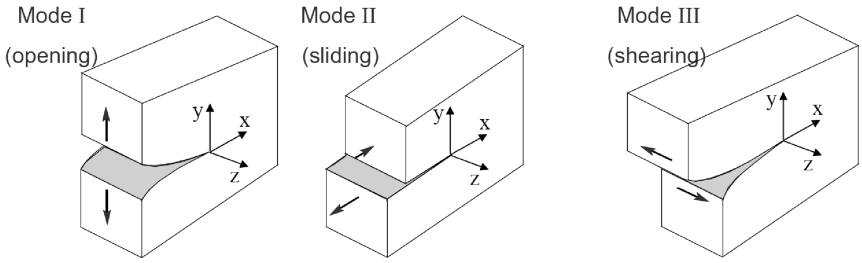

Figure 2.1: Illustration of the three fracture modes.

predict fracture resistance is based on stress intensity factors or fracture energy release. The stress intensity factors approach was presented by G. Irwin [126], where he introduced the three fracture modes depicted on Fig. 2.1: the mode I related to a normal opening, the mode II related to a sliding and mode III relative to a shearing (out-of-plane). For each mode he solved the problem of an infinite plate with a crack and extracted a stress intensity factor K. He demonstrated that near the crack tip, this one is governed by a term in $\frac{1}{\sqrt{r}}$, where r is the distance from the crack tip. This solution leads to an unphysical infinite stress at the crack tip due to the neglecting of plasticity. With this development he postulated that the stress intensity factors depend on the length of the crack and on a function taking into account the geometry. To predict the fracture resistance, the fracture toughness K_c is evaluated by experiments. If an equivalent stress intensity factor (combining K_I,K_{II} and K_{III}) of a component is larger than K_c, the crack begins to propagate.

Another fracture quantity developed by A. Griffith is the fracture energy [109]. He calculated the energy variation of a body due to an infinitesimal crack extension. Indeed, due to crack extension an amount of energy is released, so the total energy has to decrease due to the crack extension. In fact, the fracture process dissipates energy to create new crack surfaces. Phenomenologically, the work of separation process includes a contribution from the intrinsic surface energy γ_s, modeling the energy per unit area requires to form a single new surface after breaking atoms bondings, and a contribution from the plastic work of the process zone W_d. Both contributions are depending on the material, and the second, W_d depends on the geometry and is negligible for brittle materials. In fact by definition, these materials break without significant deformation and therefore show a small (negligible) plastic zone confined at the crack tip. Therefore, calling G_c the energy per unit area dissipated by the fracture process, it comes, for brittle materials, $G_c = 2\gamma_s$, which can be evaluated experimentally. Therefore if the energy released is larger than this material value then the crack propagates.

The third quantity used to characterize fracture is the J-integral concept developed by J. Rice [215]. He suggested to calculate the energy that flows to the crack tip. Indeed, for an uncracked body, the flow of energy through a closed surface is equal to zero, therefore the

computation of the flows parallel to the crack tip is able to characterize the fracture. The concept of J-integral has several advantages compared to the stress intensity factor or fracture energy approaches presented above as it is, in linear elasticity, independent of the path of further crack extension (contrarily to the fracture energy criterion assuming a straight propagation) and it just requires the definition of a potential. Therefore J-integral concept can be used for non linear fracture mechanics contrarily to the stress intensity factor. Notice than equivalence of the three concepts is demonstrated under the assumption of linear elasticity and a straight crack extension.

Since their apparition, these quantities have been used in a lot of practical and industrial applications. Nevertheless, their analytical evaluation is only possible for very simple geometries. Thus, their evaluation for complex geometries is generally performed by numerical methods. The stress intensity factors can be obtained *a posteriori* from a finite element analysis *e.g.* [68, 199, 217, 246]. In fact its value can be approximated thanks to the stress or displacement fields. The last one is generally used as it is more accurate for kinematic formulations. As this technique requires a refinement of the mesh near the crack tip to properly capture the singularity, R. Barsoum [25] suggested to modify the isoparametric elements by moving the middle nodes of a quadratic element to capture more accurately the asymptotic field. Nevertheless the technique remains time consuming due to the mesh refinement.

The crack advance technique [141] allows the evaluation of the fracture energy with a coarser mesh. The fracture energy is just evaluated by a finite difference of energies for two computations of the specimen: on one hand with the size of the crack and on the other hand with the length of the crack with a small extension. This technique is very appealing as many commercial codes supply energy as an output. This concept was extended by D. Parks [198] who introduced the virtual crack extension method to take into account non linear behavior. Furthermore de Lorenzi extended the virtual crack extension [77, 78] to avoid the numerical finite differentiation, which requires two computations.

Some numerical methods were also developed to evaluation the J-integral [215]. It can be easily computed from integration point values along a contour surrounding the crack tip. This technique has the advantage to be path independent for an elastic case and can be used in linear or non linear range as long as there is no unloading. In the case of plastic deformations, unloading can occur and the introduction of an appropriate correction is required [59, 64]. The general formulation of the J-integral, called energy domain integral, was suggested by C. Shih *et al.* [171, 229] and R. Dodds *et al.* [81]. They developed a versatile and powerful framework which can be used for quasi-static or dynamic problems and with elastic, plastic or viscoplastic materials.

The methods presented above are still used today to perform crack propagation. One of the fracture quantities is evaluated and then compared with the critical material value (*e.g.* [51, 120, 143]). If it is larger than this critical value, a remeshing operation is realized to propagate the crack, usually, in the direction of the principal hoop stress as suggested by F. Erdogan *et al.* [92]. In fact, they confirmed by experimental comparisons that the crack propagates in the direction where the stress intensity factor is larger than the toughness of pure mode I loading. Nevertheless, other kinking criteria exist as *e.g.* the one suggested by M.

Hussain *et al.* [124] who consider a global criterion based on the distribution of the energy in the neighboring of the crack tip. Moreover, a micro-void continuum damage model can also be used to determine the direction of the crack propagation as presented by J. van Vroonhoven *et al.* [253]. These three mentioned kinking criteria are compared by P. Bouchard *et al.* [56] who conclude that the criterion of F. Erdogan *et al.* [92] is the easiest to implement while it provides results as accurate as the other ones. As this technique demands small time steps and remeshing operations to follow the crack propagation, it is very time consuming. To avoid the remeshing operations, meshless techniques can also be used [42] (see Section 2.5).

2.2 Cohesive Zone Model

The cohesive zone model (CZM) was pioneered fifty years ago by G. Barenblatt [24] and D. Dugdale [89]. They developed this concept to remove the unphysical infinite stress at crack tip resulting from the linear behavior assumption. Barenblatt focused on brittle elastic bodies with a decomposition of the crack into two regions. He called the physical extent of crack, which is stress free, the ”inner region” and he named ”cohesive region” the crack extension where the surface separation is strangled by surface tractions modeling the fracture work. These tractions model the atomic separation process with a multiscale postulate, see Fig. 2.2, and lead to a finite stress at crack tip under the two following assumptions:

(i) The width of the cohesive region is small compared to the size of the whole crack. This hypothesis is justified by a fast decrease of molecular cohesive forces with the distance between atoms.

(ii) The shape of the cohesive zone is a material parameter independent of the loading conditions. This restrictive hypothesis is needed to have a local distribution of cohesive forces unvarying with loading.

With these two assumptions the singularity at crack tip is avoided by the determination of the cohesive zone size. A few year later, J. Rice introduced the *J*-integral [215] and therefore demonstrated that the second assumption is unnecessary to solve the crack tip singularity problem. Furthermore he proved that the CZM concept is equivalent to the classical Griffith energetic approach [109] for the description of brittle elastic fracture.

Dugdale, on his side, investigated a thin sheet of elastic-perfectly plastic materials with the same idea of removing the crack tip singularity. He postulated that the plastic zone is confined in a small region ahead of the crack tip and defined this region as the cohesive zone. Similarly to Barenblatt the size of the zone is such that it ensures a finite stress a crack tip.

Both models were combined by A. Hillerborg *et al.* [117] to obtain the first numerical implementation of the cohesive zone concept. They inserted such a zone along edge of elements where a crack can be formed. The gradual separation of these ones is governed by a Traction Separation Law (TSL) linking the traction to the opening. The phenomenological observations lead to consider cohesive tractions starting from zero, reaching a maximal value σ_c, which depends on the fracture mode, decreasing to zero for a critical opening Δ_c value

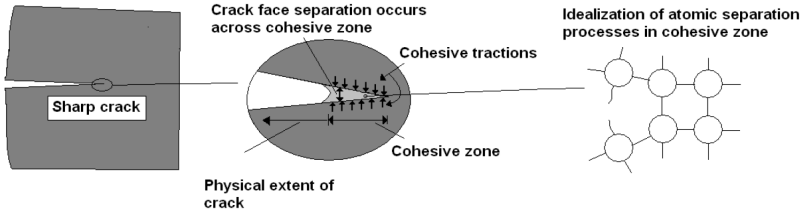

Figure 2.2: Illustration of multiscale postulate of Barenblatt with a decomposition of crack into two regions. (Picture comes from [228]).

and then remaining null as illustrated on Fig. 2.3(a). The value of σ_c is supposed to be a material parameter and the value of Δ_c is chosen by energetic considerations with regards to A. Griffith [109] works,

$$G_c = \int_0^{\Delta_c} \boldsymbol{T}(\boldsymbol{\Delta})\, d\Delta, \tag{2.1}$$

where $\boldsymbol{T}(\boldsymbol{\Delta})$ represents the TSL . This one is either relative to a fracture mode or is an effective law modeling a fracture modes combination. This model was used by A. Hillerborg *et al.* [117] to insert explicitly the discontinuity resulting from crack in a finite element mesh. The cohesive element is simply inserted between bulk elements and the crack appears due to nodal displacement jumps governed by inter-element cohesive tractions.

Furthermore, the application of J-integral on the cohesive zone [215] introduces a cohesive length equal to, for mode I fracture under static loading ($E =$ Young modulus, $\nu =$ Poisson ratio),

$$R = \frac{\pi E G_c}{2(1-\nu^2)\sigma_c^2}, \tag{2.2}$$

which conditions the mesh size. Indeed, the length of cohesive elements has to be sufficiently small to resolve R. For example for the material Al2024-T3, the mesh size is limited to approximately 6[mm] to respect this characteristic size. Therefore for large components the mesh becomes ultra thin and its sequential resolution can be an issue.

Finally, as it was demonstrated experimentally by several authors [108, 129, 131, 132] that the fracture strength is rate dependent, G. Camacho *et al.* [63] introduced a characteristic time of the cohesive zone for dynamic problems,

$$t_c = \frac{\rho c_d \Delta_c}{f_{ts}}, \tag{2.3}$$

with ρ the density, c_d the dilatational wave speed and f_{ts} the maximal quasi-static tensile strength of the material. Note that t_c is not a determining factor of the critical time step of the simulation. The Eq. (2.3) is obtained by G. Camacho *et al.* in formulating the equilibrium of

incident and transmitted wave equilibrium to establish an exponential law relying the dynamic and static values of σ_c,

$$\sigma_c^{dyn} = \sigma_c^{stat} \frac{\exp^{\frac{\tau}{t_c}}}{\exp^{\frac{\tau}{t_c}-1}}, \tag{2.4}$$

where τ is the duration of the pulse of incident wave. The choice of a finite critical opening Δ_c included this characteristic time in the TSL which ensures to a rate insensitive TSL to be strain-rate sensitive as demonstrated by G. Ruiz *et al.* [220] and thus to account for the fracture strength rate dependency.

At this point, the remaining challenging issue concerns the insertion of the cohesive elements for 3D geometries. Indeed, their insertion during the simulation requires topological mesh modifications and therefore a complex implementation. In this case the assorted cohesive law is called extrinsic as it has not to model the reversible continuum part of the deformation. The other approach, used by A. Hillerborg *et al.* [117], inserts the cohesive elements at the beginning of simulations. In this case the assorted cohesive law is called intrinsic as it models the continuum deformation. This cannot be achieved in a consistent way and leads to numerical problems as discussed here below. An example of the TSLs considered in both cases is depicted on Fig. 2.3.

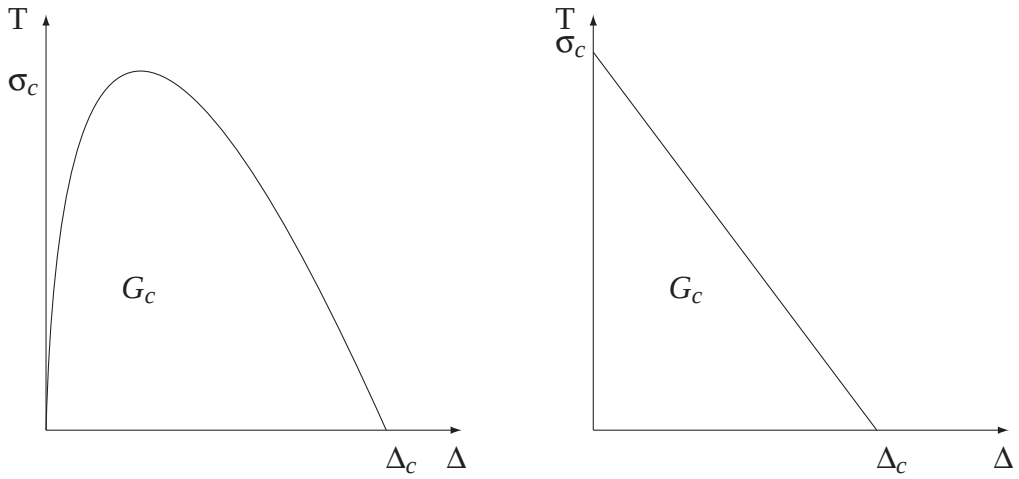

(a) Intrinsic TSL. (b) Extrinsic TSL.

Figure 2.3: Compared to the extrinsic TSL (b) the intrinsic one (a) models the reversible continuum part of the deformation thanks to an initial slope.

2.2.1 Intrinsic cohesive law

Historically the intrinsic cohesive laws were the first developed due to their easy implementation, mainly to solve interface delamination problems. Indeed in this case, the initial

slope of the TSL has a physical meaning, as it represents the interface cohesion, and the cohesive elements can be inserted along a well known crack path. Different shapes of TSL were suggested by several authors to describe different phenomena of decohesion. A. Needleman [175] introduced a polynomial potential law to study the debonding of a spherical inclusion in a ductile matrix (see Fig. 2.4(a)). Despite the fact that the delamination occurs due to the normal opening, A. Needleman took into account the tangential opening in his model. Furthermore, the shape of the TSL suggested by A. Needleman allows to model the behavior of the decohesion (*i.e.* the normal traction increases, reaches a maximal value and then decreases until zero for a finite critical opening). Even if it is not motivated by experimental evidences, the choice of a polynomial potential form leads to a path independent law. Finally, it has to be mentioned that this polynomial law is restricted to normal opening dominated problems.

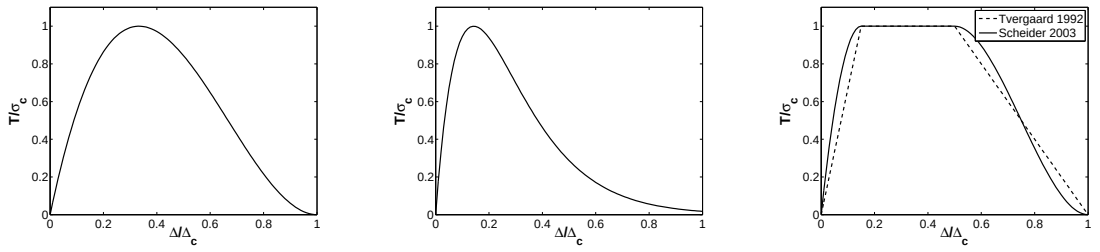

(a) Polynomial [175]. (b) Exponential [176]. (c) Trapezoidal [249, 225].

Figure 2.4: Different shapes of the intrinsic cohesive law for a uniaxial tension test.

This limitation is removed by an extension of the polynomial potential cohesive model supplied by V. Tvergaard [247]. In fact the initial model of A. Needleman was inefficient in case of mixed mode with a high normal compression as it leads to a negative normal opening. Therefore, V. Tvergaard suggested, considering a unidimensional effective opening, to model mixed mode fracture. However, as he focused on interface debonding in a fiber-reinforced metal matrix composite, the mixed mode capability of the model is not demonstrated. Indeed, pure normal separation occurs at the fiber tips and pure tangential separation occurs for fiber pull-out. Moreover, V. Tvergaard highlighted the necessity to conduct experiments to determine correct values of cohesive parameters like σ_c. This one is still generally considered as a constant despite it is known that it can vary due to material heterogeneities.

With regard to the atomistic simulations conducted by several authors [99, 218, 219], the polynomial shape of the TSL has to be reconsidered. Indeed, the simulations show a universal exponential shape between the binding energy and the atomistic separation. Following these works, A. Needleman [176, 177] adapted his model to take into account this exponential dependency of the normal opening (see Fig. 2.4(b)). Nevertheless, he kept the linear assumption on the tangential component as no data were available in this case. He included also in the model a spatial variation of σ_c to study the decohesion of a viscoplastic block from a rigid substrate under uniaxial plane strain conditions [176], extended to the multiaxial loading in [177].

In this case, as large tangential openings can arise, the linear assumption is not valid and it is replaced by an exponential potential. Therefore, based on phenomenological periodicity of the crystal lattice, the cohesive tractions are considered as periodic despite the fact that it leads to consider null interfacial work over one a period of tangential displacement.

Further simulations performed by G. Bozzolo [57] confirm the periodic behavior of tangential cohesive components in the plane of interface. For complex modes of fracture involving shear and normal separation, X.-P. Xu *et al.* [261] suggested an exponential displacement potential, based on the works of G. Beltz *et al.* [35], who introduced a maximal shearing traction τ_c different from σ_c. Notice that this model ensures the isotropy of the tangential traction in relation to the tangential sliding. X.-P. Xu *et al.* [261] considered this model to study the void nucleation by inclusion debonding in an elastic-plastic crystalline matrix. Afterward, several authors used this model to analyze different problems of dynamic crack growths, for brittle materials [160, 161, 262], for elastic-viscoplastic materials [178, 231], for functionally-graded materials [273] and for interfacial fracture [263, 264].

Although the exponential potential law is suitable for brittle materials it cannot model the dependency of fracture toughness with the plasticity. Toward this end, V. Tvergaard *et al.* developed a trapezoidal cohesive law, first restricted to mode I [249] (see Fig. 2.4(c)), and then for mixed mode fracture [250]. The dwell region introduced in this law is supposed to model the plastic work of the fracture process. In their study they varied the length of the plateau and demonstrated the little effect of the shape of cohesive law on the results except for the initial slope, which the sensitivity is discussed below. I. Scheider *et al.* [225] modified this law by inserting quadratic and cubic functions in place of linear branches to remove the slope discontinuity at the extremities of the dwell region (see Fig. 2.4(c)). With this modified model they successfully simulate the cup cone fracture of a uniaxial tension test in a 2D axisymmetric setting. However, the nature of ductile fracture cannot be modeled by this cohesive law. Indeed, ductile fracture involves nucleation, growth and coalescence of microcavities which cannot be resolved by a cohesive law with constant fracture parameters. To solve this issue V. Tvergaard *et al.* modified their model and considered a σ_c depending on the plastic strain rate [251].

Despite of this improvement, damage models as the Gurson model [110] remain more suitable to describe ductile fracture. Therefore, several works [5, 6, 230, 231, 249] have been realized to merge this continuum damage model with the cohesive approach. The main idea is to considered a representative volume element (RVE) governed by the Gurson model to extract the cohesive law. Nevertheless, it seems that the cohesive values obtained are dependent on the constraints prescribed to the RVE. In another work, V. Tvergaard [248] suggested to govern the cohesive surface by a Gurson model but with a new implementation of the cohesive surface. Finally, J. Oliver *et al.* [121, 187, 189, 188, 222] suggested a new approach where a continuum damage theory is used until the verification of Hadamard criterion [113] relative to the lost of ellipticity of the acoustic tensor. At that time, they inserted a cohesive element to take into account the local and discontinuous nature of fracture.

The specific case of thin structures was addressed in the literature by F. Cirak *et al.* [69, 70] who studied in a first time the petalling of an aluminum plate subsequent to a bullet impact

[70]. Afterward, they used the same model to study the crack propagation in an initially notched pipe subjected to a blast wave [69]. Although they performed the simulations with a shell formulation, they conserved the 3D TSL approach. Therefore to propagate the crack through the thickness they suggested using the Simpson points of the thickness integration. In fact, they computed the fracture criterion at each point and used the cohesive law only at fractured points. Nevertheless, the manner of moving neutral axis during crack propagation for bending dominant problems is not presented in their papers. Furthermore, the use of a TSL based on the stress tensor can be an issue for thin bodies formulations as for these methods, the governing equations are formulated in terms of resultant stresses, *i.e.*, stress tensor integrated on the thickness. Therefore, P. Zavattieri [268, 269] introduced a traction displacement law coupled to a bending moment rotation law to model the through-the-thickness dynamic crack propagation in thin structures. He compared the results of this model with full 3D FE models and showed that they are well correlated.

Whatever the shape of the cohesive law, the intrinsic cohesive elements are inserted at the beginning of the simulation, and thus, have to model the continuum part of the deformation field with an initial slope. This fact leads to some numerical problems as mesh dependency, lift-off and artificial compliance. The mesh dependency was not an issue in the beginning as works mainly focused on delamination or problems with an *a priori* known crack path [175, 176, 177, 247, 249, 252], allowing the insertion of cohesive elements only in a well defined zone. As promising results were obtained, it was natural to extend the method to an *a priori* unknown crack path, which became an output of the simulation. Therefore several authors investigate the fragmentation of brittle materials due to dynamic impact and the crack branching instability problem. Toward this end, X.-P. Xu *et al.* [262] used their exponential cohesive law [261] and inserted a cohesive element between all the bulk ones of their mesh built with quadrilateral elements cut in ”cross triangles” to allow crack branching. Although they modeled with success crack branching, X.-P. Xu *et al.* reported a crack path depending on the triangle orientation. They obtained a straight crack propagation for triangles with a $\pm$ 45 degrees orientation but for triangles oriented at $\pm$ 15 or $\pm$ 30 degrees they obtained a crack path in zigzag. I. Scheider *et al.* [225] noted the same phenomena. Indeed, in their cup cone fracture simulation, they obtained the correct crack path only if the cohesive elements were in the direction of the maximal tangential stress. The convergence of the solution with the mesh was only achieved for crack path confined in a single plane without crack branching as, *e.g.* , reported by A. Needleman [178] in the case of a pure Mode I crack growth in a plane-strain block with a pre-existing central crack subjected to impact tensile loading. Nevertheless, in this case as emphasized by P. Geubelle *et al.* [104], ultra thin meshes are needed to resolve the cohesive zone and achieve convergence.

The second issue related to an intrinsic cohesive law, called lift-off, is a spurious high crack speed. This one is illustrated in [177, 262] and results from the initial opening of elements along a potential crack path which can be close from the critical opening. In this case, a sufficiently large load leads to the instant crack of all these elements and therefore a crack speed faster than expected is observed.

Finally, the last drawback of the intrinsic cohesive law is an artificial compliance of the

material. Indeed, the insertion of cohesive elements which model the continuum part of deformations by an initial slope degrades the elastic modulus of material. The effective modulus becomes, in the case a one-dimensional network of cohesive surfaces at constant spacing h,

$$E_{eff} = E\frac{sh}{E+sh} \tag{2.5}$$

with s the value of the initial slope of the TSL. The softening effect of the cohesive law is negligible only if $sh >> E$, which can only be reached for very large value of s as h is typically the mesh size. Notice that for a constant s this effect will increase with the refinement of the mesh. Furthermore this artificial compliance affects the wave propagation in an anisotropic way for a multidimensional problem. The influence of s was studied by several authors [93,94,95,104,270] who concluded that the wave propagation is not affected if $s > 10\frac{E}{h}$. Nevertheless, a resolution of the initial slope in many steps is required and the time step has to be decreased with the increase of s, which can lead to very large computational time.

The drawbacks of the intrinsic TSL lead to an inefficient framework to study fragmentation problems. Indeed, in this case, interactions and propagation of stress waves play a key role. An accurate resolution can only be achieved for large initial slopes leading to very small time steps and therefore to infeasible 3D large simulations with regard to the computational time required. Beside, to our knowledge, such a case is not reported in the literature[1] and the dynamic fragmentation was only investigated for 2D cases by several authors [94, 95, 96, 160, 261]. They all highlighted a fragment size dependence on the distance between cohesive elements except if they are sufficiently closed. From these studies it is not clear whether the intrinsic TSL can predict fragmentation in case of *a priori* unknown crack paths.

As the initial slope of the TSL inherent to the intrinsic approach leads to the numerical problems highlighted above, several authors developed methods using extrinsic cohesive laws, which can be seen as an intrinsic TSL with an initial infinite slope.

2.2.2 Extrinsic cohesive law

M. Ortiz *et al.* [63, 191] pioneered the investigation of the extrinsic approach, which consists in the insertion of cohesive elements when a fracture criterion is reached. As the continuum part of the deformation has not to be modeled by the cohesive law, an infinite initial slope of the TSL can be considered avoiding artificial compliance, as well as lift-off and stress wave propagation issues. The principal drawback of this approach compared with the intrinsic one, is the topological mesh modifications required during the simulation to insert the cohesive elements. Indeed, with a continuous Galerkin method (*i.e.* with a classical FE method), elements are also continuous and there is the necessity to split nodes at interfaces where fracture occurs to model the crack lips that are initially constrained by an extrinsic cohesive law. A further challenge of the extrinsic approach is to account for the unloading after fracture initiation: the crack can close and as the normal opening cannot become negative, a contact condition has to

[1] There are 3D examples of dynamic fragmentation in literature but they use an extrinsic approach.

be implemented to constrain the normal opening to zero (otherwise this leads to the unphysical interpenetration of the medium). Such a condition is naturally inserted in the intrinsic case where the initial slope of the TSL plays the role of a penalty contact conditions.

The most popular extrinsic cohesive law was suggested by G. Camacho *et al.* [63] and was extended a few years later by M. Ortiz *et al.* [191]. As it was demonstrated from [191,249,250] that the shape of the law, as long as it is monotonically decreasing, has little effects on results for brittle materials, they used a simple linear monotonically decreasing law (as depicted on Fig. 2.3(b)) and postulated that in case of unloading, for a positive effective opening, the relation between traction and opening decreases linearly to zero in a reversible way. They assumed, based on the two first thermodynamic laws [191], that the cohesive law derives from a free energy which allows, as for the intrinsic case, considering a law which derives from a potential. By analogy with the work of V. Tvergaard [247] for intrinsic TSL, they used an effective opening, which combines normal and tangential openings, for mixed modes fracture.

The applications of the extrinsic cohesive approach focus on problems for which the intrinsic one suffers from problems and so concentrate on dynamic fragmentation and crack propagation problems for brittle materials. G. Camacho *et al.* studied [62,63] high rate impacts and fragmentation. Their results were in agreement with the experiments of J. Field [100], which proves the efficiency of the cohesive approach to model crack initiation and propagation. Furthermore, in their 2D benchmarks, they obtained convergence of crack path and crack growth rate for sufficiently small cohesive elements (tens of micrometer) when they used remeshing to propagate the crack independently of the mesh. Afterward, A. Pandolfi *et al.* [193] studied the experiment of D. Grady *et al.* [107] of a ring fragmentation. The ring is submitted to a uniform radial expansion, which leads to multiple simultaneous neck formations where fracture can happen to lead to fragmentation. The simulation reproduced quite well the general behavior of the experiment, but A. Pandolfi *et al.* [193] did not perform a convergence study as the computational cost of the method is high for 3D simulations. Another fragmentation study, performed by E. Repetto *et al.* [214], concentrates on the glass rods. Once again in this experiment they captured the initiation and propagation of the fracture waves.

Moreover, several authors focused on three-point bending simulations [192, 221]. In this case they showed that the extrinsic method is able to predict the time of fracture initiation as well as the shear lips formation at lateral surfaces. For completeness notice that this approach is also used to model in dynamics, crack propagation [220, 267], fatigue problems [179], sandwich components [265, 266] or firearm injuries to the human cranium with 3D models [172].

As all the previous studies reproduced well the fracture phenomena, the proof of convergence with the mesh size was obtained for an *a priori* known crack path, by I. Arias *et al.* [11], who performed (parallel) 2D simulations of pure mode I interfacial fracture of two weakly bonded, pre-notched Homalite plates. They also compared the numerical results with experiments. With the extrinsic approach, they reproduced the crack tip trajectory and velocity with a high level of accuracy.

Nevertheless at first sights, it seemed that for an *a priori* unknown crack path, this one

depends on the mesh size. Indeed, Z. Zhang *et al.* [274] studied the microbranching instability for brittle materials by simulating symmetric loading of a pre-cracked PMMA[2] strip and captured the crack branching. Nevertheless they reported a crack path depending on the mesh. Furthermore, G. Ruiz *et al.* [221] observed the same phenomenon despite they obtained convergence for the load-history curve. Moreover, F. Zhou *et al.* [275] studied the mesh dependency to highlight the circumstances leading to this phenomenon and concluded that a few randomness in the mesh size and orientation allows significantly reducing the mesh dependency. Finally, K. Papoulia *et al.* [197] reported the convergence for a pin-wheel based mesh. Nevertheless, if the spatial convergence seemed to be an issue, the temporal convergence was observed in the different studies.

As well as the convergence of the crack path and crack growth rate, J.-F. Molinari *et al.* [168] studied the convergence of the dissipated energy with respect to the mesh size. They focused first on symmetric impulse loading of a pre-cracked PMMA strip. For this case they reported an increase of the dissipated energy with the mesh size without convergence. In a second time, they studied the fragmentation of a ring meshed with one dimensional elements. They proved the convergence in this simple case, but for a mesh size tending to zero when a uniform mesh is used, as predicted in their earlier works [275]. For meshes with elements of various sizes a monotonic convergence was observed and achieved for ultra thin meshes.

Finally, time discontinuity drawback has to be reported. Indeed, at fracture initiation the stresses computed by the constitutive material law are replaced by values coming from the cohesive law. Therefore the continuity of the stress field is not ensured for mixed mode fracture without special care. K. Papoulia *et al.* [196] highlighted this phenomenon and they demonstrated the non convergence in time and the presence of unphysical oscillations in case of discontinuity.

The extrinsic cohesive framework can therefore be summarized as follow. It seems very appealing to model dynamic fragmentation and crack growth but it requires ultra thin meshes with a randomness on the mesh size and structure to achieve the convergence of the crack growth rate and of the dissipate fracture energy. Nevertheless, ultra thin meshes lead to high computational time and to a difficult management of memory. Indeed, for dissipative materials (as *e.g.* elasto-plastic laws) the history of the material has to be stored during the computation at each integration point. Number of Gauss points increases with the refinement of the mesh leading to memory problems. Both issues (time computation and storage) can be solved with an efficient parallel implementation, which is complicated due to the topological mesh modifications inherent to the insertion of cohesive elements. Beside difficulty of developing a parallel implementation [194], this one can suffer from low scalability unless a graph-based internal structure is used [173, 200]. To avoid this mesh modification, several authors suggested using the extrinsic cohesive law in combination with a DG formulation. Indeed, as the DG method considers discontinuous elements and ensures weakly the continuity between them, the interface elements exist at the beginning of the simulation. Therefore the substitution of an interface element by a cohesive one is straightforward. Note that another method combining advantages of both extrinsic and intrinsic approaches has been developed [4, 204, 232]. It

[2]PMMA = Polymethylmethacrylate

is based on inserting interface elements from the beginning but compatibility is enforced by Lagrangian multipliers, which, in turns, introduces new unknowns.

2.3 Discontinuous Galerkin methods

The main feature of DG methods is their ability to take into account discontinuities in the interior domain. In these methods, the integration by parts takes place element by element leading to interface terms which can be used to ensure weakly the continuity. Historically the first DG methods were introduced to study hyperbolic equations where discontinuities and numerical fluxes are naturally present in the exact solution. The first one was suggested by W. Reed *et al.* [213], who focused on the transport of neutrons. As the equations of mechanics are purely elliptic, the resolution of hyperbolic equations is out of the scope of this work and therefore is not developed herein. Nevertheless, interested reader can refer to [71, 72] for a complete review on this topic. A subsequent work by J. Nitsche [180] uses this technique to prescribed weakly boundary conditions. Furthermore, he suggested the incorporation in the formulation of a quadratic term to stabilize the method.

2.3.1 DG methods for solid mechanics problems

For continuum mechanics problems, the use of DG methods seems at the first sight useless as it considers more degrees of freedom to solve a problem than its CG counterpart. Nevertheless, they can be useful in different situations, in particular to ensure weakly the high order continuity. Indeed, in the beginning of the seventies some authors [15, 20, 84, 85, 205, 259] generalized the hybrid method of T. Pian *et al.* [206] to enforce the $\mathcal{C}^1$ continuity between elements for fourth order elliptic equations of thin body formulations. Nevertheless after these initial developments, the interest for this technique vanished to the benefit of the method combining displacement and rotation [58]. This well established technique uses independent $\mathcal{C}^0$ interpolation for displacement and rotation and enforce the $\mathcal{C}^1$ continuity through the shearing equation. This technique is very appealing from the implementation viewpoint but has the drawbacks of considering more degrees of freedom and can suffer from locking without special care. More recently, with regards to this issue, G. Engel *et al.* [91] suggested a new framework coupling CG and DG methods. Extending the past idea [15,20,84,85,180,205,259] they obtained a one-field formulation of Euler-Bernoulli beams and Kirchhoff plates. The use of $\mathcal{C}^0$ shape functions allows having recourse to continuous elements and the DG method is used at element interfaces to ensure in a weak manner the $\mathcal{C}^1$ continuity. Some improvements were brought by several authors [115, 257], who applying also the technique to strain gradient damage theory [167, 258]. Furthermore, this framework was extended to Kirchhoff-Love shells by L. Noels *et al.* , first with linear elasticity assumption [185] and in the second time to the non linear range [181]. Note that in this thesis, we suggest an original extension to full discontinuous elements (*i.e.* $\mathcal{C}^0$ is also weakly ensured) of this one-field shell formulation for further combination with ECL.

DG methods can also be useful for hp-adaptive meshes, even if it appears that this technique is commonly used for fluid mechanics [27, 49, 119] and is less developed for solid mechanics. Indeed hp-adaptivity consists in the local refinement of the mesh with elements not necessary of the same order yielding hanging nodes. The enforcement of continuity trough elements becomes an issue. Several continuous techniques exist [46, 47, 58] but the DG methods are very appealing in this case as the weak enforcement of continuity at interfaces does not require element of the same order nor conforming meshes [16, 118].

Another advantage of DG methods is that they reduce considerably the locking effects which can arise from finite element discretization. This phenomenon is particularly important for thin bodies where the membrane and bending modes are coupled. The common solution used in this case is the recourse to reduced integration [38, 271] or mixed formulation eventually coupled with assumed stains methods [28, 29, 233, 234]. Nevertheless, several authors used, with success, DG methods in this situation for beams [67, 66], plates [17] or shells [112, 111] elements.

One interesting feature appears when using DG methods in combination with the cohesive zone theory, which is the main aim of this thesis.

2.3.2 DG methods combined with extrinsic cohesive law

As a result of previous sections it appears that an efficient framework to solve dynamic fragmentation or crack propagation problems can be obtained by coupling the DG method and the extrinsic cohesive approach. Indeed, the major difficulty of this last one is the insertion of the cohesive elements at the onset of fracture. Nevertheless, as interface elements are naturally present for the mesh in the DG method, this interface element can be very easily replaced by a cohesive one when a fracture criterion is reached. Such a framework has been pioneered by J. Mergheim *et al.* [157] , R. Radovitzky *et al.* [211, 228] and M. Prechtel *et al.* [210].

Firstly, J. Mergheim *et al.* focused on mixed continuous and discontinuous Galerkin formulation first for linear elasticity [157] and then they extended the method to non linear elasticity [159]. They simulated composite material examples with a well known crack path and therefore inserted discontinuous elements only along this crack path. They observed a convergence of the results with the mesh size.

Afterward, R. Radovitzky *et al.* [211, 228] studied with this approach the longitudinal wave propagation and the resulting spall of an elastic bar. They proved that, contrarily to the intrinsic cohesive element approach, the use of discontinuous Galerkin elements does not affect the wave propagation (*i.e.* the wave propagates through discontinuous elements exactly as if they were continuous). Furthermore they suggested a scalable parallel implementation of the framework opening perspectives to treat ultra thin meshes and they revisited the high-velocity impact of ceramic plates by a hard spherical projectiles studied before in 2D with axisymmetric assumption by G. Camacho *et al.* [63]. This time R. Radovitzky *et al.* simulated this problem with a full 3D model and they captured the complex 3D fracture pattern. Moreover, in case of crack closure they introduced back the normal DG components to avoid interpenetration.

Recently, M. Prechtel *et al.* investigated the *a priori* unknown propagation of crack in a 2D composite [210]. As the fracture energy is dependent on the geometry of the fibers they implemented an optimization algorithm to obtain the best design of the fibers shape [209].

Finally, R. Abedi *et al.* [1,2,3] developed a space-time discontinuous Galerkin method for 2D elasto-dynamic problems. Their method respects energetic balance for linear and angular momentum over every space-time element and is well designed to capture shock wave without spurious oscillations. They coupled their method with an extrinsic cohesive law to model crack propagation and used an unstructured space time grid which is refined near the crack tip. Mesh independent crack propagation and convergence of crack path were observed with the refinement. Therefore their method is very accurate and efficient. Nevertheless it is very difficult to implement in a standard FE code as the usual time integration procedure has to be replaced by a more complicated space-time grid integration.

2.4 Enrichment methods

The main idea of enrichment methods is the enhancement of the unknown (displacement) field to take into account a discontinuity. In fracture mechanics, this one represents a crack which can propagates without necessary following the boundary of the mesh, as the discontinuity can pass through an element. Two kinds of enrichment have been suggested in the literature. On the one hand, the Extended Finite Element Method (XFEM), pioneered by N. Moës *et al.* [165] and T. Belytschko *et al.* [36], considers a nodal enrichment, and on the other hand the Embedded Strong Discontinuity Finite Element Method (EFEM), firstly developed by F. Armero *et al.* [12, 13, 14, 145, 146] uses the elements as support for the enrichment. The main advantage of EFEM compared to XFEM is inherent to its local enrichment which allows static condensation at elementary level and therefore facilitates its implementation in a standard FE software as the number of unknowns of the system remains constant during whole the computation. F. Armero and his coworkers, first studied the strain localization in inelastic materials [12], and afterward they investigated the crack propagation [145], by solving several elementary problems with 2D solid elements under the small strain assumption. Their embedded discontinuities method includes a cohesive law to model the fracture process. Then, they extended the method to large deformations [13], to dynamic fracture [14] and to crack branching [146]. Furthermore, G. Wells *et al.* focused on 3D problems [256]. Nevertheless, EFEM does not ensure the continuity of the crack through elements but, regardless, convergence of the results is obtained. But recently, several authors [79,212] improved the EFEM with the use of interface elements and considered discontinuities parallel to the edges or the facets of the mesh. Proceeding this way, they ensured the continuity of the crack propagation. J. Oliver *et al.* [190] compared EFEM and XFEM. They showed the methods converge with the same rate to the same results. Furthermore, they obtained more accurate results with EFEM for coarser meshes at a lower computational cost, especially in case of crack branching. Nevertheless, it seems that the XFEM remains the most popular method today and less attention is focused on EFEM.

The first uses of XFEM methods focused on specimen with an initial crack as *e.g.* the work

of N. Moës *et al.* [165] where they enhanced the nodal unknowns with Heaviside functions and with the asymptotic solution of LEFM, allowing for the capture the material behavior at the crack in an accurate way. They used the hoop stress criterion to propagate the crack. Then, these authors improved the method to model 3D crack propagation [242] as well as crack branching or intersecting [75].

Afterward, several authors modeled the displacement jump with a level set method [43, 163], which allows combining the XFEM with the cohesive approach. Thanks to the level sets they computed the jump between crack lips and the resulting cohesive traction. Toward this end, R. de Borst *et al.* [55] developed the so called "cohesive crack segment" technique to avoid any mesh bias. An extrinsic cohesive element can be inserted without mesh modification but new unknowns have to be inserted in the resolution system. N. Moës *et al.* [163] add extra enrichment functions (different from the LEFM asymptotic solution) to resolve the stress concentration near the crack tip. Nevertheless it seems that this extra enrichment is not necessary [277]. As the crack does not follow element boundaries in this method, the maximal hoop stress criterion is still used to determine the direction of crack propagation. J. Mergheim *et al.* extended the approach to inelastic material behavior [158] and R. de Brost *et al.* extended it to damage [54].

Afterward, T. Elguedj *et al.* [90] used the Hutchinson-Rice-Rosengren elasto-plastic fields [125, 216] to obtain elasto-plastic enrichment functions. Nevertheless, they kept the assumption of confined plasticity to study the fatigue crack growth in notched specimen. Then, B. Prabel [208] extended this approach to dynamic crack propagation.

These methods cannot take into account a crack initiation and only propagate existing crack. The model of crack initiation with the XFEM was achieved by P. Areias *et al.* [7], where they considered the damage as fracture initiation criterion. Recently, using the same idea N. Moës *et al.* [166] suggested the thick level set approach[3] where a crack is inserted when a damage criterion is reached.

The XFEM method was applied to a large set of mechanical problems involving composite materials [18, 82, 174], contact [37, 128], dynamic propagation [156], multiscale [101, 164] among others. Moreover, the approach was also applied to shell structures on one hand by P. Areias *et al.* [8, 10] for static propagation and on the other hand by R. Larsson *et al.* [98, 133] for dynamic crack growth. In particular, the last reference studies a notched pressurized cylinder by combining the XFEM and the cohesive approach. Despite of the shell elements reduce the computational cost of thin structure problems they fail to model accurately a 3D crack propagation. To overcome this issue E. Wyart *et al.* developed a multiscale approach where they recourse to 3D elements at the microscale to model the crack propagation and they recourse to shell elements at the macroscale.

Nevertheless, the XFEM has some drawbacks as difficulty in prescribing Dirichlet boundary conditions or Gauss integration when discontinuities get close to a node. The first drawback appears when a Dirichlet boundary condition has to be prescribed on an enriched element. In this case as there are extra nodal unknowns, the implementation of the boundary

[3]However the thick level set approach can be well suited with the XFEMit can be used in combination with another method of crack representation.

condition requires special attention [162]. The second drawback is related to the crack propagation. In fact, spurious results can be obtained if the crack cut the element very close to a node or an edge as it is difficult to have in this case integration points on every side of the crack. Therefore special attention is required in this case [239], which complicates the implementation. This integration problem is not negligible as a sufficiently thin mesh is required to capture accurately the crack path which increases the risk to have a crack cutting an element near a node. The necessity of mesh refinement was recently highlighted by M. Duflot *et al.* [88], who studied 3D multi-sites crack spread in a blade. Despite the cracks can propagate through elements, they had to refine the mesh to capture the cracks path in an accurate way and therefore to obtain a crack independent of the crack tip. The refinement is so huge that to solve the problem in a reasonable computational time, they fell back on remeshing. Nevertheless, as the crack has not to be conformed with the mesh, their remeshing operation is less costly than in the case of the approach presented in the Section 2.1 requiring to have a new mesh which an edge or face coinciding with the direction of the crack propagation.

2.5 Meshless methods

The development of meshless methods was motivated to avoid problems of mesh distortions in cases of large deformations or to avoid mesh constrained cracks propagation. Indeed, if there is no mesh, the crack can growth without following the boundary of elements. The first meshless method, called Smooth Particle Hydrodynamics (SPH), was developed by, on one hand, L. Lucy [151] and on the other hand by R. Gingold *et al.* [106] to solve astrophysics problems. The method was then applied to fluid mechanics [53, 169, 170] and afterward to solid mechanics by L. Libersky *et al.* [144] where impact problems were studied. As these problems involve large deformations, SPH has advantages compared to the FE for which high mesh distortion leads to computational issues. SPH methods are based on the strong form resolution and the first meshless method based on a weak form was presented by T. Belytschko *et al.* [42]. They developed the Element Free Galerkin Method (EFG) whose equations are close from the Reproducing Kernel Particle Method (RKPM) [149]. The only difference between both methods is the basis, which is intrinsic for EFG and extrinsic for RKPM. Finally, based on a local weak form, meshless local Petrov-Galerkin methods were developed [19]. Among the difficulties of meshless methods, their major drawbacks are the treatment of essential boundary conditions and their computational cost generally higher for the same problems than for traditional FE methods.

The extension to crack growth of meshless methods is obvious and has been pioneered by T. Belytschko *et al.* [40, 41, 44, 150]. They propagated the crack by evaluating the stress intensity factor coupled with the hoop stress criterion. Moreover to keep constant the node density at crack tip, J.-P. Ponthot *et al.* [207] suggested to use an Abritary Eulerian Lagrangian formalism. Such a method allows to study crack growth for 2D static and dynamic problems. Later, P. Krysl *et al.* [130] extended the approach to 3D cases. Furthermore, M. Duflot *et al.* [86, 87] improved the solution of the meshless method by enriching the displacement with the LEFM analytical solution at the crack tip. This enrichment allows capturing the stress

field with a moderate number of degrees of freedom. M. Duflot *et al.* simulated some fatigue crack propagation [87] as well as several crack propagation in 3D elastic media [86].

The extension of meshless methods to shell fracture problems has recently been realized by B. Maurel *et al.* [154]. They resolved the issue of modeling a shell with only one particle on the thickness and presented a SPH shell formulation. They studied fragmentation of elasto-plastic shells due to high velocity impact. They obtained phenomenological results although their fracture criterion is based on a maximal strain without modeling explicitly the fracture process (*i.e.* full opening without remaining traction is considered as soon as the strain is larger than a critical value). Furthermore F. Cayleron [61] and J. Liu [148] obtained good agreements between simulations and experimental results for respectively a tank perforation and a crack propagation in a pipe. Their fracture criterion is different (based on a critical damage for F. Cayleron and on a critical stress for J. Liu). The fracture process, of the decrease of the cohesive strength, seems unmodeled in these studies.

2.6 DG *vs.* XFEM

At this point, two methods seem appealing to model crack propagation: on one hand the DG/CZM method and one the other hand the XFEM. Both methods have advantages and disadvantages. Therefore the choice of the method is related to the aim of this thesis, which is to investigate the initiation and propagation of fracture in industrial pressurized components, especially in the case of dynamic loadings such as impact or blast. These ones often include fragmentation, which seems easier to study with the interface element approach [63, 137, 138, 168, 241, 276] than with the XFEM [240]. Besides, to our knowledge only a few 2D fragmentation cases are reported in literature for XFEM, and the interface element approach is more developed in this subject and has recently been combined with DG on this topic for 3D elements [137, 211]. Furthermore, industrial applications require (i) easy use of elasto-plasticity in the cohesive zone, (ii) thin meshes and (iii) a recourse to parallel implementation. Once again the DG/CZM method seems more suitable than XFEM to addresses these points. Finally, for industrial considerations, it is required that the developments can be easily integrated in an existing software. In this one it will be easier to add extra integration terms through elements than to incorporate nodal enrichment inherent to XFEM although more and more FE software include XFEM. For all these reasons, we choose to develop the DG/CZM framework for thin bodies formulations. As this framework used and extrinsic cohesive law we called it the DG/ECL framework.

2.7 Original developments

This chapter is a review of the different methods used to model fracture in computational mechanics. One appealing method is the CZM whose main issue is related to the introduction of the cohesive elements, which has to be performed during the simulation to obtain accurate results, especially in dynamics when the wave propagation plays a key role in the fracture

process. Two methods are suggested in the literature to solve this problem. On one hand, the XFEM inserts the cohesive elements by the level set technique. This does not require mesh modification during the simulation but enriched nodes have to be added in the system. On the other hand, as the DG method considers interface elements between discontinuous bulk elements to ensure weakly the continuity between them, these interface elements can very easily be substituted by cohesive ones to model fracture. From the previous section we decide to investigate the initiation and propagation of fracture in thin bodies under dynamic loading using the DG/ECL framework as promising results for large systems including fragmentation have been reported in the literature for 3D problems. As such a framework has never been presented for a thin bodies formulation, we extend the approach to this case. Thus this thesis introduced five new original developments:

(i) Development of an original full-DG formulation of linear Euler-Bernoulli beams under small strain assumption: this case constitutes the simplest case to study and therefore is very suitable to illustrate the formulation.

(ii) Development of an ECL for thin bodies: as, the implicit model of the thickness inherent to thin bodies formulation makes difficult the use of the usual stress-tensor-based TSL, an original cohesive law based on resultant stresses is suggested. This law is coupled to the full-DG formulation of beams to model the through-the-thickness crack propagation.

(iii) Extension of the framework to non-linear Kirchhoff-Love shells: an original full-DG formulation of shells coupled to the original cohesive law based on resultant stresses is suggested.

(iv) The study of large problems: it requires suitable temporal integration scheme, including parallel implementation. We suggest herein an original parallel implementation of the whole framework based on ghost elements at mesh partitions boundary. Furthermore, for quasi-static cases, as the inversion of stiffness matrix is prohibitive for large systems, we suggest an original adaptation of the dynamic relaxation concept, for the Hulbert-Chung [123] time integration algorithm. The choice of Hubert-Chung time integration algorithm, in place of the traditional central difference scheme, allows introducing numerical dissipation to avoid spurious crack branching.

(v) Investigation of the possibility to couple damage to crack transition using the DG/ECL framework: toward this end, we suggest to insert a cohesive element between bulk elements where a criterion based on the damage is reached.

All these developments have been published (or submitted for publication) in peer-reviewing international journals:

[32] G. **Becker** & L. **Noels**, A fracture framework for Euler-Bernoulli beams based on a full discontinuous Galerkin formulation/extrinsic cohesive law combination, *International Journal for Numerical Methods in Engineering*, John Wiley & Sons, Ltd., 2011, **85**, 1227-1251

[31] G. **Becker**, C. **Geuzaine** & L. **Noels**, A one field full discontinuous Galerkin method for Kirchhoff-Love shells applied to fracture mechanics, *Computer Methods in Applied Mechanics and Engineering*, 2011, **200**, 3223 - 3241

[34] G. **Becker** & L. **Noels**, Validation tests of the full discontinuous Galerkin / extrinsic cohesive law framework of Kirchhoff-Love shell, *International Journal of Fracture*, CFRAC2011 special issue, submitted

[33] G. **Becker** & L. **Noels**, A full discontinuous Galerkin formulation of non-linear Kirchhoff - Love shells: elasto-plastic finite deformations, parallel computation & fracture applications, *International Journal for Numerical Methods in Engineering*, submitted

Chapter 3

Discontinuous Galerkin / Extrinsic Cohesive Law framework for Euler-Bernoulli beams

The aim of this chapter [1] is to simulate the initiation and the through-the-thickness propagation of a crack in an Euler-Bernoulli beam. As a result of the previous chapter, we suggest to perform this using a combination between a discontinuous Galerkin formulation of the beam equations, modeling the continuum part of the deformation, and an extrinsic cohesive law, modeling the fracture process.

We summarize the Euler-Bernoulli beam theory to obtain the strong form of the problem in terms of the resultant stresses. Furthermore, as the main idea of this chapter is to illustrate the concept and not to solve industrial problems we restrict our analysis to:

(i) Linear small strains;

(ii) Straight rectangular beam without initial deformation;

(iii) Problems where the out-of-plane shearing is neglected;

(iv) Plane stress state.

Moreover, to simplify the notation the contribution of external forces is omitted in the establishment of the formulation. A more general and rigorous analysis will be presented for shells in the next chapter.

In a second time we present an original manner to discretize a beam with fully discontinuous elements. Then we demonstrate that our new method has the same numerical properties as a classical FE method: consistency, stability and optimal convergence rate. These properties and the ability of the formulation to simulate a continuum mechanics problem are illustrated

[1] The main results of this chapter are published in the *International Journal for Numerical Methods in Engineering* [32].

through several benchmarks. It has to be mentioned that the presented method is a generalization to discontinuous test functions of a $\mathcal{C}^0$/DG formulation of beams presented by G. Engel *et al.* [91]. This paper suggests a method for Bernoulli beams, which considers continuous test functions (*i.e.* continuous elements) but uses the DG method to ensure the $\mathcal{C}^1$ continuity required by a thin bodies formulation. Besides we establish that in case of continuous test functions both formulations are identical. To remove any ambiguity between both formulations, we call our formulation "full discontinuous Galerkin".

Third, as we did not find an appealing cohesive model for thin bodies in the literature, we present an original extrinsic cohesive law dedicated to thin bodies. Indeed in the literature two ideas are developed to propagate the crack through-the-thickness. On one hand, F. Cirak *et al.* [70] suggested to insert the stress-based cohesive law on the integration points across the thickness where the fracture criterion is reached. Such a framework allows the propagation but leads to a very complex implementation in case of a bending effort. On the other hand, P. Zavattieri idea [269] is to use the reduced quantities as tension and bending moment. We keep this idea but we adapt it in an original way to combine membrane and bending contributions with respect to the energetic balance.

Finally, we perform a numerical example of through-the-thickness crack propagation in a double clamped beam to validate our method and demonstrate its capabilities.

3.1 Balance equations of beams

We present herein the set of equations governing a beam, which traditional theory considers only the bending mode. Nevertheless, as we are interested to study fracture in the case of tension-bending coupling, we add by linear superposition the membrane contribution[2]. These equations can be rigorously obtained from the linear shell theory presented by F. Simo *et al.* [233] as we report in Appendix A.2. But to simplify this chapter, with the aim of introducing the main concepts in a more comprehensive way, we use the Euler-Bernoulli beam theory to obtain the balance of angular momentum and the equilibrium equation to derive the balance of linear momentum. Furthermore, as the main idea of F. Simo *et al.* is to integrate the stress on the thickness, we introduce this idea here to facilitate the transition to the shell theory.

In the following, we consider by convention that the beam lies in a orthonormal frame $(\boldsymbol{E}_1, \boldsymbol{E}_2, \boldsymbol{E}_3)$ with its neutral axis corresponding to $\boldsymbol{E}_1$ and the thickness of its rectangular cross section oriented along $\boldsymbol{E}_3$. The coordinate along $\boldsymbol{E}_3$ is noted ξ^3, and the unknown displacement field is written $\boldsymbol{u}$ (see Fig. 3.1).

The balance equations along $\boldsymbol{E}_3$ of a beam are written

$$(M_B)_{,1} - V_B = 0 \text{ and,} \tag{3.1}$$

$$V_{B,1} + b\, p_B(\xi^1) = \rho b h \ddot{u}_3\,, \tag{3.2}$$

where the rotational inertia is neglected, where ρ is the density and where p_B is the applied

[2]This linear assumption holds as the beam has initially no curvature and as only first order terms are considered.

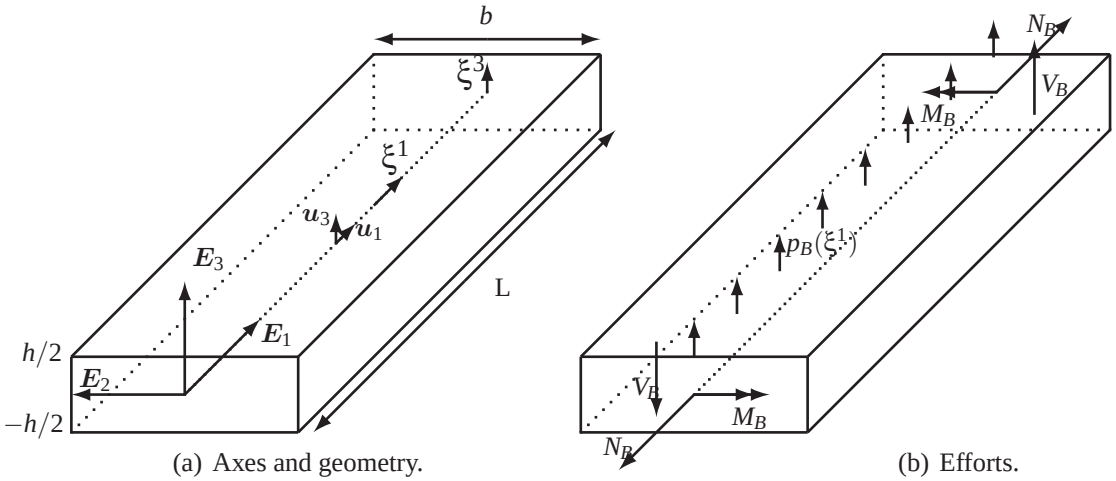

(a) Axes and geometry. (b) Efforts.

Figure 3.1: Configuration of the beam in the reference frame studied in this chapter.

load on the beam. M_B and V_B are respectively the moment in the beam and the shear loading defined by,

$$M_B = \int_A \sigma^{11}\xi^3 dA \text{ and,} \tag{3.3}$$

$$V_B = \int_A \sigma^{13} dA, \tag{3.4}$$

where $A = b \times [-h/2; h/2]$ is the area of the cross section, with b the width of the beam and where σ^{11} and $\sigma^{13}$are respectively the axial and shear stress distributions on the section. Euler-Bernoulli beams theory assumes a negligible effect of the shearing on the bending deformation, but in order to develop the full-DG formulation it is convenient to keep it, as it will be shown later.

Furthermore as it is also convenient in shell formulations to consider the moment and shear by unit width we define,

$$\tilde{m_B}^{11} = \int_{-h/2}^{h/2} \sigma^{11}\xi^3 d\xi^3 = \frac{M_B}{b} \text{ and,} \tag{3.5}$$

$${l_B}^1 = \int_{-h/2}^{h/2} \sigma^{13} d\xi^3 = \frac{V_B}{b}. \tag{3.6}$$

as well as the density by unit width,

$$\overline{\rho}_B = \int_{-h/2}^{h/2} \rho d\xi^3. \tag{3.7}$$

It has to be mentioned that for further compatibility with the shell equation, we consider the stress components in the conjugated basis $\boldsymbol{E}^I$ of $\boldsymbol{E}_I$ defined by the identity: $\boldsymbol{E}^I \cdot \boldsymbol{E}_J = \delta_{IJ}$, although both bases are identical for an orthonormal frame.

Finally, using both definitions (3.5) and (3.6) in Eqs. (3.1-3.2), it comes,

$$\tilde{m}_{B,1}^{11} - {l_B}^1 = 0 \text{ and,} \tag{3.8}$$

$$\left({l_B}^1\right)_{,1} + p_B(\xi^1) = \overline{\rho}_B \ddot{u}_3 \,. \tag{3.9}$$

Note that ${l_B}^1$ in Eq. (3.9) corresponds to the shearing along the neutral axis while ${l_B}^1$ in Eq. (3.9) corresponds to the shearing along the beam section.

The membrane behavior of the beam is governed by the equation,

$$N_{B,1} - \rho b h \ddot{u}_1 = 0 \,, \tag{3.10}$$

where N_B is the tension in the beam which reads,

$$N_B = \int_A \sigma^{11} dA \,. \tag{3.11}$$

Then, exactly as for the bending equations, we can define,

$$n_B^{11} = \int_{-h/2}^{h/2} \sigma^{11} d\xi^3 \,, \tag{3.12}$$

$$\tag{3.13}$$

the tension per unit width. With this definition, the governing equation of the beam in tension reads,

$$n_{B\ ,1}^{11} = \overline{\rho}_B \ddot{u}_1 \,, \tag{3.14}$$

This equation constitutes with the Eqs. (3.8-3.9) the set of equation formulating the strong form of Euler-Bernoulli beams considered herein. The previous relations involve two unknown fields $\boldsymbol{u}$ and $\boldsymbol{\sigma}$ which can be related using a constitutive model. Under linear elasticity assumption, the Hooke law is used.

The deformation of the section along ξ^1 results from the curvature of the neutral axis $\overline{\theta}_{,1}$ and from the extension of the neutral axis $u_{1,1}$ with,

$$\varepsilon_{11} = u_{1,1} + \overline{\theta}_{,1} \xi^3 \,. \tag{3.15}$$

The deformation in shearing of the section is assumed to be constant and reads,

$$\varepsilon_{13} = \frac{u_{3,1} + \overline{\theta}}{2} \,, \tag{3.16}$$

where $\left(u_{3,1} + \overline{\theta}\right)$ is the angle between the neutral axis and the cross section direction. Euler-Bernoulli assumption consists in neglecting this angle leading to $\overline{\theta} = -u_{3,1}$.

Finally, the stress field, using the unit metric related to $\boldsymbol{E}_1$ reads,

$$\sigma^{11} = E\varepsilon_{11} = E\left(u_{1,1} - u_{3,11}\xi^3\right) \text{ and,} \tag{3.17}$$

$$\sigma^{31} = \mu \frac{A'}{A} \varepsilon_{31} = \mu \frac{A'}{A} \left(u_{3,1} + \overline{\theta}\right) \approx 0 \,, \tag{3.18}$$

where $\frac{A'}{A}$ takes into account the reduced section for the shearing. It has to be noticed that $\boldsymbol{\sigma}^{11}$ results from the linear superposition of membrane and bending mode which are uncoupled under the assumptions mentioned at the beginning of this chapter. Indeed, using Eq. (3.17) in Eqs (3.12) and (3.5) it comes respectively,

$$n_B{}^{11} = \int_{-h/2}^{h/2} E u_{1,1} d\xi^3 - \int_{-h/2}^{h/2} E u_{3,11} \xi^3 d\xi^3 = E h u_{1,1} \text{ and,} \tag{3.19}$$

$$\tilde{m_B}{}^{11} = \int_{-h/2}^{h/2} E u_{1,1} \xi^3 d\xi^3 - \int_{-h/2}^{h/2} E u_{3,11} \xi^{3^2} d\xi^3 = -E \frac{h^3}{12} u_{3,11} \,. \tag{3.20}$$

Therefore, the membrane contribution has no influence on the angular momentum and reciprocally the bending contribution has no influence on the linear momentum.

3.2 Full-DG formulation of Euler-Bernoulli beams

In this section the full-DG FE discretization of the set of Eqs. (3.8-3.9) and (3.14) is introduced under the assumptions given at the beginning of this chapter. Once the weak formulation of the problem is established, the numerical properties of the presented method are studied and illustrated on a numerical example. In this example the full discontinuous Galerkin formulation is compared to the C^0/DG formulation introduced by G. Engel *et al.* [91]. It is observed that the full-DG formulation gives the same results as the C^0/DG approach, and has the same advantages, *i.e.* one-field locking-free approach. Obviously the purpose of developing the full-DG approach is to take into account a pre-fracture stage when combined to the ECL.

In this section, all the terms are per unit width of the beam.

3.2.1 Weak bilinear form of Euler-Bernoulli beams

For the particular case of beams of length L in small deformations and linear elasticity, illustrated on Fig. 3.1, the weak form is obtained by multiplying Eq. (3.8) by $\delta(-u_{3,1})$, Eq. (3.9) by δu_3 and Eq. (3.14) by δu_1 and integrating on the beam length. In Eq. (3.9) $l_{B,1}$ is omitted as the shearing is neglected. However it is kept temporarily in Eq. (3.8) to establish the full-DG formulation. Proceeds this way gives,

$$\int_0^L \overline{\rho}_B \ddot{\boldsymbol{u}} \cdot \delta \boldsymbol{u} dx = \int_0^L \left[n_{B,1}^{11} \delta u_1 + \tilde{m}_{B,1}^{11} \delta(-u_{3,1}) - l_B{}^1 \delta(-u_{3,1}) \right] dx \,. \tag{3.21}$$

As a reminder, we omit the external loading to simplify the equations but it can be added in a usual way. This equation can be integrated by parts on each element of length l_e of the FE discretization,

$$\begin{aligned} \sum_e \int_{l_e} \overline{\rho}_B \ddot{\boldsymbol{u}} \cdot \delta \boldsymbol{u} dx = & -\sum_e \left\{ \int_{l_e} \left[n_B{}^{11} \delta u_{1,1} + \tilde{m_B}{}^{11} \delta(-u_{3,11}) - l_{B,1}^1 \delta(-u_3) \right] dx \right. \\ & \left. + \left(n_B{}^{11} \delta u_1 \right]_{l_e} + \tilde{m_B}{}^{11} \delta(-u_{3,1}) \big]_{l_e} - l_B{}^1 \delta(-u_3) \big]_{l_e} \right) \Big\} \,, \end{aligned} \tag{3.22}$$

where an unusual integration by parts was applied on $\delta(-u_{3,1})$ instead of ${l_B}^1$ for the third term of Eq. (3.21). In the Eq. (3.22), the terms $\sum_e {n_B}^{11}\delta u_1\big]_{l_e}$, $\sum_e {l_B}^1\delta(-u_3)\big]_{l_e}$ and the term $\sum_e {\tilde{m}_B}^{11}\delta(-u_{3,1})\big]_{l_e}$ are related to discontinuities in the polynomial approximation between two elements. For a continuous Galerkin formulation, the continuity of the test functions allows to simplify the two first terms as $\sum_e \bullet]_{l_e} = \bullet]_0^L = 0$, since the test functions or the strains are null in 0 and L (assuming pure Dirichlet boundary conditions). For the DG formulation, the test functions are discontinuous and these three terms can be rewritten as a sum of jumps over the interface elements s,

$$\sum_e {n_B}^{11}\delta u_1\big]_{l_e} = -\sum_s \left[\!\left[{n_B}^{11}\delta u_1\right]\!\right]_s, \tag{3.23}$$

$$\sum_e {\tilde{m}_B}^{11}\delta(-u_{3,1})\big]_{l_e} = -\sum_s \left[\!\left[{\tilde{m}_B}^{11}\delta(-u_{3,1})\right]\!\right]_s \text{and,} \tag{3.24}$$

$$\sum_e {l_B}^1(-\delta u_3)\big]_{l_e} = -\sum_s \left[\!\left[{l_B}^1(-\delta u_3)\right]\!\right]_s, \tag{3.25}$$

with the jump operator[3] $[\![\bullet]\!]_i = [\bullet^+ - \bullet^-]_i$. The sign at right hand side of Eqs. (3.23-3.25) depends on the convention chosen for minus and plus element. Herein, we consider the convention shown on the Fig. 3.2 with the minus element at the left of the plus element yielding,

$$\sum_e {n_B}^{11}\delta u_1\big|_{l_e} = \sum_e \nu_{B_1}^+ {n_B}^{11+}\delta u_1^+ + \nu_{B_1}^- {n_B}^{11-}\delta u_1^- = -\sum_s \left[\!\left[{n_B}^{11}\delta u_1\right]\!\right]_s, \tag{3.26}$$

as normals $\nu_{B_1}^+ = -1$ and $\nu_{B_1}^- = 1$ (see Fig. 3.2). The Eqs. (3.24) and (3.25) are obtained in the same way.

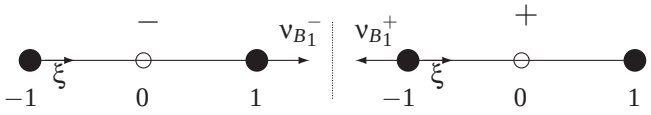

Figure 3.2: Sign of interface contributions depends on the choice of the minus and plus elements. Illustration for second order elements, the filled circles are nodes on the elements boundaries and the other circles are internal nodes. For continuous elements the node located in $\xi = 1$ of the minus element corresponds to the node located in $\xi = -1$ of the plus element. For discontinuous elements these two nodes remain very close from the interface (dotted line).

In DG formulations these jumps are commonly replaced by fluxes, which must be consistent. The developments are exactly the same for the three jumps, so in the following, only the equation (3.23) is developed and the two other terms (3.24) and (3.25) can be derived in the same way. Using the mathematical identity $[\![ab]\!] = \langle a\rangle [\![b]\!] + \langle b\rangle [\![a]\!]$, relation (3.23) is rewritten as,

$$\sum_s \left[\!\left[{n_B}^{11}\delta u_1\right]\!\right]_s = \sum_s \left[\left\langle {n_B}^{11}\right\rangle [\![\delta u_1]\!] + \left[\!\left[{n_B}^{11}\right]\!\right] \langle \delta u_1\rangle\right]_s, \tag{3.27}$$

[3] To be rigorous we should add the contributions at $\xi^1 = 0$ and $\xi^1 = L$ as it will be done for shells

with the mean operator $\langle \bullet \rangle = \frac{1}{2}(\bullet^+ + \bullet^-)$. As for the exact solution there is no jump in the stress tensor between two elements, the second term of (3.27) can be neglected without altering the consistency of the method and the flux related to (3.23) becomes,

$$\left[\!\left[{n_B}^{11} \delta u_1 \right]\!\right] \quad \rightarrow \quad \left\langle {n_B}^{11} \right\rangle \left[\!\left[\delta u_1 \right]\!\right] . \tag{3.28}$$

Nevertheless if the numerical flux (3.28) ensures the consistency of the formulation, the compatibility (continuity) between elements is not guaranteed. This requirement can be obtained in a weak way by the introduction of an extra term in the flux,

$$\left\langle E h \delta u_{1,1} \right\rangle \left[\!\left[u_1 \right]\!\right] . \tag{3.29}$$

As the exact solution of the problem is continuous ($[\![u_1]\!] = 0$), this term does not modify the consistency of the problem. It has to be mentioned that other expressions can be chosen to ensure the compatibility but the term (3.29) allows to obtain a symmetric formulation (*i.e.* stiffness matrix is symmetric) and an optimal convergence rate.

Finally, as it is well known that, for elliptic problems, such a formulation is unstable, the method is stabilized by introducing a quadratic term in the numerical flux,

$$\left[\!\left[u_1 \right]\!\right] \left\langle \frac{\beta_2 E h}{h^s} \right\rangle \left[\!\left[\delta u_1 \right]\!\right] . \tag{3.30}$$

For the exact solution this term is equal to zero so consistency is not modified. In this expression h^s is the characteristic dimension of the element allowing the respect of the dimensions. Furthermore, β_2 is a non dimensional constant, whose value has to be sufficiently large to ensure the stability of the problem as presented here below in Section 3.2.2. Pratically, the stability is generally ensured as long as β_2 is greater than 10. Such an introduction of interior penalty term is usual for discontinuous Galerkin method applied to solid mechanics, [16, 97, 140, 182] among others, and allows ensuring stability. Although the DG method is now slightly dissipative, this does not impact on the numerical accuracy as the method remains consistent and converges toward the solution with an optimal rate, see Section 3.2.2, contrarily to methods using only a penalty coefficient. This user parameter β_2 is independent of the mesh and material properties and is without dimension. Following these developments,

the mathematical fluxes related to the Eqs. (3.23), (3.24) and (3.25) are,

$$\sum_e {n_B}^{11}\delta u_1\big]_{l_e} \rightarrow$$
$$-\sum_s \left(\langle {n_B}^{11}\rangle [\![\delta u_1]\!] + \langle Eh\delta u_{1,1}\rangle [\![u_1]\!] + [\![u_1]\!] \left\langle \frac{\beta_2 Eh}{h^s} \right\rangle [\![\delta u_1]\!] \right)_s , \tag{3.31}$$
$$\sum_e \tilde{m_B}^{11}\delta(-u_{3,1})\big]_{l_e} \rightarrow$$
$$-\sum_s \left(\langle \tilde{m_B}^{11}\rangle [\![\delta(-u_{3,1})]\!] + \left\langle \frac{Eh^3}{12}\delta(-u_{3,11}) \right\rangle [\![-u_{3,1}]\!] \right.$$
$$\left. + [\![-u_{3,1}]\!] \left\langle \frac{\beta_1 Eh^3}{12h^s} \right\rangle [\![\delta(-u_{3,1})]\!] \right)_s \text{ and,} \tag{3.32}$$
$$\sum_e {l_B}^1(-\delta u_3)\big]_{l_e} \rightarrow$$
$$-\sum_s \left([\![u_3]\!] \left\langle \frac{\beta_3 Eh}{2(1+\nu)h^s} \right\rangle [\![(-\delta u_3)]\!] \right)_s , \tag{3.33}$$

as ${l_B}^1 = 0$ (Euler-Bernoulli assumption) in the relation (3.33), which implies that only the stabilization term remains in this equation. Let us note that the asymmetry in signs of relation (3.33) results from definition (3.6). Finally, after introducing the Eqs. (3.31), (3.32) and (3.33) in (3.22), the weak discretized form of the problem becomes,

$$\begin{aligned} a(\boldsymbol{u},\delta\boldsymbol{u}) \;=\; & \sum_e \int_{l_e} \left[\bar{\rho}_B \ddot{\boldsymbol{u}}\cdot\delta\boldsymbol{u} + {n_B}^{11}\delta u_{1,1} + \tilde{m_B}^{11}\delta(-u_{3,11}) \right] dx \\ & + \sum_s \left(\langle {n_B}^{11}\rangle [\![\delta u_1]\!] + \langle Eh\delta u_{1,1}\rangle [\![u_1]\!] + [\![u_1]\!] \left\langle \frac{\beta_2 Eh}{h^s} \right\rangle [\![\delta u_1]\!] \right. \\ & + \langle \tilde{m_B}^{11}\rangle [\![\delta(-u_{3,1})]\!] + \left\langle \frac{Eh^3}{12}\delta(-u_{3,11}) \right\rangle [\![-u_{3,1}]\!] \\ & \left. + [\![-u_{3,1}]\!] \left\langle \frac{\beta_1 Eh^3}{12h^s} \right\rangle [\![-\delta u_{3,1}]\!] + [\![u_3]\!] \left\langle \frac{\beta_3 Eh}{2(1+\nu)h^s} \right\rangle [\![\delta u_3]\!] \right) = 0 . \end{aligned} \tag{3.34}$$

The relation (3.34) shows that a DG framework can be easily integrated in a CG FE code. Indeed the integral part of (3.34) is exactly the same as the one of a CG formulation of the problem with, as differences, the computation of a sum on interface elements which can be easily added in the FE code. For more convenience in further developments the relation (3.34) can be expressed in the form,

$$\text{Structural terms} + \text{DG terms} = 0 , \tag{3.35}$$

with "Structural terms" and "DG terms" respectively the integral part and the interface sum part of (3.34).

Furthermore, if continuous test functions are used for displacement (ie the elements are continuous), $[\![\delta u_1]\!] = [\![\delta u_3]\!] = 0$, and the equation (3.34) can be simplified as,

$$\begin{aligned} a(\boldsymbol{u},\delta\boldsymbol{u}) &= \sum_e \int_{l_e} \left[\overline{\rho}_B \ddot{\boldsymbol{u}}\delta\boldsymbol{u} + {n_B}^{11}\delta u_{1,1} + {\tilde{m}_B}^{11}\delta(-u_{3,11})\right] dx \\ &\quad + \sum_s \left(\left\langle {\tilde{m}_B}^{11} \right\rangle [\![\delta(-u_{3,1})]\!] + \left\langle \frac{Eh^3}{12}\delta(-u_{3,11}) \right\rangle [\![-u_{3,1}]\!] \right) \\ &\quad + [\![-u_{3,1}]\!] \left\langle \frac{\beta_1 Eh^3}{12h^s} \right\rangle [\![-\delta u_{3,1}]\!] \Big) = 0\,. \end{aligned} \tag{3.36}$$

The pending part of this last equation is identical to the previously C^0/DG formulation suggested by G. Engel *et al.* [91].

3.2.2 Numerical properties

In this section the numerical properties of the weak formulation (3.34) are studied in the particular case where u_{h1} and u_{h3} are polynomial approximation of degree $k > 1$ in each element and are discontinuous between elements. The associated virtual displacements have the same properties. It is demonstrated that the framework satisfies two fundamental properties of a numerical method: consistency and stability. This last one is demonstrated if the parameters β_1 and β_2 are large enough, and if β_3 is non zero. The convergence rate of the method in the energy norm with respect to the mesh size is proved to be equal to $k-1$, with k the degree of the polynomial approximation. Finally, optimal-convergence rate in the $\mathbf{L}^2$-norm is demonstrated for at least cubic elements. Afterward, some numerical examples are presented to illustrate these properties. In this section we assume $\delta u_1 = \delta u_{3,1} = 0$ at the beam extremities as we consider Dirichlet boundary conditions.

Consistency

To prove the consistency of the method, the exact solution $\boldsymbol{u}$ of the problem is considered. As this exact solution is $\mathcal{C}^2([0;L])$, this implies $[\![u_1]\!] = [\![u_3]\!] = [\![u_{3,1}]\!] = 0$, and relation (3.34) becomes,

$$\sum_e \int_{l_e} \left[\overline{\rho}_B \ddot{\boldsymbol{u}}\cdot\delta\boldsymbol{u} + {n_B}^{11}\delta u_{1,1} + {\tilde{m}_B}^{11}\delta(-u_{3,11})\right] dx \tag{3.37}$$

$$+ \sum_s \left(\left\langle {n_B}^{11} \right\rangle [\![\delta u_1]\!] + \left\langle {\tilde{m}_B}^{11} \right\rangle [\![\delta(-u_{3,1})]\!] \right) = 0\,. \tag{3.38}$$

Integrating by parts on each element, as ${n_B}^{11}$ and ${\tilde{m}_B}^{11}$ of the exact solution are continuous, leads to,

$$\int_0^L \overline{\rho}_B \ddot{\boldsymbol{u}}\cdot\delta\boldsymbol{u}dx - \int_0^L {n_B}_{,1}^{11}\delta u_1 dx \,\text{and,} - \int_0^L {\tilde{m}_B}_{,1}^{11}(-\delta u_{3,1})dx = 0\,. \tag{3.39}$$

The arbitrary nature of the test functions leads to the two following equalities,

$$n_{B,1}^{11} = \overline{\rho}_B \ddot{u}_1 \text{ in } [0;L] \text{ and,} \tag{3.40}$$

$$\tilde{m_{B,1}^{11}} = \overline{\rho}_B \ddot{u}_3 \text{ in } [0;L]\,. \tag{3.41}$$

These two equations (3.40) and (3.41) correspond to the strong formulation of the problem where the shearing is neglected (${l_B}^1 = 0$). Thus the consistency of the method is demonstrated. This property implies that the exact solution $\boldsymbol{u}$ satisfies (3.34), which provides the orthogonality relation,

$$a(\boldsymbol{u}_h - \boldsymbol{u}, \delta\boldsymbol{u}) = a(\boldsymbol{u}_h, \delta\boldsymbol{u}) - a(\boldsymbol{u}, \delta\boldsymbol{u}) = 0\,. \tag{3.42}$$

where $\boldsymbol{u}_h$ is the FE solution.

Stability

The demonstration of the spatial stability is performed under a quasi-static assumption. Therefore the inertial term is not considered in the following. To study the stability and convergence rate with respect to the mesh size of the framework, an energy norm has to be defined. If constrained displacements $\overline{\boldsymbol{u}}$ and directions of the mid-surface $\overline{u_{3,1}}$ are assumed to be equal to zero on boundaries then the following energy norm can be considered for a field $\boldsymbol{u}$ discontinuous between elements,

$$\begin{aligned} |||\boldsymbol{u}|||^2 = & \sum_e \left|\left| \sqrt{Eh}\, u_{1,1} \right|\right|^2_{\mathbf{L}^2(l_e)} + \sum_s \left|\left| \sqrt{\frac{\beta_2 Eh}{h^s}}\, [\![u_1]\!] \right|\right|^2_{\mathbf{L}^2(s)} \\ & + \sum_e \left|\left| \sqrt{\frac{Eh^3}{12}}(-u_{3,11}) \right|\right|^2_{\mathbf{L}^2(l_e)} + \sum_s \left|\left| \sqrt{\frac{\beta_1 Eh^3}{12h^s}}\, [\![(-u_{3,1})]\!] \right|\right|^2_{\mathbf{L}^2(s)} \\ & + \sum_s \left|\left| \sqrt{\frac{\beta_3 Eh}{2(1+\nu)h^s}}\, [\![u_3]\!] \right|\right|^2_{\mathbf{L}^2(s)}, \end{aligned} \tag{3.43}$$

where,

$$\left|\left| \sqrt{\mathcal{H}}\, a \right|\right|^2_{\mathbf{L}^2(l_e)} = \int_{l_e} \mathcal{H}\, a^2 dl \text{ and,} \tag{3.44}$$

$$\sum_s \left|\left| \sqrt{\mathcal{H}}\, [\![a]\!] \right|\right|^2_{\mathbf{L}^2(s)} = \sum_e \frac{1}{2} \left|\left| \sqrt{\mathcal{H}}\, [\![a]\!] \right|\right|^2_{\mathbf{L}^2(\partial l_e)}. \tag{3.45}$$

The expression (3.43) defines a norm as $|||\boldsymbol{u}||| = 0$ only for $\boldsymbol{u} = 0$ on $[0;L]$. This is demonstrated in the following way: if $|||\boldsymbol{u}||| = 0$ then each term is equal to zero. So on each element the derivatives $u_{1,1}$ and $-u_{3,11}$ are also equal to zero, which implies that u_1 and $u_{3,1}$ are constant on each element. Moreover, as jumps are equal to zero on the interface, u_1, u_3

and $u_{3,1}$ are constant on $]0;L[$. Finally, the boundary conditions $\overline{\boldsymbol{u}} = 0$ and $\overline{u_{3,1}} = 0$ imply $u_1 = u_3 = u_{3,1} = 0$ on $[0;L]$.

To demonstrate the stability of the framework an upper and a lower bounds of the bilinear form (3.34) are needed. Both bounds are established in Appendix A.3.1 and A.3.2 and we report here only the final results. Therefore an upper bound of the linear form is given by,

$$|a(\boldsymbol{u},\delta\boldsymbol{u})|^2 \;\leq\; C''^k(\beta_1,\beta_2)\,|||\boldsymbol{u}|||^2\,|||\delta\boldsymbol{u}|||^2 \quad , \tag{3.46}$$

where $C''^k(\beta_1,\beta_2)$ is a number larger than $\max(4,(C_\alpha^k)^2/\beta_\alpha)$, with $C_\alpha^k > 0$ are constants depending only on the polynomial degree of $\boldsymbol{u}$. In case $\boldsymbol{u} = \boldsymbol{u}_h$, the degree k is the degree of the polynomial approximation.

A lower bound of the bilinear form is given by stating that there exist $0 < \varepsilon_1 < 1$ and $0 < \varepsilon_2 < 1$,

$$\begin{aligned} a(\boldsymbol{u},\boldsymbol{u}) \;\geq\; & (1-\varepsilon_2)\sum_e \left|\left|\sqrt{Eh}u_{1,1}\right|\right|^2_{\mathbf{L}^2(l_e)} + (1-\varepsilon_1)\sum_e \left|\left|\sqrt{\frac{Eh^3}{12}}u_{3,11}\right|\right|^2_{\mathbf{L}^2(l_e)} \\ & + \left(1-\frac{2(C_2^k(\beta_2))^2}{\varepsilon_2\beta_2}\right)\sum_e \left|\left|\sqrt{\frac{Eh\beta_2}{2h^s}}[\![u_1]\!]\right|\right|^2_{\mathbf{L}^2(\partial l_e)} \\ & + \left(1-\frac{2(C_1^k(\beta_1))^2}{\varepsilon_1\beta_1}\right)\sum_e \left|\left|\sqrt{\frac{Eh^3\beta_1}{24h^s}}[\![u_{3,1}]\!]\right|\right|^2_{\mathbf{L}^2(\partial l_e)} \\ & + \frac{1}{2}\sum_e \left|\left|\sqrt{\frac{\beta_3 Eh}{4(1+\nu)h^s}}[\![u_3]\!]\right|\right|^2_{\mathbf{L}^2(\partial l_e)} \quad , \end{aligned} \tag{3.47}$$

Taking into account the bounds, the spatial stability of the method is directly demonstrated from relation (3.47). Indeed by definition of the energetic norm (3.43),

$$\begin{aligned} |||\boldsymbol{u}|||^2 \;=\; & \sum_e \left|\left|\sqrt{Eh}u_{1,1}\right|\right|^2_{\mathbf{L}^2(l_e)} + \sum_e \left|\left|\sqrt{\frac{Eh^3}{12}}u_{3,11}\right|\right|^2_{\mathbf{L}^2(l_e)} + \frac{1}{2}\sum_e \left|\left|\sqrt{\frac{\beta_1 Eh^3}{12h^s}}[\![u_{3,1}]\!]\right|\right|^2_{\mathbf{L}^2(\partial l_e)} \\ & + \frac{1}{2}\sum_e \left|\left|\sqrt{\frac{\beta_2 Eh}{h^s}}[\![u_1]\!]\right|\right|^2_{\mathbf{L}^2(\partial l_e)} + \frac{1}{2}\sum_e \left|\left|\sqrt{\frac{\beta_3 Eh}{2(1+\nu)h^s}}[\![u_3]\!]\right|\right|^2_{\mathbf{L}^2(\partial l_e)} \quad . \end{aligned} \tag{3.48}$$

Comparing the right term of equation (3.48) to the right term of equation (3.47) leads to,

$$a(\boldsymbol{u}_h,\boldsymbol{u}_h) \geq C(\beta_1,\beta_2)\,|||\boldsymbol{u}_h|||^2 \,, \tag{3.49}$$

where there exists $C(\beta_1,\beta_2) > 0$ as for given $0 < \varepsilon_1 < 1$ and $0 < \varepsilon_2 < 1$ there always exist $\beta_1 > \frac{2(C_1^k)^2}{\varepsilon_1}$ and $\beta_2 > \frac{2(C_2^k)^2}{\varepsilon_2}$. This shows that the stability of the method is conditioned by sufficiently large constant β_1 and β_2. Both depend only on the degree and type of element

through respectively C_1^k and C_2^k which can be determined following the work of P. Hansbo *et al.* [116]. Note that Eq. (3.49) does not imply stability conditions on the parameter β_3 as long as $\beta_3 > 0$. Furthermore, in this equation, $a(\boldsymbol{u}_h, \boldsymbol{u}_h)$ corresponds to the work of internal forces while $C(\beta_1, \beta_2) |||\boldsymbol{u}_h|||^2$ is the internal energy of the system. Therefore, due to the DG terms, the internal energy is not equal to the work of the external forces, however the difference is negligible when the FEsolution has converged toward the solution.

Convergence rate in the energy norm

In the following the error between the FE solution and the polynomial interpolation of the exact solution is calculated to establish the convergence rate in the energy norm of the method. First some definitions and assumptions are given. Consider $\boldsymbol{u}$ the exact solution of the problem and $\boldsymbol{u}^k$ its FE interpolation defined by $\int_0^L (\boldsymbol{u} - \boldsymbol{u}^k) \cdot \delta \boldsymbol{u}_h dx = 0$. Furthermore, the errors on the exact solution and on its interpolation are respectively defined by $\boldsymbol{e} = \boldsymbol{u}_h - \boldsymbol{u}$ and $\boldsymbol{e}^k = \boldsymbol{u}_h - \boldsymbol{u}^k$.

The demonstration follows the procedure described in Appendix A.3.3 so only the final result is given here,

$$\left|\left|\left|\boldsymbol{e}^k\right|\right|\right| \leq C(\beta_1, \beta_2, \beta_3) \sum_e h^{sk-1} |\boldsymbol{u}|_{\mathbf{H}^{k+1}(l_e)} . \tag{3.50}$$

Thus, the order of convergence is one order lower than the degree of the polynomial approximation, which is consistent with the presence of high-order derivatives in the governing equations (3.34).

Convergence rate in the $\mathbf{L}^2$-norm

The convergence of the solution in the $\mathbf{L}^2$-norm is demonstrated under the assumption of a proper elliptic regularity of the problem.

As well as the convergence rate in the energy norm, the demonstration of the convergence in the $\mathbf{L}^2$-norm is presented in Appendix A.3.4, so only the final result is given here,

$$||\boldsymbol{e}||_{\mathbf{L}^2(l_e)} \leq \begin{cases} \sum_e C h^{sk+1} |\boldsymbol{u}|_{\mathbf{H}^{k+1}(l_e)} \text{ if } k > 2 \\ \sum_e C h^{s2} |\boldsymbol{u}|_{\mathbf{H}^3(l_e)} \text{ if } k = 2 \end{cases} . \tag{3.51}$$

The relation (3.51) demonstrates that the method has an optimal convergence rate in $k+1$ for at least cubic elements.

3.2.3 Implementation

This section describes the implementation, in a home-made FE software written in python, of the Eq. (3.34). Although the shell element is implemented in a C++ code-based on Gmsh software [105], which allows to investigate industrial problems, we implement separately the

beam elements to facilitate its understanding. The elementary stiffness matrix and internal forces are described as well as the Gauss quadrature rules used to integrate on elements. Notice that in the case of beams the interface between two bulk elements is just a node and there is no integration on this interface contrary to plate/shell elements for which a Gauss integration on a line is required on the interface.

The discretization of the beam in elements is represented on Fig. 3.3. To prove the independence of the method to the elements order, we implement quadratic (3 nodes) and cubic (4 nodes) elements. It has to be mention that using linear elements is impossible with the developed approach as the second derivative of the shape functions is needed for the computation of the bending contribution.

(a) Beam meshed with quadratic elements.

(b) Beam meshed with cubic elements.

(c) Isoparametric quadratic elements.

(d) Isoparametric cubic elements.

Figure 3.3: Beam meshed with quadratic and cubic elements. The circles represent the nodes, the filled ones are at element boundaries while the others represent internal nodes. The Gauss point used for the numerical integration are depicted by crosses.

Isoparametric elements are considered (see Figs. 3.3(c) and 3.3(d)) to perform the Gauss integration. Therefore the displacement and virtual displacement are approximated on each element respectively by,

$$\boldsymbol{u}_h = N^{\boldsymbol{\xi}}\boldsymbol{u}^{\boldsymbol{\xi}} \text{ and,} \tag{3.52}$$

$$\delta\boldsymbol{u}_h = N^{\boldsymbol{\xi}}\delta\boldsymbol{u}^{\boldsymbol{\xi}}, \tag{3.53}$$

where $\boldsymbol{\xi}$ is a node of the element and N represents the traditional Lagrangian shape functions. These functions of the curvilinear variable $\xi \in [-1\,;1]$ are continuous on each element. The

derivatives of the unknown and virtual fields are mandatory,

$$\boldsymbol{u}_{h,1} = \frac{\partial \xi}{\partial x} N^{\boldsymbol{\xi}}_{,\xi} \boldsymbol{u}^{\boldsymbol{\xi}}_h \,, \tag{3.54}$$

$$\boldsymbol{u}_{h,11} = \left(\frac{\partial \xi}{\partial x}\right)^2 N^{\boldsymbol{\xi}}_{,\xi\xi} \boldsymbol{u}^{\boldsymbol{\xi}}_h \,, \tag{3.55}$$

$$\delta\boldsymbol{u}_{h,1} = \frac{\partial \xi}{\partial x} N^{\boldsymbol{\xi}}_{,\xi} \delta\boldsymbol{u}^{\boldsymbol{\xi}}_h \,, \tag{3.56}$$

$$\delta\boldsymbol{u}_{h,11} = \left(\frac{\partial \xi}{\partial x}\right)^2 N^{\boldsymbol{\xi}}_{,\xi\xi} \delta\boldsymbol{u}^{\boldsymbol{\xi}}_h \,, \tag{3.57}$$

$$\tag{3.58}$$

where $\frac{\partial^2 \xi}{\partial x^2} = 0$ is taken into account for the computation of second derivative. Indeed, as a element of length l_e is represented by an isoparametric element of length 2 described by,

$$\xi = 2\frac{x - x_{left}}{l_e} - 1 \,, \tag{3.59}$$

where x_{left} is the position of the left nodes of the element if the origin is taken at left of the beam (see Figs. 3.3(a) and 3.3(b)). Therefore the Jacobian of the substitution $\frac{\partial \xi}{\partial x} = \frac{2}{l_e}$ and the derivative of this Jacobian is equal to zero.

In the following we give the expressions implemented for each term of Eq. (3.34) separately in terms of the general reduced stresses, ${n_B}^{11}$ (3.12) and ${\tilde{m}_B}^{11}$ (3.5). The thickness integration to obtain these terms can be computed analytically if a linear elastic material is assumed, or can be evaluated numerically from a 3-point Simpson quadrature rule. Such a rule (in place of a Gauss one) is generally applied [70, 114, 181] in thin bodies formulation as it allows to have an integration points at lower and upper skin of the beam.

The three elementary bulk terms (inertial, membrane and bending terms) of Eq. (3.34) can be easily computed using (3.52-3.57), and an integration on Gauss points g of weight w_g reads:

- Inertial term:

$$\begin{aligned}
\sum_e \int_{l_e} \overline{\rho}_B \ddot{\boldsymbol{u}} \cdot \delta\boldsymbol{u} dx &= \sum_e \int_{l_e} \overline{\rho}_B N^{\boldsymbol{\xi}}(x) N^{\boldsymbol{\mu}}(x) \ddot{\boldsymbol{u}}^{\boldsymbol{\xi}} dx \cdot \delta\boldsymbol{u}^{\boldsymbol{\mu}} \\
&= \sum_e \left[\int_{-1}^{1} \overline{\rho}_B \frac{\partial \xi}{\partial x} N^{\boldsymbol{\xi}}(\xi) N^{\boldsymbol{\mu}}(\xi) d\xi \ddot{\boldsymbol{u}}^{\boldsymbol{\xi}} \right] \cdot \delta\boldsymbol{u}^{\boldsymbol{\mu}} \\
&= \sum_e \left(\boldsymbol{M}^{be\boldsymbol{\mu}\boldsymbol{\xi}} \ddot{\boldsymbol{u}}^{\boldsymbol{\xi}} \right) \cdot \delta\boldsymbol{u}^{\boldsymbol{\mu}} \,,
\end{aligned} \tag{3.60}$$

  where,

$$\boldsymbol{M}^{be\boldsymbol{\xi}\boldsymbol{\mu}} = \sum_g \overline{\rho}_B \frac{\partial \xi}{\partial x} w_g \begin{bmatrix} N^{\boldsymbol{\xi}}(\xi_g) N^{\boldsymbol{\mu}}(\xi_g) & 0 & 0 \\ 0 & N^{\boldsymbol{\xi}}(\xi_g) N^{\boldsymbol{\mu}}(\xi_g) & 0 \\ 0 & 0 & N^{\boldsymbol{\xi}}(\xi_g) N^{\boldsymbol{\mu}}(\xi_g) \end{bmatrix} , \tag{3.61}$$

  is the elementary mass matrix per unit width.

- Membrane term:

$$\begin{aligned}\sum_e \int_{l_e} {n_B}^{11}(x)\delta u_{1,1}(x)dx &= \sum_e \int_{l_e} {n_B}^{11}(x)N^{\mu}_{,x}dx\delta u^{\mu}_1 \\ &= \sum_e \int_{-1}^{1} n^{11}_B(\xi)N^{\mu}_{,\xi}(\xi)d\xi\delta u^{\mu}_1 \\ &= \sum_e \boldsymbol{F}^{be\ \mu}_{int\,n}\cdot\delta\boldsymbol{u}^{\mu}, \end{aligned} \tag{3.62}$$

  where,

$$\boldsymbol{F}^{be\ \mu}_{int\,n} = \sum_g w_g n^{11}_B(\xi_g)\begin{bmatrix} N^{\mu}_{,\xi}(\xi_g) \\ 0 \\ 0 \end{bmatrix}, \tag{3.63}$$

  is the elementary membrane internal forces vector per unit width.

- Bending term:

$$\begin{aligned}\sum_e \int_{l_e} \tilde{m_B}^{11}(x)\left(-\delta u_{3,1}\right)_{,1}dx &= -\sum_e \int_{l_e} \tilde{m_B}^{11}(x)N^{\mu}_{,xx}(x)dx\delta u^{\mu}_3 \\ &= -\sum_e \int_{-1}^{1} \frac{\partial\xi}{\partial x}\tilde{m_B}^{11}(\xi)N^{\mu}_{,\xi\xi}(\xi)d\xi\delta u^{\mu}_3 \\ &= \sum_e \boldsymbol{F}^{be\ \mu}_{int\,b}\cdot\delta\boldsymbol{u}^{\mu}, \end{aligned} \tag{3.64}$$

  where,

$$\boldsymbol{F}^{be\ \mu}_{int\,b} = -\sum_g w_g\frac{\partial\xi}{\partial x}\tilde{m_B}^{11}(\xi_g)\begin{bmatrix} 0 \\ 0 \\ N^{\mu}_{,\xi\xi}(\xi_g) \end{bmatrix}, \tag{3.65}$$

  is the elementary bending internal forces vector per unit width.

The implementation of the interface part of Eq. (3.34) requires the computation of mean and jump values at interface. This computation is performed following the convention depicted on Fig. 3.2 and the quantities are evaluated at interface thanks to an interpolation of the displacement field in $\xi=-1$ and $\xi=1$, respectively, for minus and plus elements (*i.e.* the quantities are not extrapolated from their values at Gauss points of the elements). Defining the interface virtual field as,

$$\delta\boldsymbol{u}^s = \begin{bmatrix} \delta\boldsymbol{u}^- \\ \delta\boldsymbol{u}^+ \end{bmatrix}, \tag{3.66}$$

the different interface contributions of (3.34) are computed as follows:

- Consistent membrane term:

$$\begin{aligned}\sum_s \langle {n_B}^{11}(x)\rangle [\![\delta u_1]\!] &= \sum_s \frac{1}{2}\left({n_B}^{11^+}(-1)+{n_B}^{11^-}(1)\right)\\ &\quad \left(N^{\mu+}(-1)\delta u_1^{\mu+}-N^{\mu-}(1)\delta u_1^{\mu-}\right)\\ &= \sum_s {\boldsymbol{F}_{int\,cons\,n}^{bs}}^{\mu\pm}\cdot\delta\boldsymbol{u}^{s\mu\pm},\end{aligned} \tag{3.67}$$

where,

$${\boldsymbol{F}_{int\,cons\,n}^{bs}}^{\mu\pm} = \frac{1}{2}\left({n_B}^{11^+}(-1)+{n_B}^{11^-}(1)\right)\begin{bmatrix}-N^{\mu-}(1)\\0\\0\\N^{\mu+}(-1)\\0\\0\end{bmatrix}, \tag{3.68}$$

is the elementary membrane consistent internal forces vector per unit width.

- Compatibility membrane term:

$$\begin{aligned}\sum_s [\![u_1]\!]\langle Eh\delta u_{1,1}\rangle &= \sum_s \frac{Eh}{2}\left(N^{\xi+}(-1)u_1^{\xi+}-N^{\xi-}(1)u_1^{\xi-}\right)\\ &\quad \left(\frac{\partial\xi}{\partial x}^{+}N_{,\xi}^{\mu+}(-1)\delta u_1^{\mu+}+\frac{\partial\xi}{\partial x}^{-}N_{,\xi}^{\mu-}(1)\delta u_1^{\mu-}\right)\\ &= \sum_s {\boldsymbol{F}_{int\,comp\,n}^{bs}}^{\mu\pm}\cdot\delta\boldsymbol{u}^{s\mu\pm},\end{aligned} \tag{3.69}$$

where,

$${\boldsymbol{F}_{int\,comp\,n}^{bs}}^{\mu\pm} = \frac{Eh}{2}\left(N^{\xi+}(-1)u_1^{\xi+}-N^{\xi-}(1)u_1^{\xi-}\right)\begin{bmatrix}\frac{\partial\xi}{\partial x}^{-}N_{,\xi}^{\mu-}(1)\\0\\0\\\frac{\partial\xi}{\partial x}^{+}N_{,\xi}^{\mu+}(-1)\\0\\0\end{bmatrix}, \tag{3.70}$$

is the elementary membrane compatibility internal forces vector per unit width.

- Stability membrane term:

$$\begin{aligned}\sum_s [\![u_1]\!]\left\langle\frac{\beta_2 Eh}{h^s}\right\rangle [\![\delta u_1]\!] &= \sum_s \frac{\beta_2 Eh}{h^s}\left(N^{\xi+}(-1)u_1^{\xi+}-N^{\xi-}(1)u_1^{\xi-}\right)\\ &\quad \left(N^{\mu+}(-1)\delta u_1^{\mu+}-N^{\mu-}(1)\delta u_1^{\mu-}\right)\\ &= \sum_s {\boldsymbol{F}_{int\,stab\,n}^{bs}}^{\mu}\cdot\delta\boldsymbol{u}^{s\mu},\end{aligned} \tag{3.71}$$

where,

$$\boldsymbol{F}_{int\,stab\,n}^{bs\quad\boldsymbol{\mu}\pm} = \frac{\beta_2 Eh}{h^s}\left(N^{\boldsymbol{\xi}+}(-1)u_1^{\boldsymbol{\xi}+} - N^{\boldsymbol{\xi}-}(1)u_1^{\boldsymbol{\xi}-}\right)\begin{bmatrix} -N^{\boldsymbol{\mu}-}(1) \\ 0 \\ 0 \\ N^{\boldsymbol{\mu}+}(-1) \\ 0 \\ 0 \end{bmatrix}, \quad (3.72)$$

is the elementary membrane stability internal force vector per unit width.

- Consistent bending term:

$$\begin{aligned}\sum_s \left\langle \tilde{m_B}^{11}(x)\right\rangle [\![-\delta u_{3,1}]\!] &= -\sum_s \frac{1}{2}\left(\tilde{m_B}^{11+}(-1) + \tilde{m_B}^{11-}(1)\right) \\ &\quad \left(\frac{\partial\xi}{\partial x}^{+} N_{,\xi}^{\boldsymbol{\mu}+}(-1)\delta u_3^{\boldsymbol{\mu}+} - \frac{\partial\xi}{\partial x}^{-} N_{,\xi}^{\boldsymbol{\mu}-}(1)\delta u_3^{\boldsymbol{\mu}-}\right) \\ &= \sum_s \boldsymbol{F}_{int\,cons\,m}^{bs\quad\boldsymbol{\mu}\pm}\cdot\delta\boldsymbol{u}^{s\boldsymbol{\mu}\pm}, \end{aligned} \quad (3.73)$$

where,

$$\boldsymbol{F}_{int\,cons\,m}^{bs\quad\boldsymbol{\mu}\pm} = \frac{1}{2}\left(\tilde{m_B}^{11+}(-1) + \tilde{m_B}^{11-}(1)\right)\begin{bmatrix} 0 \\ 0 \\ \frac{\partial\xi}{\partial x}^{-} N_{,\xi}^{\boldsymbol{\mu}-}(1) \\ 0 \\ 0 \\ -\frac{\partial\xi}{\partial x}^{+} N_{,\xi}^{\boldsymbol{\mu}+}(-1) \end{bmatrix}, \quad (3.74)$$

is the elementary bending consistent internal force vector per unit width.

- Compatibility bending term:

$$\begin{aligned}\sum_s \left[\!\!\left[-u_{3,1}\left\langle -\frac{Eh^3}{12}\delta u_{3,11}\right\rangle\right]\!\!\right] &= \sum_s \frac{Eh^3}{24}\left(\frac{\partial\xi}{\partial x}^{+} N_{,\xi}^{\boldsymbol{\xi}+}(-1)u_3^{\boldsymbol{\xi}+} - \frac{\partial\xi}{\partial x}^{-} N_{,\xi}^{\boldsymbol{\xi}-}(1)u_3^{\boldsymbol{\xi}-}\right) \\ &\quad \left(\left(\frac{\partial\xi}{\partial x}^{+}\right)^2 N_{,\xi\xi}^{\boldsymbol{\mu}+}(-1)\delta u_3^{\boldsymbol{\mu}+} + \left(\frac{\partial\xi}{\partial x}^{-}\right)^2 N_{,\xi\xi}^{\boldsymbol{\mu}-}(1)\delta u_3^{\boldsymbol{\mu}-}\right) \\ &= \sum_s \boldsymbol{F}_{int\,comp\,m}^{bs\quad\boldsymbol{\mu}\pm}\cdot\delta\boldsymbol{u}^{s\boldsymbol{\mu}\pm}, \end{aligned} \quad (3.75)$$

where,

$$\boldsymbol{F}_{int\,compm}^{bs\qquad\quad\boldsymbol{\mu}\pm} = \frac{Eh^3}{24}\left(\frac{\partial\xi}{\partial x}^{+} N_{,\xi}^{\boldsymbol{\xi}+}(-1)u_3^{\boldsymbol{\xi}+} - \frac{\partial\xi}{\partial x}^{-} N_{,\xi}^{\boldsymbol{\xi}-}(1)u_3^{\boldsymbol{\xi}-}\right) \begin{bmatrix} 0 \\ 0 \\ \left(\frac{\partial\xi}{\partial x}^{-}\right)^2 N_{,\xi\xi}^{\boldsymbol{\mu}-}(1) \\ 0 \\ 0 \\ \left(\frac{\partial\xi}{\partial x}^{+}\right)^2 N_{,\xi\xi}^{\boldsymbol{\mu}+}(-1) \end{bmatrix}, \tag{3.76}$$

is the elementary bending compatibility internal force vector per unit width.

- Stability bending term:

$$\begin{aligned}\sum_s [\![-u_{3,1}]\!] \left\langle \frac{\beta_1 Eh^3}{12h^s} \right\rangle [\![-\delta u_{3,1}]\!] &= \sum_s \frac{\beta_1 Eh^3}{12h^s} \left(\frac{\partial\xi}{\partial x}^{+} N_{,\xi}^{\boldsymbol{\xi}+}(-1)u_3^{\boldsymbol{\xi}+} - \frac{\partial\xi}{\partial x}^{-} N_{,\xi}^{\boldsymbol{\xi}-}(1)u_3^{\boldsymbol{\xi}-}\right) \\ &\quad \left(\frac{\partial\xi}{\partial x}^{+} N_{,\xi}^{\boldsymbol{\mu}+}(-1)\delta u_3^{\boldsymbol{\mu}+} - \frac{\partial\xi}{\partial x}^{-} N_{,\xi}^{\boldsymbol{\mu}-}(1)\delta u_3^{\boldsymbol{\mu}-}\right) \\ &= \sum_s \boldsymbol{F}_{int\,stabm}^{bs\qquad\quad\boldsymbol{\mu}\pm} \cdot \delta\boldsymbol{u}^{s\boldsymbol{\mu}\pm},\end{aligned} \tag{3.77}$$

where,

$$\boldsymbol{F}_{int\,stabm}^{bs\qquad\quad\boldsymbol{\mu}\pm} = \frac{\beta_1 Eh^3}{12h^s}\left(\frac{\partial\xi}{\partial x}^{+} N_{,\xi}^{\boldsymbol{\xi}+}(-1)u_3^{\boldsymbol{\xi}+} - \frac{\partial\xi}{\partial x}^{-} N_{,\xi}^{\boldsymbol{\xi}-}(1)u_3^{\boldsymbol{\xi}-}\right) \begin{bmatrix} 0 \\ 0 \\ -\frac{\partial\xi}{\partial x}^{-} N_{,\xi}^{\boldsymbol{\mu}-}(1) \\ 0 \\ 0 \\ \frac{\partial\xi}{\partial x}^{+} N_{,\xi}^{\boldsymbol{\mu}+}(-1) \end{bmatrix}, \tag{3.78}$$

is the elementary bending stability internal force vector per unit width.

- Stability shearing term:

$$\begin{aligned}\sum_s [\![u_3]\!] \left\langle \frac{\beta_3 E h}{2(1+\nu)h^s} \right\rangle [\![\delta u_3]\!] &= \sum_s \frac{\beta_3 E h}{2(1+\nu)h^s} \left(N^{\xi+}(-1) u_3^{\xi+} - N^{\xi-}(1) u_3^{\xi-} \right) \\ &\quad \left(N^{\mu+}(-1) \delta u_3^{\mu+} - N^{\mu-}(1) \delta u_3^{\mu-} \right) \\ &= \sum_s {F^{bs}_{int\, stab\, a}}^{\mu\pm} \cdot \delta \boldsymbol{u}^{s\mu\pm}, \end{aligned} \tag{3.79}$$

where,

$${F^{bs}_{int\, stab\, a}}^{\mu\pm} = \frac{\beta_3 E h}{2(1+\nu)h^s} \left(N^{\xi+}(-1) u_3^{\xi+} - N^{\xi-}(1) u_3^{\xi-} \right) \begin{bmatrix} 0 \\ 0 \\ -N^{\mu-}(1) \\ 0 \\ 0 \\ N^{\mu+}(-1) \end{bmatrix}, \tag{3.80}$$

is the elementary shearing stability internal force vector per unit width.

The assembled form of Eq. (3.34) can be obtained using Eqs. (3.61-3.80),

$$\begin{aligned} 0 &= \sum_e M^{be} \ddot{\boldsymbol{u}} + \sum_e \left(F^{be}_{int\, n} + F^{be}_{int\, b} \right) + \sum_s \Big(F^{bs}_{int\, cons\, n} + F^{bs}_{int\, comp\, n} + F^{bs}_{int\, stab\, n} \\ &\quad + F^{bs}_{int\, cons\, m} + F^{bs}_{int\, comp\, m} + F^{bs}_{int\, stab\, m} \\ &\quad + F^{bs}_{int\, stab\, a} \Big). \end{aligned} \tag{3.81}$$

If the inertial forces are equal to zero (*i.e.* $\ddot{\boldsymbol{u}} = 0$ and the problem is static), the statement (3.81) can be solved alternatively from the expression,

$$\mathbf{K}^{\mu\xi} \boldsymbol{u}^{\xi} = 0 \tag{3.82}$$

with an appropriate application of boundary conditions, with $\boldsymbol{K}^{\mu}$ the $\boldsymbol{\mu}^{\text{th}}$ line of the matrix. This last form considers the stiffness matrix of the problem that can be computed in the general case from internal forces by numerical perturbation or to save computational time determined analytically from the material law. Therefore we present in the following the expressions of elementary stiffness matrices relying on the linear plane stress elastic behavior presented in Section 3.1. To achieve this, we first formulate the value of the resultant stresses as,

$${n_B}^{11}(\xi_g) = E h u_{1,1}(\xi_g) = E h \frac{\partial \xi}{\partial x} \begin{bmatrix} N^{\mu}_{,\xi}(\xi_g) \\ 0 \\ 0 \end{bmatrix} \cdot \boldsymbol{u}^{\mu} \text{ and,} \tag{3.83}$$

$${\tilde{m_B}}^{11}(\xi_g) = -\frac{E h^3}{12} u_{3,11}(\xi_g) = -\frac{E h^3}{12} \left(\frac{\partial \xi}{\partial x} \right)^2 \begin{bmatrix} 0 \\ 0 \\ N^{\mu}_{,\xi\xi}(\xi_g) \end{bmatrix} \cdot \boldsymbol{u}^{\mu}. \tag{3.84}$$

Then the elementary bulk stiffness matrix can be computed from their respective internal forces as,

- Membrane term from Eq. (3.63) ($\boldsymbol{K}^{be}_{int\,n}$ is the elementary membrane stiffness matrix per unit width):

$$\begin{aligned}\boldsymbol{K}^{be}_{int\,n}{}^{\mu\xi} &= \frac{\partial \boldsymbol{F}^{be}_{int\,n}{}^{\mu}}{\partial \boldsymbol{u}^{\xi}} = \frac{\partial}{\partial \boldsymbol{u}^{\xi}} \sum_g \left(w_g E h \frac{\partial \xi}{\partial x} \begin{bmatrix} N^{\nu}_{,\xi}(\xi_g) \\ 0 \\ 0 \end{bmatrix} \cdot \boldsymbol{u}^{\nu} \begin{bmatrix} N^{\mu}_{,\xi}(\xi_g) \\ 0 \\ 0 \end{bmatrix} \right) \\ &= \sum_g w_g E h \frac{\partial \xi}{\partial x} \begin{bmatrix} N^{\mu}_{,\xi}(\xi_g) \\ 0 \\ 0 \end{bmatrix} \otimes \begin{bmatrix} N^{\xi}_{,\xi}(\xi_g) \\ 0 \\ 0 \end{bmatrix} . \end{aligned} \tag{3.85}$$

- Bending term from Eq. (3.65)($\boldsymbol{K}^{be}_{int\,b}$ is the elementary bending stiffness matrix):

$$\begin{aligned}\boldsymbol{K}^{be}_{int\,b}{}^{\mu\xi} &= \frac{\partial \boldsymbol{F}^{be}_{int\,b}{}^{\mu}}{\partial \boldsymbol{u}^{\xi}} = \frac{\partial}{\partial \boldsymbol{u}^{\xi}} \sum_g \left(w_g \frac{E h^3}{12} \left(\frac{\partial \xi}{\partial x} \right)^3 \begin{bmatrix} 0 \\ 0 \\ N^{\nu}_{,\xi\xi\xi}(\xi_g) \end{bmatrix} \cdot \boldsymbol{u}^{\nu} \begin{bmatrix} 0 \\ 0 \\ N^{\mu}_{,\xi\xi\xi}(\xi_g) \end{bmatrix} \right) \\ &= \sum_g w_g \frac{E h^3}{12} \left(\frac{\partial \xi}{\partial x} \right)^3 \begin{bmatrix} 0 \\ 0 \\ N^{\mu}_{,\xi\xi\xi}(\xi_g) \end{bmatrix} \otimes \begin{bmatrix} 0 \\ 0 \\ N^{\xi}_{,\xi\xi\xi}(\xi_g) \end{bmatrix} . \end{aligned} \tag{3.86}$$

The implementation of the interface stiffness matrix is more complicated as we have to compute $\frac{\partial \boldsymbol{F}^{\xi\pm}}{\partial \boldsymbol{x}^{\pm}}$. To perform this operation and defining $\boldsymbol{u}^s = \begin{bmatrix} \boldsymbol{u}^- \\ \boldsymbol{u}^+ \end{bmatrix}$, we suggest to divide the matrix in four blocks,

$$\mathbf{K}^s = \begin{bmatrix} \mathbf{K}^{s\mu^-\xi^-} & \mathbf{K}^{s\mu^-\xi^+} \\ \mathbf{K}^{s\mu^+\xi^-} & \mathbf{K}^{s\mu^+\xi^+} \end{bmatrix} . \tag{3.87}$$

- Consistent membrane term from Eq. (3.68) ($\boldsymbol{K}^{bs}_{int\,cons\,n}$ is the elementary membrane

consistent stiffness matrix per unit width):

$$\begin{aligned}
\boldsymbol{K}^{bs}_{int\,cons\,n}{}^{\boldsymbol{\mu}^{\pm}\boldsymbol{\xi}^{\pm}} &= \frac{\partial \boldsymbol{F}^{bs}_{int\,cons\,n}{}^{\boldsymbol{\mu}^{\pm}}}{\partial \boldsymbol{u}^{\boldsymbol{\xi}^{\pm}}} \\
&= \frac{\partial}{\partial \boldsymbol{u}^{\boldsymbol{\xi}^{\pm}}}\left(\frac{Eh}{2}\left(\left[\begin{array}{c} \frac{\partial \xi}{\partial x}^{+} N^{\boldsymbol{\nu}^{+}}_{,\xi}(-1) \\ 0 \\ 0 \end{array}\right]\cdot \boldsymbol{u}^{\boldsymbol{\nu}^{+}} + \right.\right. \\
&\qquad \left.\left.\left[\begin{array}{c} \frac{\partial \xi}{\partial x}^{-} N^{\boldsymbol{\nu}^{-}}_{,\xi}(1) \\ 0 \\ 0 \end{array}\right]\cdot \boldsymbol{u}^{\boldsymbol{\nu}^{-}}\right)\left[\begin{array}{c} -N^{\boldsymbol{\mu}^{-}}(1) \\ 0 \\ 0 \\ N^{\boldsymbol{\mu}^{+}}(-1) \\ 0 \\ 0 \end{array}\right]\right) \\
&= \frac{Eh}{2}\left[\begin{array}{c} -N^{\boldsymbol{\mu}^{-}}(1) \\ 0 \\ 0 \\ N^{\boldsymbol{\mu}^{+}}(-1) \\ 0 \\ 0 \end{array}\right]\otimes\left[\begin{array}{c} \frac{\partial \xi}{\partial x}^{-} N^{\boldsymbol{\xi}^{-}}_{,\xi}(1) \\ 0 \\ 0 \\ \frac{\partial \xi}{\partial x}^{+} N^{\boldsymbol{\xi}^{+}}_{,\xi}(-1) \\ 0 \\ 0 \end{array}\right].
\end{aligned} \tag{3.88}$$

- Compatibility membrane term from Eq. (3.70) ($\boldsymbol{K}^{bs}_{int\,comp\,n}$ is the elementary membrane compatibility matrix per unit width):

$$\begin{aligned}
\boldsymbol{K}^{bs}_{int\,comp\,n}{}^{\boldsymbol{\mu}^{\pm}\boldsymbol{\xi}^{\pm}} &= \frac{\partial \boldsymbol{F}^{bs}_{int\,comp\,n}{}^{\boldsymbol{\mu}^{\pm}}}{\partial \boldsymbol{u}^{\boldsymbol{\xi}^{\pm}}} = \frac{\partial}{\partial \boldsymbol{u}^{\boldsymbol{\xi}^{\pm}}}\left(\frac{Eh}{2}\left(\left[\begin{array}{c} N^{\boldsymbol{\nu}^{+}}(-1) \\ 0 \\ 0 \end{array}\right]\cdot \boldsymbol{u}^{\boldsymbol{\nu}^{+}} - \right.\right. \\
&\qquad \left.\left.\left[\begin{array}{c} N^{\boldsymbol{\nu}^{-}}(1) \\ 0 \\ 0 \end{array}\right]\cdot \boldsymbol{u}^{\boldsymbol{\nu}^{-}}\right)\left[\begin{array}{c} \frac{\partial \xi}{\partial x}^{-} N^{\boldsymbol{\mu}^{-}}_{,\xi}(1) \\ 0 \\ 0 \\ \frac{\partial \xi}{\partial x}^{+} N^{\boldsymbol{\mu}^{+}}_{,\xi}(-1) \\ 0 \\ 0 \end{array}\right]\right) \\
&= \frac{Eh}{2}\left[\begin{array}{c} \frac{\partial \xi}{\partial x}^{-} N^{\boldsymbol{\mu}^{-}}_{,\xi}(1) \\ 0 \\ 0 \\ \frac{\partial \xi}{\partial x}^{+} N^{\boldsymbol{\mu}^{+}}_{,\xi}(-1) \\ 0 \\ 0 \end{array}\right]\otimes\left[\begin{array}{c} -N^{\boldsymbol{\xi}^{-}}(1) \\ 0 \\ 0 \\ N^{\boldsymbol{\xi}^{+}}(-1) \\ 0 \\ 0 \end{array}\right].
\end{aligned} \tag{3.89}$$

- Stability membrane term from Eq. (3.72) ($\boldsymbol{K}^{bs}_{int\,stab\,n}$ is the elementary membrane stability matrix per unit width):

$$\begin{aligned}
\boldsymbol{K}^{bs}_{int\,stab\,n}{}^{\boldsymbol{\mu}^{\pm}\boldsymbol{\xi}^{\pm}} &= \frac{\partial \boldsymbol{F}^{bs}_{int\,stab\,n}{}^{\boldsymbol{\mu}^{\pm}}}{\partial \boldsymbol{u}^{\boldsymbol{\xi}^{\pm}}} = \frac{\partial}{\partial \boldsymbol{u}^{\boldsymbol{\xi}^{\pm}}}\left(\frac{\beta_2 E h}{h^s}\left(\begin{bmatrix} N^{\boldsymbol{\nu}+}(-1) \\ 0 \\ 0 \end{bmatrix}\cdot \boldsymbol{u}^{\boldsymbol{\nu}+} - \right.\right. \\
&\qquad \left.\left. \begin{bmatrix} N^{\boldsymbol{\nu}-}(1) \\ 0 \\ 0 \end{bmatrix}\cdot \boldsymbol{u}^{\boldsymbol{\nu}-}\right)\begin{bmatrix} -N^{\boldsymbol{\mu}-}(1) \\ 0 \\ 0 \\ N^{\boldsymbol{\mu}+}(-1) \\ 0 \\ 0 \end{bmatrix}\right) \\
&= \frac{\beta_2 E h}{h^s}\begin{bmatrix} -N^{\boldsymbol{\mu}-}(1) \\ 0 \\ 0 \\ N^{\boldsymbol{\mu}+}(-1) \\ 0 \\ 0 \end{bmatrix} \otimes \begin{bmatrix} -N^{\boldsymbol{\xi}-}(1) \\ 0 \\ 0 \\ N^{\boldsymbol{\xi}+}(-1) \\ 0 \\ 0 \end{bmatrix}. \qquad (3.90)
\end{aligned}$$

- Consistency bending term from Eq. (3.74) ($\boldsymbol{K}^{bs}_{int\,cons\,m}$ is the elementary bending consistency matrix per unit width):

$$\begin{aligned}
\boldsymbol{K}^{bs}_{int\,cons\,m}{}^{\boldsymbol{\mu}^{\pm}\boldsymbol{\xi}^{\pm}} &= \frac{\partial \boldsymbol{F}^{bs}_{int\,cons\,m}{}^{\boldsymbol{\mu}^{\pm}}}{\partial \boldsymbol{u}^{\boldsymbol{\xi}^{\pm}}} = \frac{\partial}{\partial \boldsymbol{u}^{\boldsymbol{\xi}^{\pm}}}\left(-\frac{E h^3}{24}\left(\begin{bmatrix} 0 \\ 0 \\ \left(\frac{\partial \xi}{\partial x}^{+}\right)^2 N^{\boldsymbol{\nu}+}_{,\xi\xi}(-1) \end{bmatrix}\cdot \boldsymbol{u}^{\boldsymbol{\nu}+}\right.\right. \\
&\qquad \left.\left. + \begin{bmatrix} 0 \\ 0 \\ \left(\frac{\partial \xi}{\partial x}^{-}\right)^2 N^{\boldsymbol{\nu}-}_{,\xi\xi}(1) \end{bmatrix}\cdot \boldsymbol{u}^{\boldsymbol{\nu}-}\right)\begin{bmatrix} 0 \\ 0 \\ \frac{\partial \xi}{\partial x}^{-} N^{\boldsymbol{\mu}-}_{,\xi}(1) \\ 0 \\ 0 \\ -\frac{\partial \xi}{\partial x}^{+} N^{\boldsymbol{\mu}+}_{,\xi}(-1) \end{bmatrix}\right) \\
&= -\frac{E h^3}{24}\begin{bmatrix} 0 \\ 0 \\ \frac{\partial \xi}{\partial x}^{-} N^{\boldsymbol{\mu}-}_{,\xi}(1) \\ 0 \\ 0 \\ -\frac{\partial \xi}{\partial x}^{+} N^{\boldsymbol{\mu}+}_{,\xi}(-1) \end{bmatrix} \otimes \begin{bmatrix} 0 \\ 0 \\ \left(\frac{\partial \xi}{\partial x}^{-}\right)^2 N^{\boldsymbol{\xi}-}_{,\xi\xi}(1) \\ 0 \\ 0 \\ \left(\frac{\partial \xi}{\partial x}^{+}\right)^2 N^{\boldsymbol{\xi}+}_{,\xi\xi}(-1) \end{bmatrix}. \qquad (3.91)
\end{aligned}$$

- Compatibility bending term from Eq. (3.76) ($\boldsymbol{K}^{bs}_{int\,comp\,m}$ is the elementary bending

compatibility matrix per unit width):

$$\begin{aligned}
\boldsymbol{K}^{bs}_{int\,compm}{}^{\mu^{\pm}\xi^{\pm}} &= \frac{\partial \boldsymbol{F}^{bs}_{int\,compm}{}^{\mu^{\pm}}}{\partial \boldsymbol{u}^{\xi^{\pm}}} = \frac{\partial}{\partial \boldsymbol{u}^{\xi^{\pm}}}\left(\frac{Eh^3}{24}\left(\begin{bmatrix} 0 \\ 0 \\ \frac{\partial\xi}{\partial x}^{+} N^{\nu^{+}}_{,\xi}(-1) \end{bmatrix}\cdot \boldsymbol{u}^{\nu^{+}} - \right.\right. \\
&\left.\left. \begin{bmatrix} 0 \\ 0 \\ \frac{\partial\xi}{\partial x}^{-} N^{\nu^{-}}_{,\xi}(1) \end{bmatrix}\cdot \boldsymbol{u}^{\nu^{-}}\right)\begin{bmatrix} 0 \\ 0 \\ -\left(\frac{\partial\xi}{\partial x}^{-}\right)^2 N^{\mu^{-}}_{,\xi\xi\xi}(1) \\ 0 \\ 0 \\ \left(\frac{\partial\xi}{\partial x}^{+}\right)^2 N^{\mu^{+}}_{,\xi\xi\xi}(-1) \end{bmatrix}\right) \\
&= \frac{Eh^3}{24}\begin{bmatrix} 0 \\ 0 \\ \left(\frac{\partial\xi}{\partial x}^{-}\right)^2 N^{\mu^{-}}_{,\xi\xi\xi}(1) \\ 0 \\ 0 \\ \left(\frac{\partial\xi}{\partial x}^{+}\right)^2 N^{\mu^{+}}_{,\xi\xi\xi}(-1) \end{bmatrix} \otimes \begin{bmatrix} 0 \\ 0 \\ -\frac{\partial\xi}{\partial x}^{-} N^{\xi^{-}}_{,\xi}(1) \\ 0 \\ 0 \\ \frac{\partial\xi}{\partial x}^{+} N^{\xi^{+}}_{,\xi}(-1) \end{bmatrix}. \qquad (3.92)
\end{aligned}$$

- Stability bending term from Eq. (3.78) ($\boldsymbol{K}^{bs}_{int\,stabm}$ is the elementary bending stability matrix per unit width):

$$\begin{aligned}
\boldsymbol{K}^{bs}_{int\,stabm}{}^{\mu^{\pm}\xi^{\pm}} &= \frac{\partial \boldsymbol{F}^{bs}_{int\,stabm}{}^{\mu^{\pm}}}{\partial \boldsymbol{u}^{\xi^{\pm}}} = \frac{\partial}{\partial \boldsymbol{u}^{\xi^{\pm}}}\left(\frac{\beta_1 Eh^3}{12h^s}\left(\begin{bmatrix} 0 \\ 0 \\ \frac{\partial\xi}{\partial x}^{+} N^{\nu^{+}}_{,\xi}(-1) \end{bmatrix}\cdot \boldsymbol{u}^{\nu^{+}} - \right.\right. \\
&\left.\left. \begin{bmatrix} 0 \\ 0 \\ \frac{\partial\xi}{\partial x}^{-} N^{\nu^{-}}_{,\xi}(1) \end{bmatrix}\cdot \boldsymbol{u}^{\nu^{-}}\right)\begin{bmatrix} 0 \\ 0 \\ -\frac{\partial\xi}{\partial x}^{-} N^{\mu^{-}}_{,\xi}(1) \\ 0 \\ 0 \\ \frac{\partial\xi}{\partial x}^{+} N^{\mu^{+}}_{,\xi}(-1) \end{bmatrix}\right) \\
&= \frac{\beta_1 Eh^3}{12h^s}\begin{bmatrix} 0 \\ 0 \\ -\frac{\partial\xi}{\partial x}^{-} N^{\mu^{-}}_{,\xi}(1) \\ 0 \\ 0 \\ \frac{\partial\xi}{\partial x}^{+} N^{\mu^{+}}_{,\xi}(-1) \end{bmatrix} \otimes \begin{bmatrix} 0 \\ 0 \\ -\frac{\partial\xi}{\partial x}^{-} N^{\xi^{-}}_{,\xi}(1) \\ 0 \\ 0 \\ \frac{\partial\xi}{\partial x}^{+} N^{\xi^{+}}_{,\xi}(-1) \end{bmatrix}. \qquad (3.93)
\end{aligned}$$

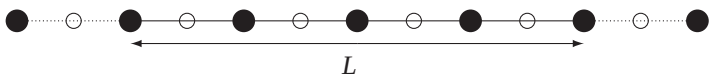

Figure 3.4: To prescribe boundary conditions on rotation virtual elements (dotted line) are used.

- Stability shearing term from Eq. (3.80) ($\boldsymbol{K}^{bs}_{int\,stab\,a}$ is the elementary shearing stability matrix per unit width)

$$\begin{aligned}
\boldsymbol{K}^{bs}_{int\,stab\,a}{}^{\mu^{\pm}\xi^{\pm}} &= \frac{\partial \boldsymbol{F}^{bs}_{int\,stab\,a}{}^{\mu^{\pm}}}{\partial \boldsymbol{u}^{\xi^{\pm}}} = \frac{\partial}{\partial \boldsymbol{u}^{\xi^{\pm}}} \left(\frac{\beta_3 E h}{2(1+\nu)h^s} \left(\begin{bmatrix} 0 \\ 0 \\ N^{\nu+}(-1) \end{bmatrix} \cdot \boldsymbol{u}^{\nu+} - \right. \right. \\
&\qquad \left. \left. \begin{bmatrix} 0 \\ 0 \\ N^{\nu-}(1) \end{bmatrix} \boldsymbol{u}^{\xi-} \right) \begin{bmatrix} 0 \\ 0 \\ -N^{\mu-}(1) \\ 0 \\ 0 \\ N^{\mu+}(-1) \end{bmatrix} \right) \\
&= \frac{\beta_3 E h}{2(1+\nu)h^s} \begin{bmatrix} 0 \\ 0 \\ -N^{\mu-}(1) \\ 0 \\ 0 \\ N^{\mu+}(-1) \end{bmatrix} \otimes \begin{bmatrix} 0 \\ 0 \\ -N^{\xi-}(1) \\ 0 \\ 0 \\ N^{\xi+}(-1) \end{bmatrix}. \qquad (3.94)
\end{aligned}$$

To finish this part on the implementation of the full-DG formulation of beams we briefly discuss the application of boundary conditions on rotation to simulate, *e.g.* a clamp. Indeed, the one-field (displacement) formulation suggested herein does not allow to apply strongly such a condition. Therefore, we prescribe the boundary conditions on rotation weakly using an interface element. This interface element considers a virtual element situated in the continuation of the beam as shown on Fig. 3.4. The rotational boundary conditions can then be applied by prescribing the displacement field of the virtual element. For example a clamp can be simulated by fixing all the displacements of the virtual element to zero. It has to be mentioned that for more efficiency this last case is implemented in the software by removing all nodes of the virtual element (*i.e.* only the components of the interface element corresponding to the "not virtual" element are computed and assembled).

Finally in the vectorial and matricial equations presented, u_2 is fixed to zero.

3.2.4 Numerical benchmarks

Some simulations are performed with the weak formulation (3.34) to demonstrate its ability to simulate continuum mechanics. In particular we compare this full-DG formulation with the C^0/DG one presented by G. Engel *et al.* [91] and with analytical values. The results of both formulations are in agreement with the analytical ones and the full-DG formulation is as accurate as the C^0/DG one. We study first a double clamped beam loaded uniformly in a quasi-static way. Then two dynamic examples focus on the stress wave propagation as it is an issue of the recourse to intrinsic cohesive law. On the contrary, it is proved herein that the full-DG formulation developed above does not affect the stress wave propagation and can thus coupled to an ECL.

Double clamped beam with uniformly distributed loading

The numerical properties demonstrated in Section 3.2 are illustrated on this example. It shows that the convergence rate of the solution with respect to the mesh size is in accordance with the theory and that the results are as accurate as the ones obtained with the C^0/DG formulation previously developed by G. Engel *et al.* [91].

The example consists in a double clamped beam (DCB), whose material and geometrical properties are given in Fig. 3.5 and Tab. 3.1 respectively, submitted to a distributed force $p = 4$ $[kN/m]$. This force induces a displacement field described analytically by (see [153]),

$$u_3(\xi^1) \quad = \quad -\frac{p{\xi^1}^2(L-\xi^1)^2}{24EI}. \tag{3.95}$$

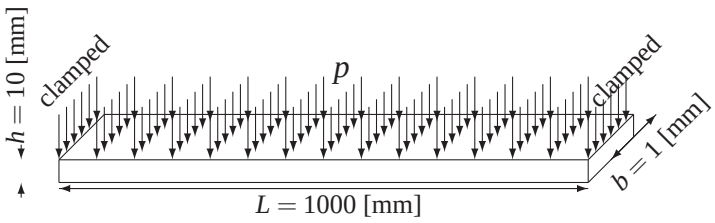

Figure 3.5: Geometry of the numerical benchmark used to demonstrate the numerical properties of the full-DG method.

This case is simulated with quadratic and cubic elements for different mesh sizes (h^s) ranging from 1000/4 to 1000/256 [mm] and different stabilization parameter values of β_1 ranging from 5 to $1e^6$

The choice of β_3 results from a study of the convergence of the normalized deflection with respect to β_3, which depends on geometry, as illustrated on Fig. 3.6 for $h^s = 1/64$, $\beta_1 = \beta_2 = 10$. On Fig. 3.6(a), the benchmark presented herein is also simulated with a thickness of 100 [mm] (in place of 10 [mm]). It appears that both convergence curves are

Property	Value
Young modulus [GPa]	10
Poisson ratio [-]	0.21
Density $[\mathrm{kg/m^3}]$	10000

Table 3.1: Material properties of the numerical benchmark used to demonstrate the numerical properties of the full-DG method.

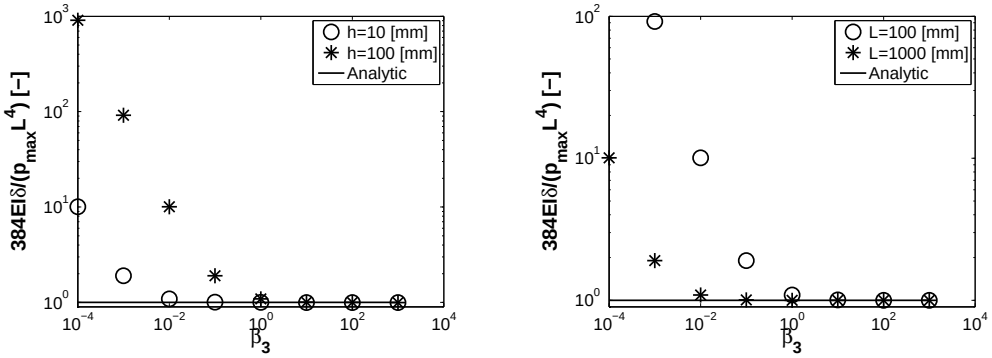

(a) Effect of thickness. (b) Effect of length.

Figure 3.6: Convergence of the normalized deflection with respect to β_3 for different geometrical parameters.

exactly the same but are scaled by a factor 100. Therefore, the convergence with β_3 depends on the geometry. To remove this dependency, β_3 has to be multiplied by a factor $(h/L)^2$. Indeed, when the height is divided by 10 the minimal value of β_3 which gives a converged solution is divided by 100. Furthermore, the same study can be realized by varying the beam length, as presented on Fig. 3.6(b), which shows than when L is divided by 10, the minimal value of β_3 which gives a converged solution is multiplied by 100. These results show that β_3 should be equal to $\beta_1/(h/L)^2$ to produce results independent of the geometry. In this work, unless specified otherwise, we choose $\beta_3 = \frac{\beta_1}{100}\left(\frac{h}{L}\right)^2$ which avoids ill conditioned matrix. Note that as this test is in pure bending[4], there is no displacement along ξ^1 (*i.e.* $u_1 = 0$) and the value of β_2 does not modify the results in this case.

For illustration, the normal deformation, obtained for $\beta_1 = 100$, is plotted on Fig. 3.7. This figure contains four graphs depending on the type of elements: quadratic elements and a C^0/DG formulation, Fig. 3.7(a), quadratic elements and the full-DG formulation, Fig. 3.7(b), cubic elements and a C^0/DG formulation, Fig. 3.7(c), and cubic elements and the full-DG formulation, Fig. 3.7(d). These graphs show that the convergence (less than 1% error) is achieved for respectively 100, 192, 128 and 168 degrees of freedom for quadratic C^0/DG ,

[4]As shearing is neglected in Euler Bernoulli beams

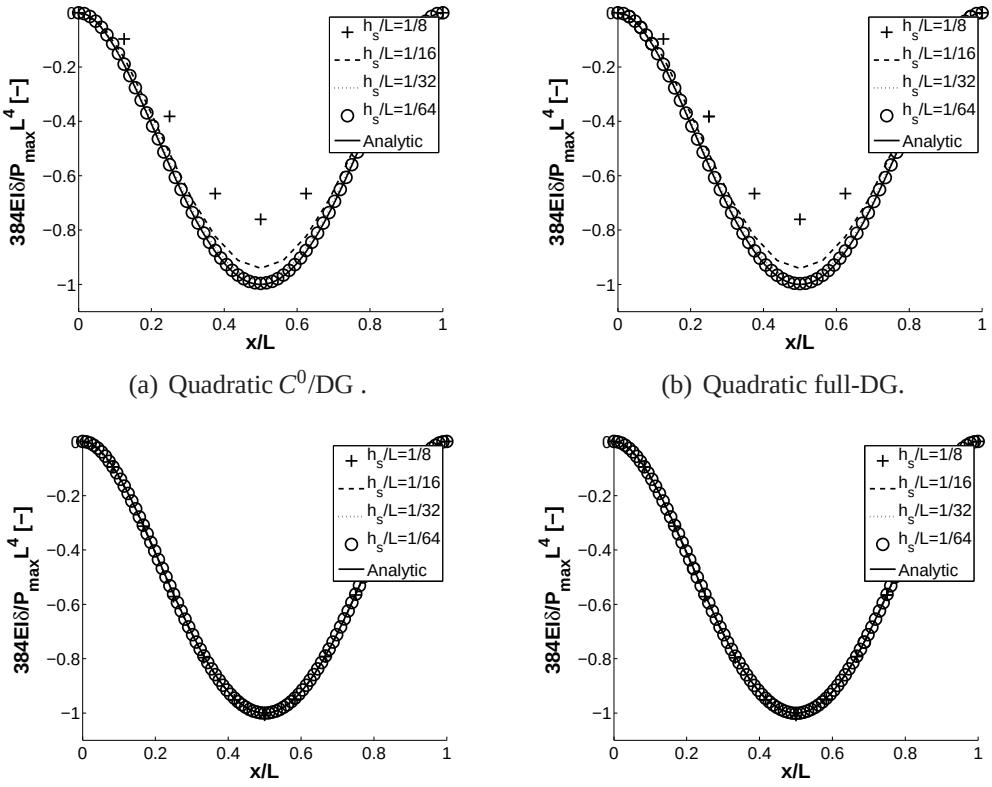

(a) Quadratic C^0/DG . (b) Quadratic full-DG.

(c) Cubic C^0/DG . (d) Cubic full-DG.

Figure 3.7: Convergence of deformation is the same for both C^0/DG and full-DG formulation no matter the element type.

quadratic full-DG, cubic C^0/DG and cubic full-DG elements. Therefore, it demonstrates that the analytical solution is very well approximated for both degrees of elements and that the full-DG formulation gives the same results as the C^0/DG method.

The convergence of displacements with the mesh size is emphasized by Fig. 3.8, which plots the normalized maximal deflection of the beam: for quadratic elements with C^0/DG formulation Fig., 3.8(a), quadratic elements with full-DG formulation Fig., 3.8(b), cubic elements with C^0/DG formulation Fig., 3.8(c) and cubic elements with full-DG formulation, Fig. 3.8(d). Furthermore, this figure shows that for any order of interpolation and for $\beta_1 \geq 5$, both C^0/DG and full-DG methods are stable. However for values of $\beta_1 > 1e^6$ (quadratic elements) and $\beta_1 > 1000$ (cubic elements) both methods suffer from locking for the finer mesh, which leads to low convergence rate in the $\mathbf{L}^2$-norms. From these graphs, it appears that as long as the stabilization parameter β_1 remains in a rather wide range [5-1000], numerical accuracy of the method is ensured. Same behavior was observed for different applications of discontinuous Galerkin methods for solids [182, 184] and for shells [181, 185], which allows concluding that this range is non-dependent from the problem under consideration.

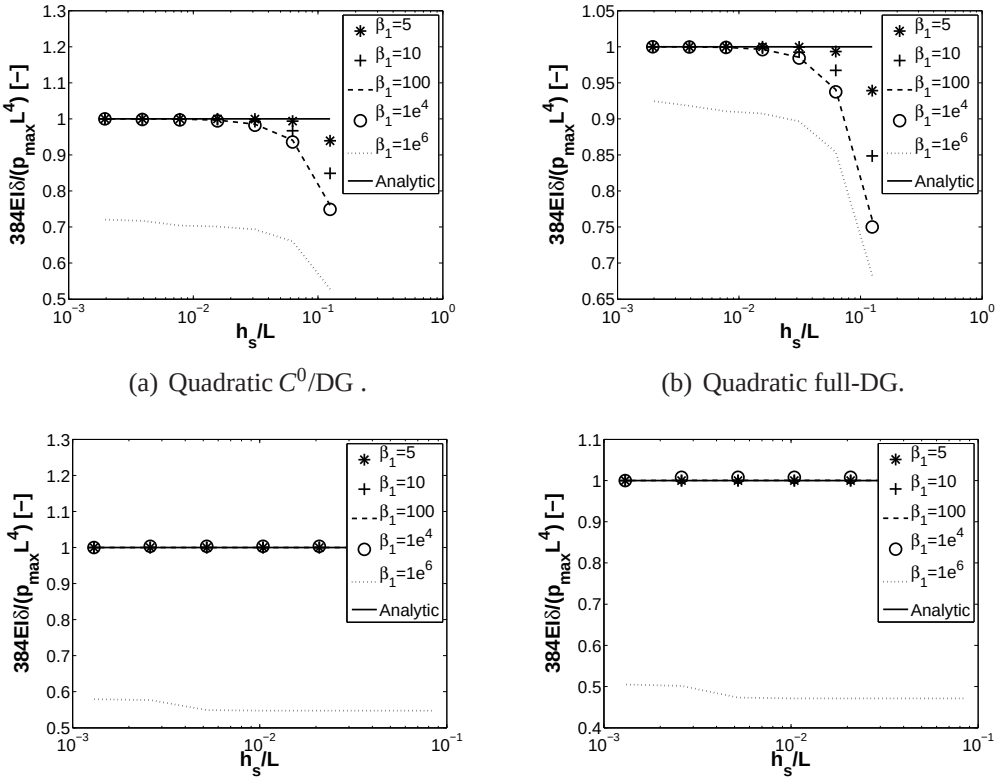

(a) Quadratic C^0/DG .

(b) Quadratic full-DG.

(c) Cubic C^0/DG .

(d) Cubic full-DG.

Figure 3.8: The accuracy of the method is ensured for a wide range [5-1000] of stability parameters β_1 as illustrated by the convergence of the maximal deflection with respect to the mesh size.

The convergence of results with the mesh size is demonstrated from previous figures and the convergence rate is studied on Figs. 3.9 and 3.10 respectively for the $\mathbf{L}^2$ and the energetic norms. Once again, this study is performed for different element types: quadratic elements with a C^0/DG formulation Figs. 3.9(a) and 3.10(a), quadratic elements with a full-DG formulation, Figs. 3.9(b) and 3.10(b), cubic elements with a C^0/DG formulation, Figs. 3.9(c) and 3.10(c), and cubic elements with a full-DG formulation, Figs. 3.9(d) and 3.10(d). These figures illustrate that both convergence rates correspond to those predicted by the theory, unless locking or numerical accuracy for low errors prevent reaching this convergence rate. In particular, the convergence rate in the $\mathbf{L}^2$-norm is less than expected for the thinnest meshes due to the smallest of the relative error (around 10^{-6}), which is too small to continue to obtain the same convergence rate. Moreover, the convergence rate in the $\mathbf{L}^2$-norm is in $k+1$ even for quadratic elements, while the theory predicts a convergence rate only in k. This observation is in agreement with what was shown by L. Noels *et al.* [185] and by G. Wells [257] for C^0/DG shells. One more time, the two figures show that the same results are obtained by the C^0/DG and full-DG methods.

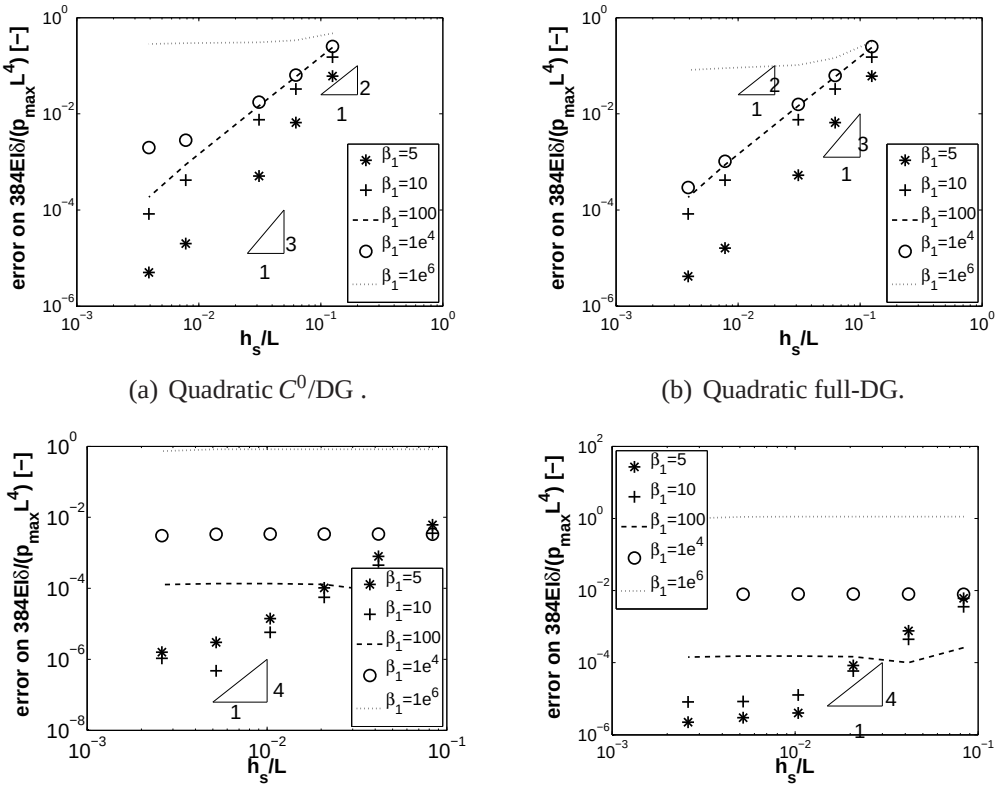

(a) Quadratic C^0/DG .

(b) Quadratic full-DG.

(c) Cubic C^0/DG .

(d) Cubic full-DG.

Figure 3.9: The theoretical convergence rate in the $\mathbf{L}^2$-norm is observed for the DCB numerical benchmark.

Finally, Fig. 3.11 illustrates the condition number of the stiffness matrix with respect to the number of elements and for different values of parameters β_i ($\beta_2 = \beta_1$ and $\beta_3 = 100\beta_1$). The condition numbers depict on the figure are divided by the condition number of the elementary bulk matrix to be independent of the material and geometry. Moreover, they are reported for both C^0/DG , on Figs. 3.11(a) and 3.11(c), and full-DG, on Figs. 3.11(b) and 3.11(d), formulations, as well as for elements of degree 2, Figs. 3.11(a) and 3.11(b), and elements of degree 3, Figs. 3.11(c) and 3.11(d). These graphs show that the condition number is approximately the same for the two formulations and the two degrees of element. Furthermore, for all the cases, the condition number increases with the fourth power of the number of elements and increases linearly with the parameter β_1. So for large stabilization parameters β_i, an ill-conditioned matrix is expected. However, in the practical range ($\beta_1 \simeq 10$), the condition numbers remain satisfactory, which justifies the use of stability parameters as low as possible for quasi-static cases.

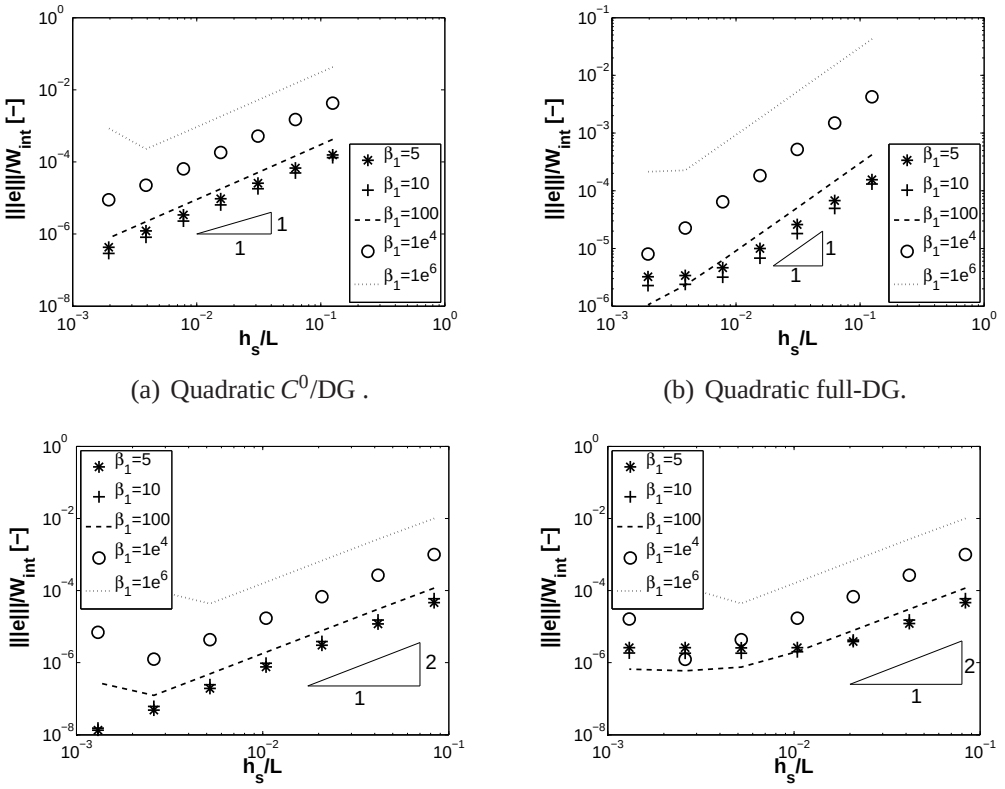

(a) Quadratic C^0/DG . (b) Quadratic full-DG.

(c) Cubic C^0/DG . (d) Cubic full-DG.

Figure 3.10: The theoretical convergence rate in the energetic norm is observed for the DCB numerical benchmark.

Stress wave propagation

The main drawback of an intrinsic cohesive approach (see Section 2.2.1) is a perturbation of the stress wave propagation through the elements due to the enforcement of continuity thanks to a penalty parameter. Despite of DG methods are interior penalty methods, they remain consistent and we illustrated in this section by two numerical examples that a correct stress wave propagation is observed for our suggested DG method.

The stress wave propagation is obviously a dynamic phenomenon and therefore we use in this section the explicit central difference algorithms [103] to solve the set of Eqs. (3.8) and (3.14). Although another temporal integration can be used we select this one for its simplicity of implementation. Nevertheless, this one is conditionally stable and a time step lower than a critical value Δt_{crit} is required to solve the problem. The value of Δt_{crit} depends on the higher natural (numerical) frequency of the model. As the DG method uses discontinuous elements, it introduces extra numerical frequencies governed by the stability parameters. L. Noels *et al.* [184] studied the variation of maximal natural frequency with respect to β_1 for their C^0/DG method. They demonstrated that the Δt_{crit} should be divided by $\sqrt{\beta_1}$ to ensure

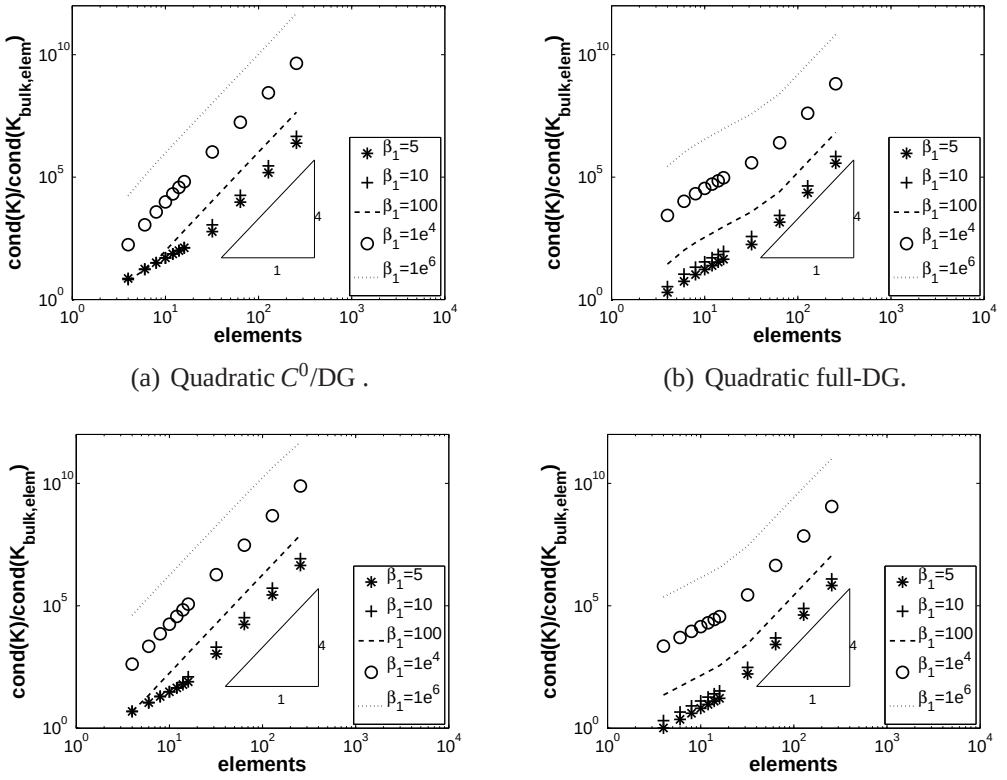

(a) Quadratic C^0/DG .

(b) Quadratic full-DG.

(c) Cubic C^0/DG .

(d) Cubic full-DG.

Figure 3.11: Satisfactory condition number of stiffness matrix is observed for low values of β_1.

the stability of the algorithm. Such a study is performed herein on the stability parameters to show the relation remains valid if we consider the maximal value of β_1, β_2 and β_3. We focus on a beam depicted on Fig. 3.12, with the same dimensions and material values than the one studied in Section 3.2.4 but with a different boundary condition as this time it is simply clamped. We compute for $\beta_1 = \beta_2 = 0.1$ and different values of β_3 the natural frequencies of the beam meshed by 20 quadratic and cubic elements and plot the maximal frequency on Fig. 3.13. Obviously as there is more degrees of freedom with the cubic mesh, the maximal frequency is higher but it remains constant until $\beta_3 = 1e^4$ and and $\beta_3 = 1e^5$ respectively for quadratic and cubic elements even if very small values are consider for other stability parameters β_1 and β_2. Therefore, in the practical range of β_3, this has no effect on the maximal natural frequency (*i.e.* the additional frequencies governed by β_3 are lower than the maximal value of the C^0/DG method) and its influence can be omitted for the computation of the critical time step. Nevertheless, for large values of $\beta_3 \geq 1e^5$, the maximal frequency varies with respect to β_3 with a factor close of $\sqrt{\beta_3}$ and therefore the relation is the same as for stability parameters β_1, β_2. Indeed, the variations of the highest frequency with respect to β_1

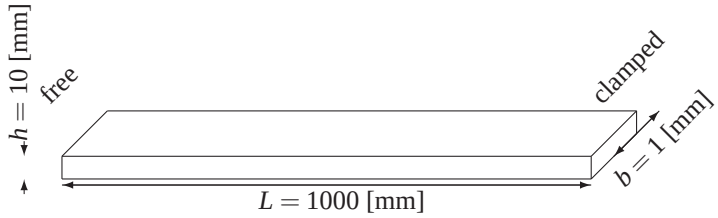

Figure 3.12: Beam configuration to study stress wave propagation.

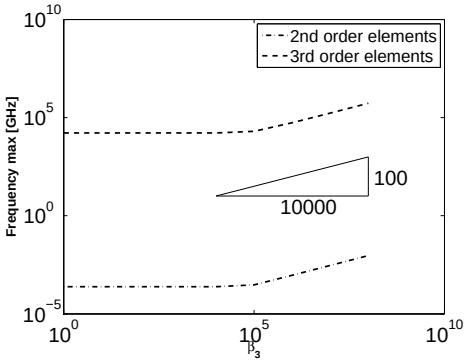

Figure 3.13: The highest natural frequency is independent of β_3 in the range of interesting values.

and β_2 are respectively illustrated on 3.14(a) and 3.14(b). In each case, the values of other stability parameters are fixed to 0.1. Therefore we suggest to adapt the criterion of L. Noels *et al.* [184] by changing the factor $\frac{1}{\sqrt{\beta_1}}$ by $\frac{1}{\sqrt{\max\beta_\alpha}}$. This study confirms our assumption to choose $\beta_1 = \beta_2$. In the following we use $\beta_1 = \beta_2 = 10$ and $\beta_3 = \frac{\beta_1}{100}\left(\frac{h}{L}\right)^2$.

With this criterion on Δt_{crit}, ensuring the stability of the explicit time integration algorithms, we can simulate the impact of the beam, whose material properties are given in Tab. 3.1, with a rigid plane. To avoid the contact modeling, we can advantageously perform the simulation with the simply clamped beam depicted on Fig. 3.12. Indeed the rigid plane is situated at the clamp (*i.e.* the last node is clamped) and we just give an initial velocity along the beam axis in direction of the clamp.

This setup generates a stress wave propagating from the clamp to the free extremity and then reflecting to return toward the clamp where a new reflection occurs. The speed of the dilatational wave $c_d = \sqrt{\frac{E}{\rho}} = 1000$ [m/s] controls the velocity of the stress wave given by $\rho c_d V_1$, with $V_1 = 1$ [m/s] the value of the prescribed initial velocity. Therefore the evolution with time of the velocity the free extremity represented on Fig. 3.15 gives an image of the stress wave propagation. As the beam's length is 1 [m], the wave takes 1 [ms] to reach at the free extremity where its reflection induces a change of the velocity sign. Then the wave comes

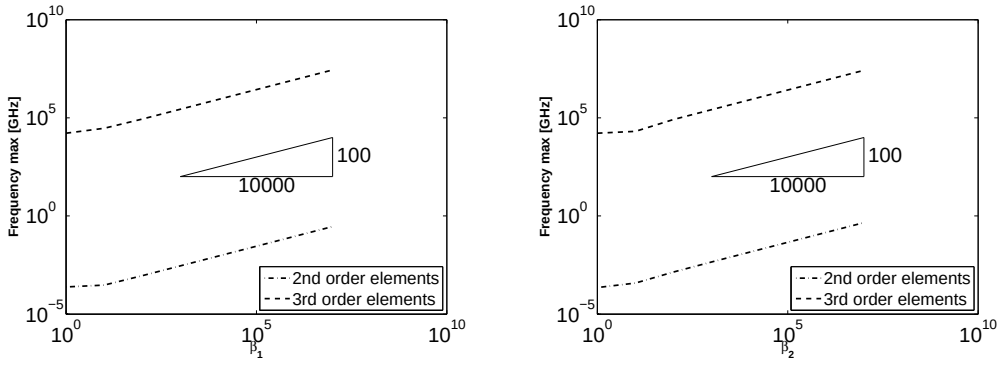

(a) β_1. (b) β_2.

Figure 3.14: Evolution of the highest natural frequency is the same for $\beta 1$ and β_2.

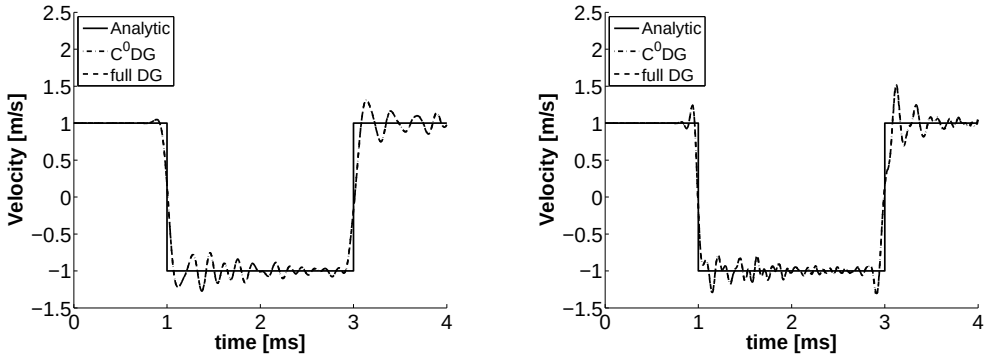

(a) Quadratic element. (b) Cubic element.

Figure 3.15: The stress wave propagation is unaffected by the use of a DG formulation.

back after 2 [ms], and causes a new change of the velocity sign.

The theoretical behavior is well captured by the simulation with height quadratic elements, Fig. 3.15(a), and height cubic elements Fig. 3.15(b). Even if there are spurious numerical oscillations, the transition of the velocity occurs at times 1 and 3 [ms] as expected. Furthermore, as the problem is also simulated with a C^0/DG method, we can conclude that the stress wave is not modified due to the discontinuity between the elements.

Finally, we suggest a benchmark to study the stress wave propagation in a beam loaded in bending. The beam has initially a displacement of 4 [mm] in direction $\boldsymbol{E}_3$ at the free extremity, and equilibrium is computed by a quasi-static analysis. Then the prescribed displacement is removed to have an initial unbalanced configuration at the beginning of an explicit simulation. As the material is elastic, the beam starts to oscillate around the undeformed configuration with a frequency corresponding to the first bending eigen mode. This value can be determined by a spectral analysis and is equal to 16.23 [Hz] for the considered beam. The oscillations at

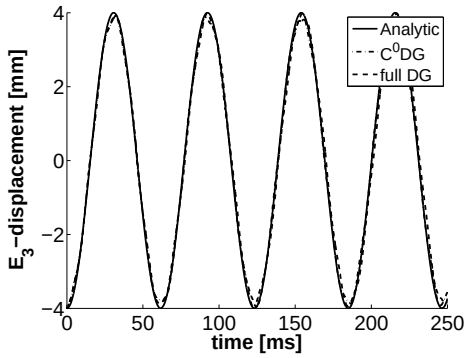

Figure 3.16: The oscillation frequency (at free extremity) is not modified by the use of the full-DG method.

the free extremity are studied on Fig. 3.16 for the beam meshed with height cubic elements. Despite of a small error in the amplitude (due to explicit numerical integration), the frequency of the oscillations is well captured by the full-DG method, which gives the same results as the C^0/DG formulation. Therefore once again the dynamic behavior is not modified by the use of discontinuous elements.

3.3 Extrinsic cohesive law for Euler-Bernoulli beams

This section introduces an original extrinsic cohesive law based on the reduced stresses (3.5) and (3.12) dedicated to the thin bodies. Afterward, we study the accuracy of the method on a benchmark. This one proves that with the DG/ECL combination we are able to simulate the initiation and through-the-thickness propagation of a crack while respecting the energetic balance (*i.e.* the dissipated energy is equal to the fracture energy of the material) for different tension/bending mixed loadings.

3.3.1 Extrinsic cohesive law for thin bodies

We develop herein an extrinsic cohesive law based on the reduced stresses (3.5) and (3.12), which can easily be coupled with the full-DG method presented in Section 3.2 as these reduced stresses appear explicitly in the formulation (3.34).

As interface elements have already been introduced in the DG method, it is not necessary to modify dynamically the mesh in order to introduce the cohesive elements, which is the critical step of classical extrinsic cohesive approaches. The cohesive elements ”substitute” simply the interface elements where the fracture criterion is reached. Mathematically the equation (3.35) can be rewritten, as introduced first by J. Mergheim *et al.* [157], as

$$\text{Structural terms} + (1-\alpha_s)\ \text{DG terms} + \alpha_s\ \text{cohesive term} \quad = \quad 0\,, \tag{3.96}$$

where α_s is evaluated at each interface element and is equal to one if there is fracture and is equal to zero if this is not the case. For Euler-Bernoulli beams, only the normal stress component is different from zero and a fracture criterion in tension can be considered,

$$\max_{\xi^3} \left\langle \sigma^{11} \right\rangle - \sigma_c \quad > \quad 0\,, \tag{3.97}$$

where the operator $\langle \bullet \rangle$ represents the mean value on the interface element and where σ_c, the fracture strength, is a material parameter.

The cohesive zone concept, initially presented by G. Barenblatt [24], is based on the existence of a residual traction while crack faces are still in a close neighborhood. In this model of perfectly brittle fracture, the traction represents the physical inter-atomic attractive forces which are exerted between atoms. After a given distance Δ_c this traction falls to zero and there is no force exerted between crack faces. In more general cases, the traction-separation law represents physical phenomena happening in the process zone. The application of the J-integral concept introduced by J. Rice [215] leads to the general form of the cohesive term,

$$\delta J \quad = \quad \int \boldsymbol{T} \cdot \delta(\boldsymbol{\Delta}) dS\,, \tag{3.98}$$

with $\boldsymbol{T}$ the traction forces exerted between crack faces and $\boldsymbol{\Delta}$ the opening between them. In this chapter the normal to the fracture surface is equal to $\boldsymbol{E}_1$ as the linear assumption is made[5]. Therefore vectors $\boldsymbol{T}$ and $\boldsymbol{\Delta}$ have a non-zero component only along axis 1, which are respectively noted t and Δ in the following. Moreover, as the cohesive term (3.98) is equal to the J-integral the area under the TSL must be equal to the energy of rupture G_c, a material parameter [109], if the crack grows straight ahead, which is the case herein as the crack growths through-the-thickness. So the two parameters of the TSL are σ_c and G_c, the critical opening value Δ_c being deduced from the traction-separation law shape, see Fig. 2.3(b).

As the focus is put on thin bodies where the thickness is implicitly modeled, it is not straightforward to take into account a through-the-thickness fracture. A solution is suggested by F. Cirak *et al.* [70], where the traction-separation-law is integrated at each Simpson points describing the thickness. As the TSL makes sense only for traction, this solution is difficult to implement in the general case when bending can occurs and an original approach considering a traction-separation law based on the resultant stresses is suggested. The cohesive integral (3.98) is replaced by the application of cohesive law on the resultant membrane $\left\langle {n_B}^{11} \right\rangle$ and bending $\left\langle \tilde{m_B}^{11} \right\rangle$ stresses, which are denoted N_{coh} and M_{coh} respectively after fracture is initiated, leading to,

$$\frac{\boldsymbol{T} \cdot \delta(\boldsymbol{\Delta}) dS}{b} \rightarrow N_{coh}(\Delta^\star)\delta(\llbracket u_1 \rrbracket) + M_{coh}(\Delta^\star)\delta(\llbracket -u_{3,1} \rrbracket)\,, \tag{3.99}$$

where $\Delta^\star$ is an effective opening, and where we have stated the expression per unit width.

[5]The normal to the fracture surface ν_s in the current configuration of the interface element can be computed as suggested by F. Cirak *et al.* [70] by, $\nu_s = \frac{\langle \nu_s \rangle}{\| \langle \nu_s \rangle \|}$, with $\nu_s^\pm$ equal to, $\nu_s^\pm = \boldsymbol{\tau}^\pm \wedge \boldsymbol{t}^\pm$, where $\boldsymbol{t}$ and $\boldsymbol{\tau}$ are respectively the normal of the neutral axis and the tangent vector at the interface element. For beam elements these quantities are equal to, $\boldsymbol{t} = \boldsymbol{E}_3 - u_{3,1}\boldsymbol{E}_1$ and, $\boldsymbol{\tau} = \boldsymbol{E}_2$, which leads to, $\nu_s = \frac{\boldsymbol{E}_1 + \langle u_{3,1} \rangle \boldsymbol{E}_3}{\sqrt{1 + \langle u_{3,1} \rangle^2}} \approx \boldsymbol{E}_1$.

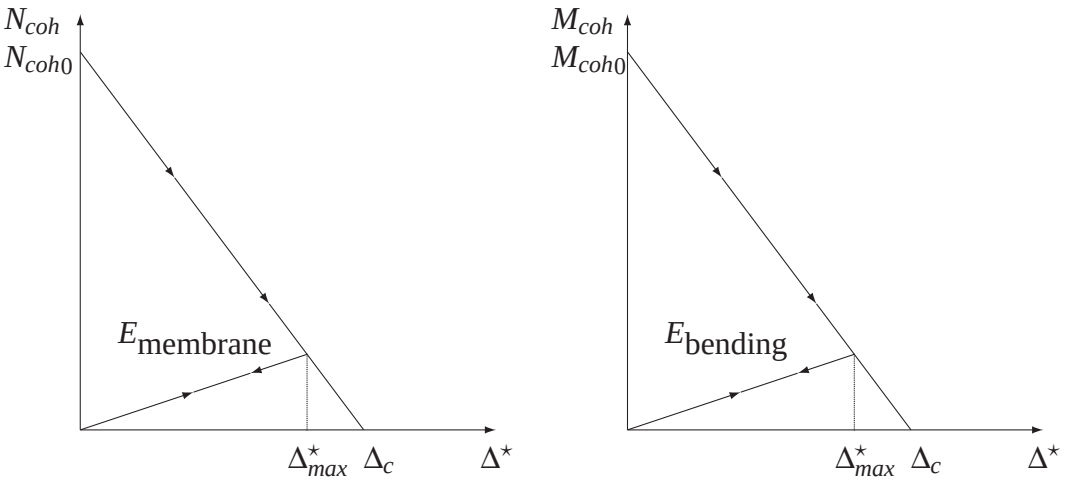

(a) Resultant membrane law.

(b) Resultant bending law.

Figure 3.17: Linearly decreasing monotonic cohesive law based on reduced stresses.

What remains to be defined is the shape of the new TSLs $N_{coh}(\Delta^\star)$ and $M_{coh}(\Delta^\star)$, as well as the definition of the effective opening $\Delta^\star$. The conditions that should be satisfied are:

- $N_{coh} = M_{coh} = 0$ when $\Delta^\star \geq \Delta_c$;
- Laws $N(\Delta^\star)$ and $M(\Delta^\star)$ must be monotonically decreasing;
- Continuity in resultant stresses[6] between unfractured and fractured stage at $\Delta^\star = 0$ should be ensured. This is the case if $N_{coh}(0) = N_{coh0}$ and $M_{coh}(0) = M_{coh0}$, where N_{coh0} and M_{coh0} are respectively the values of $\langle n^{11} \rangle$ and $\langle m^{11} \rangle$ at fracture initialization.
- At the end of the fracture process, the work induced by the TSLs $\int N_{coh}(\Delta^\star) d([\![u_1]\!]) + \int M_{coh}(\Delta^\star) d([\![-u_{3,1}]\!])$ should correspond to hG_c;
- In case of unloading during the fracture process a linearly decreasing law is used to have $N_{coh} = M_{coh} = 0$ when $\Delta^\star = 0$ as suggested by G.T. Camacho *et al.* [63] (see Fig. 3.17).

The relations $N_{coh}(\Delta^\star)$ and $M_{coh}(\Delta^\star)$ can be determined experimentally, but in the case of this

[6] It has been demonstrated by K.D. Papoulia *et al.* [196] that if the continuity is not ensured between unfractured and fractured stages, convergence problems can occur.

work a monotonically linearly decreasing law is chosen to illustrate the idea,

$$N_{coh}(\Delta^\star) = \begin{cases} N_{coh0}\left(1-\frac{\Delta^\star}{\Delta_c}\right) \text{ if } \Delta^\star_{\max} \leq \Delta^\star \leq \Delta_c \\ N_{coh0}\left(\frac{\Delta^\star}{\Delta^\star_{\max}}-\frac{\Delta^\star}{\Delta_c}\right) \text{ if } \Delta^\star < \Delta^\star_{\max} < \Delta_c \\ 0 \text{ if } \Delta^\star > \Delta_c \end{cases} \text{ and,} \tag{3.100}$$

$$M_{coh}(\Delta^\star) = \begin{cases} M_{coh0}\left(1-\frac{\Delta^\star}{\Delta_c}\right) \text{ if } \Delta^\star_{\max} \leq \Delta^\star \leq \Delta_c \\ M_{coh0}\left(\frac{\Delta^\star}{\Delta^\star_{\max}}-\frac{\Delta^\star}{\Delta_c}\right) \text{ if } \Delta^\star < \Delta^\star_{\max} < \Delta_c \\ 0 \text{ if } \Delta^\star > \Delta_c \end{cases} . \tag{3.101}$$

where $\Delta^\star_{max}$ is the maximal effective opening reached during the simulation. These curves are illustrated on Figs. 3.17(a) and 3.17(b).

In order to define the effective opening $\Delta^\star$ the simple pure membrane and pure bending cases are studied. In these cases, the value $\Delta^\star$ can be determined easily as the energy released must be equal to hG_c where $G_c = \frac{\Delta_c \sigma_c}{2}$. If the beam is in pure tension the energy released is given by,

$$\int_0^{\Delta_c} N_{coh}(\Delta_1) d\Delta_1 = \frac{N_{coh0}\Delta_c}{2} = \frac{2h\sigma_c G_c}{2\sigma_c} = hG_c\,, \tag{3.102}$$

with Δ_1 the jump of displacement along x-axis ($[\![u_1]\!]$) and where $N_{coh0} = h\sigma_c$ as fracture initiates when the tensile stress $\frac{N_B}{h} = \frac{N_{coh}}{h}$ reaches σ_c. This shows that in pure tension $\Delta^\star = \Delta_1$.

In the case of pure bending this energetic consideration leads to the following choice for the opening,

$$\Delta^\star = \frac{h}{6}\Delta_r\,, \tag{3.103}$$

with Δ_r the opening in rotation given by $[\![-u_{3,1}]\!]$ if the fracture is initialized for positive bending ($M_{coh0} > 0$) and by $[\![u_{3,1}]\!]$ otherwise ($M_{coh0} < 0$). Indeed,

$$\begin{aligned} \int_0^{\Delta_{rc}} M_{coh}(\Delta^\star) d\,[\![-u_{3,1}]\!] &= \int_0^{\Delta_c} \pm\frac{6}{h} M_{coh0}\left(1-\frac{\Delta^\star}{\Delta_c}\right) d\Delta^\star \\ &= \frac{6}{h}\frac{h^2\sigma_c}{6}\frac{\Delta_c}{2} = hG_c\,, \end{aligned} \tag{3.104}$$

as $M_{coh0} = \pm\frac{h^2\sigma_c}{6}$ if the fracture is initialized for positive or negative bending respectively. Indeed, fracture initiates when the tensile stress at beam skin reaches σ_c. For elastic behavior, this is obtained when $\sigma = \pm\frac{6M_B}{h^2} = \sigma_c$. In the non linear case, ratio $h/6$ can be computed, assuming that the bending stress is equivalent to a tensile stress applied on an equivalent thickness defined by,

$$h_I^{\text{eq}} = \frac{|M_{coh}|}{h\sigma_c - N_{coh}}\,. \tag{3.105}$$

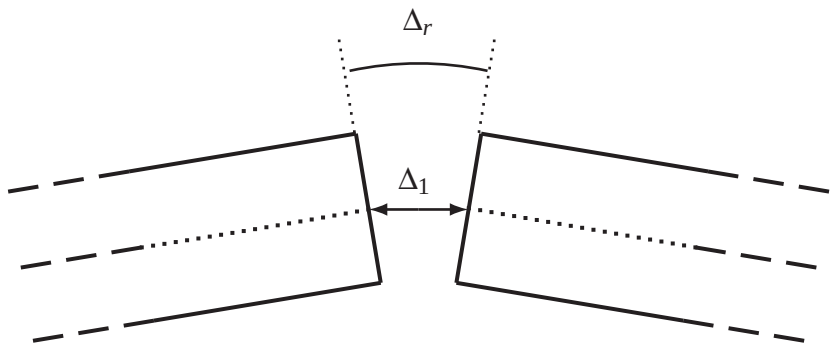

Figure 3.18: The two components of the opening. The neutral axis is drawn with a dotted line.

In elasticity, at fracture initiation $\sigma^{\text{skin}} = \frac{6|M_{coh}|}{h^2} + \frac{N_{coh}}{h} = \sigma_c$. Thus, $\frac{6|M_{coh}|}{h} = h\sigma_c - N_{coh} = \frac{|M_{coh}|}{h_I^{\text{eq}}}$. This implies that in the elastic case $h_I^{\text{eq}} = \frac{h}{6}$, which is the value used in Eq. (3.103).

For combined cases (see Fig. 3.18 for a view of the two openings), the application of the superposition principle gives the value for $\Delta^\star$,

$$\Delta^\star = (1-\eta_I)\Delta_1^\star + \eta_I h_I^{\text{eq}} \Delta_r^\star \,, \tag{3.106}$$

where the parameter η_I has to be equal to zero if the loading is in tension only and equal to one for a pure bending problem. This is ensured by choosing η_I as the ratio at fracture initialization between the bending part of stress and the fracture strength σ_c,

$$\eta_I = \frac{|M_{coh}|/h_I^{\text{eq}}}{h\sigma_c} = 1 - \frac{N_{coh}}{h\sigma_c} \,. \tag{3.107}$$

In case of bending rupture, for a beam under tension, η_I will be between zero and one, but in case of a beam under compression, fracture can still happen for higher bending stress. In that case η_I is larger than one. This definition of $\Delta^\star$ allows releasing an energy quantity equal to hG_c for any coupled loading.

Nevertheless, as the DG method ensures weakly the continuity, there is an initial jump before fracture and so at fracture initialization $\Delta_0 \neq 0$. To guarantee the continuity between pre-fracture and fracture stages, the initial jump at fracture initialization Δ_0 is subtracted from Δ,

$$\Delta_1^\star = \Delta_1 - \Delta_{10} \text{ and,} \tag{3.108}$$
$$\Delta_r^\star = \Delta_r - \Delta_{r0} \,, \tag{3.109}$$

which is the values considered in Eq. (3.106) .

Finally, the use of relations (3.34) and (3.99) leads to the new weak formulation of the

problem

$$
\begin{aligned}
0 \;=\; & \sum_n \int_{l_e} \left[\overline{\rho}_B \ddot{\boldsymbol{u}} \cdot \delta\boldsymbol{u} + {n_B}^{11} \delta u_{1,1} + \tilde{m_B}^{11} \delta(-u_{3,11}) \right] dx \\
& + \sum_s \left\{ (1-\alpha_s) \left(\left\langle {n_B}^{11} \right\rangle [\![\delta u_1]\!] + \langle E h \delta u_{1,1} \rangle [\![u_1]\!] + [\![u_1]\!] \left\langle \frac{\beta_2 E h}{h^s} \right\rangle [\![\delta u_1]\!] \right. \right. \\
& \left. \left. + \left\langle \tilde{m_B}^{11} \right\rangle [\![\delta(-u_{3,1})]\!] + \left\langle \frac{E h^3}{12} \delta(-u_{3,11}) \right\rangle [\![-u_{3,1}]\!] + [\![-u_{3,1}]\!] \left\langle \frac{\beta_1 E h^3}{12 h^s} \right\rangle [\![-\delta u_{3,1}]\!] \right) \right. \\
& \left. + \gamma_s [\![\delta u_3]\!] \left\langle \frac{\beta_3 E h}{2(1+\nu) h^s} \right\rangle [\![\delta u_3]\!] \right\} \\
& + \sum_s \alpha_s \left(N_{coh}(\Delta^\star_{true}) \delta [\![u_1]\!] + M_{coh}(\Delta^\star_{true}) \delta [\![-u_{3,1}]\!] \right). \qquad (3.110)
\end{aligned}
$$

In this relation α_s is equal to zero before fracture initiation and is shifted to one when the fracture criterion (3.97) is met. Also γ_s is equal to one during fracture process (*i.e.* while $\Delta^\star < \Delta_c$). This DG term has to be kept until the end of fracture as the shearing continuity has to be constrained even during the fracture.

3.3.2 Implementation

The implementation of the full-DG method presented in Section 3.2.3 has to be slightly adapted to integrate the cohesive law in the scheme. Indeed we can take advantage to the fact that the membrane and bending cohesive terms (3.99) have a similar form than respectively the membrane (3.31) and bending (3.32) consistency interface terms. For each time step the fracture criterion (3.97) is evaluated on each interface (upper and lower skin). As long as the fracture criterion is not verified nothing changes but when fracture is detected the initial opening ($\Delta_0^\star$) is computed from Eq. (3.106) with,

$$
\begin{aligned}
\Delta_1 &= N^{\boldsymbol{\xi}^+}(-1) u_1^{\boldsymbol{\xi}^+} - N^{\boldsymbol{\xi}^-}(1) u_1^{\boldsymbol{\xi}^-} , \qquad (3.111) \\
\Delta_r &= \left[\frac{\partial \xi}{\partial x}^{+} N_{,\xi}^{\boldsymbol{\xi}^+}(-1) u_3^{\boldsymbol{\xi}^+} - \frac{\partial \xi}{\partial x}^{-} N_{,\xi}^{\boldsymbol{\xi}^-}(1) u_3^{\boldsymbol{\xi}^-} \right] , \qquad (3.112)
\end{aligned}
$$

with the convention of Fig. 3.2. These initial values are stored to be used in the following time steps. The initial efforts N_{coh0} and M_{coh0} can also be computed from Eqs. (3.5) and (3.12), respectively, and stored. After initialization, the value of $\Delta^\star$ is still computed from Eqs. (3.106) and (3.108) and the values of N_{coh} and M_{coh} are directly obtained from the cohesive law (3.100-3.101). These values are then integrated in a similar way as the consistency internal forces expressions (3.68) and (3.74) where they replace the mean value of ${n_B}^{11}$ and $\tilde{m_B}^{11}$

leading to the expressions,

$$\boldsymbol{F}_{int\,coh\,n}^{bs\quad\boldsymbol{\mu}\pm} = N_{coh}(\Delta^\star)\begin{bmatrix} -N^{\boldsymbol{\mu}-}(1) \\ 0 \\ 0 \\ N^{\boldsymbol{\mu}+}(-1) \\ 0 \\ 0 \end{bmatrix}, \tag{3.113}$$

$$\boldsymbol{F}_{int\,coh\,m}^{bs\quad\boldsymbol{\mu}\pm} = M_{coh}(\Delta^\star)\begin{bmatrix} 0 \\ 0 \\ \frac{\partial\xi}{\partial x}^{-} N_{,\xi}^{\boldsymbol{\mu}-}(1) \\ 0 \\ 0 \\ -\frac{\partial\xi}{\partial x}^{+} N_{,\xi}^{\boldsymbol{\mu}+}(-1) \end{bmatrix}, \tag{3.114}$$

respectively the membrane and bending elementary internal cohesive force vectors per unit width. Notice that the similitude between these terms and their consistency counterpart, Eqs. (3.68) and (3.74) leads to a straightforward implementation. Using, Eqs. (3.113-3.114) in Eq. (3.99) gives the implemented form of the cohesive term, which reads,

$$\sum_s \left(\boldsymbol{F}_{int\,coh\,n}^{bs\quad\boldsymbol{\mu}\pm} + \boldsymbol{F}_{int\,coh\,m}^{bs\quad\boldsymbol{\mu}\pm}\right)\cdot\delta\boldsymbol{u}^{s\boldsymbol{\mu}\pm}. \tag{3.115}$$

The values of other interface terms are not computed thanks to the Boolean value α_s except in case of negative $\Delta_1^\star$. Indeed, a negative $\Delta_1^\star$ means an interpenetration and the compatibility and stability components can advantageously be used as contact terms to ensure $\Delta_1^\star = 0$.

For a static case, the stiffness matrix of the cohesive terms has to be defined. This one can be computed analytically for the monotonically linearly decreasing law (Fig. (3.17)):

- Cohesive membrane term ($\boldsymbol{K}_{int\,coh\,n}^{bs}$ is the elementary membrane cohesive stiffness ma-

trix per unit width):

$$
\begin{aligned}
\boldsymbol{K}^{bs}_{int\,coh\,n}{}^{\boldsymbol{\mu}^{\pm}\boldsymbol{\xi}^{\pm}} &= \frac{\partial \boldsymbol{F}^{bs}_{int\,coh\,n}{}^{\boldsymbol{\mu}^{\pm}}}{\partial \boldsymbol{u}^{\boldsymbol{\xi}^{\pm}}} \\
&= \left(k_{NN} \begin{bmatrix} -N^{\boldsymbol{\mu}-}(1) \\ 0 \\ 0 \\ N^{\boldsymbol{\mu}+}(-1) \\ 0 \\ 0 \end{bmatrix} \otimes \begin{bmatrix} -N^{\boldsymbol{\xi}-}(1) \\ 0 \\ 0 \\ +N^{\boldsymbol{\xi}+}(-1) \\ 0 \\ 0 \end{bmatrix} + \operatorname{sign}(M_{coh0}) \right. \\
&\quad \left. \times k_{MN} \begin{bmatrix} -N^{\boldsymbol{\mu}-}(1) \\ 0 \\ 0 \\ N^{\boldsymbol{\mu}+}(-1) \\ 0 \\ 0 \end{bmatrix} \otimes \begin{bmatrix} \frac{\partial \xi}{\partial x}^{-} N^{\boldsymbol{\xi}-}_{,\xi}(1) \\ 0 \\ 0 \\ -\frac{\partial \xi}{\partial x}^{+} N^{\boldsymbol{\xi}+}_{,\xi}(-1) \\ 0 \\ 0 \end{bmatrix} \right)
\end{aligned}
\tag{3.116}
$$

with,

$$
k_{NN} = \begin{cases} (1-\eta_I)\dfrac{N_{coh0}}{\Delta_c} & \text{loading} \\ (1-\eta_I)\dfrac{-N_{coh0}}{\Delta^{\star}_{\max}-\Delta_c} & \text{unloading} \end{cases} \tag{3.117}
$$

$$
k_{NM} = \begin{cases} \eta_I h_I^{\text{eq}} \dfrac{N_{coh0}}{\Delta_c} & \text{loading} \\ \eta_I h_I^{\text{eq}} \dfrac{-N_{coh0}}{\Delta^{\star}_{\max}-\Delta_c} & \text{unloading} \end{cases} \tag{3.118}
$$

- Cohesive bending term ($\boldsymbol{K}^{bs}_{int\,coh\,m}$ is the elementary bending cohesive stiffness matrix

per unit width):

$$\begin{aligned}
\boldsymbol{K}^{bs}_{int\,coh\,m}{}^{\boldsymbol{\mu}^{\pm}\boldsymbol{\xi}^{\pm}} &= \frac{\partial \boldsymbol{F}^{bs}_{int\,coh\,n}{}^{\boldsymbol{\mu}^{\pm}}}{\partial \boldsymbol{u}^{\boldsymbol{\xi}^{\pm}}} \\
&= \operatorname{sign}(M_{coh0}) \left(k_{MN} \begin{bmatrix} 0 \\ 0 \\ -\frac{\partial \xi}{\partial x}^{-} N^{\boldsymbol{\mu}-}_{,\xi}(1) \\ 0 \\ 0 \\ \frac{\partial \xi}{\partial x}^{+} N^{\boldsymbol{\mu}+}_{,\xi}(-1) \end{bmatrix} \otimes \begin{bmatrix} 0 \\ 0 \\ -N^{\boldsymbol{\xi}-}(1) \\ 0 \\ 0 \\ N^{\boldsymbol{\xi}+}(-1) \end{bmatrix} \right. \\
&\quad \left. + k_{MM} \begin{bmatrix} 0 \\ 0 \\ -\frac{\partial \xi}{\partial x}^{-} N^{\boldsymbol{\mu}-}_{,\xi}(1) \\ 0 \\ 0 \\ \frac{\partial \xi}{\partial x}^{+} N^{\boldsymbol{\mu}+}_{,\xi}(-1) \end{bmatrix} \otimes \begin{bmatrix} 0 \\ 0 \\ \frac{\partial \xi}{\partial x}^{-} N^{\boldsymbol{\xi}-}_{,\xi}(1) \\ 0 \\ 0 \\ -\frac{\partial \xi}{\partial x}^{+} N^{\boldsymbol{\xi}+}_{,\xi}(-1) \end{bmatrix} \right)
\end{aligned} \tag{3.119}$$

with,

$$k_{MN} = \begin{cases} (1-\eta_I)\dfrac{M_{coh0}}{\Delta_c} & \text{loading} \\ (1-\eta_I)\dfrac{-M_{coh0}}{\Delta^{\star}_{\max}-\Delta_c} & \text{unloading} \end{cases} \tag{3.120}$$

$$k_{MM} = \begin{cases} \eta_I h_I^{\text{eq}} \dfrac{M_{coh0}}{\Delta_c} & \text{loading} \\ \eta_I h_I^{\text{eq}} \dfrac{-M_{coh0}}{\Delta^{\star}_{\max}-\Delta_c} & \text{unloading} \end{cases} \tag{3.121}$$

3.3.3 Numerical benchmark: Double Clamped Beam

To demonstrate the ability of the presented framework to model fracture phenomena, studies are performed on a double clamped beam, whose material properties are given in Tab. 3.2. The beam is firstly loaded only in bending before the investigation of membrane-bending coupled loadings. For all the following tests, the beam is meshed with 16 full-DG cubic elements, so there are 128 degrees of freedom in the model, and the parameters β_1, β_2 and β_3 are respectively fixed to 10, 10 and $\beta_1 \left(\frac{h}{L}\right)^2$.

Pure bending fracture test

This benchmark, presented in Fig. 3.19, consists in applying a downward vertical displacement at the middle of the beam. This introduces a vertical displacement field symmetric

Property	Value
Young modulus [GPa]	71
Poisson ratio [-]	0.21
fracture strength [MPa]	400
energy strength [J/m^2]	8800

Table 3.2: Material properties of the double clamped beam.

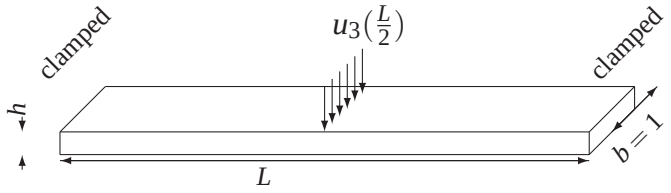

Figure 3.19: Setup used to show the through-the-thickness crack initiation and propagation by the suggested DG/ECL framework.

with respect to the center of the beam described by [153]

$$u_3(\xi^1) \;=\; 4\frac{{\xi^1}^2(3L-4\xi^1)}{L^3}u_3(\frac{L}{2})\;\xi^1\in[0;L/2]\,, \tag{3.122}$$

where $u_3(\frac{L}{2})$ is the applied vertical displacement. Stress is maximal at clamping (at upper skin of the beam) and at the middle of the beam (at lower skin). This maximal value is given by,

$$\sigma_{\max} \;=\; \frac{12Eh}{L^2}u_3(\frac{L}{2})\,. \tag{3.123}$$

In this example, fracture at clamping is not allowed so it will be localized at the center of the beam. After fracture, the double clamped beam (DCB) of length L becomes two simply clamped beams (SCB) of length $L/2$. Note that in the simulation the vertical displacement is applied on both nodes of beam's center. Consequently, as the reported force is measured at one of the two nodes, in the pre-fractured stage it is equal to half the force corresponding to the prescribed displacement and the energies computed numerically will have to account for this too.

The energy release rate G occurring during the transition can be computed by,

$$G\Delta a \;=\; W_{ext}-W_{int}\,, \tag{3.124}$$

where in this last equation Δa is the length of the crack at the end of the simulations (*i.e.* h), where W_{ext} is the work of external forces until complete fracture of the beam, and where W_{int} is the internal energy of the beam, see Fig. 3.20. In the following simulations the relation

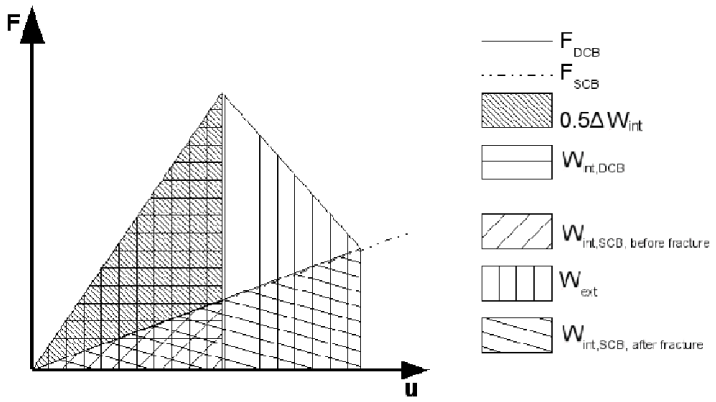

Figure 3.20: Different energetic quantities can be extracted from the force *vs.* displacement curve to compute the energetic balance.

force-displacement is archived and the different areas of Fig. 3.20 are computed numerically at the end of simulation. Furthermore, the fracture energy hG_c can be computed by,

$$hG_c = W_{ext\,\text{after fracture}} - W_{int\,\text{after fracture}}\,, \tag{3.125}$$

Another useful quantity is the difference of internal energy (ΔW_{int}) between the fractured and unfractured cases. Indeed this quantity can be used to predict if there is a need of external energy to achieve a complete fracture on the beam thickness. If $\Delta W_{int} > hG_c$, once the crack is initiated, the unique solution of the problem is a complete rupture of the beam, while, on the contrary if $\Delta W_{int} < hG_c$, energy from the loading, and thus a further displacement increment, is required in order to achieve complete rupture. ΔW_{int} of the beam can be computed analytically (see Appendix A.4)

$$\Delta W_{int\,\text{bending}} = \frac{hL_{DCB}}{24E}\sigma_{c\,\text{bending}}^{2}\,, \tag{3.126}$$

where $\sigma_{c\ \text{bending}}$ is the bending stress at the skin reached when fracture is initiated.

The simulation is first performed for a beams of 200 [mm] in length and 20 [mm] in height. The $\Delta W_{int\,\text{bending}}$ of the beam computed thanks to equation (3.126) is equal to 375.58[J/m] while the fracture energy is equal to $0.02G_c = 176$[J/m]. As $\Delta W_{int\,\text{bending}}$ is larger than the fracture energy, the fracture happens in one increment of displacement as illustrated on Fig. 3.21.

Fig. 3.21(a) plots the maximal stress at the center of the beam in terms of the prescribed displacement. The stress increases until it reaches the value of the fracture strength (400 [MPa]). It then falls down to zero as the center of the DCB becomes a free extremity of a SCB. Fig. 3.21(b) gives the relation between the force and the prescribed displacement at the middle of the DCB. This curve is in agreement with the picture (a) as the force follows the analytical value of a DCB and a SCB respectively before and after the fracture. Moreover

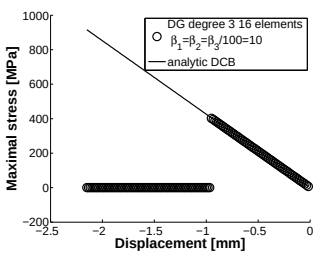

(a) Lower skin stress at beam center.

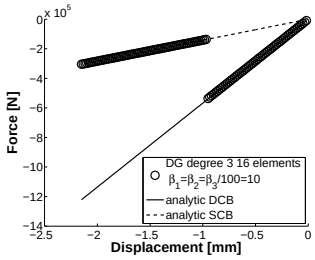

(b) Force *vs.* displacement curve.

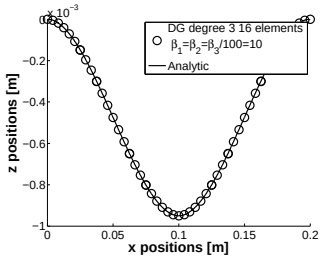

(c) Displacement field at fracture initiation.

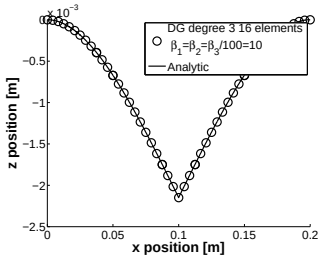

(d) Displacement field at the end of the fracture process.

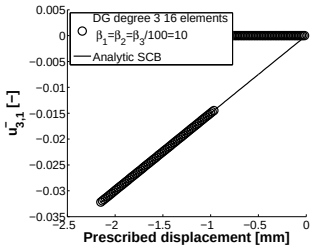

(e) Angle $u_{3,1}$ at beam's center.

Figure 3.21: Unstable crack propagation for a DCB of $L = 200$ [mm] and $h = 20$ [mm].

$\Delta W_{int\,\text{bending}}$ can be computed by numerical integration of this curve. The calculation gives a result of 381.47 [J/m], which is very close of the analytical value. Figs. 3.21(c) and 3.21(d) represent the deformation map respectively before and after fracture. Again before fracture the deformation map is the one of a DCB and after fracture, it is the one of two SCBs. Finally, Fig. 3.21(e) depicts the relation between the angle $u_{3,1}$ at the center of the DCB versus the prescribed displacement. This picture shows that before fracture the angle is equal to zero and it is equal to the analytical value of a SCB after fracture.

Another simulation is performed on a DCB of 50 [mm] in length and of 2.5 [mm] in height. For this DCB the application of formula (3.126) yields $\Delta W_{int\,\text{bending}} = 11.737$ [J/m]. As $\Delta W_{int\,\text{bending}}$ is lower than the fracture energy of 22 [J/m] there is a fracture process. This process is illustrated on the pictures of Fig. 3.22. Picture 3.22(a) depicts the maximal stress at the middle of the beam. As for the previous case, there is fracture when the stress reaches the fracture strength, but this time, the stress decreases linearly with the prescribed displacement after fracture onset. The same conclusion is valid for the force-displacement relation plotted on Fig. 3.22(b). This picture shows that after fracture the force decreases linearly with the displacement until it reaches the force-displacement curve of a SCB. The numerical integration gives a value of 12.33 [J/m] for $\Delta W_{int\,\text{bending}}$ which is in accordance with its analytical value. Moreover, the use of equation (3.124) yields an energy released equal to 21.98 [J/m], which is very close to its analytical value. Figs. 3.22(c) and 3.22(d) show, as for the previous case, that the displacement field is equal, before and at the end of the fracture process, to the displacement field of a DCB and of a SCB respectively. Finally, Fig. 3.22(e) depicts the value

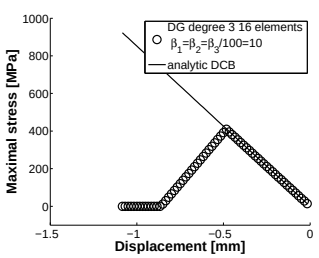

(a) Lower skin stress at beam center.

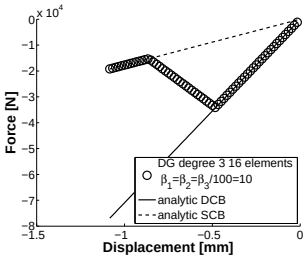

(b) Force *vs.* displacement curve.

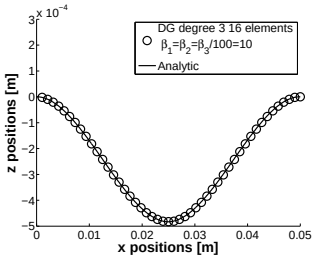

(c) Displacement field at fracture initiation.

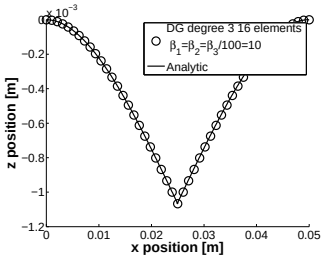

(d) Displacement field at the end of the fracture process.

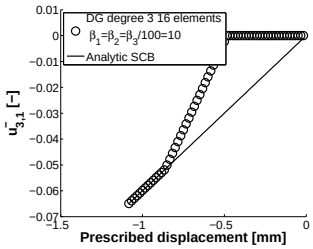

(e) Angle $u_{3,1}$ at beam center.

Figure 3.22: Stable crack propagation for a DCB of $L = 50$ [mm] and $h = 2.5$ [mm].

of the angle $u_{3,1}$ in function of the prescribed displacement. As for the stress and force fields, the value of $u_{3,1}$ increases linearly after fracture initialization to reach, at the end of fracture process, the analytical value of a SCB.

Combined tension-bending fracture test

In order to demonstrate that the model of fracture presented releases the right amount of energy for any loading conditions, a test involving combined tension and bending is presented. The benchmark is the same as for the pure bending test except that a constant $\boldsymbol{E}_1$-displacement

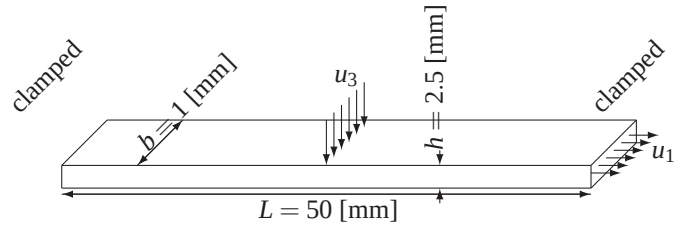

Figure 3.23: Setup to illustrate a through-the-thickness crack initiation and propagation with a coupled membrane-bending loading.

is added (see Fig. 3.23). The simulations are performed on a DCB of 50 [mm] in length and

2.5 [mm] in height.

The characteristic quantity ΔW_{int} has now to consider the internal energy in tension, which gives the relation (see Appendix A.4),

$$\Delta W_{int} = \frac{hL_{DCB}}{2E}\left(\frac{13}{12}\eta_I^2 - 2\eta_I + 1\right)\sigma_c^2, \tag{3.127}$$

where η_I is the coupling parameter (3.107). The force-displacement relation depicted on Fig. 3.20 illustrates now the energy released in bending only ($W_{int\,\text{bending}}$). The total released energy is obtained after adding to $W_{int\,\text{bending}}$ the energy released in tension ($W_{int\,\text{membrane}}$). This last contribution is given by,

$$W_{int\,\text{membrane}} = \Delta W_{int\,\text{membrane}} = \frac{Eh}{2L}u_{1\text{ prescribed}}^2, \tag{3.128}$$

as there is no work of external forces in tension.

$u_{1\text{ prescribed}}$ [mm]	η_I [-]	ΔW_{int} [J/m]	$W_{int\,\text{bending}}$ [J/m]	$W_{int\,\text{membrane}}$ [J/m]	hG [J/m]
$-2e^{-2}$	1.0692	14.8043	21.26	0.71	21.98
0	1	12.33	21.98	0	21.98
$2e^{-2}$	0.93	11.39	21.26	0.71	21.98
$4e^{-2}$	0.86	11.99	19.14	2.84	21.98
$6e^{-2}$	0.79	14.11	15.59	6.39	21.98
$8e^{-2}$	0.72	17.76	10.63	11.36	21.99
$10e^{-2}$	0.66	22.95	–	–	–

Table 3.3: Double Clamped Beam with combined loadings: Values of different energetic quantities for different prescribed $\boldsymbol{E}_1$-displacement. For stable case $hG \approx hG_c$.

The energies obtained for different loading conditions are collected in Tab. 3.3. This table shows that the total energy released (hG) at the end of the fracture process is equal to the fracture energy for any $u_{1\text{ prescribed}}$, the small differences being due to the application of the prescribed displacements by step increments. For $u_{1\text{ prescribed}} = 10e^{-5}$, the difference of internal energy between unfractured and fractured case is larger than $hG_c = 22$ [J/m]. Therefore for this prescribed displacement the fracture occurs in one increment of displacement and the computation of the energies released in tension and in bending is meaningless. Furthermore the simulation is performed for a negative $u_{1\text{ prescribed}} = -2e^{-5}$ to show that the method remains valid in the compression case. As no contact is taken into account during the simulation an energy quantity equal to $W_{int\,\text{membrane}}$ is released in compression and so the energetic balance is exactly the same as for $u_{1\text{ prescribed}} = 2e^{-5}$. The difference between the two cases is the value of the prescribed u_3 leading to fracture (see Fig. 3.24), which explains the difference of ΔW_{int} between both simulations.

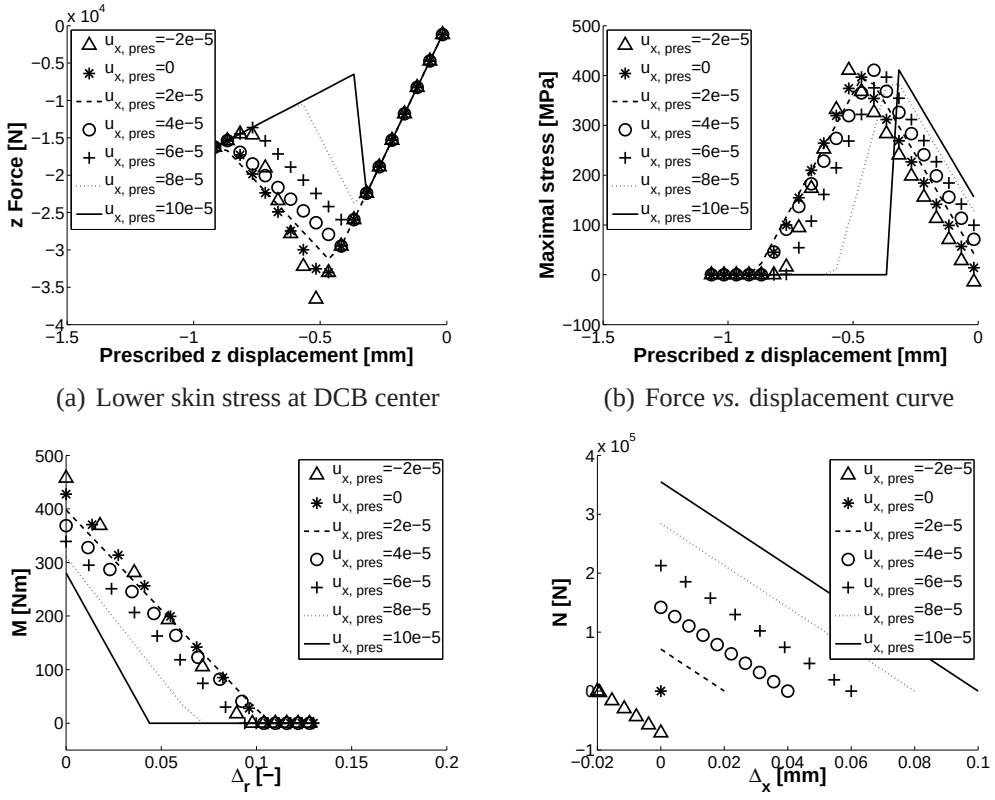

(a) Lower skin stress at DCB center

(b) Force *vs.* displacement curve

(c) Resultant bending cohesive stress

(d) Resultant membrane cohesive stress

Figure 3.24: Double Clamped Beam with combined loadings for different prescribed $\boldsymbol{E}_1$-displacements.

Fig. 3.24 illustrates the results for the different prescribed displacements. Fig. 3.24(a) depicts the maximal stress at the center of the DCB and shows that for every value of the prescribed displacement, the fracture begins when the stress reaches the value of σ_c. Fig. 3.24(b) represents the relation force-displacement in the $\boldsymbol{E}_3$-direction. It can be seen that as $u_{1\,\text{prescribed}}$ increases the value of the $\boldsymbol{E}_3$-force decreases and the complete fracture happens for a lower value of u_3. This result is consistent with the fact than when $u_{1\,\text{prescribed}}$ increases the bending part of the stress is lower at fracture initialization, which implies a lower resultant bending stress at fracture initialization (see picture 3.24(c)) and therefore a lower $\boldsymbol{E}_3$-force. Finally, Figs. 3.24(c) and 3.24(d) represent respectively the relations $M_{coh}(\Delta_r^\star)$ and $N_{coh}(\Delta_1^\star)$. These graphs show that, when $u_{1,\,\text{prescribed}}$ increases, both the resultant stress at fracture initialization N_{coh} and the value of Δ_1 reached at the end of the fracture process increase, which is physically explained due to the fact that there is more energy to be released in tension.

3.4 Conclusion on the full-DG/ECL framework for Euler-Bernoulli beams

This chapter describes the two main concepts of this works (full-DG formulation for thin structures and extrinsic cohesive law for thin bodies) in the particular case of Euler-Bernoulli beams. It allows presenting both concepts in the most comprehensible way. Indeed in the next chapter, the non linear shell formulation is tackled and in this case the integration on interface is required with special care to formulate all quantities in the basis of the interface.

First we developed a full-DG formulation of beams, which has the traditional properties of a numerical method (consistency, stability, optimal convergence rate). The full-DG method provides results in good agreement with theory and with the C^0/DG method previously presented by G. Engel *et al.* [91]. Compared to this method our original method considers discontinuous test functions and so provides a discretization with discontinuous elements. This discontinuity can be exploited at onset of fracture to insert a cohesive element without mesh modification. Indeed, the terms ensuring weakly the continuity are just replaced by the cohesive ones.

Secondly, we develop an original cohesive law based on reduced stresses to account for the implicit thickness discretization of the beam. This law has been shown to respect the energetic balance. This property of the framework is illustrated through a numerical example.

In the next chapters, we suggest an extension of this framework to the non linear Kirchhoff-Love shell formulation.

Chapter 4

Full discontinuous Galerkin formulation of Kirchhoff-Love shells

The aim of this chapter[1] is to extend the discontinuous Galerkin formulation of the Euler-Bernoulli beams, presented in the previous chapter, to Kirchhoff-Love shells. The combination of this formulation with an extrinsic cohesive law will be discussed in the next chapter. In the following, we first introduce the J. Simo *et al.* [235, 236, 233, 234, 237, 238] shell theory to obtain a strong form of the problem. Nevertheless, compared to the previous chapter, we remove several assumptions to keep only the hypothesis inherent to Kirchhoff-Love shells,

(i) The effect of the out-of-plane shearing on the deformation is negligible;

(ii) Plane stress state.

These assumptions are general as they are related to the aspect ratio of the structures that present one dimension (the thickness) smaller than the two other ones[2]. Although the formulation is established in the general case of finite deformations, it is then particularized to small deformations and linear behavior as some benchmarks used to validate the framework are computed under these assumptions. Although, during the thesis, we developed first the linear formulation before its extension to the non-linear range, we introduce directly the most general case leading to a more fluent presentation.

Once the strong form obtained from the J. Simo *et al.* theory, the original full discontinuous Galerkin formulation of non-linear Kirchhoff-Love shells is presented. This one is a generalization of the formulation presented in the previous chapter for Euler-Bernoulli beams (see Section 3.2) and thus the out-of-plane shearing is again considered to weakly ensure the continuity of normal displacement.

Then, we introduce the three constitutive behaviors that are used to perform the numerical benchmarks. These examples come from the literature and are used to prove the ability of the

[1] The main results of this chapter are published in *Computer Methods in Applied Mechanics and Engineering* [31] for the linear formulation. The non linear formulation is presented in a paper submitted for publication in *International Journal for Numerical Methods in Engineering* [33].

[2] We will discuss later the validity of both assumptions in case of fracture at the begining of the Chapter 5.

original discontinuous formulation developed herein to provide results as accurate as other continuous shell formulations presented by other authors in the case of Galerkin methods. Furthermore, the benchmarks cover different loading conditions and quasi-static as well as dynamic cases.

Finally, although the full discontinuous Galerkin formulation seems prohibitive in continuum mechanics, as it considers more degrees of freedom than its continuous counterpart, a mix between continuous and discontinuous formulations can be used to obtain an efficient parallel implementation. Indeed, in a parallel computation, the mesh is partitioned between different processors. On each partition a continuous formulation can be used and the continuity between them can be ensured thanks to the discontinuous formulation. In the following, we present an original implementation of the explicit Hulbert-Chung algorithm [123] using this mix formulation to demonstrate its efficiency.

4.1 Continuum mechanics of thin bodies

The basic equations of the shell theory are the linear and angular momentum equilibrium balance equations of the continuum mechanics. Both equations are developed in the particular case of thin bodies. In fact, compared with the classical 3D theory the integration on the thickness is treated separately. This is realized thanks to the particular kinematics developed below for thin bodies. This kinematics is then exploited to obtain the strong form of the continuum mechanics of thin structures.

4.1.1 Kinematics of thin bodies

We base our thin bodies formulation on the one first introduced by J. Simo *et al.* [235, 236, 233, 234, 237, 238]. The particularity of this formulation is to formulate all the equations in the metric of the shell description in place of the inertial orthonormal frame. So, three different frames are introduced:

(i) The inertial orthonormal reference basis denoted $\boldsymbol{E}_I$;

(ii) The convected frame denoted $\boldsymbol{g}_I$, which is linked to the shell (and thus moves with it);

(iii) The conjugated frame to this convected basis denoted $\boldsymbol{g}^I$, which verifies by definition the relation $\boldsymbol{g}_I \cdot \boldsymbol{g}^J = \delta_{IJ}$. This basis has to be introduced as $\boldsymbol{g}_I$ is not an orthonormal frame.

As the thickness is small compared to the other dimensions of the structure, by definition of a thin body, it is generally differently covered in the derivation of the equations. Therefore J. Simo *et al.* [233] suggested to represent the shell by its mid-surface, as a Cosserat plane $\mathcal{A}$, and by a third coordinate describing the thickness belonging to the interval $[h_{\min}; h_{\max}]$. As depicted on Fig. 4.1, the shell is therefore considered in the reference frame as a plane,

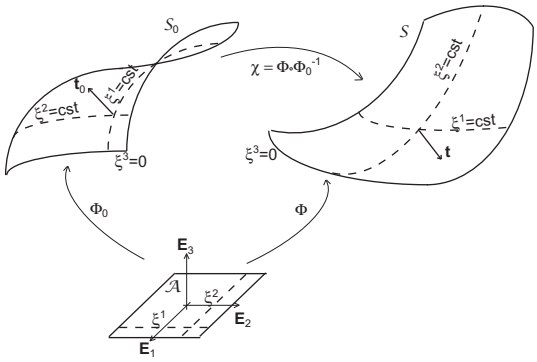

Figure 4.1: Description of the different configurations of the shell (courtesy of [185]).

included in the plane $\boldsymbol{E}_1, \boldsymbol{E}_2$. The thickness of the shell is described in this frame by the third coordinate varying along $\boldsymbol{E}_3$, which is mathematically formulated as,

$$\boldsymbol{\xi} \;=\; \xi^I \boldsymbol{E}_I : \mathcal{A} \times [h_{\min}; h_{\max}] \to \mathbb{R}^3 , \tag{4.1}$$

where ξ^I are the coordinates of the shell in the reference frame. Then, any configuration $\mathcal{S}$ of the shell can be described in relation to the reference frame by the mapping,

$$\boldsymbol{\Phi} : \mathcal{A} \times [h_{\min}; h_{\max}] \;\to\; \mathcal{S} , \tag{4.2}$$

which defines the manifold of positions $\boldsymbol{x}$ of the shell,

$$\boldsymbol{x} \;=\; \boldsymbol{\Phi}\left(\xi^I\right) = \boldsymbol{\varphi}(\xi^\alpha) + \xi^3 \lambda_h \boldsymbol{t}(\xi^\alpha) . \tag{4.3}$$

The last relation follows from the representation of the shell in the reference frame dividing the mapping $\boldsymbol{\Phi}$ as a mapping of the mid-surface $\boldsymbol{\varphi}(\xi^1, \xi^2) : \mathcal{A} \to \mathbb{R}^3$ and the value of the director of this mid-surface $\boldsymbol{t} : \mathcal{A} \to \mathrm{S}^2 = \left\{ \boldsymbol{t} \in \mathbb{R}^3 |_{\|\boldsymbol{t}\|=1} \right\}$, with S^2 the unit sphere manifold. Finally in this relation, λ_h describes a change of thickness due to the deformations.

As any configuration of the shell can be described by $\boldsymbol{\Phi}$, its initial configuration is formulated by ($\lambda_{h0} = 1$),

$$\boldsymbol{x}_0 = \boldsymbol{\Phi}_0(\xi^I) \;=\; \boldsymbol{\varphi}_0(\xi^\alpha) + \xi^3 \boldsymbol{t}_0(\xi^\alpha) . \tag{4.4}$$

If $j_0 = \det \nabla \boldsymbol{\Phi}_0$ we can define the mid-surface $\boldsymbol{\varphi}_0$ to verify,

$$\int_{h_{\min}}^{h_{\max}} \xi^3 j_0 \rho_0 d\xi^3 \;=\; 0 . \tag{4.5}$$

Thus the mid-surface is not necessarily the geometric center of the cross-section.

Therefore, the transformation between the initial and current configuration ($\mathcal{S}_0 \to \mathcal{S}$) is described by the two-point deformation mapping,

$$\boldsymbol{\chi} \;=\; \boldsymbol{\Phi} \circ \boldsymbol{\Phi}_0^{-1} . \tag{4.6}$$

This mapping is characterized by the two-point deformation gradient $\mathcal{S}_0 \to GL_+(3,\mathbb{R})$,

$$\mathbf{F} = \nabla\mathbf{\Phi} \circ [\nabla\mathbf{\Phi}_0]^{-1}, \tag{4.7}$$

where $GL_+(3,\mathbb{R})$ is the invertible Lie group of dimension 3 with a positive Jacobian $J = \det\mathbf{F}$. By definition of the gradient operator [3]

$$\begin{aligned} \nabla\mathbf{\Phi} &= \boldsymbol{\varphi}_{,1} \otimes \boldsymbol{E}^1 + \boldsymbol{\varphi}_{,2} \otimes \boldsymbol{E}^2 + \xi^3 (\lambda_h \boldsymbol{t})_{,1} \otimes \boldsymbol{E}^1 + \xi^3 (\lambda_h \boldsymbol{t})_{,2} \otimes \boldsymbol{E}^2 \\ &\quad \left(\lambda_h + \xi^3 \lambda_{h,3}\right) \boldsymbol{t} \otimes \boldsymbol{E}^3, \\ &= \boldsymbol{g}_I \otimes \boldsymbol{E}^I, \end{aligned} \tag{4.8}$$

after neglecting $\xi^3\lambda_{h,3}$. As we consider λ_h equal to the value at mid-surface, the convected frame $\boldsymbol{g}_I$ linked to the shell is defined by,

$$\boldsymbol{g}_\alpha = \boldsymbol{\varphi}_{,\alpha} + \xi^3 (\lambda_h \boldsymbol{t})_{,\alpha} \text{ and,} \tag{4.9}$$

$$\boldsymbol{g}_3 = \lambda_h \boldsymbol{t}(\xi^\alpha). \tag{4.10}$$

Furthermore, calling $j = \det\nabla\mathbf{\Phi}$, we can compute the Jacobian of the deformation as,

$$J = \det\mathbf{F} = \frac{j}{j_0}, \tag{4.11}$$

which is written on the mid-surface ($\xi^3 = 0$) as,

$$\bar{J} = \frac{\bar{j}}{j_0}. \tag{4.12}$$

Finally, as the shearing deformations are neglected by assumption in the particular case of Kirchhoff-Love shells, the unit vector $\boldsymbol{t}$ remains perpendicular to the convected basis at the mid-surface leading to,

$$\boldsymbol{t} = \frac{\boldsymbol{\varphi}_{,1} \wedge \boldsymbol{\varphi}_{,2}}{\|\boldsymbol{\varphi}_{,1} \wedge \boldsymbol{\varphi}_{,2}\|}. \tag{4.13}$$

Thus for Kirchhoff-Love shells,

$$\bar{j} = (\boldsymbol{\varphi}_{,1} \wedge \boldsymbol{\varphi}_{,2}) \cdot \lambda_h \boldsymbol{t} = \lambda_h \|\boldsymbol{\varphi}_{,1} \wedge \boldsymbol{\varphi}_{,2}\|. \tag{4.14}$$

The gradient of the unit vector $\boldsymbol{t}$ can be derived as [181],

$$\boldsymbol{t}_{,\alpha} = \lambda_h \frac{\varepsilon_{\beta\gamma 3}}{j} \boldsymbol{\varphi}_{,\beta\alpha} \wedge \boldsymbol{\varphi}_{,\gamma} - \frac{\lambda_h \boldsymbol{t}}{j} \varepsilon_{\beta\gamma 3} \left(\boldsymbol{\varphi}_{,\beta\alpha} \wedge \boldsymbol{\varphi}_{,\gamma}\right) \cdot \boldsymbol{t}, \tag{4.15}$$

with ε_{ijk} the Levi-Civita permutation tensor.

[3] for a n-order tensor $\mathbf{x}$, $\nabla\mathbf{x} = \mathbf{x}_{,I} \otimes \boldsymbol{E}^I$

4.1.2 Governing equations of thin bodies

The governing equations of thin bodies are established by integration on the shell volume of the linear and angular momentum balance equations, respectively

$$\nabla \cdot \boldsymbol{\sigma}^T = \rho \ddot{\boldsymbol{\Phi}} - \boldsymbol{B}, \tag{4.16}$$

$$\boldsymbol{\Phi} \wedge \nabla \cdot \boldsymbol{\sigma}^T = \boldsymbol{\Phi} \wedge \left(\rho \ddot{\boldsymbol{\Phi}}\right) - \boldsymbol{\Phi} \wedge \boldsymbol{B}, \tag{4.17}$$

where $\boldsymbol{\sigma}$ is the Cauchy stress tensor and $\boldsymbol{B}$ are the external applied forces per unit volume.

We first investigate the integration on the shell $\mathcal{S}$ of the linear momentum Eq. (4.16). Applying the Gauss theorem for the term $\nabla \cdot \boldsymbol{\sigma}^T$, we have

$$\int_{\partial \mathcal{S}} \boldsymbol{\sigma} \cdot \boldsymbol{n} d\partial \mathcal{S} = \int_{\mathcal{S}} \left(\rho \ddot{\boldsymbol{\Phi}} - \boldsymbol{B}\right) d\mathcal{S} \tag{4.18}$$

with $\boldsymbol{n}$ the outward unit normal to the body in the current configuration. This value can be formulated in the reference inertial frame by using the Nanson formula,

$$d\partial \mathcal{S} \boldsymbol{n} = j d\Gamma \nabla \boldsymbol{\Phi}^{-T} \cdot \boldsymbol{n}_{iner}, \tag{4.19}$$

Thus Eq. (4.18) can be formulated in the reference frame,

$$\int_{\Gamma} j \boldsymbol{\sigma} \left(\nabla \boldsymbol{\Phi}\right)^{-T} \cdot \boldsymbol{n}_{iner} d\Gamma = \int_{\mathcal{A} \times [h_{\min}; h_{\max}]} j \left(\rho \ddot{\boldsymbol{\Phi}} - \boldsymbol{B}\right) dV, \tag{4.20}$$

where Γ the external surface in the reference configuration, and $\boldsymbol{n}_{iner}$ its unit normal.

Then, the main idea of the thin bodies formulation is to separate the integration on the inertial volume in an integration on the Cosserat plane representing the mid-surface and on an integration over the thickness. Toward this end, the surface $\Gamma = \partial \left(\mathcal{A} \times [h_{\min}; h_{\max}]\right)$ can be divided into three terms (the top and bottom parts and the lateral surface), as depicted on Fig. 4.2 leading to,

$$\int_{\partial(\mathcal{A} \times [h_{\min}; h_{\max}])} j \boldsymbol{\sigma} \left(\nabla \boldsymbol{\Phi}\right)^{-T} \cdot \boldsymbol{n}_{iner} d\Gamma = \int_{\mathcal{A}} \int_{h_{\min}}^{h_{\max}} j \left(\rho \left(\ddot{\boldsymbol{\varphi}} + \xi^3 \left(\ddot{\lambda_h} \boldsymbol{t}\right)\right) - \boldsymbol{B}\right) d\xi^3 d\mathcal{A}, \tag{4.21}$$

or again,

$$\begin{aligned} &\int_{h_{\min}}^{h_{\max}} \int_{\partial \mathcal{A}} j \boldsymbol{\sigma} \left(\nabla \boldsymbol{\Phi}\right)^{-T} \cdot \boldsymbol{\nu} d\partial \mathcal{A} d\xi^3 \\ &\quad + \int_{\mathcal{A}} j \boldsymbol{\sigma} \left(\nabla \boldsymbol{\Phi}\right)^{-T} \cdot \boldsymbol{E}_3 d\mathcal{A} \Big]_{h_{\min}}^{h_{\max}} = \int_{h_{\min}}^{h_{\max}} \int_{\mathcal{A}} j \left(\rho \ddot{\boldsymbol{\varphi}} - \boldsymbol{B}\right) d\mathcal{A} d\xi^3, \end{aligned} \tag{4.22}$$

where identity (4.5) has been used and where $\boldsymbol{\nu}$ is defined as the outward unit normal of the shell in the inertial frame.

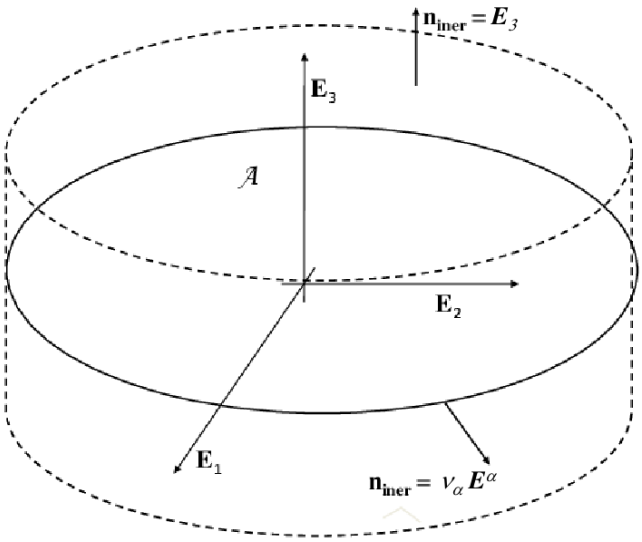

Figure 4.2: The choice for the normal to Γ is illustrated on a 3D representation of the shell in the inertial frame.

Furthermore, the value of $\nabla\boldsymbol{\Phi}^{-T}$ can be determined by the definition of the conjugated frame: $\boldsymbol{g}^I \cdot \boldsymbol{g}_J = \delta_{IJ}$, which gives $\boldsymbol{g}^I = \nabla\boldsymbol{\Phi}^{-T}\boldsymbol{E}^I$. Indeed using (4.8),

$$\boldsymbol{g}^I \cdot \boldsymbol{g}_J = \left(\nabla\boldsymbol{\Phi}^{-T}\boldsymbol{E}^I\right) \cdot (\nabla\boldsymbol{\Phi})\,\boldsymbol{E}_J = \nabla\boldsymbol{\Phi}^{-1}_{ki}\boldsymbol{E}^I_k \nabla\boldsymbol{\Phi}_{ip}\boldsymbol{E}_{Jp} = \boldsymbol{E}^I_p \boldsymbol{E}_{Jp} = \delta_{IJ}\,. \tag{4.23}$$

Thus,

$$\nabla\boldsymbol{\Phi}^{-T} \cdot \boldsymbol{\nu} = \left(\nabla\boldsymbol{\Phi}^{-T}\boldsymbol{E}^I\right)(\boldsymbol{E}_I \cdot \boldsymbol{\nu}) = \boldsymbol{g}^\alpha \nu_\alpha\,, \tag{4.24}$$

as $\boldsymbol{\nu}$ is in the plane[4] $\boldsymbol{E}_1$, $\boldsymbol{E}_2$. Finally, Eq. (4.22) can be rewritten, by taking into account Eq. (4.24) as,

$$\int_{\partial\mathcal{A}} \bar{j}\boldsymbol{n}^\alpha \nu_\alpha d\partial\mathcal{A} = \int_{\mathcal{A}} \left(\bar{j}\bar{\rho}\ddot{\boldsymbol{\varphi}} - \bar{j}\boldsymbol{n}^{\mathcal{A}}\right) d\mathcal{A}\,, \tag{4.25}$$

[4] as $\boldsymbol{\nu}$ is in the middle plane, $dl = \bar{j}dL\overline{g^\alpha}\nu_\alpha$ and therefore $\boldsymbol{n} = \overline{g^\alpha}\nu_\alpha$. Thus, ν_β can be computed as $\boldsymbol{n} \cdot \boldsymbol{\varphi}_{,\beta} = \delta_{\alpha\beta}\nu_\alpha = \nu_\beta$

with the following definitions,

$$\boldsymbol{n}^{\alpha} = \frac{1}{j}\int_{h_{\min}}^{h_{\max}} j\boldsymbol{\sigma}\boldsymbol{g}^{\alpha} d\xi^3 , \tag{4.26}$$

$$\overline{\rho} = \frac{1}{j}\int_{h_{\min}}^{h_{\max}} j\rho d\xi^3 \text{ and,} \tag{4.27}$$

$$\boldsymbol{n}^{\mathcal{A}} = \frac{1}{j}\left[\int_{h_{\min}}^{h_{\max}} \boldsymbol{B}\, j d\xi^3 + j\boldsymbol{\sigma}\boldsymbol{g}^3\right]_{h_{\min}}^{h_{\max}} . \tag{4.28}$$

Term $\boldsymbol{n}^{\alpha}$ is the resultant stress and represents the force per unit width on the shell section, $\overline{\rho}$ is the density per unit surface of the shell, and $\boldsymbol{n}^{\mathcal{A}}$ represents the membrane external loading per unit surface on the shell.

Applying the divergence theorem on Eq. (4.25) leads to,

$$\int_{\mathcal{A}} \left[(\overline{j}\boldsymbol{n}^{\alpha})_{,\alpha} + \overline{j}\boldsymbol{n}^{\mathcal{A}}\right] d\mathcal{A} = \int_{\mathcal{A}} \overline{j}\overline{\rho}\ddot{\boldsymbol{\phi}} d\mathcal{A} , \tag{4.29}$$

and due to the arbitrary choice of the part of the Cosserat plane where the integration has been performed, the resultant strong form of the linear momentum equation reads,

$$\frac{1}{j}(\overline{j}\boldsymbol{n}^{\alpha})_{,\alpha} + \boldsymbol{n}^{\mathcal{A}} = \overline{\rho}\ddot{\boldsymbol{\phi}} . \tag{4.30}$$

The angular momentum equation can be obtained with the same argumentation. Integration of Eq. (4.17) on an arbitrary volume with application of Gauss theorem on $\nabla\cdot\boldsymbol{\sigma}^T$ yields[5],

$$\int_{\partial\mathcal{S}} \boldsymbol{\Phi}\wedge(\boldsymbol{\sigma}\boldsymbol{n})\, d\mathcal{S} = \int_{\mathcal{S}} \frac{d}{dt}\left(\boldsymbol{\Phi}\wedge\rho\dot{\boldsymbol{\Phi}}\right) d\mathcal{S} - \int_{\mathcal{S}} \boldsymbol{\Phi}\wedge\boldsymbol{B} d\mathcal{S} . \tag{4.31}$$

[5]By definition of vectorial product,

$$\left(\int_{\mathcal{S}} \boldsymbol{\Phi}\wedge\left(\nabla\cdot\boldsymbol{\sigma}^T\right) d\mathcal{S}\right)_i = \int_{\mathcal{S}} \varepsilon_{ijk}\Phi_j\nabla_l\sigma_{kl} d\mathcal{S}$$

This last relation can be integrated by parts,

$$\left(\int_{\mathcal{S}} \boldsymbol{\Phi}\wedge\left(\nabla\cdot\boldsymbol{\sigma}^T\right) d\mathcal{S}\right)_i = \int_{\mathcal{S}} \varepsilon_{ijk}\Phi_j\sigma_{kl}n_k d\mathcal{S} - \int_{\mathcal{S}} \nabla_l\Phi_j\varepsilon_{ijk}\sigma_{kl} d\mathcal{S} ,$$

and, using the Gauss theorem for the first term, as $\nabla_l\Phi_j = \delta_{lj}$ and due to the symmetry of $\boldsymbol{\sigma}$ one has,

$$\int_{\mathcal{S}} \boldsymbol{\Phi}\wedge\left(\nabla\cdot\boldsymbol{\sigma}^T\right) d\mathcal{S} = \int_{\partial\mathcal{S}} \boldsymbol{\Phi}\wedge(\boldsymbol{\sigma}\cdot\boldsymbol{n})\, d\partial V .$$

Then, Eq. (4.19) is used to formulate Eq. (4.31) in the reference inertial frame yielding,

$$\begin{aligned}\int_{\partial(\mathcal{A}\times[h_{\min};h_{\max}])}\left(\boldsymbol{\varphi}+\xi^3\lambda_h\boldsymbol{t}\right)\wedge\left[\boldsymbol{\sigma}\,j\nabla\boldsymbol{\Phi}^{-T}\boldsymbol{n}_{iner}\right]d\Gamma \;=\\ \int_{\mathcal{A}}\int_{h_{\min}}^{h_{\max}}\frac{d}{dt}\left[j\rho\left(\boldsymbol{\varphi}+\xi^3\lambda_h\boldsymbol{t}\right)\wedge\left(\dot{\boldsymbol{\varphi}}+\xi^3\left(\dot{\lambda_h}\boldsymbol{t}\right)\right)\right]d\xi^3 d\mathcal{A} \;-\\ \int_{\mathcal{A}}\int_{h_{\min}}^{h_{\max}} j\left(\boldsymbol{\varphi}+\xi^3\lambda_h\boldsymbol{t}\right)\wedge\boldsymbol{B}\,d\xi^3 d\mathcal{A}\,. \end{aligned}\tag{4.32}$$

Furthermore, dividing the integral of the first member according to Fig. 4.2 and taking into account the identity (4.24) this first term can be written,

$$\begin{aligned}\int_{\partial\mathcal{A}}\boldsymbol{\varphi}\wedge\left[\int_{h_{\min}}^{h_{\max}} j\boldsymbol{\sigma}\boldsymbol{g}^{\alpha}d\xi^3\right]\nu_{\alpha}d\partial\mathcal{A}+\int_{\partial\mathcal{A}}\lambda_h\boldsymbol{t}\wedge\left[\int_{h_{\min}}^{h_{\max}}\xi^3 j\boldsymbol{\sigma}\boldsymbol{g}^{\alpha}d\xi^3\right]\nu_{\alpha}d\partial\mathcal{A}\\ +\int_{\mathcal{A}}\boldsymbol{\varphi}\wedge\left[j\boldsymbol{\sigma}\boldsymbol{g}^3\right]_{h_{\min}}^{h_{\max}}+\lambda_h\boldsymbol{t}\wedge\left(\xi^3 j\boldsymbol{\sigma}\boldsymbol{g}^3\right)\Big]_{h_{\min}}^{h_{\max}}\Big]\,d\mathcal{A}\,.\end{aligned}\tag{4.33}$$

Moreover, the inertial term of Eq. (4.32) can be rewritten after distributing the vectorial product as,

$$\begin{aligned}\int_{\mathcal{A}}\int_{h_{\min}}^{h_{\max}}\frac{d}{dt}\Big[j\rho\left(\boldsymbol{\varphi}\wedge\dot{\boldsymbol{\varphi}}\right)+j\rho\xi^3\left(\boldsymbol{\varphi}\wedge\left(\dot{\lambda_h}\boldsymbol{t}\right)+\lambda_h\boldsymbol{t}\wedge\dot{\boldsymbol{\varphi}}\right)+\\ j\rho(\xi^3)^2\left(\lambda_h\boldsymbol{t}\wedge\left(\dot{\lambda_h}\boldsymbol{t}\right)\right)\Big]d\xi^3 d\mathcal{A}\,.\end{aligned}\tag{4.34}$$

Then, taking into account Eq. (4.5) and the fundamental properties of vectorial product,

$$\int_{\mathcal{A}}\int_{h_{\min}}^{h_{\max}} j\rho d\xi^3\boldsymbol{\varphi}\wedge\ddot{\boldsymbol{\varphi}}d\mathcal{A}+\int_{\mathcal{A}}\int_{h_{\min}}^{h_{\max}}(\xi^3)^2 j\rho d\xi^3\lambda_h\boldsymbol{t}\wedge\left(\ddot{\lambda_h}\boldsymbol{t}\right)d\mathcal{A}\,.\tag{4.35}$$

Then terms (4.33) and (4.35) can then be substitued in Eq. (4.32) yielding,

$$\begin{aligned}&\int_{\partial\mathcal{A}}\left[\boldsymbol{\varphi}\wedge\boldsymbol{n}^{\alpha}+\lambda_h\boldsymbol{t}\wedge\tilde{\boldsymbol{m}}^{\alpha}\right]\nu_{\alpha}d\partial\mathcal{A}+\\ &\int_{\mathcal{A}}\boldsymbol{\varphi}\wedge\left(j\boldsymbol{\sigma}\boldsymbol{g}^3\right)\Big]_{h_{\min}}^{h_{\max}}d\mathcal{A}+\int_{\mathcal{A}}\lambda_h\boldsymbol{t}\wedge\tilde{\boldsymbol{m}}^{\mathcal{A}}d\mathcal{A}=\\ &\int_{\mathcal{A}}\int_{h_{\min}}^{h_{\max}}\boldsymbol{\varphi}\wedge\left(j\rho\ddot{\boldsymbol{\varphi}}\right)d\xi^3 d\mathcal{A}+\int_{\mathcal{A}}\bar{jI}_p\dot{\boldsymbol{w}}_{\boldsymbol{t}}d\mathcal{A}-\int_{\mathcal{A}}\boldsymbol{\varphi}\wedge\int_{h_{\min}}^{h_{\max}} j\boldsymbol{B}d\xi^3 d\mathcal{A}\,,\end{aligned}\tag{4.36}$$

with the definitions,

$$\tilde{\boldsymbol{m}}^{\alpha} = \frac{1}{j}\int_{h_{\min}}^{h_{\max}} j\xi^3\boldsymbol{\sigma}\boldsymbol{g}^{\alpha}d\xi^3\,,\tag{4.37}$$

$$\tilde{\boldsymbol{m}}^{\mathcal{A}} = \frac{1}{j}\left[\xi^3 j\boldsymbol{\sigma}\boldsymbol{g}^3\right]_{h_{\min}}^{h_{\max}}+\int_{h_{\min}}^{h_{\max}}\xi^3 j\boldsymbol{B}d\xi^3\Big]\,,\tag{4.38}$$

$$I_p = \frac{1}{j}\int_{h_{\min}}^{h_{\max}} j\rho\xi^{3^2}d\xi^3\,\text{and,}\tag{4.39}$$

$$\dot{\boldsymbol{w}}_{\boldsymbol{t}} = \lambda_h\boldsymbol{t}\wedge\left(\ddot{\lambda_h}\boldsymbol{t}\right)\,.\tag{4.40}$$

Term $\tilde{\boldsymbol{m}}^{\alpha}$ is the resultant torque and represents the moment per unit width on the shell section, $\tilde{\boldsymbol{m}}^{\mathcal{A}}$ represents the bending external loading per unit surface on the shell, I_p is the polar moment of mass inertia and $\dot{\boldsymbol{w}}_{\boldsymbol{t}}$ is the rotational inertia of the shell.

Finally, using the divergence theorem, the definitions (4.26-4.28) and taking into account the linear momentum equation (4.29), we obtain the expression of the angular momentum equilibrium,

$$\frac{1}{j}(\lambda_h \boldsymbol{t} \wedge \bar{j}\tilde{\boldsymbol{m}}^{\alpha})_{,\alpha} + \boldsymbol{\varphi}_{,\alpha} \wedge \boldsymbol{n}^{\alpha} + \lambda_h \boldsymbol{t} \wedge \tilde{\boldsymbol{m}}^{\mathcal{A}} = I_p \dot{\boldsymbol{w}}_{\boldsymbol{t}}\,. \tag{4.41}$$

as an arbitrary part of the Cosserat plane was considered. In this equation the inertial term $I_p \dot{\boldsymbol{w}}_{\boldsymbol{t}}$ can be neglected. Indeed, thin bodies have by definition a thickness small compared with the other dimensions and thus the inertia of eccentricity is generally negligible. This assumption is used herein. Moreover, Eq. (4.41) can be written under another form with regard to the symmetric nature of the stress tensor $\boldsymbol{\sigma}$. This tensor can be formulated in the convected basis as,

$$\boldsymbol{\sigma} = \sigma^{IJ}(\boldsymbol{g}_I \otimes \boldsymbol{g}_J)\,. \tag{4.42}$$

Multiplying both terms by $\boldsymbol{g}^k$ one has,

$$\boldsymbol{\sigma} \cdot \boldsymbol{g}^K = \sigma^{IJ}(\boldsymbol{g}_I \otimes \boldsymbol{g}_J) \cdot \boldsymbol{g}^K = \sigma^{IJ}\boldsymbol{g}_I\left(\boldsymbol{g}_J \cdot \boldsymbol{g}^K\right) = \sigma^{IJ}\boldsymbol{g}_I \delta_{JK} = \sigma^{IK}\boldsymbol{g}_I\,. \tag{4.43}$$

This last relation can be vectorially premultiplied by $\boldsymbol{g}_k$ leading to,

$$\boldsymbol{g}_K \wedge \left(\boldsymbol{\sigma}\boldsymbol{g}^K\right) = \sigma^{IK}\boldsymbol{g}_K \wedge \boldsymbol{g}_I = \frac{1}{2}\sigma^{IK}(\boldsymbol{g}_K \wedge \boldsymbol{g}_I + \boldsymbol{g}_I \wedge \boldsymbol{g}_K) = 0\,, \tag{4.44}$$

as $\sigma^{IK} = \sigma^{KI}$. Then, using the definition of the convected basis Eqs. (4.9-4.10) the Eq. (4.43) reads,

$$\left(\boldsymbol{\varphi}_{,\alpha} + \xi^3(\lambda_h \boldsymbol{t})_{,\alpha}\right) \wedge (\boldsymbol{\sigma}\boldsymbol{g}^{\alpha}) + \lambda_h \boldsymbol{t} \wedge \left(\boldsymbol{\sigma}\boldsymbol{g}^3\right) = 0\,. \tag{4.45}$$

Afterward, this equation is multiplied by j and integrated on the thickness,

$$\int_{h_{\min}}^{h_{\max}} j\left(\boldsymbol{\varphi}_{,\alpha} + \xi^3(\lambda_h \boldsymbol{t})_{,\alpha}\right) \wedge (\boldsymbol{\sigma}\boldsymbol{g}^{\alpha})\, d\xi^3 + \int_{h_{\min}}^{h_{\max}} j\lambda_h \boldsymbol{t} \wedge \left(\boldsymbol{\sigma}\boldsymbol{g}^3\right) d\xi^3 = 0\,. \tag{4.46}$$

Finally, using definitions (4.26) and (4.37) and the invariance of $\boldsymbol{\varphi}_{,\alpha}$ and $\boldsymbol{t}$ with the thickness one has,

$$\boldsymbol{\varphi}_{,\alpha} \wedge \bar{j}\boldsymbol{n}^{\alpha} + (\lambda_h \boldsymbol{t})_{,\alpha} \wedge \bar{j}\tilde{\boldsymbol{m}}^{\alpha} + \lambda_h \boldsymbol{t} \wedge \bar{j}\boldsymbol{l} = 0\,, \tag{4.47}$$

with the following definition of the resultant out-of-plane stress,

$$\boldsymbol{l} = \frac{1}{j}\int_{h_{\min}}^{h_{\max}} j\boldsymbol{\sigma}\boldsymbol{g}^3 d\xi^3\,. \tag{4.48}$$

Finally, Eq. (4.47) can be incorporated in Eq. (4.41), which becomes,

$$\lambda_h \boldsymbol{t} \wedge (\bar{j}\tilde{\boldsymbol{m}}^{\alpha})_{,\alpha} - \lambda_h \boldsymbol{t} \wedge \bar{j}\bar{\boldsymbol{l}} + \lambda_h \boldsymbol{t} \wedge \bar{j}\tilde{\boldsymbol{m}}^{\mathcal{A}} = 0\,, \tag{4.49}$$

or again, if λ is an undefined pressure,

$$(\bar{j}\tilde{\boldsymbol{m}}^{\alpha})_{,\alpha} - \bar{j}\bar{\boldsymbol{l}} + \bar{j}\tilde{\boldsymbol{m}}^{\mathcal{A}} + \bar{j}\lambda \boldsymbol{t} = 0\,. \tag{4.50}$$

The set of Eqs. (4.30) and (4.50) constitutes the strong formulation of the problem, which is the starting point to derive the full-DG weak form presented in Section 4.2. This set of equations has to be completed by appropriate boundary conditions. Toward this end, the boundary of the mid-plane $\partial\mathcal{A}$, where the boundary conditions are applied, is decomposed into four parts verifying,

$$\partial_T\mathcal{A} \cap \partial_M\mathcal{A} = 0 \quad \text{and} \quad \partial_T\mathcal{A} \cup \partial_M\mathcal{A} = \partial\mathcal{A}\,, \tag{4.51}$$

$$\partial_U\mathcal{A} \cap \partial_N\mathcal{A} = 0 \quad \text{and} \quad \partial_U\mathcal{A} \cup \partial_N\mathcal{A} = \partial\mathcal{A}\,. \tag{4.52}$$

These four parts are,

(i) $\partial_M\mathcal{A}$, the part of $\partial\mathcal{A}$ where the applied torque is constrained to $\bar{\tilde{\boldsymbol{m}}}$:

$$\tilde{\boldsymbol{m}}^{\alpha}\nu_{\alpha} = \bar{\tilde{\boldsymbol{m}}} \quad \forall\,(\xi^1,\xi^2) \in \partial_M\mathcal{A}\,, \tag{4.53}$$

(ii) $\partial_N\mathcal{A}$, the part of $\partial\mathcal{A}$ where the tractions are constrained to $\bar{\boldsymbol{n}}$:

$$\boldsymbol{n}^{\alpha}\nu_{\alpha} = \bar{\boldsymbol{n}} \quad \forall\,(\xi^1,\xi^2) \in \partial_N\mathcal{A}\,, \tag{4.54}$$

(iii) $\partial_T\mathcal{A}$, the part of $\partial\mathcal{A}$ where the direction of the mid-surface $\boldsymbol{t}$ is constrained to $\bar{\boldsymbol{t}}$:

$$\boldsymbol{t} = \bar{\boldsymbol{t}} \quad \forall\,(\xi^1,\xi^2) \in \partial_T\mathcal{A}\,, \tag{4.55}$$

(iv) $\partial_U\mathcal{A}$, the part of $\partial\mathcal{A}$ where the positions are constrained to $\bar{\boldsymbol{\varphi}}$:

$$\boldsymbol{\varphi} = \bar{\boldsymbol{\varphi}} \quad \forall\,(\xi^1,\xi^2) \in \partial_U\mathcal{A}\,. \tag{4.56}$$

4.2 Full-DG formulation of Kirchhoff-Love shells

In this section, a framework for the numerical approximation of the shell equations described in Section 4.1.2 based on a discontinuous polynomial approximation of the unknown field $\boldsymbol{\varphi}$ is suggested. In this formulation, the resulting discontinuities in the surface mapping $\boldsymbol{\varphi}$ and in the surface director $\boldsymbol{t}$ are accounted for using a new full discontinuous Galerkin formulation. Let us remind that as $\boldsymbol{t} = \boldsymbol{t}(\boldsymbol{\varphi})$ through Eq. (4.13) the developments leads to a one-field formulation.

The mid-surface $\mathcal{A}$ is approximated by a discretization $\mathcal{A}_h$ into finite-elements $\mathcal{A}_e$. Given $\bar{\mathcal{A}}_e$ as the union of the open domain $\mathcal{A}_e$ with its boundary $\partial\mathcal{A}_e$, we have $\mathcal{A} \simeq \mathcal{A}_h = \bigcup_e \bar{\mathcal{A}}_e$. Furthermore, the boundary $\partial\mathcal{A}_e$ of an element $\mathcal{A}_e$ can be either common with the boundary of $\mathcal{A}_h$

$$\begin{aligned} \partial_U\mathcal{A}_e = &\quad \partial\mathcal{A}_e \cap \partial_U\mathcal{A}_h\,,\ \partial_T\mathcal{A}_e &&= \partial\mathcal{A}_e \cap \partial_T\mathcal{A}_h\,, \\ \partial_M\mathcal{A}_e = &\quad \partial\mathcal{A}_e \cap \partial_M\mathcal{A}_h\,, \text{ and } \partial_N\mathcal{A}_e &&= \partial\mathcal{A}_e \cap \partial_N\mathcal{A}_h\,, \end{aligned} \tag{4.57}$$

or shared with another finite element and is then part of the interior boundary $\partial_I\mathcal{A}_h$,

$$\partial_I\mathcal{A}_e \;= \partial\mathcal{A}_e \backslash_{\partial\mathcal{A}_h} = \partial\mathcal{A}_e \cap \partial_I\mathcal{A}_h\,, \text{ with } \partial_I\mathcal{A}_h \;= \bigcup_e \partial\mathcal{A}_e \backslash_{\partial\mathcal{A}_h}\,. \tag{4.58}$$

Then, instead of seeking the exact solution $\boldsymbol{\varphi}$, a polynomial approximation $\boldsymbol{\varphi}_h$ constitutes the solution to the finite element problem. In this work, a discontinuous polynomial approximation is considered, leading to a discretization with discontinuous elements. Therefore the continuity of the FE solution has to be ensured weakly.

The purpose of this section is to establish a weak form of the problem stated in the strong form by the set of equations (4.30) and (4.50) for an approximation $\boldsymbol{\varphi}_h$. Multiplying Eq. (4.30) by a test function $\delta\boldsymbol{\varphi}$ and equation (4.50) by the corresponding variation of unit vector $\lambda_h\delta\boldsymbol{t} = \lambda_h\boldsymbol{t}(\delta\boldsymbol{\varphi})$, adding both equations and integrating on $\mathcal{A}_h$ state the problem as finding $\boldsymbol{\varphi}_h$ such that,

$$\begin{aligned} \sum_e \int_{\bar{\mathcal{A}}_e} \bar{\rho}\ddot{\boldsymbol{\varphi}}_h \cdot \delta\boldsymbol{\varphi} d\mathcal{A} \;=\; & \sum_e \int_{\bar{\mathcal{A}}_e} (\bar{j}\boldsymbol{n}^\alpha(\boldsymbol{\varphi}_h))_{,\alpha} \cdot \delta\boldsymbol{\varphi} d\mathcal{A} + \\ & \sum_e \int_{\bar{\mathcal{A}}_e} \left[(\bar{j}\tilde{\boldsymbol{m}}^\alpha(\boldsymbol{\varphi}_h))_{,\alpha} - \bar{j}\boldsymbol{l}\right] \cdot \delta\boldsymbol{t}\lambda_h d\mathcal{A} \\ & + \int_{\mathcal{A}_h} \boldsymbol{n}^{\mathcal{A}} \cdot \delta\boldsymbol{\varphi}\bar{j} d\mathcal{A} + \int_{\mathcal{A}_h} \tilde{\boldsymbol{m}}^{\mathcal{A}} \cdot \delta\boldsymbol{t}\lambda_h \bar{j} d\mathcal{A}\,. \end{aligned} \tag{4.59}$$

The kinematically admissible virtual fields $\delta\boldsymbol{\varphi}$ and $\delta\boldsymbol{t}$ are belonging to the same manifolds as $\boldsymbol{\varphi}_h$ and $\boldsymbol{t}$ respectively, but they satisfy the essential boundary conditions $\delta\boldsymbol{\varphi} = 0$ on $\partial_U\mathcal{A}_h$ and $\delta\boldsymbol{t} = 0$ on $\partial_T\mathcal{A}_h$.

Notice that the chosen variation of the unit vector omits the variation of λ_h. This equation, governing the change of the thickness, is replaced by the enforcement of the plane stress state when solving the material behavior as described in Section 4.3.

Integration by parts of these integrals, followed by the application of the Gauss theorem in the Cosserat plane, leads to

$$\begin{aligned} \sum_e a_d^e(\boldsymbol{\varphi}_h, \delta\boldsymbol{\varphi}) \;=\; & -\sum_e a_n^e(\boldsymbol{\varphi}_h, \delta\boldsymbol{\varphi}) + \sum_e \int_{\partial\mathcal{A}_e} \bar{j}\boldsymbol{n}^\alpha(\boldsymbol{\varphi}_h) \cdot \delta\boldsymbol{\varphi}\nu_\alpha d\mathcal{A} - \\ & \sum_e a_m^e(\boldsymbol{\varphi}_h, \delta\boldsymbol{\varphi}) + \sum_e \int_{\partial\mathcal{A}_e} \bar{j}\tilde{\boldsymbol{m}}^\alpha(\boldsymbol{\varphi}_h) \cdot \delta\boldsymbol{t}\lambda_h\nu_\alpha d\mathcal{A} + \\ & \sum_e a_s^e(\boldsymbol{\varphi}_h, \delta\boldsymbol{\varphi}) - \sum_e \int_{\partial\mathcal{A}_e} \bar{j}\boldsymbol{l} \cdot \int_\alpha \delta\boldsymbol{t}\lambda_h d\alpha' \nu_\alpha d\mathcal{A} + \\ & b_{\text{ext}}(\boldsymbol{\varphi}_h, \delta\boldsymbol{\varphi})\,. \end{aligned} \tag{4.60}$$

with the following forms,

$$b_{\text{ext}}(\boldsymbol{\varphi}_h,\delta\boldsymbol{\varphi}) = \int_{\mathcal{A}_h} \boldsymbol{n}^{\mathcal{A}}\cdot\delta\boldsymbol{\varphi}\,\bar{j}d\mathcal{A} + \int_{\mathcal{A}_h} \tilde{\boldsymbol{m}}^{\mathcal{A}}\cdot\delta\boldsymbol{t}\lambda_h\bar{j}d\mathcal{A}\,, \tag{4.61}$$

$$a_d^e(\boldsymbol{\varphi}_h,\delta\boldsymbol{\varphi}) = \int_{\mathcal{A}_e} \bar{\rho}\ddot{\boldsymbol{\varphi}}_h\cdot\delta\boldsymbol{\varphi}d\mathcal{A}\,, \tag{4.62}$$

$$a_n^e(\boldsymbol{\varphi}_h,\delta\boldsymbol{\varphi}) = \int_{\bar{\mathcal{A}}_e} \bar{j}\boldsymbol{n}^{\alpha}(\boldsymbol{\varphi}_h)\cdot\delta\boldsymbol{\varphi}_{,\alpha}d\mathcal{A}\,, \tag{4.63}$$

$$a_m^e(\boldsymbol{\varphi}_h,\delta\boldsymbol{\varphi}) = \int_{\bar{\mathcal{A}}_e} \bar{j}\tilde{\boldsymbol{m}}^{\alpha}(\boldsymbol{\varphi}_h)\cdot(\delta\boldsymbol{t}\lambda_h)_{,\alpha}d\mathcal{A}\,,\text{and} \tag{4.64}$$

$$a_s^e(\boldsymbol{\varphi}_h,\delta\boldsymbol{\varphi}) = \int_{\bar{\mathcal{A}}_e} (\bar{j}\bar{\boldsymbol{l}})_{,\alpha}\cdot\int_{\alpha}\delta\boldsymbol{t}\lambda_h d\alpha' d\mathcal{A} \approx 0\,. \tag{4.65}$$

In the last Eq. (4.65), the integration by parts of the resultant out-of-plane stress is written in an unusual manner. Indeed, it is performed on $\delta\boldsymbol{t}\lambda_h$ in place of $(\bar{j}\bar{\boldsymbol{l}})_{,\alpha}$ to ensure weakly the out-of plane continuity at the interfaces as discussed in what follows. Also, the notations $a(\boldsymbol{\varphi}_h,\delta\boldsymbol{\varphi})$ reduce to bilinear forms on the case of small deformations and linear behavior as it will be shown in Section 4.4.2. Finally $b_{\text{ext}}(\boldsymbol{\varphi}_h,\delta\boldsymbol{\varphi})$ depends on $\boldsymbol{\varphi}_h$ through λ_h. In the linear case, this term reduces to $b_{\text{ext}}(\delta\boldsymbol{u})$ as shown in Section 4.4.2. For the time being they are non-linear expressions.

As continuity is not ensured across the internal boundary, jump $[\![\bullet]\!]$ and mean $\langle\bullet\rangle$ operators are defined, as

$$[\![\bullet]\!] = \bullet^+ - \bullet^-,\ \text{and}\ \langle\bullet\rangle = \frac{1}{2}\left(\bullet^+ + \bullet^-\right). \tag{4.66}$$

In these relations the bullets represent generic vector fields formulated in the inertial frame as,

$$\bullet^{\pm} = \lim_{\varepsilon\to 0^+} \bullet\left(\xi^1 \pm \varepsilon\zeta^1, \xi^2 \pm \varepsilon\zeta^2\right), \tag{4.67}$$

where ζ^{α} are the components of the outer unit normal $\boldsymbol{\zeta}$ of $\mathcal{A}_e$ in the basis $(\boldsymbol{E}_1,\boldsymbol{E}_2)$. If definition (4.66) of the jump operator is not independent of the choice of the $+$ and $-$ sides of an element edge, when this jump is used in combination with the outward unit normal of the $-$ element $\boldsymbol{\nu}^-$, the formulation becomes consistent and independent on this choice. The extension of these definitions to the boundary $\partial_N\mathcal{A}_e$ is straightforward,

$$[\![\boldsymbol{\varphi}]\!] = \bar{\boldsymbol{\varphi}} - \boldsymbol{\varphi},\ [\![\delta\boldsymbol{\varphi}]\!] = -\delta\boldsymbol{\varphi} \quad \text{and} \quad \langle\boldsymbol{n}^{\alpha}\rangle = \boldsymbol{n}^{\alpha}\ \text{on}\ \partial_U\mathcal{A}\,, \tag{4.68}$$

$$[\![\boldsymbol{t}]\!] = \bar{\boldsymbol{t}} - \boldsymbol{t},\ [\![\delta\boldsymbol{t}]\!] = -\delta\boldsymbol{t} \quad \text{and} \quad \langle\tilde{\boldsymbol{m}}^{\alpha}\rangle = \tilde{\boldsymbol{m}}^{\alpha}\ \text{on}\ \partial_T\mathcal{A}\,. \tag{4.69}$$

From these definitions and as $\delta\boldsymbol{\varphi} = 0$ on $\partial_U\mathcal{A}_h$ and $\delta\boldsymbol{t} = 0$ on $\partial_T\mathcal{A}_h$, the boundary terms of

equation (4.60) are rewritten

$$\sum_e \int_{\partial \mathcal{A}_e} \bar{j}\boldsymbol{n}^\alpha(\boldsymbol{\varphi}_h)\cdot\delta\boldsymbol{\varphi}\nu_\alpha d\mathcal{A} =$$
$$\int_{\partial_N \mathcal{A}_h} \bar{j}\boldsymbol{n}^\alpha(\boldsymbol{\varphi}_h)\cdot\delta\boldsymbol{\varphi}\nu_\alpha d\mathcal{A} - \int_{\partial_I \mathcal{A}_h} [\![\bar{j}\boldsymbol{n}^\alpha(\boldsymbol{\varphi}_h)\cdot\delta\boldsymbol{\varphi}]\!]\nu_\alpha^- d\mathcal{A}\,, \tag{4.70}$$
$$\sum_e \int_{\partial \mathcal{A}_e} \bar{j}\tilde{\boldsymbol{m}}^\alpha(\boldsymbol{\varphi}_h)\cdot\delta t\lambda_h\nu_\alpha d\mathcal{A} =$$
$$\int_{\partial_M \mathcal{A}_h} \bar{j}\tilde{\boldsymbol{m}}^\alpha(\boldsymbol{\varphi}_h)\cdot\delta t\lambda_h\nu_\alpha d\mathcal{A} - \int_{\partial_I \mathcal{A}_h} [\![\bar{j}\tilde{\boldsymbol{m}}^\alpha(\boldsymbol{\varphi}_h)\cdot\delta t\lambda_h]\!]\nu_\alpha^- d\mathcal{A}\,, \text{ and} \tag{4.71}$$
$$-\sum_e \int_{\partial \mathcal{A}_e} \bar{j}\boldsymbol{l}\cdot\int_\alpha \delta t\lambda_h d\alpha'\nu_\alpha d\mathcal{A} =$$
$$-\int_{\partial_M \mathcal{A}_h} \bar{j}\boldsymbol{l}\cdot\int_\alpha \delta t\lambda_h d\alpha'\nu_\alpha d\mathcal{A} + \int_{\partial_I \mathcal{A}_h} \left[\!\!\left[\bar{j}\boldsymbol{l}\cdot\int_\alpha \delta t\lambda_h d\alpha'\right]\!\!\right]\nu_\alpha^- d\mathcal{A}\,. \tag{4.72}$$

At this stage, the main idea of DG methods, which consists in the substitution of the jumps by consistent numerical fluxes $\boldsymbol{h}$, can be applied. Following the same argumentation as for the beam case, see Section 3.2, as the stress tensor is continuous between two elements for the exact solution, $[\![\bar{j}\boldsymbol{n}^\alpha(\boldsymbol{\varphi}_h)\cdot\delta\boldsymbol{\varphi}]\!]\nu_\alpha^-$ can be replaced by $\boldsymbol{h}[\![\delta\boldsymbol{\varphi}]\!]$, and similarly for the other terms. The traditional average fluxes are considered herein,

$$\boldsymbol{h}\left((\bar{j}\boldsymbol{n}^\alpha)^+,(\bar{j}\boldsymbol{n}^\alpha)^-,\nu_\alpha^-\right) = \langle\bar{j}\boldsymbol{n}^\alpha\rangle\nu_\alpha^-\,, \tag{4.73}$$
$$\boldsymbol{h}\left((\bar{j}\lambda_h\tilde{\boldsymbol{m}}^\alpha)^+,(\bar{j}\lambda_h\tilde{\boldsymbol{m}}^\alpha)^-,\nu_\alpha^-\right) = \langle\bar{j}\lambda_h\tilde{\boldsymbol{m}}^\alpha\rangle\nu_\alpha^-\,, \text{ and} \tag{4.74}$$
$$\boldsymbol{h}\left((\bar{j}\boldsymbol{l})^+,(\bar{j}\boldsymbol{l})^-,\nu_\alpha^-\right) = \langle\bar{j}\boldsymbol{l}\rangle\nu_\alpha^-\,. \tag{4.75}$$

These ones can be injected in equations (4.70 - 4.72) and using (4.53-4.54), Eq. (4.60) becomes,

$$\begin{aligned}\sum_e a_d^e(\boldsymbol{\varphi}_h,\delta\boldsymbol{\varphi}) &= -\sum_e a_n^e(\boldsymbol{\varphi}_h,\delta\boldsymbol{\varphi}) - \sum_e a_m^e(\boldsymbol{\varphi}_h,\delta\boldsymbol{\varphi}) + \sum_e a_s^e(\boldsymbol{\varphi}_h,\delta\boldsymbol{\varphi}) - \\ &\quad \sum_s a_{nI1}^s(\boldsymbol{\varphi}_h,\delta\boldsymbol{\varphi}) - \sum_s a_{mI1}^s(\boldsymbol{\varphi}_h,\delta\boldsymbol{\varphi}) + \sum_s a_{sI1}^s(\boldsymbol{\varphi}_h,\delta\boldsymbol{\varphi}) + \\ &\quad b_{\text{ext}}(\boldsymbol{\varphi}_h,\delta\boldsymbol{\varphi}) + b_{\text{bound}}(\boldsymbol{\varphi}_h,\delta\boldsymbol{\varphi})\,.\end{aligned} \tag{4.76}$$

with,

$$a_{nI1}^s(\boldsymbol{\varphi}_h,\delta\boldsymbol{\varphi}) = \int_s \langle\bar{j}\boldsymbol{n}^\alpha\rangle\cdot[\![\delta\boldsymbol{\varphi}]\!]\nu_\alpha^- d\partial\mathcal{A}_e\,, \tag{4.77}$$
$$a_{mI1}^s(\boldsymbol{\varphi}_h,\delta\boldsymbol{\varphi}) = \int_s \langle\bar{j}\lambda_h\tilde{\boldsymbol{m}}^\alpha\rangle\cdot[\![\delta t]\!]\nu_\alpha^- d\partial\mathcal{A}_e\,, \tag{4.78}$$
$$a_{sI1}^s(\boldsymbol{\varphi}_h,\delta\boldsymbol{\varphi}) = \int_s \langle\bar{j}\boldsymbol{l}\rangle\cdot\left[\!\!\left[\int_\alpha \delta t\lambda_h d\alpha'\right]\!\!\right]\nu_\alpha^- d\partial\mathcal{A}_e \approx 0\,, \text{ and} \tag{4.79}$$
$$b_{\text{bound}}(\boldsymbol{\varphi}_h,\delta\boldsymbol{\varphi}) = \int_{\partial_N \mathcal{A}_h} \bar{j}\bar{\boldsymbol{n}}\cdot\delta\boldsymbol{\varphi}d\mathcal{A} + \int_{\partial_M \mathcal{A}_h} \bar{j}\bar{\tilde{\boldsymbol{m}}}\cdot\delta t\lambda_h d\mathcal{A}\,. \tag{4.80}$$

The identity (4.79) results from the Kirchhoff-Love and isotropic behavior assumptions leading to $\boldsymbol{l} \approx 0$.

Equation (4.76) describes a consistent weak form of the problem but as a discontinuous polynomial approximation is considered, the continuity is not ensured at element boundaries, and the solution is not unique. The weak continuities (C^0 and C^1) enforcement can be achieved with the same argumentation as for beams see Section 3.2, which results into a compatibility equation,

$$\begin{aligned} 0 \;=\; & \int_{\partial_I \mathcal{A}_h \cup \partial_U \mathcal{A}_h} [\![\boldsymbol{\varphi}]\!] \cdot \boldsymbol{h}\left(\delta(\bar{j}\boldsymbol{n}^\alpha)^+, \delta(\bar{j}\boldsymbol{n}^\alpha)^-, \nu_\alpha^-\right) d\mathcal{A} \\ & + \int_{\partial_I \mathcal{A}_h \cup \partial_T \mathcal{A}_h} [\![\boldsymbol{t}(\boldsymbol{\varphi}_h)]\!] \cdot \boldsymbol{h}\left(\delta(\bar{j}\bar{\lambda}_h \tilde{\boldsymbol{m}}^\alpha)^+, \delta(\bar{j}\bar{\lambda}_h \tilde{\boldsymbol{m}}^\alpha)^-, \nu_\alpha^-\right) d\mathcal{A} \\ & + \int_{\partial_I \mathcal{A}_h} \left[\!\!\left[\int_\alpha \lambda_h \boldsymbol{t} d\alpha' \right]\!\!\right] \cdot \boldsymbol{h}\left(\delta(\bar{j}\bar{\boldsymbol{l}})^+, \delta(\bar{j}\bar{\boldsymbol{l}})^-, \nu_\alpha^-\right) d\mathcal{A} \,. \end{aligned} \tag{4.81}$$

In this last expression, $\delta(\bar{j}\boldsymbol{n}^\alpha)$, $\delta(\bar{j}\bar{\lambda}_h\tilde{\boldsymbol{m}}^\alpha)$ and $\delta(\bar{j}\bar{\boldsymbol{l}})$ have to be defined. As it has been demonstrated in previous works for non-linear solid mechanics [181, 182, 183, 184], these expressions would actually depend on the tangent moduli of the constitutive models as $\delta x = \frac{\partial x}{\partial \boldsymbol{\varphi}} \cdot \delta\boldsymbol{\varphi}$. But, since the purpose of this term is to enforce continuity while being energetically consistent with (4.76), another form of the flux can be chosen, as long as the consistency condition remains satisfied. Ideally these terms should, when linearized, lead to a symmetric formulation as suggested by L. Noels [181] for the C^0/DG formulation. Thus, the compatibility fluxes are obtained by linearization of $\delta(\bar{j}\boldsymbol{n}^\alpha)$ and $\delta(\bar{j}\bar{\lambda}_h\tilde{\boldsymbol{m}}^\alpha)$ (see Appendix B.1 for details),

$$\begin{aligned} \delta(\bar{j}\boldsymbol{n}^\alpha) \;=\; & \frac{\bar{j}_0}{2} \mathcal{H}_n^{\alpha\beta\gamma\delta}\left(\delta\boldsymbol{\varphi}_{,\gamma}\cdot\boldsymbol{\varphi}_{h,\delta} + \boldsymbol{\varphi}_{h,\gamma}\cdot\delta\boldsymbol{\varphi}_{,\delta}\right)\boldsymbol{\varphi}_{h,\beta} + \bar{j}\boldsymbol{n}^\alpha \cdot \boldsymbol{\varphi}_h{}^{,\beta}\delta\boldsymbol{\varphi}_{,\beta} \\ & + \frac{\bar{j}_0}{\lambda_h}\lambda_\mu^\beta \mathcal{H}_m^{\alpha\mu\gamma\delta}\left(\delta\boldsymbol{\varphi}_{,\gamma}\cdot\boldsymbol{t}_{,\delta} + \boldsymbol{\varphi}_{h,\gamma}\cdot\delta\boldsymbol{t}_{,\delta}\right)\boldsymbol{\varphi}_{h,\beta} \\ & + \bar{j}\bar{\lambda}_h\tilde{m}^{\alpha\mu}\left(\delta\boldsymbol{t}_{,\mu}\cdot\boldsymbol{\varphi}_h{}^{,\beta} - \frac{\lambda_\mu^\zeta}{\lambda_h}\boldsymbol{\varphi}_h{}^{,\beta}\cdot\delta\boldsymbol{\varphi}_{,\zeta}\right)\boldsymbol{\varphi}_{h,\beta}\,, \end{aligned} \tag{4.82}$$

$$\delta(\bar{j}\bar{\lambda}_h\tilde{\boldsymbol{m}}^\alpha) \;=\; \bar{j}_0\mathcal{H}_m^{\alpha\beta\gamma\delta}\left(\delta\boldsymbol{\varphi}_{,\gamma}\cdot\boldsymbol{t}_{,\delta} + \boldsymbol{\varphi}_{h,\gamma}\cdot\delta\boldsymbol{t}_{,\delta}\right)\boldsymbol{\varphi}_{h,\beta} + \bar{j}\bar{\lambda}_h\tilde{\boldsymbol{m}}^\alpha\cdot\boldsymbol{\varphi}_h{}^{,\beta}\delta\boldsymbol{\varphi}_{,\beta}\,, \tag{4.83}$$

where [6] $\tilde{m}^{\alpha\mu} = \tilde{\boldsymbol{m}}^\alpha \cdot \boldsymbol{\varphi}^{,\mu}$ is the component of $\tilde{\boldsymbol{m}}^\alpha$ in the convected basis, $\lambda_\mu^\beta = \lambda_h \boldsymbol{t}_{,\mu}\cdot\boldsymbol{\varphi}^{,\beta}$ characterizes the curvature of the shell and where the linearized membrane $\mathcal{H}_n$ and bending

[6] Notice that $\boldsymbol{\varphi}^{,\mu}$ is the conjugated basis to $\boldsymbol{\varphi}_{,\mu}$ with an abuse of notation and $\boldsymbol{\varphi}^{,\mu} = \overline{\boldsymbol{g}^\mu}$.

$\mathcal{H}_m$ stiffness result from an isotropic assumption,

$$\begin{aligned}\mathcal{H}_n^{\alpha\beta\gamma\delta} &= \frac{E\,(h_{\max}-h_{\min})}{1-\nu^2}\left[\nu\boldsymbol{\varphi}_0^{,\alpha}\cdot\boldsymbol{\varphi}_0^{,\beta}\ \boldsymbol{\varphi}_0^{,\gamma}\cdot\boldsymbol{\varphi}_0^{,\delta}+\frac{1}{2}(1-\nu)\,\boldsymbol{\varphi}_0^{,\alpha}\cdot\boldsymbol{\varphi}_0^{,\gamma}\ \boldsymbol{\varphi}_0^{,\delta}\cdot\boldsymbol{\varphi}_0^{,\beta}+\right.\\ &\left.\frac{1}{2}(1-\nu)\,\boldsymbol{\varphi}_0^{,\alpha}\cdot\boldsymbol{\varphi}_0^{,\delta}\ \boldsymbol{\varphi}_0^{,\gamma}\cdot\boldsymbol{\varphi}_0^{,\beta}\right], \qquad (4.84)\\ \mathcal{H}_m^{\alpha\beta\gamma\delta} &= \frac{E\,(h_{\max}-h_{\min})^3}{12\,(1-\nu^2)}\left[\nu\boldsymbol{\varphi}_0^{,\alpha}\cdot\boldsymbol{\varphi}_0^{,\beta}\ \boldsymbol{\varphi}_0^{,\gamma}\cdot\boldsymbol{\varphi}_0^{,\delta}+\frac{1}{2}(1-\nu)\,\boldsymbol{\varphi}_0^{,\alpha}\cdot\boldsymbol{\varphi}_0^{,\gamma}\ \boldsymbol{\varphi}_0^{,\delta}\cdot\boldsymbol{\varphi}_0^{,\beta}+\right.\\ &\left.\frac{1}{2}(1-\nu)\,\boldsymbol{\varphi}_0^{,\alpha}\cdot\boldsymbol{\varphi}_0^{,\delta}\ \boldsymbol{\varphi}_0^{,\gamma}\cdot\boldsymbol{\varphi}_0^{,\beta}\right]. \qquad (4.85)\end{aligned}$$

Finally, as by assumption $\boldsymbol{l}\approx 0$, we can take $\delta(\bar{j}\bar{\lambda}_h\boldsymbol{l})=0$ in order to keep a linearized symmetric formulation. However, doing so remove the constraint on the continuity of $\boldsymbol{\varphi}_h\cdot\boldsymbol{t}$, which will be enforced using the quadrature stabilizing terms.

Introduction of equations (4.82) and (4.83) in equation (4.76) leads to

$$\begin{aligned}a_d^e(\boldsymbol{\varphi}_h,\delta\boldsymbol{\varphi}) &= -\sum_e a_n^e(\boldsymbol{\varphi}_h,\delta\boldsymbol{\varphi})-\sum_e a_m^e(\boldsymbol{\varphi}_h,\delta\boldsymbol{\varphi})+\sum_e a_s^e(\boldsymbol{\varphi}_h,\delta\boldsymbol{\varphi})\\ &-\sum_s a_{nI1}^s(\boldsymbol{\varphi}_h,\delta\boldsymbol{\varphi})-\sum_s a_{mI1}^s(\boldsymbol{\varphi}_h,\delta\boldsymbol{\varphi})+\sum_s a_{sI1}^s(\boldsymbol{\varphi}_h,\delta\boldsymbol{\varphi})\\ &-\sum_s a_{nI2}^s(\boldsymbol{\varphi}_h,\delta\boldsymbol{\varphi})-\sum_s a_{mI2}^s(\boldsymbol{\varphi}_h,\delta\boldsymbol{\varphi})+\sum_s a_{sI2}^s(\boldsymbol{\varphi}_h,\delta\boldsymbol{\varphi})\\ &+b_{\text{ext}}(\boldsymbol{\varphi}_h,\delta\boldsymbol{\varphi})+b_{\text{bound}}(\boldsymbol{\varphi}_h,\delta\boldsymbol{\varphi}), \qquad (4.86)\end{aligned}$$

with the forms,

$$\begin{aligned}a_{nI2}^s(\boldsymbol{\varphi}_h,\delta\boldsymbol{\varphi}) &= \int_s [\![\boldsymbol{\varphi}_h]\!]\cdot\langle\delta(\bar{j}\boldsymbol{n}^\alpha)\rangle\,\nu_\alpha^-\,d\partial\mathcal{A}_e, \qquad (4.87)\\ a_{mI2}^s(\boldsymbol{\varphi}_h,\delta\boldsymbol{\varphi}) &= \int_s [\![\boldsymbol{t}(\boldsymbol{\varphi}_h)]\!]\cdot\langle\delta(\bar{j}\bar{\lambda}_h\tilde{\boldsymbol{m}}^\alpha)\rangle\,\nu_\alpha^-\,d\partial\mathcal{A}_e, \text{ and} \qquad (4.88)\\ a_{sI2}^s(\boldsymbol{\varphi}_h,\delta\boldsymbol{\varphi}) &= \int_s \left[\!\!\left[\int_\alpha \lambda_h\boldsymbol{t}\,d\alpha'\right]\!\!\right]\cdot\langle\delta(\bar{j}\bar{\boldsymbol{l}})\rangle\,\nu_\alpha^-\,d\partial\mathcal{A}_e\approx 0. \qquad (4.89)\end{aligned}$$

Although this formulation is consistent (consistency results from the introduction of consistent fluxes) and $\boldsymbol{\varphi}_h\cdot\boldsymbol{\varphi}_{,\alpha}$ as well as $\boldsymbol{t}\cdot\boldsymbol{\varphi}_{,\alpha}$ continuity are weakly ensured, the stability and continuity in $\boldsymbol{\varphi}_h\cdot\boldsymbol{t}$ are not ensured. Moreover, for elliptic problem DG formulations are unstable without the introduction of stabilization term. Thus, we stabilize the formulation thanks to extra quadratic terms as it is suggested in [181, 185] and as presented in Chapter 3 for Euler-Bernoulli beams. Such an introduction of interior penalty terms is usual for the DG method applied to solid mechanics (see [16, 97, 139, 140, 182, 183] among others). Although the DG method is now slightly dissipative, this does not impact on the numerical accuracy as the method remains consistent and converges toward the solution with an optimal rate. These terms depend on dimensionless stabilization parameters β_i, which are sufficiently large

constants, and which are independent of the mesh and material properties. The mesh independence is ensured by the introduction of the characteristic element size h^s in the stability terms. By inspection of Eqs. (4.77-4.79) and (4.81) the quadratic terms can be deduced as,

$$\begin{aligned} a^s_{nI3}(\boldsymbol{\varphi}_h,\delta\boldsymbol{\varphi}) &= \int_s [\![\boldsymbol{\varphi}_h]\!]\cdot\boldsymbol{\varphi}_{h,\gamma}\nu^-_\delta \left\langle \frac{\beta_2 \mathcal{H}_n^{\alpha\beta\gamma\delta}\overline{j_0}}{h^s}\right\rangle [\![\delta\boldsymbol{\varphi}]\!]\cdot\boldsymbol{\varphi}_{h,\beta}\nu^-_\alpha d\partial\mathcal{A}_e + \\ &\quad \int_s [\![\boldsymbol{\varphi}_h]\!]\cdot\boldsymbol{\varphi}_{h,\gamma}\nu^-_\delta \left\langle \lambda^\beta_\mu \frac{\beta_2 \mathcal{H}_m^{\alpha\mu\gamma\delta}\overline{j_0}}{h^s}\right\rangle [\![\delta\boldsymbol{t}]\!]\cdot\boldsymbol{\varphi}_{h,\beta}\nu^-_\alpha d\partial\mathcal{A}_e + \\ &\quad \int_s [\![\boldsymbol{t}]\!]\cdot\boldsymbol{\varphi}_{h,\gamma}\nu^-_\delta \left\langle \lambda^\beta_\mu \frac{\beta_2 \mathcal{H}_m^{\alpha\mu\gamma\delta}\overline{j_0}}{h^s}\right\rangle [\![\delta\boldsymbol{\varphi}]\!]\cdot\boldsymbol{\varphi}_{h,\beta}\nu^-_\alpha d\partial\mathcal{A}_e\,, \end{aligned} \tag{4.90}$$

$$a^s_{mI3}(\boldsymbol{\varphi}_h,\delta\boldsymbol{\varphi}) = \int_s [\![\boldsymbol{t}(\boldsymbol{\varphi}_h)]\!]\cdot\boldsymbol{\varphi}_{h,\gamma}\nu^-_\delta \left\langle \frac{\beta_1 \mathcal{H}_m^{\alpha\beta\gamma\delta}\overline{j_0}}{h^s}\right\rangle [\![\delta\boldsymbol{t}(\boldsymbol{\varphi}_h)]\!]\cdot\boldsymbol{\varphi}_{h,\beta}\nu^-_\alpha d\partial\mathcal{A}_e\,, \tag{4.91}$$

$$a^s_{sI3}(\boldsymbol{\varphi}_h,\delta\boldsymbol{\varphi}) = \int_s [\![\boldsymbol{\varphi}_h]\!]\cdot\boldsymbol{t}(\boldsymbol{\varphi}_h)\nu^-_\beta \left\langle \frac{\beta_3 \mathcal{H}_s^{\alpha\beta}\overline{j_0}}{h^s}\right\rangle [\![\delta\boldsymbol{\varphi}]\!]\cdot\boldsymbol{t}(\boldsymbol{\varphi}_h)\nu^-_\alpha d\partial\mathcal{A}_e\,, \tag{4.92}$$

with the shearing stiffness,

$$\mathcal{H}_s^{\alpha\beta} = \mu(h_{\max}-h_{\min})\frac{A'}{A}\boldsymbol{\varphi}_0^{,\alpha}\cdot\boldsymbol{\varphi}_0^{,\beta}\,. \tag{4.93}$$

In this last expression A'/A characterizes the reduced shear area. The expressions of two first terms (4.90-4.91) result from (4.82-4.83). Note that (4.90) remains symmetric. The third stability term $a^s_{sI3}(\boldsymbol{\varphi}_h,\delta\boldsymbol{\varphi})$ (4.92) is obtained by considering a quadratic form coming from expression of $a^s_{sI1}(\boldsymbol{\varphi}_h,\delta\boldsymbol{\varphi})$ (4.79) and $a^s_{sI2}(\boldsymbol{\varphi}_h,\delta\boldsymbol{\varphi})$ (4.89) before assuming Kirchhoff-Love state, yielding

$$\begin{aligned} a^s_{sI3}(\boldsymbol{\varphi}_h,\delta\boldsymbol{\varphi})' &= \int_s \left\{ \left[\!\!\left[\int_\mu \lambda_h t_I \overline{\boldsymbol{g}}^I_h d\mu' \right]\!\!\right]\cdot\boldsymbol{\varphi}_{h,\alpha}\nu^-_\mu \left\langle \frac{\beta_3 \mathcal{H}_s^{\alpha\beta}\overline{j_0}}{h^s}\right\rangle \right. \\ &\qquad \left. \boldsymbol{\varphi}_{h,\beta}\cdot\left[\!\!\left[\int_\nu \lambda_h \delta t_J \overline{\boldsymbol{g}}^J_h d\nu' \right]\!\!\right]\nu^-_\nu \right\} d\partial\mathcal{A}_e\,. \end{aligned} \tag{4.94}$$

In this expression we use the notation $\boldsymbol{t} = t_I\overline{\boldsymbol{g}^I}$. However the presence of a primitive $\int_\mu$ in this expression leads to an implementation issue. This term has to (weakly) ensure the compatibility of the deflection normal to the mid-surface and therefore a consistent approximation of this term can be assumed as long as this enforcement remains satisfied. Toward this end, we suggest to neglect curvature effect, leading to equation (4.92) as presented in Appendix B.2. Note that under this hypothesis the two last terms of $a^s_{nI3}(\boldsymbol{\varphi}_h,\delta\boldsymbol{\varphi})$ (4.90) can and are also be neglected. Finally in Eqs. (4.90-4.92), expression $[\![\boldsymbol{\varphi}_h]\!]\cdot\boldsymbol{\varphi}_{,\gamma}$ means the scalar product of the jump of $\boldsymbol{\varphi}_h$ at interface with the vector $\boldsymbol{\varphi}_{h,\gamma}$ defined at the interface element which is typically the average of $\boldsymbol{\varphi}^-_{h,\gamma}$ and $\boldsymbol{\varphi}^+_{h,\gamma}$, see Section 4.5.

These three quadratic terms depend on dimensionless stabilization parameters β_i that have to be chosen large enough to stabilize the weak statement of the problem. They are independent of the geometry and of material properties by construction. Therefore, after adding such contributions, the final weak statement of the problem is finding $\boldsymbol{\varphi}_h$ such that,

$$a(\boldsymbol{\varphi}_h, \delta\boldsymbol{\varphi}) = b_{\text{ext}}(\boldsymbol{\varphi}_h, \delta\boldsymbol{\varphi}) + b_{\text{bound}}(\boldsymbol{\varphi}_h, \delta\boldsymbol{\varphi}), \tag{4.95}$$

for all $\delta\boldsymbol{\varphi}$ kinematically admissible and with,

$$\begin{aligned} a(\boldsymbol{\varphi}_h, \delta\boldsymbol{\varphi}) &= \sum_e (a_d^e(\boldsymbol{\varphi}_h, \delta\boldsymbol{\varphi}) + a_n^e(\boldsymbol{\varphi}_h, \delta\boldsymbol{\varphi}) + a_m^e(\boldsymbol{\varphi}_h, \delta\boldsymbol{\varphi})) + \\ &\quad \sum_s (a_{nI}^s(\boldsymbol{\varphi}_h, \delta\boldsymbol{\varphi}) + a_{mI}^s(\boldsymbol{\varphi}_h, \delta\boldsymbol{\varphi}) - a_{sI}^s(\boldsymbol{\varphi}_h, \delta\boldsymbol{\varphi})), \qquad (4.96) \\ a_{nI}^s(\boldsymbol{\varphi}_h, \delta\boldsymbol{\varphi}) &= a_{nI1}^s(\boldsymbol{\varphi}_h, \delta\boldsymbol{\varphi}) + a_{nI2}^s(\boldsymbol{\varphi}_h, \delta\boldsymbol{\varphi}) + a_{nI3}^s(\boldsymbol{\varphi}_h, \delta\boldsymbol{\varphi}), \qquad (4.97) \\ a_{mI}^s(\boldsymbol{\varphi}_h, \delta\boldsymbol{\varphi}) &= a_{mI1}^s(\boldsymbol{\varphi}_h, \delta\boldsymbol{\varphi}) + a_{mI2}^s(\boldsymbol{\varphi}_h, \delta\boldsymbol{\varphi}) + a_{mI3}^s(\boldsymbol{\varphi}_h, \delta\boldsymbol{\varphi}), \text{ and} \qquad (4.98) \\ a_{sI}^s(\boldsymbol{\varphi}_h, \delta\boldsymbol{\varphi}) &= a_{sI3}^s(\boldsymbol{\varphi}_h, \delta\boldsymbol{\varphi}). \qquad (4.99) \end{aligned}$$

Furthermore, if continuous test and trial functions are used, $[\![\boldsymbol{\varphi}_h]\!] = [\![\delta\boldsymbol{\varphi}]\!] = 0$ and for a quasi-static problem (*i.e.* $a_d^e(\boldsymbol{\varphi}_h, \delta\boldsymbol{\varphi}) = 0$), equation (4.95) simplifies into

$$\begin{aligned} a(\boldsymbol{\varphi}_h, \delta\boldsymbol{\varphi}) &= \sum_e (a_n^e(\boldsymbol{\varphi}_h, \delta\boldsymbol{\varphi}) + a_m^e(\boldsymbol{\varphi}_h, \delta\boldsymbol{\varphi})) + \sum_s a_{mI}^s(\boldsymbol{\varphi}_h, \delta\boldsymbol{\varphi}) \\ &= b_{\text{ext}}(\boldsymbol{\varphi}_h, \delta\boldsymbol{\varphi}) + b_{\text{bound}}(\boldsymbol{\varphi}_h, \delta\boldsymbol{\varphi}), \end{aligned} \tag{4.100}$$

which is identical to the non-linear C^0/DG formulation presented by L. Noels [181].

The final resulting form $a(\boldsymbol{\varphi}_h, \delta\boldsymbol{\varphi})$ (4.96) of the problem contains the classical terms of shells theory, $a_n^e(\boldsymbol{\varphi}_h, \delta\boldsymbol{\varphi})$ and $a_m^e(\boldsymbol{\varphi}_h, \delta\boldsymbol{\varphi})$, while the sum on s is a collection of boundary integrals resulting from the inter-element discontinuities. They enforce respectively

(i) the consistency of the formulation for the terms $a_{nI1}^s(\boldsymbol{\varphi}_h, \delta\boldsymbol{\varphi})$ and $a_{mI1}^s(\boldsymbol{\varphi}_h, \delta\boldsymbol{\varphi})$,

(ii) the compatibility and the symmetric nature of the Jacobian for the terms $a_{nI2}^s(\boldsymbol{\varphi}_h, \delta\boldsymbol{\varphi})$ and $a_{mI2}^s(\boldsymbol{\varphi}_h, \delta\boldsymbol{\varphi})$, and,

(iii) the the compatibility and the stability for the terms $a_{nI3}^s(\boldsymbol{\varphi}_h, \delta\boldsymbol{\varphi})$, $a_{mI3}^s(\boldsymbol{\varphi}_h, \delta\boldsymbol{\varphi})$ and for the term $a_{sI}^s(\boldsymbol{\varphi}_h, \delta\boldsymbol{\varphi})$.

Although terms $a_{nI2}^s(\boldsymbol{\varphi}_h, \delta\boldsymbol{\varphi})$ and $a_{mI2}^s(\boldsymbol{\varphi}_h, \delta\boldsymbol{\varphi})$ can be omitted without compromising the stability, these terms are mandatory to get an optimal convergence rate in the $\mathbf{L}^2$-norm, see Section 4.4.

The weak form (4.95) is a general large deformations formulation which can be used whatever the constitutive behavior. This weak form is completed by the equation describing the constitutive behavior.

4.3 Constitutive behavior

This work considers three different constitutive behaviors. Two assume a pure elastic response of the material and are used to validate the method on some numerical benchmarks. The first one is the Hooke law linking stresses to deformations under a linear small strain assumption. This law can be generalized to non-linear large deformations and is then called Neo-Hookean law. Finally, a J_2-flow elasto-plastic law can be considered to take into account the plasticity effects for finite deformations.

4.3.1 Hooke law

The Hooke law assumes a linear elastic response between the deformation and stress tensors. Furthermore, this law considers a small displacement field $\boldsymbol{u}$, leading to,

$$\boldsymbol{\varphi} = \boldsymbol{\varphi}_0 + \boldsymbol{u} \text{ and,} \tag{4.101}$$

$$\boldsymbol{t}(\boldsymbol{u}) = \boldsymbol{t}_0 + \Delta\boldsymbol{t} \ . \tag{4.102}$$

with,

$$\Delta\boldsymbol{t} = \varepsilon_{\alpha\beta 3}\left[\frac{\boldsymbol{\varphi}_{0,\alpha}\wedge\boldsymbol{u}_\beta}{j_0} + \boldsymbol{t}_0\boldsymbol{u}_{,\alpha}\cdot\frac{\boldsymbol{t}_0\wedge\boldsymbol{\varphi}_{0,\beta}}{j_0}\right], \tag{4.103}$$

whose the gradient is formulated as,

$$\begin{aligned}
\boldsymbol{\Delta t}_{,\gamma} = {} & \frac{\varepsilon_{\alpha\beta 3}\boldsymbol{t}_{0,\gamma}}{j_0}\boldsymbol{u}_{,\alpha}\cdot\left(\boldsymbol{t}_0\wedge\boldsymbol{\varphi}_{0,\beta}\right) - \frac{\varepsilon_{\alpha\beta 3}\boldsymbol{t}_0}{j_0}\boldsymbol{u}_{,\alpha\gamma}\cdot\left(\boldsymbol{t}_0\wedge\boldsymbol{\varphi}_{0,\beta}\right) + \\
& \frac{\varepsilon_{\alpha\beta 3}\boldsymbol{t}_0}{j_0}\boldsymbol{u}_{,\alpha}\cdot\left[\boldsymbol{t}_0\wedge\boldsymbol{\varphi}_{0,\beta\gamma} + \boldsymbol{t}_{0,\gamma}\wedge\boldsymbol{\varphi}_{0,\beta}\right] - \\
& \frac{\varepsilon_{\alpha\beta 3}\boldsymbol{t}_0}{j_0}\boldsymbol{u}_{,\alpha}\cdot\left(\boldsymbol{t}_0\wedge\boldsymbol{\varphi}_{0,\beta}\right)\frac{\varepsilon_{\eta\mu 3}}{j_0}\boldsymbol{t}_0\cdot\left(\boldsymbol{\varphi}_{0,\eta\gamma}\wedge\boldsymbol{\varphi}_{0,\mu}\right) + \\
& \frac{\varepsilon_{\alpha\beta 3}}{j_0}\left[\boldsymbol{\varphi}_{0,\alpha\gamma}\wedge\boldsymbol{u}_{,\beta} + \boldsymbol{\varphi}_{0,\alpha}\wedge\boldsymbol{u}_{,\beta\gamma}\right] - \\
& \frac{\varepsilon_{\alpha\beta 3}}{j_0}\left[\boldsymbol{\varphi}_{0,\alpha}\wedge\boldsymbol{u}_{,\beta}\frac{\varepsilon_{\eta\mu 3}}{j_0}\boldsymbol{t}_0\cdot\left(\boldsymbol{\varphi}_{0,\eta\gamma}\wedge\boldsymbol{\varphi}_{0,\mu}\right)\right].
\end{aligned} \tag{4.104}$$

The last relation is a first order approximation of the director unit vector, under Kirchhoff-Love assumption Eq. (4.13), where the symbol $\varepsilon_{\alpha\beta 3}$ is the Levi-Civita permutation tensor. Such an approximation can be used as the second and higher order terms are negligible in the linear range.

The resultant stresses Eqs. (4.26), (4.37) and (4.48) can been decomposed into membrane, shearing and bending stresses in the mid-surface convected basis, following [233],

$$\boldsymbol{n}^\alpha = n^{\alpha\beta}\boldsymbol{\varphi}_{,\beta} + q^\alpha\lambda_h\boldsymbol{t} = \left(\tilde{n}^{\alpha\beta} + \lambda^\beta_\mu\tilde{m}^{\alpha\mu}\right)\boldsymbol{\varphi}_{,\beta} + \lambda_h q^\alpha\boldsymbol{t}, \tag{4.105}$$

$$\tilde{\boldsymbol{m}}^\alpha = \tilde{m}^{\alpha\beta}\boldsymbol{\varphi}_{,\beta} + \tilde{m}^{3\alpha}\lambda_h\boldsymbol{t} \ , \text{ and} \tag{4.106}$$

$$\boldsymbol{l} = l^\alpha\boldsymbol{\varphi}_{,\alpha} + l^3\lambda_h\boldsymbol{t} = \left(\tilde{l}^\alpha + \lambda^\alpha_\mu\tilde{m}^{3\mu}\right)\boldsymbol{\varphi}_{,\alpha} + l^3\lambda_h\boldsymbol{t}. \tag{4.107}$$

Under small deformation assumption, these equations read,

$$\boldsymbol{n}^{\alpha} = n^{\alpha\beta}\boldsymbol{\varphi}_{0,\beta} + q^{\alpha}\boldsymbol{t} = \left(\tilde{n}^{\alpha\beta} + \lambda_{\mu}^{\beta}\tilde{m}^{\alpha\mu}\right)\boldsymbol{\varphi}_{0,\beta} + \lambda_h q^{\alpha}\boldsymbol{t}\,, \tag{4.108}$$

$$\tilde{\boldsymbol{m}}^{\alpha} = \tilde{m}^{\alpha\beta}\boldsymbol{\varphi}_{0,\beta} + \tilde{m}^{3\alpha}\boldsymbol{t}\ \text{, and} \tag{4.109}$$

$$\boldsymbol{l} = l^{\alpha}\boldsymbol{\varphi}_{0,\alpha} + l^{3}\boldsymbol{t} = \left(\tilde{l}^{\alpha} + \lambda_{\mu}^{\alpha}\tilde{m}^{3\mu}\right)\boldsymbol{\varphi}_{0,\alpha} + l^{3}\boldsymbol{t}\,. \tag{4.110}$$

In these expressions, $\tilde{n}^{\alpha\beta}$ is the membrane stress resultant (defined in Appendix B.3), $\tilde{m}^{\alpha\beta}$ is the stress couple resultant, l^{α} is the out-of-plane stress resultant, $\tilde{m}^{\alpha 3}$ is the out-of-plane stress couple, q^{α} is the transverse shear stress and $\lambda_{\mu}^{\beta} = \lambda_h \boldsymbol{t}_{,\mu}\cdot\boldsymbol{\varphi}^{,\beta} \approx \boldsymbol{t}_{0,\mu}\cdot\boldsymbol{\varphi}^{0,\beta}$ characterizes the curvature of the shell. Due to the symmetry of the Cauchy stress tensor and as $\lambda_{h,\alpha}$ is neglected, one has $q^{\alpha} = l^{\alpha} - \lambda_{\mu}^{\alpha}\tilde{m}^{3\mu} = \tilde{l}^{\alpha}$, see Appendix B.3 for details. Also, $\tilde{l}^{\alpha} \simeq l^{\alpha}$, as $\tilde{m}^{3\mu}$ vanishes for thin plates.

Similarly, the deformations are also decomposed into membrane ε, shearing δ and torque ρ strain components,

$$\varepsilon_{\alpha\beta} = \frac{1}{2}\boldsymbol{\varphi}_{,\alpha}\cdot\boldsymbol{\varphi}_{,\beta} - \frac{1}{2}\boldsymbol{\varphi}_{0,\alpha}\cdot\boldsymbol{\varphi}_{0,\beta} \approx \frac{1}{2}\boldsymbol{\varphi}_{0,\alpha}\cdot\boldsymbol{u}_{,\beta} + \frac{1}{2}\boldsymbol{u}_{,\alpha}\cdot\boldsymbol{\varphi}_{0,\beta}\,, \tag{4.111}$$

$$\delta_{\alpha} = \frac{\boldsymbol{u}_{,\alpha}\cdot\boldsymbol{t}_0 + \Delta\boldsymbol{t}\cdot\boldsymbol{\varphi}_{0,\alpha}}{2} \approx 0 \text{ and,} \tag{4.112}$$

$$\begin{aligned}\rho_{\alpha\beta} &= \boldsymbol{\varphi}_{,\alpha}\cdot\boldsymbol{t}_{,\beta} - \boldsymbol{\varphi}_{0,\alpha}\cdot\boldsymbol{t}_{0,\beta}\\ &\approx \boldsymbol{\varphi}_{0,\alpha\beta}\cdot\boldsymbol{t}_0\frac{\varepsilon_{\mu\eta 3}}{j_0}\boldsymbol{u}_{,\mu}\cdot\left(\boldsymbol{\varphi}_{0,\eta}\wedge\boldsymbol{t}_0\right)\\ &\quad + \frac{\varepsilon_{\mu\eta 3}}{j_0}\boldsymbol{u}_{,\mu}\cdot\left(\boldsymbol{\varphi}_{0,\alpha\beta}\wedge\boldsymbol{\varphi}_{0,\eta}\right) - \boldsymbol{u}_{,\alpha\beta}\cdot\boldsymbol{t}_0\,.\end{aligned} \tag{4.113}$$

Then, for thin bodies this law can be written in the plane-stress state by prescribing the value of ε_{33} in the mid-surface (in place of an iterative procedure on the integration points of the thickness, see Section 4.3.2),

$$\begin{aligned}\lambda_h = 1 + \varepsilon_{33} &= 1 - \frac{\nu}{1-\nu}\boldsymbol{\varphi}_0^{,\alpha}\cdot\boldsymbol{\varphi}_0^{,\beta}\left(\frac{1}{2}\boldsymbol{\varphi}_{,\alpha}\cdot\boldsymbol{\varphi}_{,\beta} - \frac{1}{2}\boldsymbol{\varphi}_{0,\alpha}\cdot\boldsymbol{\varphi}_{0,\beta}\right)\\ &\approx 1 - \frac{\nu}{2(1-\nu)}\boldsymbol{\varphi}_0^{,\alpha}\cdot\boldsymbol{\varphi}_0^{,\beta}\left(\boldsymbol{u}_{,\alpha}\cdot\boldsymbol{\varphi}_{0,\beta} + \boldsymbol{u}_{,\beta}\cdot\boldsymbol{\varphi}_{0,\alpha}\right).\end{aligned} \tag{4.114}$$

Then, using $\boldsymbol{\varepsilon} = \varepsilon_{\alpha\beta}\boldsymbol{\varphi}_0^{,\alpha}\otimes\boldsymbol{\varphi}_0^{,\beta} + \varepsilon_{33}\boldsymbol{\varphi}_0^{,\alpha}\otimes\boldsymbol{\varphi}_0^{,\beta} + \delta_{\alpha}\left[\boldsymbol{\varphi}_0^{,\alpha}\otimes\boldsymbol{t}_0 + \boldsymbol{t}_0\otimes\boldsymbol{\varphi}_0^{,\alpha}\right] + \rho_{\alpha\beta}\xi^3\boldsymbol{\varphi}_0^{,\alpha}\otimes\boldsymbol{\varphi}_0^{,\beta}$ and using $\boldsymbol{\sigma} = \mathcal{H} : \boldsymbol{\varepsilon}$ with $\mathcal{H}$ the usual Hooke tensor, the elastic constitutive relations between the effective (linearized) stresses and strains read, [233]

$$\tilde{n}^{\alpha\beta} = \mathcal{H}_n^{\alpha\beta\gamma\delta}\varepsilon_{\gamma\delta}\,, \tag{4.115}$$

$$\tilde{m}^{\alpha\beta} = \mathcal{H}_m^{\alpha\beta\gamma\delta}\rho_{\gamma\delta}\text{, and} \tag{4.116}$$

$$\tilde{l}^{\alpha} = \mathcal{H}_s^{\alpha\beta}\gamma_{\beta} \approx 0\,, \tag{4.117}$$

where $\gamma = 2\delta$ and where $\mathcal{H}_n$, $\mathcal{H}_m$ and $\mathcal{H}_s^{\alpha\beta}$ are respectively, the linearized membrane, bending and shearing stiffness given by Eqs. (4.84), (4.85) and (4.93).

4.3.2 Hyperelastic based constitutive behaviors

A hyperelastic approach can be used to link the stresses to the finite deformations. Such an approach assumes that the linear part of the material derives from an internal potential W, which depends only on the right Cauchy tensor defined by,

$$\mathbf{C} = \mathbf{F}^T\mathbf{F} = \boldsymbol{g}_i \cdot \boldsymbol{g}_j \boldsymbol{g}_0^i \otimes \boldsymbol{g}_0^j . \tag{4.118}$$

Thus, depending on the potential, the material response will be different. In this work two different potentials will be considered regarding the application (either elastic Neo-Hookean or elasto-plastic). For both laws, the Kirchhoff stress tensor $\boldsymbol{\tau} = J\boldsymbol{\sigma}$ can be related to the deformation gradient thanks to,

$$\boldsymbol{\tau} = \frac{\partial W}{\partial \mathbf{F}}\mathbf{F}^T = \mathbf{P}\mathbf{F}^T . \tag{4.119}$$

Furthermore, as plane stress state is assumed in the shell convected basis, it is convenient to formulate Eq. (4.119) in this basis,

$$\boldsymbol{\tau} = \tau^{ij}\boldsymbol{g}_i \otimes \boldsymbol{g}_j = 2\frac{\partial W}{\partial \mathrm{g}_{ij}}\boldsymbol{g}_i \otimes \boldsymbol{g}_j . \tag{4.120}$$

As $\lambda_{h,\alpha}$ is neglected, as $\boldsymbol{t}\cdot\boldsymbol{t}_{,\alpha} = 0$ ($\boldsymbol{t}\cdot\boldsymbol{t} = 1$) and as $\boldsymbol{t}\cdot\boldsymbol{\varphi}_{,\alpha}$ (Kirchhoff-Love assumption), $\boldsymbol{g}_3 \cdot \boldsymbol{g}_\alpha = 0$ with regard to the definitions (4.9-4.10). From the definition (4.118), for an isotropic behavior, this implies,

$$\tau^{\alpha 3} = \tau^{3\alpha} = 0 , \tag{4.121}$$

for elasticity as well as for J2-plasticity. Therefore the plane stress state can be ensured by enforcing only,

$$\tau^{33} = 2\frac{\partial W}{\partial \mathrm{g}_{33}} = 0 , \tag{4.122}$$

all across the shell thickness. This requirement is numerically achieved by a discretization of the thickness with 11 integration points following a Simpson integration rule. Then, the local λ_h^p stretch is determined at each point using Newton-Raphson iterations satisfying locally the plane stress requirement $\tau^{33} = 0$. Finally, the global thickness stretch λ_h is determined by the Simpson integration on the 11 local values λ_h^p. Note that formally, because of the bending effect, λ_h has a dependence along ξ^3 but we assume it constant in the previous development and equal to the value at mid-surface.

Once $\boldsymbol{\tau}$ known, the reduced stress and torque are respectively computed from (4.26) and (4.37), as $\boldsymbol{\sigma} = \frac{\boldsymbol{\tau}}{J}$ and $\boldsymbol{l} = 0$.

Neo-Hookean law

The neo-Hookean constitutive model considers an elastic response with the internal potential,

$$W = \left(\frac{K_0}{2} - \frac{\mu_0}{3}\right) \log^2 J - \mu_0 \log J + \frac{\mu_0}{2} \left(\mathrm{tr}\mathbf{C} - 3\right), \tag{4.123}$$

where K_0 and μ_0 are respectively the equivalent bulk and shear moduli of the material. Using this potential in Eq. (4.119) the Kirchhoff stress tensor reads,

$$\boldsymbol{\tau}^{ij} = \left(K_0 - \frac{2}{3}\mu_0\right) \log J \boldsymbol{g}^i \cdot \boldsymbol{g}^j - \mu_0 \left(\boldsymbol{g}^i \cdot \boldsymbol{g}^j - \boldsymbol{g}_0^i \cdot \boldsymbol{g}_0^j\right). \tag{4.124}$$

Finally, the tangent modulus in the convected basis reads,

$$\begin{aligned} \mathcal{C}^{ijkl} = & \left(K_0 - \frac{2}{3}\mu_0\right) \boldsymbol{g}^i \cdot \boldsymbol{g}^j \, \boldsymbol{g}^k \cdot \boldsymbol{g}^l - \\ & \left[\left(K_0 - \frac{2}{3}\mu_0\right) \log J - \mu_0\right] \left(\boldsymbol{g}^i \cdot \boldsymbol{g}^k \, \boldsymbol{g}^j \cdot \boldsymbol{g}^l + \boldsymbol{g}^i \cdot \boldsymbol{g}^l \, \boldsymbol{g}^j \cdot \boldsymbol{g}^k\right). \end{aligned} \tag{4.125}$$

J_2-flow elasto-plastic law

In the J_2-flow elasto-plastic model, lengthy described in [74, 76], the plastic behavior of the material is taken into account through the J_2-flow theory. In this work we restrict the model to isotropic linear hardening. The model is based on a hyperelastic formulation, which implies the assumption of a multiplicative decomposition of the deformation gradient $\mathbf{F}$ into an elastic part $\mathbf{F}^e$ and a plastic part $\mathbf{F}^p$ *i.e.* ,

$$\mathbf{F} = \mathbf{F}^e \cdot \mathbf{F}^p. \tag{4.126}$$

As W should only depend on the elastic deformation, the elastic right Cauchy strain tensor is considered in the internal energy, defined by $\mathbf{C}^e = \mathbf{F}^{eT}\mathbf{F}^e$. Using these definitions the first Piola-Kirchhoff stress tensor can be written

$$\mathbf{P} = \frac{\partial W}{\partial \mathbf{F}} = 2\mathbf{F} \cdot \left[\left(\mathbf{F}^p\right)^{-1} \frac{\partial W\left(\mathbf{C}^e\right)}{\partial \mathbf{C}^e} \left(\mathbf{F}^p\right)^{-T}\right]. \tag{4.127}$$

Thus, the internal energy depends only on the elastic Cauchy tensor and a bi-logarithmic potential, *e.g.*, reads,

$$W\left(\mathbf{C}^e\right) = \frac{K_0}{2} \log^2 J + \frac{\mu_0}{4} \left[\log \mathbf{C}^e\right]^{\mathrm{dev}} : \left[\log \mathbf{C}^e\right]^{\mathrm{dev}} \tag{4.128}$$

where K_0 and μ_0 are respectively the bulk and shear moduli of material and with $\left[\log \mathbf{C}^e\right]^{\mathrm{dev}}$ the deviatoric part of $\log \mathbf{C}^e$.

In order to obtain the elastic and plastic parts of the deformation gradient in equation (4.126), the J_2-flow theory, expressed in terms of the von Mises stress, is used herein. Toward this end, the Cauchy stress tensor is computed as,

$$\boldsymbol{\sigma} = p'\mathbf{I} + J^{-1}\mathbf{F}^e \left[2\mu_0 \mathbf{C}^{e-1} \cdot (\log\sqrt{\mathbf{C}^e})^{\mathrm{dev}}\right] \mathbf{F}^{e\mathrm{T}} \tag{4.129}$$

where $p' = (K \log J)/J$ is the pressure, and where the second term on the right hand side of equation (4.129) is the deviatoric part of the Cauchy stress, which allows computing the equivalent von Mises stress $\sigma^{\mathrm{eq}} = \sqrt{\frac{3}{2}\boldsymbol{\sigma}^{\mathrm{dev}} : \boldsymbol{\sigma}^{\mathrm{dev}}}$. According to J_2 elastic-plasticity, the von Mises stress criterion reads

$$f = \sigma^{\mathrm{eq}} - R(p) - \sigma_{\mathrm{Y}}^0 \leqslant 0\,, \tag{4.130}$$

where f is the yield surface, σ_{Y}^0 is the initial yield stress, $R(p) \geqslant 0$ is the isotropic hardening stress, and where p is an internal variable characterizing the irreversible behavior, as the equivalent plastic strain in small deformations. Practically the yield criterion can also be written in terms of the Kirchhoff tensor $\boldsymbol{\tau} = J\boldsymbol{\sigma}$. In case of $f = 0$, Equation (4.130) is completed by the normal plastic flow, which gives the increment of plastic deformation gradient between time step "n" to "$n+1$", and reads

$$\begin{cases} \mathbf{F}^p{}_{n+1} = \exp(\triangle p \mathbf{N}^p)\mathbf{F}^p{}_n \\ \mathbf{N}^p = \frac{\partial f}{\partial \boldsymbol{\sigma}} = \frac{3}{2}\frac{\boldsymbol{\sigma}^{\mathrm{dev}}}{\sigma^{\mathrm{eq}}} \end{cases} . \tag{4.131}$$

Practically, the normal of the yield surface $\mathbf{N}^p$ is calculated from the elastic predictor. Details can be found in reference [74].

4.4 Numerical properties

In this section, the numerical properties of consistency, stability and convergence rate of the full discontinuous Galerkin formulation of Kirchhoff-Love shells Eq. (4.95) are demonstrated. In particular it is proved that the suggested method has an optimal convergence rate in the energy norm as well as in the $\mathbf{L}^2$-norm. The properties of stability and convergence are proved after linearization for the bilinear form as it is usually done in the non-linear range.

4.4.1 Consistency

The proof of consistency follows from the recourse to consistent numerical fluxes in the formulation. Indeed $\boldsymbol{\varphi}$, the exact solution of the physical problem, is $\mathcal{C}^2(\mathcal{A}_h)$. Thus, the jumps of displacements and of normal unit vectors are identically equal to 0 on $\partial_I\mathcal{A}$. Nevertheless, as discontinuous shape functions have been considered, the virtual fields $[\![\delta\boldsymbol{\varphi}]\!]$ and $[\![\delta\boldsymbol{t}]\!]$ remain discontinuous. On the external boundary, following Eqs. (4.68-4.69) we have $[\![\boldsymbol{\varphi}]\!] = \bar{\boldsymbol{\varphi}} - \boldsymbol{\varphi} = 0$ on $\partial_U\mathcal{A}_h$ and $[\![\boldsymbol{t}]\!] = \bar{\boldsymbol{t}} - \boldsymbol{t} = 0$ on $\partial_T\mathcal{A}_h$. Similarly, the virtual fields read on this boundary

$[\![\delta\boldsymbol{\varphi}]\!] = -\delta\boldsymbol{\varphi} = 0$ and $[\![\delta t]\!] = -\delta t = 0$. Furthermore, the resultant stress $\boldsymbol{n}^\alpha$ and torque $\tilde{\boldsymbol{m}}^\alpha$ vectors, as well as the thickness ratio λ_h of the exact solution are continuous across inter-element boundaries, which allows rewriting the weak form[7] (4.95) as,

$$\begin{aligned}
&\int_{\mathcal{A}_h} \overline{\rho}\ddot{\boldsymbol{\varphi}}\cdot\delta\boldsymbol{\varphi}\, d\mathcal{A} + \int_{\mathcal{A}_h} \overline{j}\boldsymbol{n}^\alpha\cdot\delta\boldsymbol{\varphi}_{,\alpha}\, d\mathcal{A} + \int_{\mathcal{A}_h} \overline{j}\tilde{\boldsymbol{m}}^\alpha\cdot(\delta t\lambda_h)_{,\alpha}\, d\mathcal{A} + \int_{\mathcal{A}_h} \overline{j}\boldsymbol{l}\cdot\delta t\lambda_h d\mathcal{A} + \\
&\int_{\partial_I\mathcal{A}_h\cup\partial_U\mathcal{A}_h} [\![\delta\boldsymbol{\varphi}]\!]\cdot\overline{j}\boldsymbol{n}^\alpha\nu_\alpha^- d\partial\mathcal{A} + \int_{\partial_I\mathcal{A}_h\cup\partial_T\mathcal{A}_h} [\![\delta t]\!]\cdot\overline{j}\lambda_h\tilde{\boldsymbol{m}}^\alpha\nu_\alpha^- d\partial\mathcal{A} = \\
&\int_{\partial_N\mathcal{A}_h} \overline{j}\overline{\boldsymbol{n}}\cdot\delta\boldsymbol{\varphi} d\mathcal{A} + \int_{\partial_M\mathcal{A}_h} \overline{j}\overline{\tilde{\boldsymbol{m}}}\cdot\delta t\lambda_h d\mathcal{A} + \int_{\mathcal{A}_h} \boldsymbol{n}^{\mathcal{A}}\cdot\delta\boldsymbol{\varphi}\overline{j} d\mathcal{A} + \int_{\mathcal{A}_h} \tilde{\boldsymbol{m}}^{\mathcal{A}}\cdot\delta t\lambda_h\overline{j} d\mathcal{A}\,.
\end{aligned} \tag{4.132}$$

After integration by parts, on each element $\mathcal{A}_e$, of the terms in $\boldsymbol{n}^\alpha$ and $\tilde{\boldsymbol{m}}^\alpha$, this expression reads,

$$\begin{aligned}
&\int_{\mathcal{A}_h} \overline{\rho}\ddot{\boldsymbol{\varphi}}\cdot\delta\boldsymbol{\varphi} d\mathcal{A} + \int_{\partial_N\mathcal{A}_h} \overline{j}\boldsymbol{n}^\alpha\cdot\delta\boldsymbol{\varphi}\nu_\alpha d\partial\mathcal{A} - \int_{\partial_I\mathcal{A}_h\cup\partial_U\mathcal{A}_h} \overline{j}\boldsymbol{n}^\alpha\cdot[\![\delta\boldsymbol{\varphi}]\!]\nu_\alpha^- d\partial\mathcal{A} - \\
&\int_{\mathcal{A}_h} (\overline{j}\boldsymbol{n}^\alpha)_{,\alpha}\cdot\delta\boldsymbol{\varphi} d\mathcal{A} + \int_{\partial_M\mathcal{A}_h} \overline{j}\tilde{\boldsymbol{m}}^\alpha\cdot\delta t\lambda_h\nu_\alpha d\partial\mathcal{A} - \int_{\partial_I\mathcal{A}_h\cup\partial_T\mathcal{A}_h} \overline{j}\tilde{\boldsymbol{m}}^\alpha\cdot[\![\delta t]\!]\lambda_h\nu_\alpha^- d\partial\mathcal{A} - \\
&\int_{\mathcal{A}_h} (\overline{j}\tilde{\boldsymbol{m}}^\alpha)_{,\alpha}\cdot\delta t\lambda_h d\mathcal{A} + \int_{\mathcal{A}_h} \overline{j}\boldsymbol{l}\cdot\delta t\lambda_h d\mathcal{A} + \int_{\partial_I\mathcal{A}_h\cup\partial_U\mathcal{A}_h} [\![\delta\boldsymbol{\varphi}]\!]\cdot\overline{j}\boldsymbol{n}^\alpha\nu_\alpha^- d\partial\mathcal{A} + \\
&\int_{\partial_I\mathcal{A}_h\cup\partial_T\mathcal{A}_h} [\![\delta t]\!]\cdot\overline{j}\lambda_h\tilde{\boldsymbol{m}}^\alpha\nu_\alpha^- d\partial\mathcal{A} = \int_{\partial_N\mathcal{A}_h} \overline{j}\overline{\boldsymbol{n}}\cdot\delta\boldsymbol{\varphi} d\mathcal{A} + \int_{\partial_M\mathcal{A}_h} \overline{j}\overline{\tilde{\boldsymbol{m}}}\cdot\delta t\lambda_h d\mathcal{A} + \\
&\qquad\qquad \int_{\mathcal{A}_h} \boldsymbol{n}^{\mathcal{A}}\cdot\delta\boldsymbol{\varphi}\overline{j} d\mathcal{A} + \int_{\mathcal{A}_h} \tilde{\boldsymbol{m}}^{\mathcal{A}}\cdot\delta t\lambda_h\overline{j} d\mathcal{A}\,.
\end{aligned} \tag{4.133}$$

The arbitrary nature of the virtual fields $\delta\boldsymbol{\varphi}$ and δt reduces the weak form to the set of equations

$$(\overline{j}\boldsymbol{n}^\alpha)_{,\alpha} + \overline{j}\boldsymbol{n}^{\mathcal{A}} = \overline{\rho}\ddot{\boldsymbol{\varphi}} \quad \text{in} \quad \mathcal{A}_h\,, \tag{4.134}$$

$$(\overline{j}\tilde{\boldsymbol{m}}^\alpha)_{,\alpha} - \overline{j}\boldsymbol{l} + \overline{j}\tilde{\boldsymbol{m}}^{\mathcal{A}} = \lambda_1\boldsymbol{t} \quad \text{in} \quad \mathcal{A}_h\,, \tag{4.135}$$

$$\overline{\tilde{\boldsymbol{m}}} = \boldsymbol{m}^\alpha\nu_\alpha + \lambda_2\boldsymbol{t} \quad \text{on} \quad \partial_M\mathcal{A}_h\,, \tag{4.136}$$

$$\overline{\boldsymbol{n}} = \boldsymbol{n}^\alpha\nu_\alpha \quad \text{on} \quad \partial_N\mathcal{A}_h\,, \tag{4.137}$$

which correspond respectively to the governing equations (4.30), (4.50), (4.53) and (4.54), up to undefined values λ_i. Consistency of the weak formulation (4.95) is thus ensured in the non-linear range.

Derivation of the numerical properties of stability and convergence rate requires a linearization of the equations that we present here below. In fact, it is usual done for FE, to postulate that if the linear form is stable its non-linear extension is stable too, although this is not always true.

[7] For completeness we do not neglect $a_s(\boldsymbol{\varphi}_h, \delta\boldsymbol{\varphi})$ in this form although $\boldsymbol{l} \approx 0$

4.4.2 Linearization of the weak form

The linearization of the weak form (4.95) is performed under the assumption of a small displacements field and with Hooke constitutive behavior assumption (see Section 4.3.1). Thus, the displacements field is expressed by Eq. (4.101) and the first order approximation of the unit normal Eq. (4.102) is considered. Furthermore, using the linear forms of the membrane (4.115) and bending (4.116) stresses and the definition $\lambda_\mu^\alpha = \lambda_h \boldsymbol{t}_{,\mu} \cdot \boldsymbol{\varphi}^{,\alpha}$ implying for small displacements $\lambda_\mu^\alpha \cdot \boldsymbol{\varphi}_{0,\alpha} = \boldsymbol{t}_{0,\mu}$, the first order approximations of the terms of Eq. (4.95) read,

$$a_{ld}^e(\boldsymbol{u}_h, \delta\boldsymbol{u}) = \int_{\mathcal{A}_e} \overline{\rho}\ddot{\boldsymbol{u}}_h \cdot \delta\boldsymbol{u} d\mathcal{A}\,, \tag{4.138}$$

$$\begin{aligned} a_{ln}^e(\boldsymbol{u}_h, \delta\boldsymbol{u}) &= \int_{\mathcal{A}_e} \bar{j}_0 \frac{1}{4} \left(\boldsymbol{\varphi}_{0,\gamma} \cdot \boldsymbol{u}_{h,\delta} + \boldsymbol{\varphi}_{0,\delta} \cdot \boldsymbol{u}_{h,\gamma}\right) \mathcal{H}_n^{\alpha\beta\gamma\delta} \left(\boldsymbol{\varphi}_{0,\beta} \delta\boldsymbol{u}_{,\alpha} + \boldsymbol{\varphi}_{0,\alpha} \delta\boldsymbol{u}_{,\beta}\right) d\mathcal{A} \\ &\quad + \int_{\mathcal{A}_e} \bar{j}_0 \left(\boldsymbol{u}_{h,\gamma} \cdot \boldsymbol{t}_{0,\delta} + \boldsymbol{\varphi}_{0,\gamma} \cdot \boldsymbol{\Delta t}_{,\delta}\right) \mathcal{H}_m^{\alpha\beta\gamma\delta} \boldsymbol{t}_{0,\beta} \cdot \delta\boldsymbol{u}_{,\alpha} d\mathcal{A}\,, \end{aligned} \tag{4.139}$$

$$a_{lm}^e(\boldsymbol{u}_h, \delta\boldsymbol{u}) = \int_{\mathcal{A}_e} \bar{j}_0 \left(\boldsymbol{u}_{h,\gamma} \cdot \boldsymbol{t}_{0,\delta} + \boldsymbol{\varphi}_{0,\gamma} \cdot \boldsymbol{\Delta t}_{,\delta}\right) \mathcal{H}_m^{\alpha\beta\gamma\delta} \boldsymbol{\varphi}_{0,\beta} \cdot \delta\boldsymbol{\Delta t}_{,\alpha} d\mathcal{A}\,, \tag{4.140}$$

$$\begin{aligned} a_{lnI1}^s(\boldsymbol{u}_h, \delta\boldsymbol{u}) &= \int_s \frac{1}{2} \Big\langle \bar{j}_0 \mathcal{H}_n^{\alpha\beta\gamma\delta} \left(\boldsymbol{\varphi}_{0,\gamma} \cdot \boldsymbol{u}_{h,\delta} + \boldsymbol{\varphi}_{0,\delta} \cdot \boldsymbol{u}_{h,\gamma}\right) \\ &\quad + \lambda_\mu^\beta \bar{j}_0 \mathcal{H}_m^{\alpha\mu\gamma\delta} \left(\boldsymbol{\varphi}_{0,\gamma} \cdot \Delta\boldsymbol{t}_{,\delta} + \boldsymbol{u}_{h,\gamma} \cdot \boldsymbol{t}_{0,\delta}\right) \Big\rangle \boldsymbol{\varphi}_{0,\beta} \cdot [\![\delta\boldsymbol{u}]\!] \nu_\alpha^- d\partial\mathcal{A}_e\,, \end{aligned} \tag{4.141}$$

$$a_{lmI1}^s(\boldsymbol{u}_h, \delta\boldsymbol{u}) = \int_s [\![\delta\boldsymbol{\Delta t}]\!] \cdot \left\langle \bar{j}_0 \mathcal{H}_m^{\alpha\beta\gamma\delta} \left(\boldsymbol{u}_{h,\gamma} \cdot \boldsymbol{t}_{0,\delta} + \boldsymbol{\varphi}_{0,\gamma} \cdot \boldsymbol{\Delta t}_{,\delta}\right) \boldsymbol{\varphi}_{0,\beta} \right\rangle \nu_\alpha^- d\partial\mathcal{A}_e\,, \tag{4.142}$$

$$\begin{aligned} a_{lnI2}^s(\boldsymbol{u}_h, \delta\boldsymbol{u}) &= \int_s [\![\boldsymbol{u}_h]\!] \cdot \Big\langle \bar{j}_0 \boldsymbol{\varphi}_{0,\beta} \Big[\frac{1}{2} \mathcal{H}_n^{\alpha\beta\gamma\delta} \left(\delta\boldsymbol{u}_{,\gamma} \cdot \boldsymbol{\varphi}_{0,\delta} + \boldsymbol{\varphi}_{0,\gamma} \cdot \delta\boldsymbol{u}_{,\delta}\right) \\ &\quad + \lambda_\mu^\beta \mathcal{H}_m^{\alpha\mu\gamma\delta} \left(\delta\boldsymbol{u}_{,\gamma} \cdot \boldsymbol{t}_{0,\delta} + \boldsymbol{\varphi}_{0,\gamma} \cdot \delta\Delta\boldsymbol{t}_{,\delta}\right) \Big] \Big\rangle \nu_\alpha^- d\partial\mathcal{A}_e\,, \end{aligned} \tag{4.143}$$

$$a_{lmI2}^s(\boldsymbol{u}_h, \delta\boldsymbol{u}) = \int_s [\![\boldsymbol{\Delta t}]\!] \cdot \left\langle \bar{j}_0 \boldsymbol{\varphi}_{0,\beta} \mathcal{H}_m^{\alpha\beta\gamma\delta} \left(\delta\boldsymbol{u}_{,\gamma} \cdot \boldsymbol{t}_{0,\delta} + \boldsymbol{\varphi}_{0,\gamma} \cdot \delta\boldsymbol{\Delta t}_{,\delta}\right) \right\rangle \nu_\alpha^- d\partial\mathcal{A}_e\,, \tag{4.144}$$

$$a_{lnI3}^s(\boldsymbol{u}_h, \delta\boldsymbol{u}) = \int_s [\![\boldsymbol{u}_h]\!] \cdot \boldsymbol{\varphi}_{0,\gamma} \nu_\delta^- \left\langle \frac{\beta_2 \mathcal{H}_n^{\alpha\beta\gamma\delta} \bar{j}_0}{h^s} \right\rangle [\![\delta\boldsymbol{u}]\!] \cdot \boldsymbol{\varphi}_{0,\beta} \nu_\alpha^- d\partial\mathcal{A}_e\,, \tag{4.145}$$

$$a_{lmI3}^s(\boldsymbol{u}_h, \delta\boldsymbol{u}) = \int_s [\![\boldsymbol{\Delta t}]\!] \cdot \boldsymbol{\varphi}_{0,\beta} \left\langle \frac{\beta_1 \bar{j}_0 \mathcal{H}_m^{\alpha\beta\gamma\delta}}{h^s} \right\rangle [\![\delta\boldsymbol{\Delta t}]\!] \cdot \boldsymbol{\varphi}_{0,\gamma} \nu_\alpha^- \nu_\delta^- d\partial\mathcal{A}_e\,, \tag{4.146}$$

$$a_{lsI3}^s(\boldsymbol{u}_h, \delta\boldsymbol{u}) = \int_s [\![\boldsymbol{u}_h]\!] \cdot \boldsymbol{t}_0 \nu_\beta^- \left\langle \frac{\beta_3 \mathcal{H}_q^{\alpha\beta} \bar{j}_0}{h^s} \right\rangle [\![\delta\boldsymbol{u}]\!] \cdot \boldsymbol{t}_0 \nu_\alpha^- d\partial\mathcal{A}_e\,. \tag{4.147}$$

In the stability expressions (4.145-4.147), the effect of curvature λ_μ^β has been neglected without compromising the stability as earlier presented and the expression of $a_{lsI3}^s(\boldsymbol{u}_h, \delta\boldsymbol{u})$ is obtained as presented in Appendix B.2. These developments allow writing the weak form (4.95)

as finding $\boldsymbol{u}_h$ such that,

$$\sum_e a^e_{ld}(\boldsymbol{u}_h,\delta\boldsymbol{u})+\sum_e a^e_{ln}(\boldsymbol{u}_h,\delta\boldsymbol{u})+\sum_e a^e_{lm}(\boldsymbol{u}_h,\delta\boldsymbol{u})+\sum_s a^s_{lnI}(\boldsymbol{u}_h,\delta\boldsymbol{u})$$
$$+\sum_s a^s_{lmI}(\boldsymbol{u}_h,\delta\boldsymbol{u})+\sum_s a^s_{lsI}(\boldsymbol{u}_h,\delta\boldsymbol{u})=b_{\text{ext}}(\delta\boldsymbol{u})+b_{\text{bound}}(\delta\boldsymbol{u})\,, \tag{4.148}$$

for all $\delta\boldsymbol{u}$ kinematically admissible and with the bilinear forms,

$$a^s_{lnI}(\boldsymbol{u}_h,\delta\boldsymbol{u}) = a^s_{lnI1}(\boldsymbol{u}_h,\delta\boldsymbol{u})+a^s_{lnI2}(\boldsymbol{u}_h,\delta\boldsymbol{u})+a^s_{lnI3}(\boldsymbol{u}_h,\delta\boldsymbol{u})\,, \tag{4.149}$$
$$a^s_{lmI}(\boldsymbol{u}_h,\delta\boldsymbol{u}) = a^s_{lmI1}(\boldsymbol{u}_h,\delta\boldsymbol{u})+a^s_{lmI2}(\boldsymbol{u}_h,\delta\boldsymbol{u})+a^s_{lmI3}(\boldsymbol{u}_h,\delta\boldsymbol{u})\,, \tag{4.150}$$
$$a^s_{lsI}(\boldsymbol{u}_h,\delta\boldsymbol{u}) = a^s_{lsI3}(\boldsymbol{u}_h,\delta\boldsymbol{u})\,, \tag{4.151}$$

and where it has been accounted for that $b_{\text{ext}}(\delta\boldsymbol{u})$ and $b_{\text{bound}}(\delta\boldsymbol{u})$ become linear forms at the first order ($\lambda_h\approx 1$).

Finally, as the consistency of the formulation is proved, it implies that the exact solution $\boldsymbol{u}$ satisfies (4.148), which provides the orthogonality relation,

$$a_l(\boldsymbol{u}_h-\boldsymbol{u},\delta\boldsymbol{u})=a_l(\boldsymbol{u}_h,\delta\boldsymbol{u})-a_l(\boldsymbol{u},\delta\boldsymbol{u}) = 0\,. \tag{4.152}$$

where $\boldsymbol{u}_h$ is the FE solution.

4.4.3 Stability

The stability of the weak form (4.148) is established following the same argumentation as for Euler-Bernoulli beams. For simplicity, the prescribed displacement $\bar{\boldsymbol{u}}$ and direction $\bar{\boldsymbol{\Delta t}}$ are taken to be 0 and that there is no inertial forces. Thus the following energetic norm can be suggested,

$$\begin{aligned}
|||\boldsymbol{u}|||^2 = &\sum_e \left\| \sqrt{\mathcal{H}_n \bar{j}_0}^{\alpha\beta} \frac{1}{2}\left(\boldsymbol{\varphi}_{0,\alpha}\cdot\boldsymbol{u}_{,\beta}+\boldsymbol{u}_{,\alpha}\cdot\boldsymbol{\varphi}_{0,\beta}\right)\right\|^2_{\mathrm{L}^2(\mathcal{A}_e)} + \\
&\sum_e \left\| \sqrt{\mathcal{H}_m \bar{j}_0}^{\alpha\beta} \left(\boldsymbol{\varphi}_{0,\alpha}\cdot\boldsymbol{\Delta t}_{,\beta}+\boldsymbol{u}_{,\alpha}\cdot\boldsymbol{t}_{0,\beta}\right)\right\|^2_{\mathrm{L}^2(\mathcal{A}_e)} + \\
&\sum_s \left\| \sqrt{\frac{\beta_1\mathcal{H}_m \bar{j}_0}{h_s}}^{\alpha\beta} \boldsymbol{\varphi}_{0,\alpha}\cdot[\![\boldsymbol{\Delta t}]\!]\,\nu^-_\beta\right\|^2_{\mathrm{L}^2(s)} + \\
&\sum_s \left\| \sqrt{\frac{\beta_2\mathcal{H}_n \bar{j}_0}{h_s}}^{\alpha\beta} \boldsymbol{\varphi}_{0,\alpha}\cdot[\![\boldsymbol{u}]\!]\,\nu^-_\beta\right\|^2_{\mathrm{L}^2(s)} + \\
&\sum_s \left\| \sqrt{\frac{\beta_3\mathcal{H}_s \bar{j}_0}{h_s}}^{\beta} \boldsymbol{t}_0\cdot[\![\boldsymbol{u}]\!]\,\nu^-_\beta\right\|^2_{\mathrm{L}^2(s)}\,,
\end{aligned} \tag{4.153}$$

with the abuses of notation,

$$\left\| \sqrt{\mathcal{H}}^{\alpha\beta} a_{\alpha\beta} \right\|^2_{\mathrm{L}^2(\mathcal{A}_e)} = \int_{\mathcal{A}_e} a_{\alpha\beta} \mathcal{H}^{\alpha\beta\gamma\delta} a_{\gamma\delta} d\mathcal{A} \text{ and,} \tag{4.154}$$

$$\sum_s \left\| \sqrt{\mathcal{H}}^{\alpha\beta} [\![a_\alpha]\!] \nu^-_\beta \right\|^2_{\mathrm{L}^2(s)} = \sum_e \frac{1}{2} \int_{\partial\mathcal{A}_e} \mathcal{H}^{\alpha\beta\gamma\delta} [\![a_\alpha]\!] \nu^-_\beta \ [\![a_\gamma]\!] \ \nu^-_\delta \, d\partial\mathcal{A}_e \,. \tag{4.155}$$

In Eq. (4.155), integration on all sides s is equivalent to one half of the integration on all the element boundaries. Indeed, the sum on all the element boundaries accounts twice for a side s[8].

Expression (4.153) is a norm, *i.e.* its value is equal to zero only for $\boldsymbol{u} = 0$ on $\mathcal{A}_h$. Indeed, if $|||\boldsymbol{u}|||$ is equal to zero, then all the contributions are also equal to zero but, if this is the case, the only solution is $\boldsymbol{u} = 0$ on $\mathcal{A}_h$, as it is shown in the following lines. If the membrane energy (first term of Eq. (4.153)) is equal to zero, then the solution of the problem is $\boldsymbol{u}_{,\alpha}$ parallel to $\boldsymbol{t}_0$ on every $\mathcal{A}_e$. If the bending term (second term of Eq. (4.153)) is equal to zero, it means that $\rho_{\alpha\beta} = 0$ on $\mathcal{A}_e$. Using Eq. (4.113), and since $\boldsymbol{u}_{,\alpha}$ is parallel to $\boldsymbol{t}_0$, the solution $\rho_{\alpha\beta} = 0$ implies $C = \boldsymbol{u}_{,\alpha} \cdot \boldsymbol{t}_0$ is constant on each $\mathcal{A}_e$. Since the jump in the variation $\boldsymbol{\Delta t}$ ($\boldsymbol{\Delta t}$ depends on $\boldsymbol{u}_{,\alpha}$ see Eq. (4.103)) is equal to zero between two elements (third term of Eq. (4.153) equal to zero), this product is constant on the whole domain, as $\boldsymbol{\Delta t}$ cannot be perpendicular to $\boldsymbol{\varphi}_{0,\alpha}$ by definition (see [185]). So the solution of the problem would be $\boldsymbol{u}_{,\alpha} \cdot \boldsymbol{t}_0 = 0$ on the whole domain as $\boldsymbol{\Delta t} = 0$ on $\partial_T \mathcal{A}_h$. As $\boldsymbol{u}_{,\alpha} \cdot \boldsymbol{t}_0 = 0$ everywhere and as $\boldsymbol{u}$ is continuous on U_h this means $\boldsymbol{u}$ is constant on $\mathcal{A}_h$. Because of the constrained displacement $\overline{\boldsymbol{u}} = 0$, the only remaining solution is $\boldsymbol{u} = 0$ on $\mathcal{A}_h$.

With the aim of demonstrating the stability of the method an upper and a lower bound of the bi-linear form (4.148) are given. These bounds can be obtained as in [185] with the addition of the supplementary interface terms related to the full-DG formulation. After some developments given in Appendix B.4, an upper bound of the bilinear form is,

$$|a_l(\boldsymbol{u}_h, \delta\boldsymbol{u})|^2 \leq C^k(\beta_\alpha) \, |||\boldsymbol{u}|||^2 \, |||\delta\boldsymbol{u}|||^2 \,, \tag{4.156}$$

for all $\boldsymbol{u}$ and $\delta\boldsymbol{u}$ satisfying the essential boundary conditions and where $C^k(\beta_\alpha)$ is a value larger than $\max(4, (C'^k_\alpha)^2/\beta_\alpha)$, where $C'^k_\alpha > 0$ are constants depending only on the polynomial degree k of $\boldsymbol{u}$ and $\delta\boldsymbol{u}$. In case of the FE approximation $\boldsymbol{u}_h$ is considered, then k is the degree of the polynomial approximation.

[8] Except on the domain boundary $\partial_T \mathcal{A}_h \cup \partial_U \mathcal{A}_h$, where the correction is omitted here for clarity.

Furthermore, a lower bound of the bi-linear form can be written as,

$$
\begin{aligned}
a(\boldsymbol{u},\boldsymbol{u}) \;\geq\; & (1-\varepsilon_n)\sum_e \left\| \sqrt{\mathcal{H}_n \bar{j}_0}^{\alpha\beta} \frac{1}{2}\left(\boldsymbol{\varphi}_{0,\alpha}\cdot\boldsymbol{u}_{,\beta}+\boldsymbol{u}_{,\alpha}\cdot\boldsymbol{\varphi}_{0,\beta}\right)\right\|^2_{\mathrm{L}^2(\mathcal{A}_e)} + \\
& (1-\varepsilon_m)\sum_e \left\| \sqrt{\mathcal{H}_m \bar{j}_0}^{\alpha\beta} \left(\boldsymbol{\varphi}_{0,\alpha}\cdot\boldsymbol{\Delta t}_{,\beta}+\boldsymbol{u}_{,\alpha}\cdot\boldsymbol{t}_{0,\beta}\right)\right\|^2_{\mathrm{L}^2(\mathcal{A}_e)} + \\
& \left(1-2\frac{C_n^{k\,2}}{\varepsilon_n\beta_2}\right)\sum_e \left\| \sqrt{\frac{\beta_2\mathcal{H}_n\bar{j}_0}{2h^s}}^{\gamma\delta} \boldsymbol{\varphi}_{0,\gamma}\cdot[\![\boldsymbol{u}]\!]\,\nu^-_\delta\right\|^2_{\mathrm{L}^2(\partial\mathcal{A}_e)} + \\
& \left(1-2\frac{C_m^{k\,2}}{\varepsilon_m\beta_1}\right)\sum_e \left\| \sqrt{\frac{\beta_1\mathcal{H}_m\bar{j}_0}{2h^s}}^{\gamma\delta} \boldsymbol{\varphi}_{0,\gamma}\cdot[\![\boldsymbol{\Delta t}(\boldsymbol{u})]\!]\,\nu^-_\delta\right\|^2_{\mathrm{L}^2(\partial\mathcal{A}_e)} + \\
& \sum_e \left\| \sqrt{\frac{\beta_3\mathcal{H}_s\bar{j}_0}{2h^s}}^{\gamma} \boldsymbol{t}_0\cdot[\![\boldsymbol{u}]\!]\,\nu^-_\gamma\right\|^2_{\mathrm{L}^2(\partial\mathcal{A}_e)}, \qquad (4.157)
\end{aligned}
$$

for all $\boldsymbol{u}$ satisfying the boundary conditions and where ε_n and ε_m are constants larger than zero coming from the so-called ε-inequality[9].

The stability of the method can be proved directly from this last relation. Indeed the comparison of the right hand terms of (4.153) and (4.157) leads to,

$$
b(\boldsymbol{u}_h) = a(\boldsymbol{u}_h,\boldsymbol{u}_h) \;\geq\; C(\beta_\alpha)\,|||\boldsymbol{u}_h|||^2\,, \qquad (4.158)
$$

where $C(\beta_\alpha)>0$ as for given $0<\varepsilon_n<1$ and $0<\varepsilon_m<1$ there always exist $\beta_1 > \frac{2(C_n^k)^2}{\varepsilon_n}$ and $\beta_2 > \frac{2(C_m^k)^2}{\varepsilon_m}$. This shows that the stability of the method is conditioned by the constant β_1 and β_2 which must be large enough as the energy norm is bounded by the work of the external forces. Note that Eq. (4.158) does not imply stability conditions on the parameter β_3 as long as $\beta_3>0$.

4.4.4 Convergence rate in the energy norm

The convergence rate in the energy norm of the bilinear form (4.148) can be demonstrated in the same way as presented in Appendix B.4 and only the main results are reported herein. In the following, the error between the FE solution $\boldsymbol{u}_h$ and the polynomial interpolation $\boldsymbol{u}^k$of the exact solution is calculated to establish the convergence rate in the energy norm of the method. First some definitions and hypotheses are given. If $\boldsymbol{u}$ is the exact solution of the problem and satisfies the essential boundary conditions, its interpolant $\boldsymbol{u}^k$, satisfying also the essential boundary conditions, is defined by,

$$
\int_{\mathcal{A}_h}\left(\boldsymbol{u}-\boldsymbol{u}^k\right)\cdot\delta\boldsymbol{u}\,\bar{j}_0\,d\mathcal{A} = 0\,. \qquad (4.159)
$$

[9] $\forall\varepsilon>0 : |ab| \leq \frac{\varepsilon}{2}a^2+\frac{1}{2\varepsilon}b^2$ or $\forall\varepsilon>0 : |ab|\leq \varepsilon a^2+\frac{1}{4\varepsilon}b^2$

The error is defined as,

$$\boldsymbol{e} = \boldsymbol{u}_h - \boldsymbol{u}\,, \tag{4.160}$$

whereas the error on the exact solution interpolant is defined as,

$$\boldsymbol{e}^k = \boldsymbol{u}_h - \boldsymbol{u}^k\,. \tag{4.161}$$

Both errors satisfy the essential boundary conditions. After some developments presented in Appendix B.4 and written for Euler-Bernoulli beams in Appendix A.3, it can be found that,

$$\left|\left|\left|\boldsymbol{e}^k\right|\right|\right| \;\leq\; C(\beta_1,\beta_2,\beta_3)\sum_e h^{s\,k-1}\,|\boldsymbol{u}|_{\mathbf{H}^{k+1}(l_e)}\,. \tag{4.162}$$

The order of convergence is one order lower than the degree of the polynomial approximation, which is consistent with the presence of high-order derivatives in the governing equations (4.50).

4.4.5 Convergence rate in the $\mathbf{L}^2$-norm

The convergence rate in the $\mathbf{L}^2$-norm of the solution of the bilinear form (4.148) is demonstrated under the two assumptions:

1. Proper elliptic regularity of the problem;
2. Pure Dirichlet boundary conditions (*i.e.* $\overline{\boldsymbol{u}} = \overline{\boldsymbol{t}} = 0$ on $\partial\mathcal{A}_h$).

As well as the convergence rate in the energy norm, the demonstration of the convergence in the $\mathbf{L}^2$-norm is performed in Appendix B.4, so only the final result is reported here,

$$||\boldsymbol{e}||_{\mathbf{L}^2(l_e)} \;\leq\; \begin{cases} \sum_e Ch^{s\,k+1}\,|\boldsymbol{u}|_{\mathbf{H}^{k+1}(l_e)} \text{ if } k>2 \\ \sum_e Ch^{s2}\,|\boldsymbol{u}|_{\mathbf{H}^{3}(l_e)} \text{ if } k=2 \end{cases}\,, \tag{4.163}$$

where the case $k=2$ is obtained by following the work of G. Wells *et al.* [257]. The relation (4.163) demonstrates that the method has an optimal convergence rate for at least cubic elements.

4.5 Implementation

This section discusses the implementation of the formulations (4.95) and (4.148). The structure discretization (mesh) is performed via Gmsh [105], which is a 3D finite element grid generator with a build-in CAD engine and post-processor. Its design goal is to provide a fast, light and user-friendly meshing tool with parametric input and advanced visualization capabilities. As Gmsh possesses also utility tools (solver, mathematics, geometry ...) we

decided to use it as a base for a C++ library. Furthermore, Gmsh is a open source software that is used industrially (Cenaero, EDF,...) for pre-post operations.

Furthermore, Gmsh has the particularity to create the dofs through a dof manager making these ones independent of the nodes. We exploit this particularity to allow importing a conventional mesh without interface element. Then from this mesh the interface elements are created before the association of dofs to each elements individually which thus do not share dofs each others.

Then, we separate the implementation in two parts. On one hand, a non-linear solver library is implemented, which uses all C++ classes defined in Gmsh to describe the geometry and the mesh, facilitating the management of the mesh and the post processing, as all results are stored directly via Gmsh. As we focus on various research projects, this non-linear library performs only the basic tools, with parallel feature: material library, integration point manager, Newton-Raphson iterations and explicit resolution schemes ... As part of this thesis we developed this parallel feature.

On the other hand, the specific feature of the dg-shell approach as functional spaces, management of elements, integration of material laws... are implemented in a separate project which includes the non-linear solver library and communicates with the solver mainly through an interface class called *partDomain* which is common to all projects. The *partDomain* class is purely virtual and has to be derived by the conceptor of the project. By this approach, different projects can use the same tools while being developed in (almost) independent codes, allowing research in different fields to be performed simultaneously. Both parts are developed in the following.

4.5.1 Dg-shell project

We describe in this section the implementation of the internal force vector and stiffness matrix which are specific to our formulation and which are therefore implemented in a separate projects. Their implementation is a generalization of the Euler-Bernoulli full Discontinuous Galerkin formulation presented in Section 3.2.3. Furthermore, the linear Eq. (4.148) as well as the non-linear Eq. (4.95) are implemented separately. For the first one the stiffness matrix can be obtained analytically. On the contrary, for the non-linear case, an analytical tangent stiffness matrix is not obvious since the iterative procedure ensuring the plane stress state (see Section 4.3.2). Therefore in this case the tangent stiffness matrix will be evaluated numerically by differentiation of the internal forces vector. This one can be divided into two parts: the bulk terms and the interface terms leading to $\boldsymbol{F}_{int} = \boldsymbol{F}_{bulk} + \boldsymbol{F}_{inter}$. The implementation of both $\boldsymbol{F}_{bulk}$ and $\boldsymbol{F}_{inter}$ is discussed below.

Bulk internal forces vector

The bulk terms are computed in the reference frame $\boldsymbol{E}_\alpha$ where the shell is represented by an isoparametric element with coordinates $(\xi^1, \xi^2) \in [-1,1] \times [-1,1]$ as depicted on Fig. 4.3(a). Then the unknown field $\boldsymbol{\varphi}_h$, as well as the virtual field $\delta\boldsymbol{\varphi}$, are decomposed in terms of

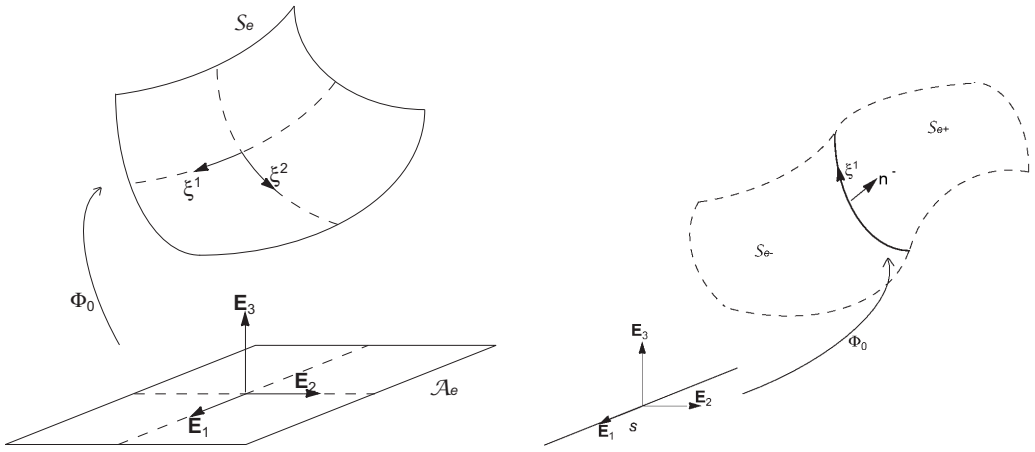

(a) Isoparametric element.

(b) Integration of the interface term on the side s common to element $\mathcal{A}_e^-$ and $\mathcal{A}_e^+$.

Figure 4.3: The numerical integration is performed (a) on to the isoparametric element for bulk terms and (b) with the convention of picture for interface integration. Courtesy of [185].

the nodal displacements using traditional Lagrangian shape functions,

$$\boldsymbol{\varphi}_h = N^{\boldsymbol{\xi}}\boldsymbol{\varphi}^{\boldsymbol{\xi}} \text{ and,} \tag{4.164}$$

$$\delta\boldsymbol{\varphi} = N^{\boldsymbol{\xi}}\delta\boldsymbol{\varphi}^{\boldsymbol{\xi}}. \tag{4.165}$$

Then, the coordinates in the reference basis $\boldsymbol{x}$ are used to compute the convected basis of the mid-surface and its derivative as,

$$\boldsymbol{\varphi}_{h,\alpha} = \frac{\partial N^{\boldsymbol{\xi}}}{\partial\xi^\alpha}\boldsymbol{x}^{\boldsymbol{\xi}} \text{ and,} \tag{4.166}$$

$$\boldsymbol{\varphi}_{h,\alpha\beta} = \frac{\partial^2 N^{\boldsymbol{\xi}}}{\partial\xi^\alpha\partial\xi^\beta}\boldsymbol{x}^{\boldsymbol{\xi}}. \tag{4.167}$$

From these definitions, the computation of the initial convected basis of the mid-surface is straightforwardly obtained using the initial position $\boldsymbol{X}^{\boldsymbol{\xi}}$ in the reference frame,

$$\boldsymbol{\varphi}_{0,\alpha} = \frac{\partial N^{\boldsymbol{\xi}}}{\partial\xi^\alpha}\boldsymbol{X}^{\boldsymbol{\xi}} \text{ and,} \tag{4.168}$$

$$\boldsymbol{\varphi}_{0,\alpha\beta} = \frac{\partial^2 N^{\boldsymbol{\xi}}}{\partial\xi^\alpha\partial\xi^\beta}\boldsymbol{X}^{\boldsymbol{\xi}}. \tag{4.169}$$

Note that as the shell formulation is written in the inertial reference frame, the determination of (4.168-4.169) does not involve a Jacobian of a transformation see Fig. 4.3(a).

Once the convected basis of the mid-surface is known, the computations of the unit vector $\boldsymbol{t}$, and of the convected basis $\boldsymbol{g}_I$ follow respectively from (4.13) and (4.9-4.10). Moreover, the

development of $j = \nabla\Phi$ allows computing the Jacobian as,

$$j = \boldsymbol{g}_3 \cdot (\boldsymbol{g}_1 \wedge \boldsymbol{g}_2) \text{ and,} \tag{4.170}$$

$$\bar{j} = \lambda_h \left|\left| \boldsymbol{\varphi}_{h,1} \wedge \boldsymbol{\varphi}_{h,2} \right|\right| . \tag{4.171}$$

In the non-linear case, the thickness ratio λ_h is determined following Section 4.3.2 and a Simpson integration rule (discretizing the thickness) is used to evaluated the reduced stresses $\boldsymbol{n}^\alpha$ (4.26) and torque $\tilde{\boldsymbol{m}}^\alpha$ (4.37). In the linear case, the reduced stresses $\boldsymbol{n}^\alpha$ (4.26) and torque $\tilde{\boldsymbol{m}}^\alpha$ (4.37) follow from Section 4.3.1.

At this point everything is known to compute the bulk internal forces vector (4.172) of non linear formulation (4.95) as well as those of the linear formulation (4.148). This vector reads,

$$\boldsymbol{F}_{bulk} = \sum_e (\boldsymbol{F}^e_{int\,n} + \boldsymbol{F}^e_{int\,b}) , \tag{4.172}$$

where $\boldsymbol{F}^e_{int\,n}$ is the elementary internal membrane forces vector corresponding to $a^e_n(\boldsymbol{\varphi}_h, \delta\boldsymbol{\varphi})$ (4.63) and where $\boldsymbol{F}^e_{int\,b}$ is the elementary internal bending forces vector corresponding to $a^e_m(\boldsymbol{\varphi}_h, \delta\boldsymbol{\varphi})$ (4.64). The detailed expressions in the non-linear range of both elementary vectors are given in Appendix B.5.

Interface internal forces vector

For the interface terms the integration on interface elements has to be specified. Unfortunately, as illustrated on Fig. 4.3(b), the basis vectors of the neighboring elements $\boldsymbol{\varphi}^-_{,\alpha}$ and $\boldsymbol{\varphi}^+_{,\alpha}$ differ in general, requiring special care. The interface is a curve that is represented in the reference frame $\boldsymbol{E}_1$ like a 1D isoparametric element with the coordinate $\xi^{s1} \in [-1\,;1]$. A Gauss quadrature rule is used to perform the integration on the interface element. It has to be mentioned that a Gauss-Lobatto quadrature rule had also be implemented but no benefit due to the presence of quadrature points at the extremities of the element was observed. As a finite element is created at interface, 1D Lagrangian shape functions $N^{\boldsymbol{\xi}}_s$ are associated to each of its nodes $\boldsymbol{\xi}$. Using these nodes the convected basis of the interface is computed as,

$$\boldsymbol{\varphi}_{0,1} = \frac{\partial N^{\boldsymbol{\xi}}_s}{\partial \xi^{s1}} \boldsymbol{X}^{\boldsymbol{\xi}} \text{ and,} \tag{4.173}$$

$$\boldsymbol{\varphi}_{h,1} = \frac{\partial N^{\boldsymbol{\xi}}_s}{\partial \xi^{s1}} \boldsymbol{x}^{\boldsymbol{\xi}} . \tag{4.174}$$

The unit normal vector at interface is set to the mean value of minus and plus elements[10] evaluated at the common element edge,

$$\boldsymbol{t}_0 = \frac{\boldsymbol{t}^+_0 + \boldsymbol{t}^-_0}{\left|\left| \boldsymbol{t}^+_0 + \boldsymbol{t}^-_0 \right|\right|} \text{ and,} \tag{4.175}$$

$$\boldsymbol{t} = \frac{\boldsymbol{t}^+ + \boldsymbol{t}^-}{||\boldsymbol{t}^+ + \boldsymbol{t}^-||} . \tag{4.176}$$

[10] A test is performed to ensure that the two normals are defined in the same direction, which is the case if all elements are defined in the same manner (clockwise or anti-clockwise).

The in-plane normal to the interface ($\boldsymbol{\nu}^-$) is then equal to $\boldsymbol{\varphi}_{,2}$ (or $\boldsymbol{\varphi}_{0,2}$ in the linear formulation) which can be determined by, see Fig. 4.3(b),

$$\boldsymbol{\varphi}_{0,2} = \frac{\boldsymbol{t}_0 \wedge \boldsymbol{\varphi}_{0,1}}{||\boldsymbol{t}_0 \wedge \boldsymbol{\varphi}_{0,1}||} \text{ and,} \tag{4.177}$$

$$\boldsymbol{\varphi}_{h,2} = \frac{\boldsymbol{t} \wedge \boldsymbol{\varphi}_{h,1}}{\left|\left|\boldsymbol{t} \wedge \boldsymbol{\varphi}_{h,1}\right|\right|}. \tag{4.178}$$

With these definitions the Jacobian of the interface is still computed by,

$$\bar{j_0} = ||\boldsymbol{\varphi}_{0,1} \wedge \boldsymbol{\varphi}_{0,2}|| \text{ and,} \tag{4.179}$$

$$\bar{j} = \lambda_h \left|\left|\boldsymbol{\varphi}_{h,1} \wedge \boldsymbol{\varphi}_{h,2}\right|\right| \tag{4.180}$$

Then, at each quadrature point of the interface the different quantities $\boldsymbol{n}^{\alpha^\pm}$,$\tilde{\boldsymbol{m}}^{\alpha^\pm}$, $\mathcal{H}_n^\pm$, $\mathcal{H}_m^\pm$ and $\mathcal{H}_q^\pm$ are first evaluated on the common edge of the plus and minus elements. However the basis of the plus and minus elements do not match with the basis of the interface element requiring the use of push-forward tensors, defined as,

$$\mathbf{T}^\alpha_{\beta^\pm} = \boldsymbol{\varphi}_h{}^{,\alpha} \cdot \boldsymbol{\varphi}_{h,\beta^\pm} \text{ and,} \tag{4.181}$$

$$\mathbf{T}^\alpha_{0\beta^\pm} = \boldsymbol{\varphi}^{0,\alpha} \cdot \boldsymbol{\varphi}_{0,\beta^\pm}. \tag{4.182}$$

Using these tensors and calling $\widehat{\bullet}$ the quantities formulated in the interface convected basis, it successively yields,

$$\widehat{\boldsymbol{n}^{\alpha^\pm}} = \mathbf{T}^\alpha_{\beta^\pm} \boldsymbol{n}^{\beta^\pm}, \tag{4.183}$$

$$\widehat{\tilde{\boldsymbol{m}}^{\alpha^\pm}} = \mathbf{T}^\alpha_{\beta^\pm} \tilde{\boldsymbol{m}}^{\beta^\pm}, \tag{4.184}$$

$$\widehat{\mathcal{H}_n}^{\alpha\beta\gamma\delta\pm} = \mathbf{T}^\alpha_{\mu^\pm} \mathbf{T}^\beta_{\nu^\pm} \mathcal{H}_n^{\mu\nu\zeta o\pm} \mathbf{T}^\gamma_{\zeta^\pm} \mathbf{T}^\delta_{o^\pm}, \tag{4.185}$$

$$\widehat{\mathcal{H}_m}^{\alpha\beta\gamma\delta\pm} = \mathbf{T}^\alpha_{\mu^\pm} \mathbf{T}^\beta_{\nu^\pm} \mathcal{H}_m^{\mu\nu\zeta o\pm} \mathbf{T}^\gamma_{\zeta^\pm} \mathbf{T}^\delta_{o^\pm} \text{ and,} \tag{4.186}$$

$$\widehat{\mathcal{H}_q}^{\alpha\beta\pm} = \mathbf{T}^\alpha_{\mu^\pm} \mathcal{H}_q^{\mu\nu\pm} \mathbf{T}^\beta_{\nu^\pm}. \tag{4.187}$$

Then, the $\widehat{\bullet}$ quantities are used to evaluate the jump and mean values at each Gauss integration point of the interface. Therefore everything is known to compute the different interface terms $a^s_{nI}(\boldsymbol{\varphi}_h, \delta\boldsymbol{\varphi})$ (4.97), $a^s_{mI}(\boldsymbol{\varphi}_h, \delta\boldsymbol{\varphi})$ (4.98) and $a^s_{sI}(\boldsymbol{\varphi}_h, \delta\boldsymbol{\varphi})$ (4.99) of the non-linear weak form (4.95) as well as the different terms $a^s_{lnI}(\boldsymbol{u}_h, \delta\boldsymbol{u})$ (4.149), $a^s_{lmI}(\boldsymbol{u}_h, \delta\boldsymbol{u})$ (4.150) and $a^s_{lsI}(\boldsymbol{u}_h, \delta\boldsymbol{u})$ (4.151) of the linear formulation (4.148). Then the interface internal forces vector is formulated as,

$$\begin{aligned}\boldsymbol{F}_{inter} = \sum_s \big(&\boldsymbol{F}^s_{int\,cons\,n} + \boldsymbol{F}^s_{int\,comp\,n} + \boldsymbol{F}^s_{int\,stab\,n} + \boldsymbol{F}^s_{int\,cons\,m} + \boldsymbol{F}^s_{int\,comp\,m} \\ &+ \boldsymbol{F}^s_{int\,stab\,m} + \boldsymbol{F}^s_{int\,stab\,a}\big)\end{aligned} \tag{4.188}$$

where the terms of the right members are the elementary interface force vectors computed from either the weak form (4.95) or the weak form (4.148). The detailed expressions in the non-linear range of these different vectors are given in Appendix B.5.

Elements library

The recourse to DG leads to a thickness-locking free method, when considering under-integrated quadratic elements or fully integrated cubic elements. The implementation described above is employed to build a library of four elements, having three (displacement) dofs per node,

(i) 6-node quadratic triangles with 3 Gauss points for bulk integration and 3 Gauss points on each edge for interface integration (T6);

(ii) 8 or 9-node quadratic quadrangles with 4 Gauss points for bulk integration and 3 Gauss points on each edge for interface integration (Q8RI and Q9RI);

(iii) 10-node cubic triangles with 6 Gauss points for bulk integration and 4 Gauss points on each edge for interface integration (T10);

(iv) 16-node quadratic quadrangles with 16 Gauss points for bulk integration and 4 Gauss points on each edge for interface integration (Q16).

Note that linear elements cannot be used as the second derivative of shape functions have to be computed.

4.5.2 Non-linear solver

The non-linear solver implemented as a project of Gmsh includes three computational schemes: explicit Hulbert-Chung [123], dynamic relaxation [195] and quasi-static [122]. The implementation of these three schemes is discussed here below.

Explicit Hulbert-Chung dynamic scheme

A dynamic explicit solver based on the α-generalized method introduced by G. Hulbert *et al.* [123] is implemented, which allows introducing numerical damping in the problem. Once again we use the same approach than in Gmsh and we develop this explicit solver as an interface to a powerful library, which can perform vector operations (there is no matrix-vector operations in this resolution scheme). The interface is implemented for two libraries: PETSc [21, 22, 23] and BLAS [52, 83, 134]. Notice that this last interface is written in such a way that a (less efficient) default implementation is provided if the code is not linked to BLAS.

In the Hulbert-Chung time integration algorithm [123], the evaluation of the nodal unknowns vector $\underline{\boldsymbol{x}}$ at time step $n+1$ is realized from the nodal internal $\boldsymbol{F}_{\text{int}}$ and external $\boldsymbol{F}_{\text{ext}}$

forces vectors at time n,

$$\left[\underline{\ddot{\boldsymbol{x}}}^{n+1}\right]^{\xi} = \frac{1}{1-\alpha_M}\left[\mathbf{M}^{-1}\right]^{\xi\mu}\left[\boldsymbol{F}_{ext}^{n}-\boldsymbol{F}_{int}^{n}\right]^{\mu}-\frac{\alpha_M}{1-\alpha_M}\left[\underline{\ddot{\boldsymbol{x}}}^{n}\right]^{\xi}, \tag{4.189}$$

$$\left[\underline{\dot{\boldsymbol{x}}}^{n+1}\right]^{\xi} = \left[\underline{\dot{\boldsymbol{x}}}^{n}\right]^{\xi}+\Delta t\left[1-\gamma\right]\left[\underline{\ddot{\boldsymbol{x}}}^{n}\right]^{\xi}+\Delta t\gamma\left[\underline{\ddot{\boldsymbol{x}}}^{n+1}\right]^{\xi}, \text{ and} \tag{4.190}$$

$$\left[\underline{\boldsymbol{x}}^{n+1}\right]^{\xi} = \left[\underline{\boldsymbol{x}}^{n}\right]^{\xi}+\Delta t\left[\underline{\dot{\boldsymbol{x}}}^{n}\right]^{\xi}+\Delta t^2\left[\frac{1}{2}-\beta_N\right]\left[\underline{\ddot{\boldsymbol{x}}}^{n}\right]^{\xi}+\Delta t^2\beta_N\left[\underline{\ddot{\boldsymbol{x}}}^{n+1}\right]^{\xi}, \tag{4.191}$$

for the unknown at node ξ and where $\boldsymbol{F}_{ext}$ and $\boldsymbol{F}_{int}$ are evaluated from Section 4.5.1 in the case of the full-DG formulation.

An original parallel partitioning of this scheme, based on ghost elements, is suggested herein. Compared with previous parallel implementations [184] this one allows communicating the nodal unknowns between the different processors instead of the material law resultant $\boldsymbol{n}^{\alpha}$, $\tilde{\boldsymbol{m}}^{\alpha}$, $\mathcal{H}_n$, $\mathcal{H}_m$, $\mathcal{H}_q$,... Thus, the main advantages of the suggested implementation are, on one hand, to be independent of the material law, and on the other hand, to decrease the number of communications. Furthermore, this approach leads to an extra memory cost on each processor as the ghost elements have to be stored. Nevertheless, this extra cost is relatively limited if we assume that the number of elements by partition remains large compared with the number of duplicated elements (only one layer of elements is duplicated as illustrated on Fig. 4.4(c)). This assumption is generally verified as tens of processor are used with meshes containing thounsands of elements.

The set of Eqs. (4.189-4.191) shows that if the mass matrix is diagonalized the evaluation can be done unknown by unknown, leading to an easy resolution on different processors. Therefore the coupling of the unknowns only results from the evaluation of the force vectors. Then, METIS [127] is used through Gmsh to partition the mesh between the different processors, see Fig. 4.4(a). So each processor owns a partition of the mesh, see Fig. 4.4(b), but also the ghost boundary elements, which are elements of the other processors having a common interface, see Fig. 4.4(c). Thus, using the ghost elements, each processor can create the interface elements in its own partition and at partition interfaces. Finally the interface terms $a^s_{nI1}(\boldsymbol{\varphi}_h,\delta\boldsymbol{\varphi})$, $a^s_{mI1}(\boldsymbol{\varphi}_h,\delta\boldsymbol{\varphi})$, $a^s_{nI2}(\boldsymbol{\varphi}_h,\delta\boldsymbol{\varphi})$, $a^s_{mI2}(\boldsymbol{\varphi}_h,\delta\boldsymbol{\varphi})$, $a^s_{nI3}(\boldsymbol{\varphi}_h,\delta\boldsymbol{\varphi})$, $a^s_{mI3}(\boldsymbol{\varphi}_h,\delta\boldsymbol{\varphi})$, and $a^s_{sI3}(\boldsymbol{\varphi}_h,\delta\boldsymbol{\varphi})$ are integrated on all the interface elements[11]. As partitions are discontinuous, they do not share common degrees of freedom (dofs), and the Gmsh dof manager creates new dofs on each partition, independently on the node number (in Gmsh the dof is not directly linked to the node), leading to a straightforward computation of $\boldsymbol{F}_{bulk}$ and $\boldsymbol{F}_{inter}$ in each partition. However, this statement is not true for the ghost elements, which nodal values have to be communicated through the network via MPI when evaluating the interface terms as depicted on Fig. 4.4(d). Also, as interface terms at the interface of ghost elements, are actually computed on two partitions, only the part related to the degrees of freedom really belonging to the partition is assembled into the local $\boldsymbol{F}_{inter}$ in order to avoid duplication. At the end of

[11] On interfaces internal to the partition, if the C^0/DG method is used instead of the full-DG method, only $a^s_{mI1}(\boldsymbol{\varphi}_h,\delta\boldsymbol{\varphi})$, $a^s_{mI2}(\boldsymbol{\varphi}_h,\delta\boldsymbol{\varphi})$ and $a^s_{mI3}(\boldsymbol{\varphi}_h,\delta\boldsymbol{\varphi})$ are integrated as the displacement field is continuous from one element to another

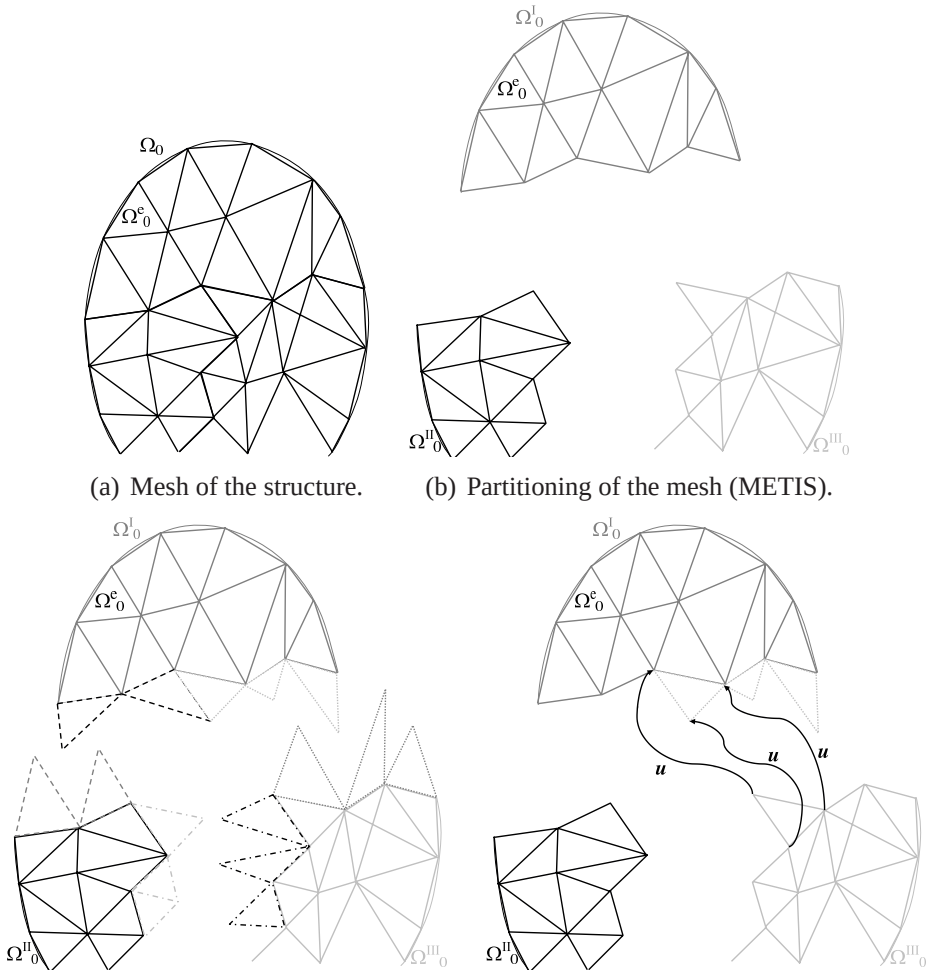

(a) Mesh of the structure.

(b) Partitioning of the mesh (METIS).

(c) The ghost elements in dashed lines allow performing the interface integration on both partitions.

(d) Nodal unknowns are exchanged through MPI communications.

Figure 4.4: Different stages of a parallel computation. The steps a) to c) are performed once during initiation of the computation. The last one is performed before each assembling step of the internal forces vector (and of the stiffness matrix in the quasi-static case).

the assembly process, the set of equations (4.189 - 4.191) is solved locally in each partition. So the time integration from time t_n to time t_{n+1} follows the chart flow:

- Knowing values at time t_n, determine the critical time step and compute successively the accelerations (4.189), velocities (4.190) and displacements (4.191);
- Send nodal values to ghost elements, see Fig. 4.4(d);
- Following Section 4.3, compute the stress field in each bulk and interface elements belonging to the processor, including the ghost elements and processor boundary interface

elements;

- Compute $\boldsymbol{F}_{int}$ of the bulk elements from (4.172) and the interface forces of the interface elements $\boldsymbol{F}_{inter}$ from (4.188) belonging to the processor, including the ghost elements and processor boundary interface elements;

- Assemble the elementary force vectors in each processor, but at the interface of ghost elements consider only the part on the boundary belonging to the processor.

Dynamic relaxation

As convergence problems occur when studying crack propagation and as it can be useful to neglect the inertia forces for some problems, we suggest an original adaptation of the dynamic relaxation concept first presented by M. Papadrakakis [195]. In fact, this technique can be used to prescribe a quasi-static loading with an explicit dynamic scheme. The main idea of dynamic relaxation is to annihilate the dynamic effects by the introduction of damping on the velocity field in such a way that the static solution is reached after a minimum number of time steps. This principle is commonly applied with the explicit central difference method [186,195,272], among others, and is adapted herein to the explicit scheme of Hulbert-Chung [123] in an original manner. From the developments of M. Papadrakakis [195], the dynamic relaxation can be generalized to Hulbert-Chung algorithm by introducing a damping factor in equation (4.190) which becomes,

$$\left[\underline{\dot{\boldsymbol{x}}}^{n+1}\right]^{\xi} = \mathrm{c}^{\,n+1}\left\{\left[\underline{\dot{\boldsymbol{x}}}^{n}\right]^{\xi} + \Delta t\,[1-\gamma]\left[\underline{\ddot{\boldsymbol{x}}}^{n}\right]^{\xi} + \Delta t\gamma\left[\underline{\ddot{\boldsymbol{x}}}^{n+1}\right]^{\xi}\right\}, \tag{4.192}$$

where c is the damping factor to be determined. The modification introduced in equation (4.192) is the only one in the algorithm, which allows an easy implementation and facilitates the switch between the two schemes (*i.e.* switch from dynamic relaxation to Hulbert-Chung or conversely). The computation of the damping factor is based on the work of Z. Zhang *et al.* [272], which avoids the computation of the stiffness matrix, except that we compute a global damping factor and not a local damping factor by nodes as suggested in [272]. The reason of using a global damping factor is related to our implementation. Indeed as we use a dof manager to create dofs independently of nodes, it is very time consuming to identify the three displacements related to a node. Keeping these considerations in mind the value chosen for damping factor is,

$$\mathrm{c}^{\,n+1} = \frac{1}{1+2\xi_{n+1}\Delta t} \text{ with } \xi_{n+1} = \frac{\underline{\boldsymbol{x}}^{n}\cdot\boldsymbol{F}^{n}_{\mathrm{int}}}{\underline{\boldsymbol{x}}^{n}\cdot\mathbf{M}\cdot\underline{\boldsymbol{x}}^{n}}, \tag{4.193}$$

where $\underline{\boldsymbol{x}}^{n}$ and $\boldsymbol{F}^{n}_{\mathrm{int}}$ are respectively the nodal positions and internal forces at time n, and where $\mathbf{M}$ is the diagonalized mass matrix. In this work Δt is lower or equal to the value of the critical time step for the explicit Hulbert-Chung scheme.

For the application of an external effort, the convergence depends on the fundamental period of the problem. Therefore increase of density has no influence on the convergence as

an augmentation of the time step involves the same increase of the fundamental period (*i.e.* the number of time steps needed to achieve convergence is the same no matter the time step value). The external effort is applied at the beginning of the simulation and is kept constant until convergence, which is based on the criterion (at iteration $n+1$),

$$\frac{\|\boldsymbol{F}_{\text{ext}} - \boldsymbol{F}_{\text{int}}^{n+1}\|}{\|\boldsymbol{F}_{\text{ext}} + \boldsymbol{F}_{\text{int}}^{n+1}\|} \leq e_{\text{tol}}, \tag{4.194}$$

where $\boldsymbol{F}_{\text{ext}}$ is the vector of external forces prescribed and where e_{tol} is a convergence parameter, which is independant of the problem as we use a relative value. A value of 10^{-3} seems to give accurate results with a minimal computational effort as presented through a numerical example in Appendix B.6. Notice that this scheme can be easily used for parallel computation by computing the scalar vector product on each processor before summing the different values.

Quasi-static solver

Gmsh includes a linear static solver, which resolves $\mathbf{K}\underline{\boldsymbol{x}} = \boldsymbol{F}_{ext}$, with $\mathbf{K}$ the stiffness matrix, $\underline{\boldsymbol{x}}$ the unknowns vector and $\boldsymbol{F}_{ext}$ the external force vector. This solver provides in fact interfaces with powerful and widely used libraries for matrix vector operations as, Taucs [244,245] or PETSc [21,22,23]. We extended this solver by derivation of classes. Indeed, we implement a non linear quasi-static solver based on Newton-Raphson iterations to solve $\boldsymbol{F}_{int} = \boldsymbol{F}_{ext}$ with $\boldsymbol{F}_{int}$ and $\boldsymbol{F}_{ext}$ are computed from Section 4.5.1 in the case of the full-DG formulation. Yet, at each iteration, we have to solve a problem $\mathbf{K}\Delta\underline{\boldsymbol{x}} = \boldsymbol{F}_{ext}$, which is performed by the solver included in Gmsh.

Furthermore, the parallel implementation described before can be used for the non linear quasi-static solver. In fact, the PETSc library is able to solve the (linear) system $\mathbf{K}\underline{\boldsymbol{x}} = \boldsymbol{F}_{ext}$ in parallel, once it is assembled. We implemented this parallel scheme using the algorithm described above for explicit scheme. Moreover PETSc used an iterative solver to solve the problem simultaneously on several processors a good preconditioner is required. We tried the different standard ones provided by PETSc but they seem inefficient for large systems. A study will have to be performed on this point to use the quasi-static scheme in parallel but this is out of the scope of this thesis. Notice that for serial computation, PETSc solves the problem thanks to a direct solver without any difficulty.

4.6 Numerical benchmarks

This section regroups the results of benchmarks simulated to validate the developed full-DG shell formulations (linear and non linear). Furthermore, the results of the C^0/DG formulation (4.100) are compared with those of the full-DG formulations (4.95) on several examples. In particular, the comparison of both formulations proves the ability of the full-DG method developed in this thesis to provide results as accurate as a method using continuous elements.

Results are also compared to analytical solutions when available and to results from the literature using mixed shell formulations. The drawback of the full-DG method is to consider more dofs, but it can be advantageously used to solve fracture mechanic problems by combination with a cohesive law, see Chapter 5, or to perform parallel simulations in which case the full-DG can be limited to processor interfaces. Unless specified otherwise, the stability parameters are set to $\beta_1 = \beta_2 = \left(\frac{L_c}{h}\right)^2 \beta_3 = 10$, with h the initial shell thickness and L_c, the largest length of the problem. This choice of a low value for β_1 is motivated by the conclusions arising from the Euler-Bernoulli beam case in Chapter 3. These conclusions are confirmed by the first numerical example of this section, which studies the effect of β_i and where it is explained that for thin meshes, stable results are obtained for this low value of β_i. Also as for explicit problems the critical time step is proportional to $\frac{1}{\max\sqrt{\beta_i}}$ low β_i values allow simulating the processes in a reasonable time.

4.6.1 Quasi-static benchmarks

We first present several quasi-static benchmarks: a hemisphere with different constitutive behaviors and a cut plate ring. These simulations regroup several benchmarks commonly used in the literature to validate a numerical model of shells. Due to the good correlation between our new formulation and the literature we can prove the validity of our approach.

Elastic pinched open hemisphere with small strains

This first example is used to illustrate the numerical properties of the full-DG method presented in Section 4.4. It considers a pinched open hemisphere, with radius R, thickness t

Property	Value
Radius R [m]	10
Thickness h [m]	0.04
Opening $\theta[^o]$	18
Young modulus [MPa]	68.25
Poisson's ratio [-]	0.3
Applied force P [N]	40

Table 4.1: Material and geometrical properties for the pinched open hemisphere test.

and an opening of a spherical sector angle θ (see values given in Tab. 4.1). It is subjected to radial loads P applied on two diametrical directions, see Fig. 4.5(a). The load is compressive in the y-direction and tensile in the x-direction. One quarter of the structure is modeled by exploiting the symmetries of the problem. The maximal deflection along x or y is $|\delta_x| = |\delta_y| = 0.093(mN^{-1})\frac{P}{2}$ (see [234]) and is used as the reference value. This problem is simulated with 9-node bi-quadratic elements with reduced integration (Q9RI) for several meshes 2×2, 4×4,

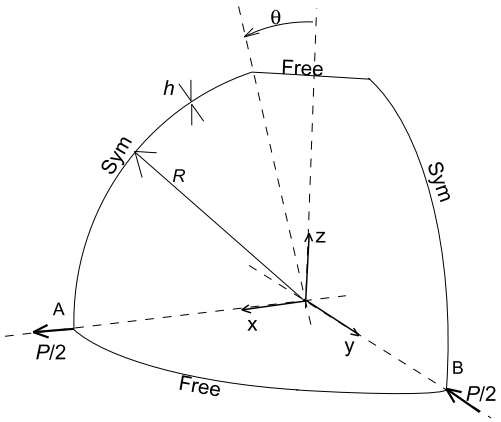

(a) One fourth of the open hemisphere is meshed.

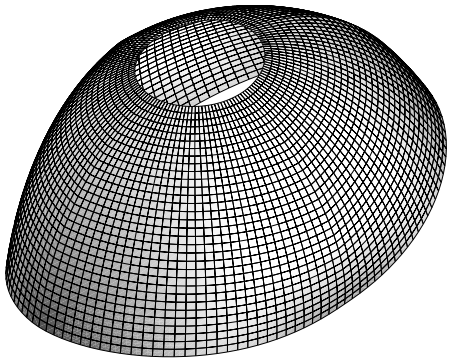

(b) Magnified deformation of the complete hemisphere for a regular mesh of thirty-two quadratic-quadrangular elements on each side.

Figure 4.5: Study of the pinched open hemisphere. Problem dimensions: radius R, thickness h, opening θ, concentrated loading P.

8×8,..., 32×32 elements and for different values of stability parameters $\beta_1=\beta_2=\beta_3\left(\frac{R}{h}\right)^2=10,1e^3,1e^6$.

Results obtained by the presented full-DG formulation are compared with the C^0/DG formulation previously presented in [185]. As it can be seen on the Fig. 4.6, there is no noticeable difference for reduced mesh sizes. The displacements (Figs. 4.6(a) and 4.6(c)) and convergence orders (Figs. 4.6(b) and 4.6(d)), are the same for both methods[12]. Note that for the lowest value of stability parameters, the convergence is not monotonic as it appears on the Figs. 4.6(c) and 4.6(d). This is due to the fact that $\beta_1=10$ is close to the stability limit, and thus stability is only ensured for fine-enough meshes.

Elastic pinched open hemisphere with finite deformations

The previous example was also performed for finite deformations in the literature by several authors [9, 50, 152, 181] with the Neo-Hookean constitutive behavior given in Tab. 4.1. They used this benchmark with the aim of demonstrating the ability of their respective method to remain locking free even when the mesh is distorted. To avoid locking phenomena M. Bischoff *et al.* [50] had recourse to a mixed enhanced assumed strains formulation with 6 dofs per nodes (3 displacements, 2 rotations and the thickness). For their part, P. Areias *et al.* [9] use a mixed formulation based on mid-side rotations and L. Noels [181] suggested the C^0/DG method from which we extended our full discontinuous formulation.

[12]Note that even if the formula (4.163) predicts a convergence in k for $k=2$ it is numerically observed that the convergence is in $k+1$ (see [91, 185]).

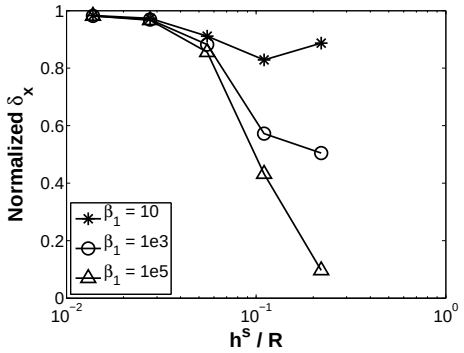

(a) Normalized deflection for Q9RI with C^0/DG formulation.

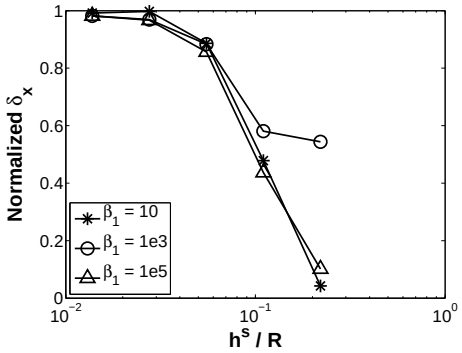

(b) Normalized deflection for Q9RI with full-DG formulation.

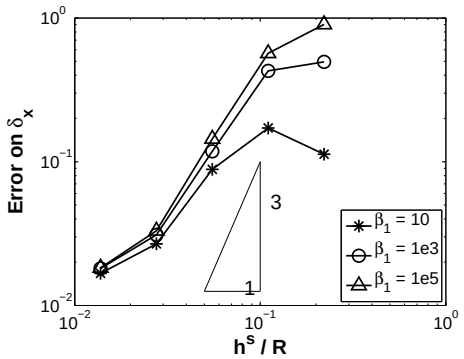

(c) Error on the deflection for Q9RI with C^0/DG formulation.

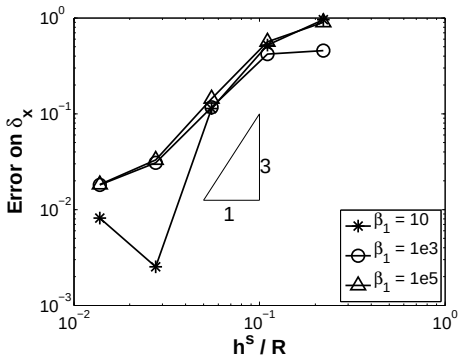

(d) Error on the deflection for Q9RI with full-DG formulation.

Figure 4.6: Influence of mesh size and stabilization parameters on the deflection for the pinched open hemisphere.

We compare the results obtained for different loads $P \in [0\,;\,800]$ [N] by studying the responses at both points A and B. It is obvious from pictures of Fig. 4.7 that all methods provide similar results and therefore that our suggested new full-DG method is as accurate as a continuous method even in case of large deformations.

Elasto-plastic pinched hemisphere with finite deformations

The example of a (not open) hemisphere, with a radius of 10 [m] and a thickness of 0.5 [m], depicted on Fig. 4.8, is also presented in the literature [48, 236] with the J_2-flow constitutive behavior reported in Tab. 4.2.

As in previous benchmarks, the hemisphere is loaded on two opposite diameters (one in tension, the other one in compression). Once again this example is performed with the full-DG method for quadratic and cubic triangles as well as for quadratic and cubic quadrangles. The structured quadrangular mesh is formed by 27 elements (six elements along each edge)

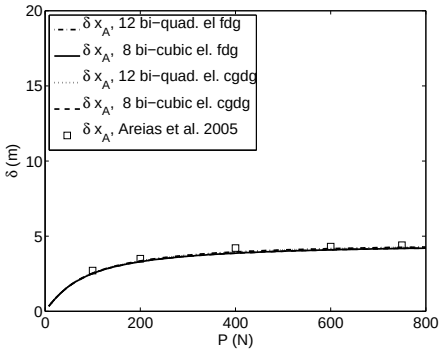

(a) Deflection of point A.

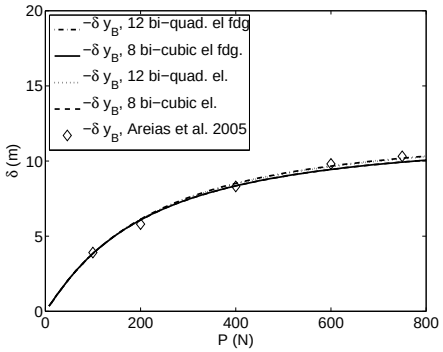

(b) Deflection of point B.

Figure 4.7: Results of the full-DG formulation for elast pinched open hemisphere finite deformations are in agreement with literature [9, 181].

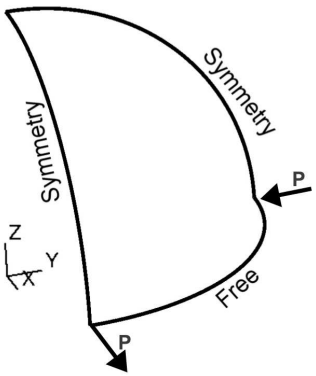

(a) One fourth of the open hemisphere is meshed.

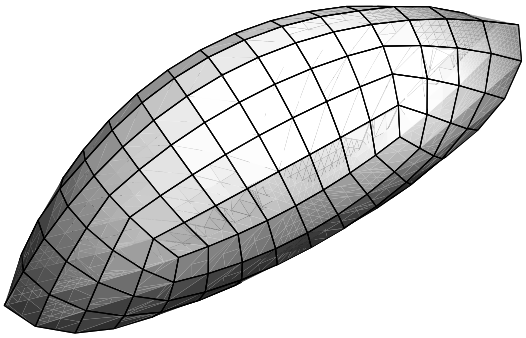

(b) Deformation of the complete hemisphere for a regular mesh of height quadratic-quadrangular elements on each side.

Figure 4.8: Pinched elasto-plastic hemisphere benchmark.

and the unstructured triangular mesh contains approximately 70 elements. The deflection *vs.* force curves at loaded points are plotted on Fig. 4.9 for triangular elements and 4.10 (quadrangular elerments). These curves are compared to J. Simo *et al.* [236] and to P. Betsch *et al.* [48] results. These pictures give rise to the avoidance of the locking that could be present for triangular quadratic elements. With the full-DG formulation this locking is avoided. Furthermore, except for quadratic triangles with the C^0/DG formulation which strongly suffers from locking, the other simulations give results in agreement with P. Betsch shell formulation. In their paper, P. Betsch *et al.* explained the difference with J. Simo formulation [236], by the difference of constitutive model. Indeed, the stress-resultant plasticity model used in [236] leads to less hardening than the J_2-flow theory used in [48] and in this work. This example proves that the full-DG framework provides accurate results no matter the type and order (at

Property	Value
Young modulus [Pa]	10
Poisson ratio [-]	0.2
Yield stress [Pa]	0.2
Hardening modulus [Pa]	9

Table 4.2: Material properties of the pinched elasto-plastic hemisphere benchmark.

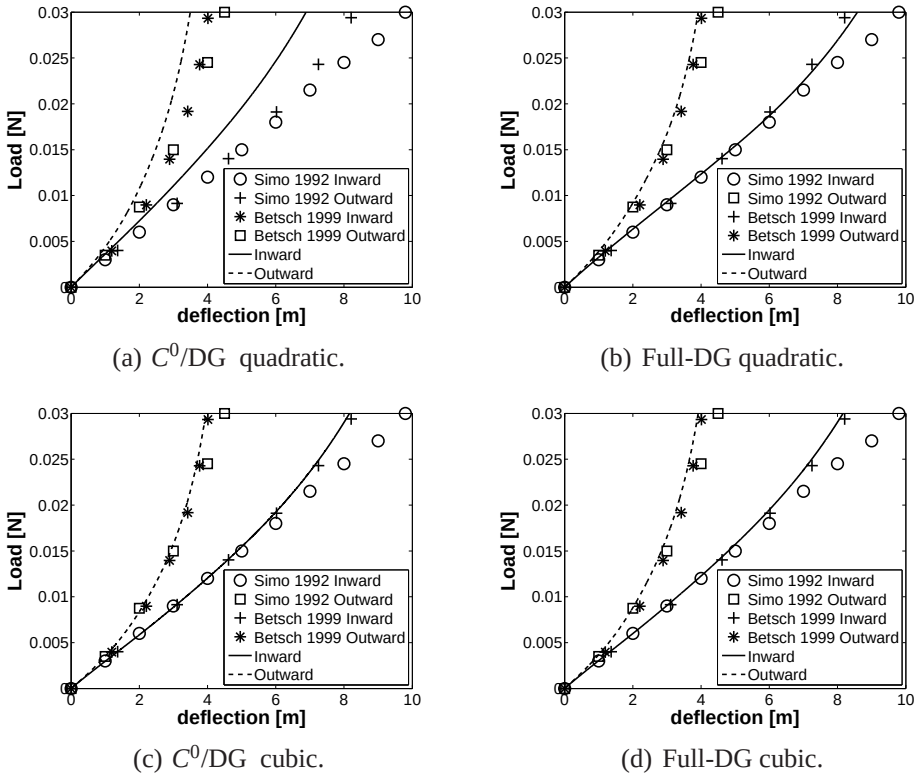

(a) C^0/DG quadratic. (b) Full-DG quadratic.

(c) C^0/DG cubic. (d) Full-DG cubic.

Figure 4.9: Pinched elasto-plastic hemisphere benchmark results for triangular elements. The locking is avoided with the full-DG method, which is in agreement with the literature [236,48].

least quadratic) of the element.

Elastic plate ring with finite deformations

This last quasi-static benchmark was first performed in [26] and consists into a thin plate ring, with inner radius $R_i = 6$ [m], outer radius $R_e = 10$ [m] and thickness $t = 3$ [cm], with the geometry depicted in Fig. 4.11 and the properties reported in Tab. 4.3. This ring is cut along a radius AB, and, on one side of this cutting, the plate is clamped, while a uniform vertical loading $q = 12000$ [N/m] is applied on the other side, see Fig. 4.11. This test has widely

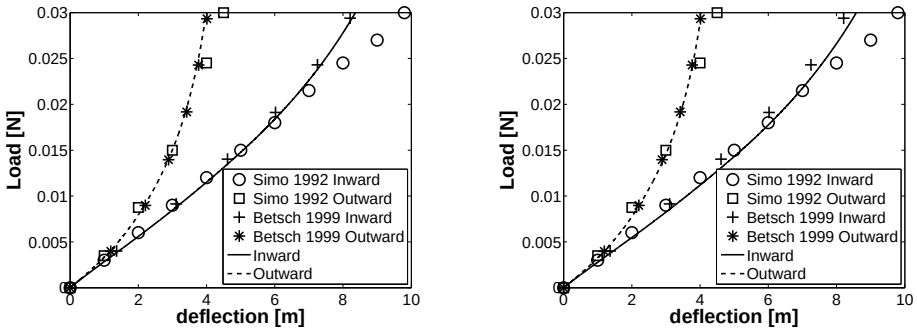

(a) C^0/DG quadratic. (b) Full-DG quadratic.

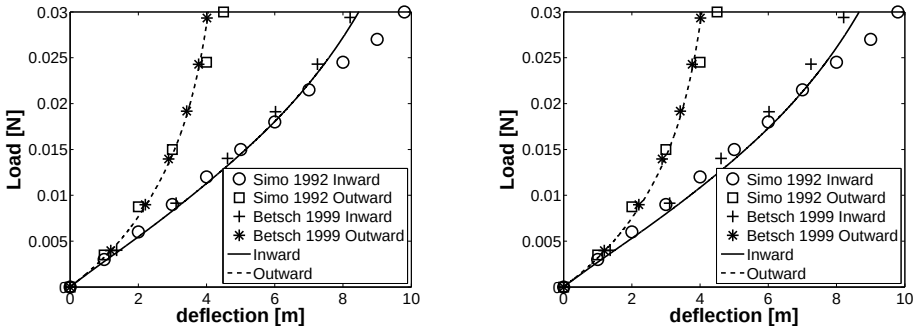

(c) C^0/DG cubic. (d) Full-DG cubic.

Figure 4.10: Pinched elasto-plastic hemisphere benchmark results for quadrangular elements there is no locking and results are in agreement with the iterature [236, 48].

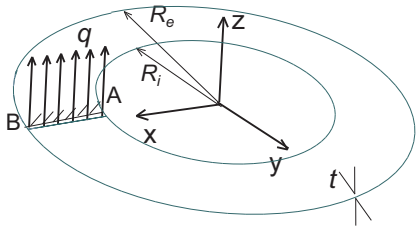

Figure 4.11: Elastic non-linear plate ring benchmark. Courtesy of [181].

been used in the literature, see *e.g.* [9, 60, 223, 224] to compare shell formulations when large deformations and rotations arise.

This simulation is computed using the suggested discontinuous Galerkin formulations (C^0/DG and full-DG) with 8-nodes bi-quadratic elements and a neo-Hookean model. The final deformed configuration is illustrated in Fig. 4.12(b), and the displacement evolutions of nodes A and B located at the cutting are shown in Fig. 4.12(a). Although the mesh experiences large distortions during the deformation process, the solutions are in good agreement

Property	Value
Young modulus [GPa]	210
Poisson ratio [-]	0

Table 4.3: Material properties of the elastic non-linear plate ring benchmark.

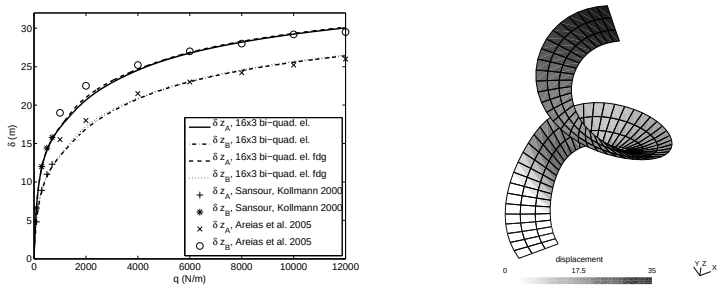

(a) Nodes A & B force *vs.* displacement.

(b) Final configuration.

Figure 4.12: Elastic plate ring results for C^0/DG and full-DG methods are in agreement with literature [9, 224].

with the ones obtained in the literature, and in particular with:

- The hybrid stress formulation proposed by C. Sansour *et al.* [224], whose results are displayed for $q <$3000 [N/m] (which is the maximum loading considered in this reference).
- The mixed formulation based on mid-side rotations proposed by P. Areias *et al.* [9], which converges for an applied linear force reaching 12000 [N/m].

This proves once again that the use of the full-DG framework gives results similar to the existing formulations.

4.6.2 Dynamic benchmarks

We present two dynamic benchmarks with finite deformations to demonstrate the ability of our formulation to model correctly a structure submitted to a dynamic loading. Both benchmarks use a J_2-flow constitutive model and are reported in the literature. In particular, the second example contains experimental data that are used to validate our new method.

Simply supported perfectly plastic square plate subjected to uniform loading

This example studies the central deflection history of the square plate, depicted on Fig. 4.13 which is suddenly submitted to a uniform pressure $p_0 = 20.7$ [bars]. This plate has sides of 254 [mm], a thickness of 12.7 [mm] and its material properties are reported in Tab. 4.4.

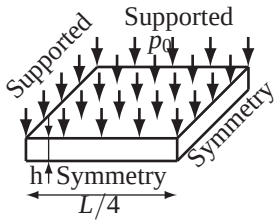

Figure 4.13: Simply supported elasto-plastic plate subjected to uniform loading benchmark.

Property	Value
Density [kg/m^3]	2768
Young modulus [MPa]	69000
Poisson ratio [-]	0.3
Yield stress [MPa]	207
Hardening modulus [MPa]	0

Table 4.4: Material properties of the simply supported elasto-plastic plate subjected to uniform loading benchmark.

This benchmark has first been presented by T. Belytschko *et al.* [39] and performed again some years later by S. Swaddiwudhipong *et al.* [243]. The central deflection is computed using the explicit algorithm of Hulbert-Chung [123] without numerical dissipation, for both C^0/DG and full-DG formulations and for successively 8×8 quadratic and cubic quadrangles. Results are reported on Fig. 4.14 showing the good correlation with the literature for all the studied elements. This benchmark demonstrates the ability of the full-DG formulation to capture accurately the solution in case of a dynamic loading.

Perfectly plastic cylindrical panel

This second dynamic benchmark, presented by T. Belytschko *et al.* [39, 45], focuses on a cylindrical panel loaded impulsively as depicted on Fig. 4.15. The perfectly plastic material properties are reported in Tab. 4.5. As for the square plate example, this example is simulated

Property	Value
Density [kg/m^3]	2675
Young modulus [MPa]	72400
Poisson ratio [-]	0.33
Yield stress [MPa]	303
Hardening modulus [MPa]	0

Table 4.5: Material properties of the perfectly plastic cylindrical panel benchmark.

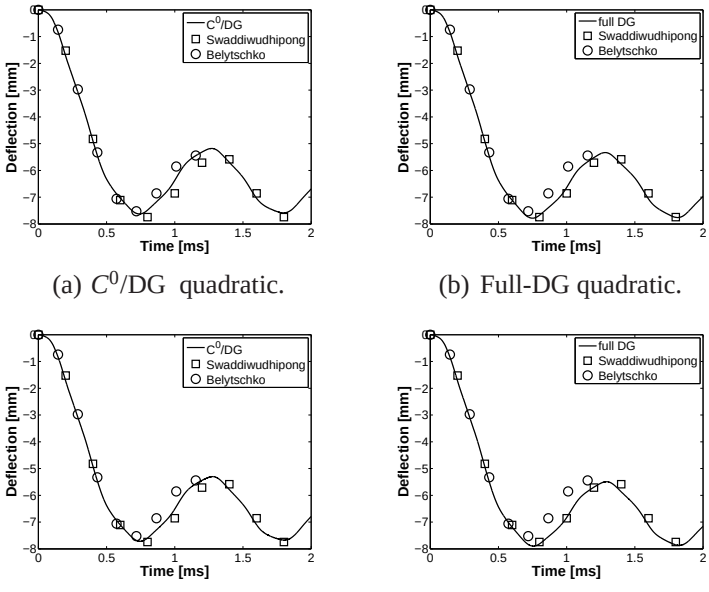

(a) C^0/DG quadratic. (b) Full-DG quadratic.

(c) C^0/DG cubic. (d) Full-DGcubic.

Figure 4.14: Results of the simply supported elasto-plastic plate subjected to uniform loading are in agreement with literature [39, 243].

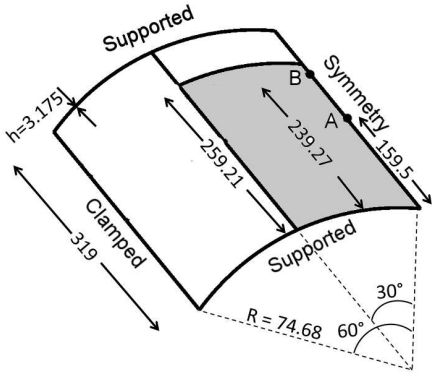

Figure 4.15: Perfectly plastic cylindrical panel benchmark. The Grey part is the zone where a normal initial velocity of $143.51[m/s]$ is prescribed.

using the explicit Hulbert-Chung time-integration algorithm without numerical dissipation, and using both the C^0/DG and the full-DG formulations. The results obtained with a 4×11 cubic quadrangles are displayed on Fig. 4.16 and are compared with the experimental data of T. Belytschko *et al.* [39, 45]. This Fig. shows that the developed method fits well the experimental data. Furthermore, snapshots of the deformation process are shown on Fig. 4.17 in the case of the full-DG formulations.

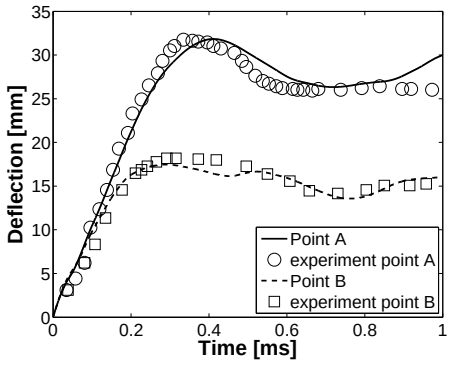

(a) C^0/DG .

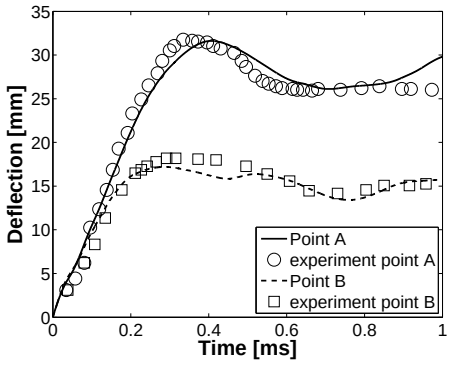

(b) Full-DG.

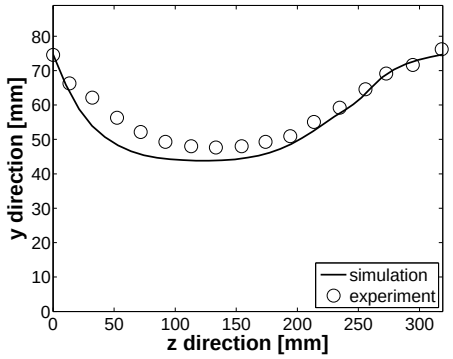

(c) Final symmetry plane outline for the full-DG.

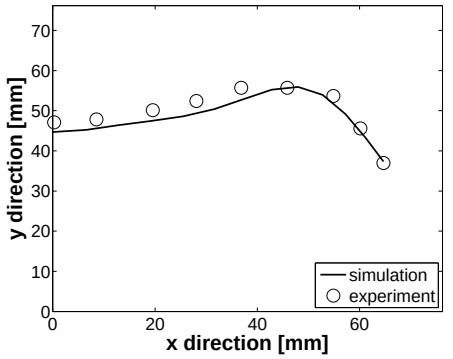

(d) Final radial section passing by point A for the full-DG.

Figure 4.16: Perfectly plastic cylindrical panel results for C^0/DG and full-DG formulations compared with T. Belytschko experiments [39].

MPI benchmarks

The efficiency of the parallel implementation is discussed on two previous examples by evaluating the speed-up. This number compares the time t_1 needed to perform the simulation on one processor with the time t_n needed to solve the simulation on n processors. Ideally, the speed-up has to be equal to,

$$\text{speed-up}_{\text{theoretical}} = \frac{t_n}{t_1} = \frac{1}{n}. \tag{4.195}$$

Nevertheless in practice, some data have to be exchanged during parallel computations and these MPI communications require time leading to a lower speed-up. However if the scheme is well implemented and if the cost of MPI communications is negligible, a value near the theoretical one is expected.

If the number of interface elements introduced between the mesh partitions is low compared with the number of elements in each partition, then the MPI communications are neg-

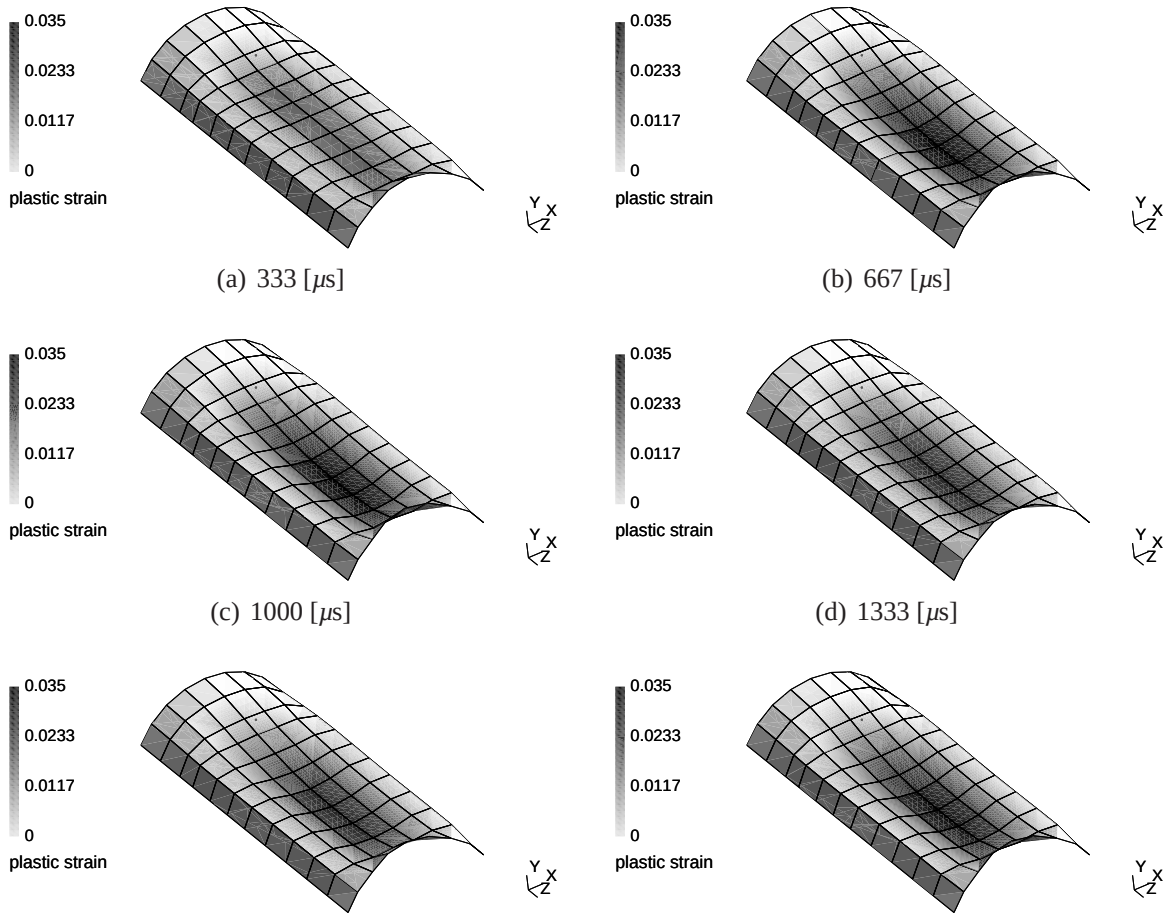

(a) 333 [μs] (b) 667 [μs]

(c) 1000 [μs] (d) 1333 [μs]

(e) 1667 [μs] (f) 2000 [μs]

Figure 4.17: Snapshots of the deformations process with the full-DG formulation for the perfectly plastic cylindrical panel.

ligible. In practice a finite element mesh includes thousands or millions of elements and is performed on tens or hundreds of processors and therefore acceptable speed-up can be obtained. To illustrate this, the two explicit benchmarks presented here-above are computed with thinner meshes on the supercomputer of our University called ”nic3”, which has height processors per node. For the square plate example a 60×60 and a 120×120 elements meshes are considered, and for the cylinder, a 24×76 as well as a 48×152 elements meshes are used. As these meshes represent a large computational cost on one processor and as we are interested only by the speed-up measure, only 1% of simulations are computed from one to sixteen processors with coarser mesh and the thinner meshes are used to perform simulation from sixteen to ninety-six processors. The speed-up ratios obtained in all cases are reported on Figure 4.18. For the plate example, a very good speed-up is obtained until height processors with the coarser mesh. After, the cost of MPI communications is not negligible and therefore

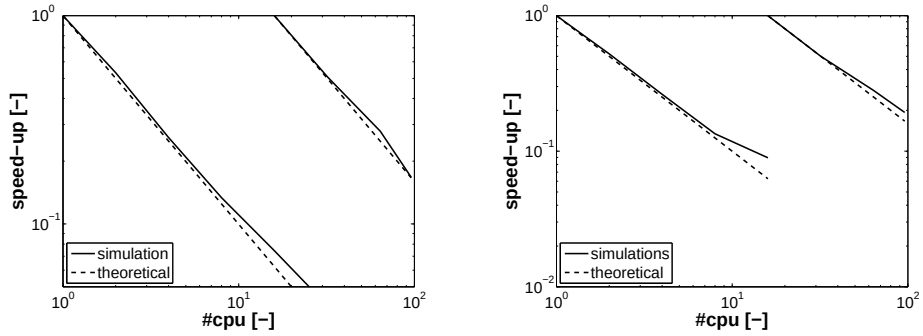

(a) Square plate. (b) Cylindrical panel.

Figure 4.18: Speed-up measures are near the theoretical value while the number of elements by partitions remains large compared with the number of interface elements between partitions.

the speed-up is lower than the theoretical one but it remains acceptable until 16 processors. For the cylinder example, an excellent speed-up is founded until height processors. Then for sixteen processors the reduced number of elements by partition (around one hundred) compared to the number of interface elements (around thirty) explains the lack of efficiency. This point is highlighted by the simulation with the thinner meshes showing a speed-up near the theoretical value until ninety-six processors as the number of elements by partition remains large compared to the number of ghost elements. This condition is generally met for classical problems where the speed-up of the suggested method will be near the theoretical value. Practically we will study larger problems, see Section 5.2 with more than one hundred thousand elements (*i.e.* problems with more than one million of dofs) with a high speed-up.

4.7 Conclusions

In this chapter, we present an original full-DG formulation of non-linear Kirchhoff-Love shells. The main difference of this method compared with other shell formulations is to consider discontinuous polynomial approximation between elements. The $\mathcal{C}^0$ and $\mathcal{C}^1$ continuity between elements are then ensured weakly by boundary interface terms. These ones are obtained similarly to other DG methods reported in the literature. Furthermore, although the out-of-plane shearing is negligible in Kirchhoff-Love theory, the stability term related to this shearing is used to guaranty the continuity of the normal displacement. This results in a one-field (displacement) formulation contrarily to usual shell implementations which use mixed formulation.

As it considers more degrees of freedom, the full-DG formulation is time consuming compared to the C^0/DG formulation where only $\mathcal{C}^1$ continuity is weakly ensured, while $\mathcal{C}^0$ continuity arises from continuous polynomial approximations. Nevertheless, on one hand, this formulation provides a powerful tool to perform parallel computation. Indeed, as it is demon-

strated in this chapter, the parallel implementation of the explicit Hulbert-Chung algorithm is mandatory with the recourse to DG. Indeed, we suggested an original parallel implementation, based on ghost elements between partitions to obtain a parallel scheme independent of the constitutive behavior. On the other hand, as it will be discussed in the next chapter the full-DG method developed herein can easily be combined with an extrinsic law to obtain a powerful and versatile tool to perform fracture mechanics simulations. In such a framework, the full-DG method has to model the continuum part of the deformation. Therefore, several numerical benchmarks are presented in this chapter to prove the ability of the full-DG formulation to be as accurate as other (continuous) shell formulations to model a continuum mechanics problem.

Chapter 5

Full-DG/ ECL framework for fracture mechanics of thin bodies

This chapter[1] extends the full-DG/ECL framework developed for Euler-Bernoulli beams in Chapter 3 to Kirchhoff-Love shells. The full-DG formulation was presented in Chapter 4 where it was demonstrated that this method is able to simulate a continuum mechanics problem with discontinuous elements. In particular, it was proved that the full-DG method provides in this case results as accurate as other methods presented in the literature. The advantage to have recourse to the discontinuous Galerkin method appears clearly in this chapter when simulating fracture mechanics problem. Indeed it allows inserting an extrinsic cohesive element during the computation without any change in the topology of the mesh. In fact, the interface elements naturally present in such a formulation can be easily replaced by a cohesive one at the onset of fracture.

Furthermore, as well as for the Euler-Bernoulli beams case, see Chapter 3, we suggest applying the cohesive principle directly on the reduced stresses to avoid the requirement of moving the neutral axis during the through-the-thickness crack propagation. Therefore the model presented in Section 3.3 is originally extended to the shells. As we neglect the out-of-plane shearing by assumption, the fracture mode III cannot be modeled and we also assumed, as in Chapter 4, a plane stress state. Therefore it limits the applicability of the suggested framework to cases where the 3D behavior of the crack is negligible. If it is not the case, we think that the recourse to a 3D FEmodel or at least a 3D crack model is needed to capture accurately the crack path. Such a 3D crack model can be combined to a shell formulation by having recourse to a multiscale approach as suggested by E. Wyart *et al.* [260]. Therefore in the following we focus on problems involving mode I or a combination of mode I and II. This modes combination is realized using the work of G. Camacho *et al.* [63], which consider a unique effective opening combining the contributions of the different modes. In fact, the recourse to an effective opening is an assumption widely admitted in the literature [73, 142, 168, 194, 196, 268, 274].

[1]The main applications presented in this chapter are submitted for publication in *International Journal of Fracture* [34].

Then, we perform several benchmarks to prove that our model is a powerful and versatile tool to simulate dynamic fracture mechanics. Indeed, we apply our framework to crack propagation as well as to fragmentation that are two very different fracture phenomena. Moreover, the loading conditions include concentrate force, pressure, blast and (rigid) impact demonstrating that the method can be used for different loading conditions. Furthermore, as we solve the constitutive behavior in the bulk and interface elements before fracture, the framework is suitable in linear small elastic strains as well as elasto-plastic finite deformations cases, as long as the fracture involves small scale yielding or brittle materials.

5.1 Combined full-DG/ECL

The idea of combining a full-DG method with an extrinsic cohesive law was pioneered by J. Mergheim *et al.* [157] and by R. Radovitzky *et al.* [211,228] in order to avoid the difficulties inherent to the classical cohesive approaches (as lengthy described in the Chapter 2). The main idea of this method can be summarized by substituting the full-DG weak formulation of shell (4.95) by,

$$\sum_e a^e_{\text{bulk}}(\boldsymbol{\varphi}_h,\delta\boldsymbol{\varphi}) + \sum_s \left[(1-\alpha_s)\, a^s_{\text{inter}}(\boldsymbol{\varphi}_h,\delta\boldsymbol{\varphi}) + \alpha_s a^s_{\text{cohesive}}(\llbracket\boldsymbol{\varphi}_h\rrbracket,\llbracket\delta\boldsymbol{\varphi}\rrbracket)\right] = b_{\text{ext}}(\boldsymbol{\varphi}_h,\delta\boldsymbol{\varphi}) + b_{\text{bound}}(\boldsymbol{\varphi}_h,\delta\boldsymbol{\varphi})\,, \tag{5.1}$$

with,

$$a^e_{\text{bulk}}(\boldsymbol{\varphi}_h,\delta\boldsymbol{\varphi}) = a^e_d(\boldsymbol{\varphi}_h,\delta\boldsymbol{\varphi}) + a^e_n(\boldsymbol{\varphi}_h,\delta\boldsymbol{\varphi}) + a^e_m(\boldsymbol{\varphi}_h,\delta\boldsymbol{\varphi})\,, \tag{5.2}$$

$$\begin{aligned} a^s_{\text{inter}}(\boldsymbol{\varphi}_h,\delta\boldsymbol{\varphi}) = {} & a^s_{nI1}(\boldsymbol{\varphi}_h,\delta\boldsymbol{\varphi}) + a^s_{nI2}(\boldsymbol{\varphi}_h,\delta\boldsymbol{\varphi}) + a^s_{nI3}(\boldsymbol{\varphi}_h,\delta\boldsymbol{\varphi}) + \\ & a^s_{mI1}(\boldsymbol{\varphi}_h,\delta\boldsymbol{\varphi}) + a^s_{mI2}(\boldsymbol{\varphi}_h,\delta\boldsymbol{\varphi}) + a^s_{mI3}(\boldsymbol{\varphi}_h,\delta\boldsymbol{\varphi}) - \\ & a^s_{sI3}(\boldsymbol{\varphi}_h,\delta\boldsymbol{\varphi})\,, \text{ and} \end{aligned} \tag{5.3}$$

$a^s_{\text{cohesive}}(\llbracket\boldsymbol{\varphi}_h\rrbracket,\llbracket\delta\boldsymbol{\varphi}\rrbracket)$ the bi-(non)-linear form of the cohesive terms that has to be defined. Furthermore, the different bulk terms $a^e_d(\boldsymbol{\varphi}_h,\delta\boldsymbol{\varphi})$ (4.62), $a^e_n(\boldsymbol{\varphi}_h,\delta\boldsymbol{\varphi})$ (4.63), $a^e_m(\boldsymbol{\varphi}_h,\delta\boldsymbol{\varphi})$ (4.64), as well as the interface terms $a^s_{nI1}(\boldsymbol{\varphi}_h,\delta\boldsymbol{\varphi})$ (4.77), $a^s_{nI2}(\boldsymbol{\varphi}_h,\delta\boldsymbol{\varphi})$ (4.87), $a^s_{nI3}(\boldsymbol{\varphi}_h,\delta\boldsymbol{\varphi})$ (4.90), $a^s_{mI1}(\boldsymbol{\varphi}_h,\delta\boldsymbol{\varphi})$ (4.78), $a^s_{mI2}(\boldsymbol{\varphi}_h,\delta\boldsymbol{\varphi})$ (4.88), $a^s_{mI3}(\boldsymbol{\varphi}_h,\delta\boldsymbol{\varphi})$ (4.91) and $a^s_{sI3}(\boldsymbol{\varphi}_h,\delta\boldsymbol{\varphi})$ (4.92) can be replaced by their linear counterparts in case of small deformations (see Section 4.4.2). Notice that compared with the Euler-Bernoulli beams case Eq. (3.110) there is no parameter γ_s in front of the term $a^s_{sI3}(\boldsymbol{\varphi}_h,\delta\boldsymbol{\varphi})$. In fact, this parameter is introduced for the beams to ensure the continuity of the normal displacement until the end of the fracture process, but in the case of shells this continuity is ensured implicitly thanks to the adjacent Gauss points making the recourse to the parameter γ_s useless.

In Eq. (5.1), α_s is a Boolean value, which switches from "false" to "true" when a fracture criterion is met. Indeed, before onset of fracture, Eq. (5.1) corresponds to the weak form of the shell problem (4.95) or (4.148), and thus inherits from its numerical properties of consistency and stability. Upon onset of fracture, the interface terms related to the DG framework are replaced by an extrinsic cohesive law, which has still to be defined. Note that in practice the

Boolean α_s is evaluated at each Gauss points of interface elements and therefore all Gauss points of an element are not necessarily fractured.

As it is discussed in Chapter 3 for beams, when considering the theory of thin structures, it is very difficult to separate the thickness part under tension from the part under compression, during a through-the-thickness crack propagation. So it was suggested, with success for Euler-Bernoulli beams, to apply the cohesive principle to the resultant stresses $\boldsymbol{n}^{\alpha}$ and $\tilde{\boldsymbol{m}}^{\alpha}$, which appear in thin bodies equations. The same concept is extended herein to take into account a mode I or II fracture, or a combination of modes I and II simultaneously.

Toward this end, an effective opening is defined herein for each mode and the combination of both modes is performed by following the idea suggested by G. Camacho *et al.* [63]. Note that in Kirchhoff-Love theory the out-of-plane shearing is neglected, which implies the impossibility to take into account a fracture in mode III.

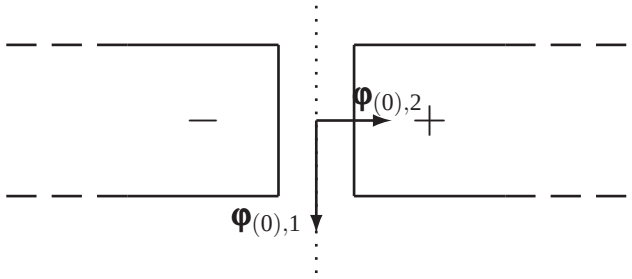

Figure 5.1: Local basis vectors on the interface element tangential to the shell surface. The interface is drawn with dotted line. By convention, $\boldsymbol{\varphi}_{(0),1}$ is parallel and $\boldsymbol{\varphi}_{(0),2}$ is normal to the interface.

Before developing the cohesive law, we assume that the convected basis, tangential to the shell, at the interface element obeys the following rules: vector $\boldsymbol{\varphi}_{(0),1}$ is parallel to the interface element and $\boldsymbol{\varphi}_{(0),2}$ is perpendicular to the interface element, as it is illustrated on Fig. 5.1. In the linear range (4.148), everything can be computed in the reference convected basis $\boldsymbol{\varphi}_{0,\alpha}$. On the contrary, in the non linear range (4.95) the different quantities have to be evaluated in the current convected basis $\boldsymbol{\varphi}_{,\alpha}$. Thus we unify both cases by using the notation $\boldsymbol{\varphi}_{(0),\alpha}$.

5.1.1 Mode I

Let us first discuss the case of the mode I opening, see Fig. 5.2. Considering the basis of the interface element as shown on Fig. 5.1, the resulting efforts are related to an effective opening whose aim is to consider the two parts (tension and bending) of the normal opening represented on Fig. 5.2.

Similarly to what has been suggested for Euler-Bernoulli beams (see Section 3.3), an original normal effective opening, corresponding to the mode I, is deduced from the tension

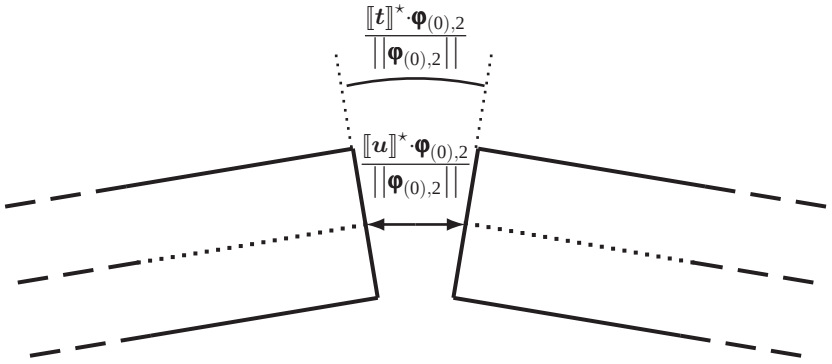

Figure 5.2: The two components of the normal opening $\Delta_n^\star$, view perpendicular to the shell. The neutral axis is drawn with a dotted line.

and bending openings

$$\Delta_n^\star = (1-\eta_I)\frac{[\![\boldsymbol{u}]\!]^\star \cdot \boldsymbol{\varphi}_{(0),2}}{||\boldsymbol{\varphi}_{(0),2}||} \pm \eta_I h_I^{\text{eq}} \frac{[\![\boldsymbol{t}]\!]^\star \cdot \boldsymbol{\varphi}_{(0),2}}{||\boldsymbol{\varphi}_{(0),2}||}. \tag{5.4}$$

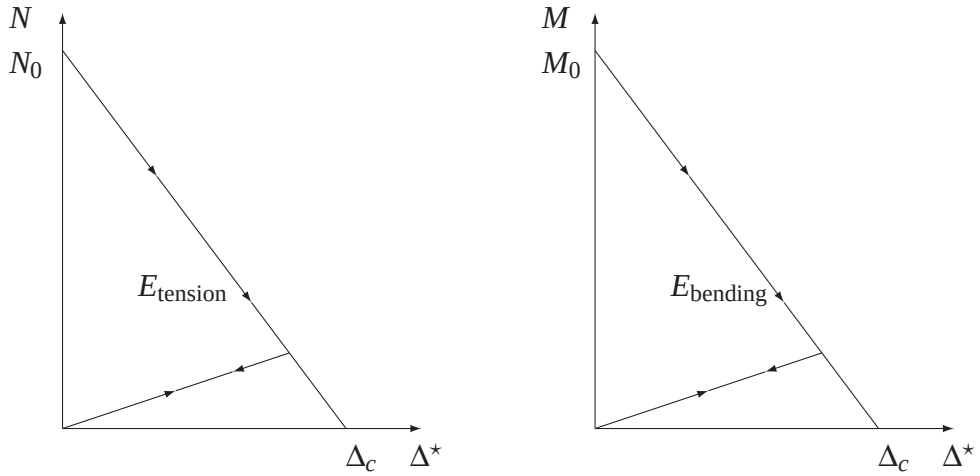

(a) Resultant membrane stress. (b) Resultant bending stress.

Figure 5.3: Linearly decreasing monotonic law.

In this expression $[\![\boldsymbol{u}]\!]^\star$ and $[\![\boldsymbol{t}]\!]^\star$ are respectively the effective openings in displacement and in rotation, resulting from the use of a DG method before fracture activation. Indeed at fracture initiation the opening in displacement $[\![\boldsymbol{u}]\!]$ and $[\![\boldsymbol{t}]\!]$ are not exactly equal to zero due to the weak enforcement of compatibility. In order to have null openings at fracture initialization

these initial values $[\![\boldsymbol{u}]\!]_0$ and $[\![\boldsymbol{t}]\!]_0$ are subtracted from $[\![\boldsymbol{u}]\!]$ and $[\![\boldsymbol{t}]\!]$, yielding

$$[\![\boldsymbol{u}]\!]^\star = [\![\boldsymbol{u}]\!] - [\![\boldsymbol{u}]\!]_0 \,, \tag{5.5}$$

$$[\![\boldsymbol{t}]\!]^\star = [\![\boldsymbol{t}]\!] - [\![\boldsymbol{t}]\!]_0 \,. \tag{5.6}$$

Moreover, the parameter η_I ensures that the coupling between the resulting tensile stress and the resulting bending stress respects the energetic balance (*i.e.* that the fracture process releases the correct amount of energy), which is obtained for

$$\eta_I = \frac{\frac{1}{h_I^{\text{eq}}}\left|\tilde{m}_0^{22}\right|}{n_0^{22} + \frac{1}{h_I^{\text{eq}}}\left|\tilde{m}_0^{22}\right|}, \tag{5.7}$$

where n_0^{22} and $\tilde{m}_0^{22}$ are respectively the traction effort and the bending couple at fracture initialization. The factor h_I^{eq} in Eqs. (5.4) and (5.7) ensures the respect of energetic balance, as it is shown below for a pure bending case. Considering the linearly decreasing cohesive law as on Fig. 5.3[2],

$$\left\langle \tilde{m}^{22} \right\rangle_{\text{coh}} = \tilde{m}_0^{22}\left(1 - \frac{\Delta_n^\star}{\Delta_c}\right), \tag{5.8}$$

assuming that the bending leading to fracture is equivalent to a tensile stress, the critical bending stress writes,

$$\frac{\tilde{m}_0^{22}}{h_I^{\text{eq}}} = h\sigma_{\text{c}} \,, \tag{5.9}$$

and using the definition of the resulting normal opening (5.4),

$$\begin{aligned}\int_0^{\Delta_{rc}} \left\langle \tilde{m}^{22} \right\rangle_{\text{coh}} d\left[\frac{[\![\boldsymbol{t}]\!]^\star \cdot \boldsymbol{\varphi}_{(0),2}}{\left|\left|\boldsymbol{\varphi}_{(0),2}\right|\right|}\right] &= \int_0^{\Delta_c} \pm\frac{1}{h_I^{\text{eq}}}\left\langle \tilde{m}_0^{22} \right\rangle \left(1 - \frac{\Delta_n^\star}{\Delta_c}\right) d\Delta_n^\star \\ &= \frac{1}{h_I^{\text{eq}}} h_I^{\text{eq}} h\sigma_{\text{c}} \frac{\Delta_c}{2} = hG_c \,,\end{aligned} \tag{5.10}$$

where $\Delta_{rc} = \frac{[\![\boldsymbol{t}]\!]_c^\star \cdot \boldsymbol{\varphi}_{(0),2}}{\left|\left|\boldsymbol{\varphi}_{(0),2}\right|\right|} = \frac{1}{h_I^{\text{eq}}}\Delta_c'$ is the critical opening in rotation, for which the fracture process is completed, where G_c and σ_{c} are respectively the fracture energy and a spall stress depending on the material only, where $\Delta_c = \frac{2G_c}{\sigma_{\text{c}}}$ is critical opening for a linear cohesive law (see Fig. 5.3), and where $\pm$ sign depends on the direction of bending. Let us remark that in relation (5.4), sign $+$ is used if $\tilde{m}_0^{22} < 0$, while sign $-$ is used otherwise. The assumption (5.9) provides a relation to compute the value of h_I^{eq}. For a pure bending problem in linear elasticity the fracture at skin occurs for,

$$\tilde{m}_0^{22} = \frac{h^2\sigma_{\text{c}}}{6} \,, \tag{5.11}$$

[2]The demonstration remains valid with another cohesive law.

and thus, using Eq. (5.9) $h_I^{\text{eq}} = \frac{h}{6}$.

Nevertheless, in the case of a tension/bending coupled problem, the equivalent thickness has to be computed considering the bending part of the stress leading to,

$$h_I^{\text{eq}} = \frac{\tilde{m}_0^{22}}{h\sigma_c - n_0^{22}}, \tag{5.12}$$

which under linear elasticity hypothesis, as fracture occurs when $\frac{6\tilde{m}_0^{22}}{h^2} + \frac{n_0^{22}}{h} = \sigma_c$ becomes,

$$h_I^{\text{eq}} = \frac{h}{6}, \tag{5.13}$$

as presented for Euler-Bernoulli beam in Chapter 3.

5.1.2 Mode II

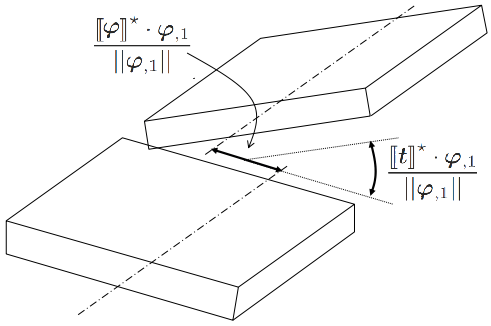

Figure 5.4: The two components of the tangential opening $\Delta_t^\star$. Before opening, the element axes are the same and the two crack lips are in the same plane.

Following exactly the same argumentation for the tangential effective opening in mode II as drawn on Fig. 5.4 reads,

$$\Delta_t^\star = (1-\eta_{II}) \frac{[\![\boldsymbol{u}]\!]^\star \cdot \boldsymbol{\varphi}_{(0),1}}{\left|\left|\boldsymbol{\varphi}_{(0),1}\right|\right|} \pm \eta_{II} h_{II}^{\text{eq}} \frac{[\![\boldsymbol{t}]\!]^\star \cdot \boldsymbol{\varphi}_{(0),1}}{\left|\left|\boldsymbol{\varphi}_{(0),1}\right|\right|}. \tag{5.14}$$

In this expression, the parameter η_{II} ensures that the coupling between the resulting shear stress and the resulting torsion respects the energetic balance, which is obtained for

$$\eta_{II} = \frac{\frac{1}{h_{II}^{\text{eq}}} \left|\left\langle \tilde{m}_0^{21} \right\rangle\right|}{\left\langle n_0^{21} \right\rangle + \frac{1}{h_{II}^{\text{eq}}} \left|\left\langle \tilde{m}_0^{21} \right\rangle\right|}, \tag{5.15}$$

where n_0^{21} and $\tilde{m}_0^{21}$ are respectively the shearing effort and the torsion torque at fracture initialization and where the equivalent thickness of mode II ensuring the energetic balance is given by,

$$h_{II}^{\text{eq}} = \frac{\tilde{m}_0^{21}}{h\tau_c - n_0^{21}} = \frac{\tilde{m}_0^{21}}{h\beta\sigma_c - n_0^{21}}, \tag{5.16}$$

where $\tau_c = \beta\sigma_c$ is the shearing critical strength and where $\beta = \frac{K_{IIc}}{K_{Ic}}$ is the fracture mode coupling parameter. Finally, sign $+$ is used in Eq. (5.14) when $\tilde{m}_0^{21} < 0$, and otherwise the sign $-$ is used, following the same convention given for $\tilde{m}_0^{22}$ in mode I.

5.1.3 Modes Combination

Now the combination between modes I and II is realized in a similar way as achieved by several authors [73, 142, 168, 194, 196, 268, 274] when considering Cauchy stress tensors for 3D TSL. This method, which was first suggested by G. Camacho *et al.* [63], and extended a few years later by M. Ortiz *et al.* [191], considers an effective stress σ_{eff} to detect fracture initialization, with the criteria: $\sigma_{\text{eff}} > \sigma_c$, and allows fracture in compression happening if the shearing stress is sufficiently large,

$$\sigma_{\text{eff}} = \begin{cases} \sqrt{\sigma^2 + \beta^{-2}\tau^2} & \text{if } \sigma \geq 0 \\ \frac{1}{\beta} \ll |\tau| - \mu_c |\sigma| \gg & \text{if } \sigma < 0 \end{cases}. \tag{5.17}$$

In this criterion, σ and τ are respectively the normal and tangential Cauchy stress at the integration point where fracture is evaluated and μ_c is the friction parameter, depending on the material only. The operator $\ll \bullet \gg$ is equal to $\bullet$ if $\bullet \geq 0$ and 0 otherwise. The initiation criterion (5.17) can still be considered in the present work. Indeed, from the resulting stresses of the shell formulation, the Cauchy stress tensor can be directly evaluated through-the-thickness of the body, either analytically for linear elasticity or at Simpson points on the thickness for non-linear shells.

Furthermore, in the coupled case, the equivalent thickness of modes I and II are determined respectively with the values of $\sigma = \sigma_I$ and $\tau = \tau_{II}$ reached in Eq. (5.17) when $\sigma_{\text{eff}} = \sigma_c$ leading to,

$$h_I^{\text{eq}} = \frac{\tilde{m}_0^{22}}{h\sigma_I - n_0^{22}} \text{ and,} \tag{5.18}$$

$$h_{II}^{\text{eq}} = \frac{\tilde{m}_0^{21}}{h\tau_{II} - n_0^{21}}. \tag{5.19}$$

However, in this new formulation for thin structures the cohesive law should be written in terms of resulting values instead of Cauchy stress, and some quantities and notations have to be first introduced:

- The effective opening $\Delta^\star$ is a combination of the two effective openings $\Delta_n^\star$ (5.4) and $\Delta_t^\star$ (5.14). So $\Delta^\star$ allows taking into account a coupling between the two fracture modes. Its value is an extension of the formulation, presented by M. Ortiz *et al.* in [191], to thin structures:

$$\Delta^\star = \sqrt{\ll \Delta_n^\star \gg^2 + \beta^2 \Delta_t^{\star 2}}. \tag{5.20}$$

  The use of the operator $\ll \bullet \gg$ is mandatory. Indeed if the rupture occurs in compression, the normal opening has to be equal to zero, as in compression the normal opening is negative, which means that there is a penetration between elements. Obviously this latter case has no physical meaning and forces have to be introduced between elements. In place of contact forces, the DG terms $a^s_{nI2}(\boldsymbol{\varphi}_h, \delta\boldsymbol{\varphi})$ and $a^s_{nI3}(\boldsymbol{\varphi}_h, \delta\boldsymbol{\varphi})$ (see equations (4.87) and (4.90)) can also be used to weakly enforce a zero penetration.

- The critical opening Δ_c is the opening for which the fracture process is completed, meaning no remaining forces exist between the fractured sides. Therefore, for this value, the energy released has to be equal to G_c, and for linear decreasing monotonic cohesive laws, $\Delta_c = \frac{2G_c}{\sigma_c}$.

- The maximal effective opening reached during the simulation $\Delta^\star_{max}$, is an internal variable tracking the maximum opening history.

Now the cohesive law can be formulated in terms of these new definitions. As it is well known that for brittle materials the shape of the cohesive law has little influence on numerical results, as long as the law is monotonically decreasing, a simple linear decreasing law is considered in this work. In case of unloading the effort decreases linearly to zero (see Fig. 5.3). By application of cohesive principle on stress resultant vectors, the following cohesive model reads,

1. Tensile case ($\sigma \geq 0$ at mid-surface)[3],

   - if $\Delta^\star \geq \Delta^\star_{max}$ (loading case),

$$\left\langle \tilde{m}^{22} \right\rangle_{\text{coh}} = \tilde{m}_0^{22} \left(1 - \frac{\Delta^\star}{\Delta_c}\right) \frac{\Delta_n^\star}{\Delta^\star} \tag{5.21}$$

$$\left\langle n^{22} \right\rangle_{\text{coh}} = n_0^{22} \left(1 - \frac{\Delta^\star}{\Delta_c}\right) \frac{\Delta_n^\star}{\Delta^\star} \tag{5.22}$$

$$\left\langle \tilde{m}^{21} \right\rangle_{\text{coh}} = \tilde{m}_0^{21} \beta \left(1 - \frac{\Delta^\star}{\Delta_c}\right) \frac{|\Delta_t^\star|}{\Delta^\star} \tag{5.23}$$

$$\left\langle n^{21} \right\rangle_{\text{coh}} = n_0^{21} \beta \left(1 - \frac{\Delta^\star}{\Delta_c}\right) \frac{|\Delta_t^\star|}{\Delta^\star} \tag{5.24}$$

[3]Note that the cohesive zone is in term of the traction components $n^{\alpha\beta}$ and not $\tilde{n}^{\alpha\beta}$ even in the linear range.

- if $\Delta^\star < \Delta^\star_{max}$ (unloading case),

$$\left\langle \tilde{m}^{22} \right\rangle_{\text{coh}} = \tilde{m}_0^{22} \left(\frac{\Delta^\star}{\Delta^\star_{max}} - \frac{\Delta^\star}{\Delta_c} \right) \frac{\Delta^\star_n}{\Delta^\star} \tag{5.25}$$

$$\left\langle n^{22} \right\rangle_{\text{coh}} = n_0^{22} \left(\frac{\Delta^\star}{\Delta^\star_{max}} - \frac{\Delta^\star}{\Delta_c} \right) \frac{\Delta^\star_n}{\Delta^\star} \tag{5.26}$$

$$\left\langle \tilde{m}^{21} \right\rangle_{\text{coh}} = \tilde{m}_0^{21} \beta \left(\frac{\Delta^\star}{\Delta^\star_{max}} - \frac{\Delta^\star}{\Delta_c} \right) \frac{|\Delta^\star_t|}{\Delta^\star} \tag{5.27}$$

$$\left\langle n^{21} \right\rangle_{\text{coh}} = n_0^{21} \beta \left(\frac{\Delta^\star}{\Delta^\star_{max}} - \frac{\Delta^\star}{\Delta_c} \right) \frac{|\Delta^\star_t|}{\Delta^\star} \tag{5.28}$$

2. Compression case ($\sigma < 0$ at mid-surface),

- if $\Delta^\star \geq \Delta^\star_{max}$ (loading case),

$$\left\langle \tilde{m}^{21} \right\rangle_{\text{coh}} = \tilde{m}_0^{21} \left(1 - \frac{\Delta^\star}{\Delta_c} \right) \tag{5.29}$$

$$\left\langle n^{21} \right\rangle_{\text{coh}} = n_0^{21} \left(1 - \frac{\Delta^\star}{\Delta_c} \right) \tag{5.30}$$

- if $\Delta^\star < \Delta^\star_{max}$ (unloading case),

$$\left\langle \tilde{m}^{21} \right\rangle_{\text{coh}} = \tilde{m}_0^{21} \left(\frac{\Delta^\star}{\Delta^\star_{max}} - \frac{\Delta^\star}{\Delta_c} \right) \tag{5.31}$$

$$\left\langle n^{21} \right\rangle_{\text{coh}} = n_0^{21} \left(\frac{\Delta^\star}{\Delta^\star_{max}} - \frac{\Delta^\star}{\Delta_c} \right) \tag{5.32}$$

where in this last case the condition $\frac{|\Delta^\star_t|}{\Delta^\star} = \frac{1}{\beta}$ (*cf.* equation (5.20)) is taken into account.

The use of n_0^{22}, $\tilde{m}_0^{22}$, n_0^{21}, $\tilde{m}_0^{21}$ allows guarantying the continuity of stresses at fracture initialization. If this continuity is not ensured, K. Papoulia *et al.* [196] have demonstrated that there are some convergence problems. Furthermore, as at fracture initialization the ratios $\frac{\Delta^\star_n}{\Delta^\star}$ and $\frac{|\Delta^\star_t|}{\Delta^\star}$ are undetermined, their initial values are chosen respectively equal to one and $\frac{1}{\beta}$ in order to ensure the continuity of efforts. It must be noticed that the choice of tensile or compressive case is performed at fracture initialization. Therefore, although unloading and/or compression/tension shifts can be accounted for during the fracture process, as shown on Fig. 5.3, this model is not able to shift from a fracture process in tension to a fracture process in compression (*e.g.* start the fracture in compression and end up the fracture in tension). Finally, with these definitions, the cohesive terms $a^s_{\text{cohesive}}(\llbracket \boldsymbol{\varphi}_h \rrbracket, \llbracket \delta\boldsymbol{\varphi} \rrbracket)$ of equation (5.1) can be written

$$\begin{aligned} a^s_{\text{cohesive}}(\llbracket \boldsymbol{\varphi}_h \rrbracket, \llbracket \delta\boldsymbol{\varphi} \rrbracket) = & \int_s \left\langle \bar{j}\boldsymbol{n} \right\rangle_{\text{coh}} \cdot \llbracket \delta\boldsymbol{\varphi} \rrbracket \, \nu_\alpha^- \, d\partial\mathcal{A}_e \\ & + \int_s \left\langle \bar{j}\bar{\lambda}_h \tilde{\boldsymbol{m}} \right\rangle_{\text{coh}} \cdot \llbracket \delta\boldsymbol{t} \rrbracket \, \nu_\alpha^- \, d\partial\mathcal{A}_e \,, \end{aligned} \tag{5.33}$$

where the components of $\langle \boldsymbol{n} \rangle_{\text{coh}}$ and $\langle \tilde{\boldsymbol{m}} \rangle_{\text{coh}}$ are computed thanks to the set of equations (5.21 - 5.32), with others components of the resultant stresses equal to zero. Note that all these definitions depend on the choice of manifold used on the interface. As mentioned earlier, this paper follows this convention: $\boldsymbol{\varphi}_{(0),1}$ is parallel to the interface and $\boldsymbol{\varphi}_{(0),2}$ is perpendicular to the interface, as it is illustrated on Fig. 5.1.

5.2 Full-DG/ECL framework applications

The full-DG formulation presented in Chapter 4 and the extrinsic cohesive model developed above are combined in this section to solve several fracture mechanics problems. As previously discussed our suggested framework is suitable to dynamic fracture mechanics and we restrict the application to this field as it is the topic of this thesis. Nevertheless we try to cover a large variety of phenomena in the dynamic range. In particular, it is proved herein that our framework can be applied to crack propagation as well as fragmentation which are two very different fracture phenomena. The first one is investigated in linear and non-linear range and the second one is restricted to linear range. We validate our method by comparing results with numerical and experimental data coming from the literature.

5.2.1 Dynamic crack propagations

We present in this section several benchmarks which study the dynamic crack propagation in initially notched specimen.

Mode I dynamic crack propagation: spall test of a notched specimen

This example, performed by P. Zavattieri [269], considers the dynamic crack propagation of the single-edge notched specimen represented on Fig. 5.5. The different material properties are summarized in Tab. 5.1. Contrarily to [269], where cohesive elements are only inserted along a predefined crack path, with this full-DG framework, the crack can *a priori* follows any direction. As the crack should propagate straightforwardly, for symmetry reasons, the test is numerically performed using structured and unstructured meshes, successively, in order to show the convergence of the method for both mesh configurations. Results on a structured mesh of $3200 = 40 \times 80$ (width $\times$ length) bi-cubic quadrangles are considered as the reference solution.

The test is performed using an explicit time integration algorithm without numerical dissipation (spectral radius equal to one). The force *vs.* displacement curve at the top edge of the plate is illustrated on Fig. 5.6(a), where some characteristic points obtained by P. Zavattieri [269] are also reported, showing an excellent correlation between the results. This force *vs.* displacement curve shows the effect of a wave propagation in the bar, reflecting on the symmetry axis before propagating the crack. Fig. 5.6(b) plots the energy released during the simulation with the structured mesh:

$$G = \frac{W_{ext} - W_{int}}{h\Delta a}, \tag{5.34}$$

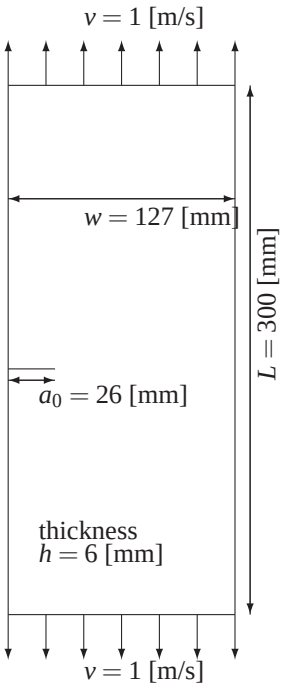

Figure 5.5: Single-edge notched specimen.

Property	Value
Young modulus [GPa]	200
Poisson ratio [-]	0.3
Density [kg/m^3]	7850
Fracture energy [J/m^2]	12250
Fracture stress [MPa]	700
Coupling parameter [-]	1
Frictional coefficient [-]	0.

Table 5.1: Material properties for the single-edge notched test.

where W_{ext} is the work of external forces, W_{int} is the work of internal forces, h is the thickness and Δa is the total increment of crack length (101 [mm] in this case). The graphs shows that G increases (linearly) only during crack propagation and stabilizes itself at 12.021 [kJ/m^2] which is close to the material fracture energy of 12.250 [kJ/m^2] within a 1.8% relative gap. This test demonstrates the ability of the presented fracture model to dissipate the correct amount of energy during the fracture process.

Furthermore, this example is also simulated with two unsymmetric unstructured meshes. These two meshes are built with quadratic 6-node triangles, which are generated by prescribing a distance between two nodes at the crack tip of 2.5 and 5 [mm] successively. Further from the crack, the element size is twice larger. These specifications produce a coarse mesh of ap-

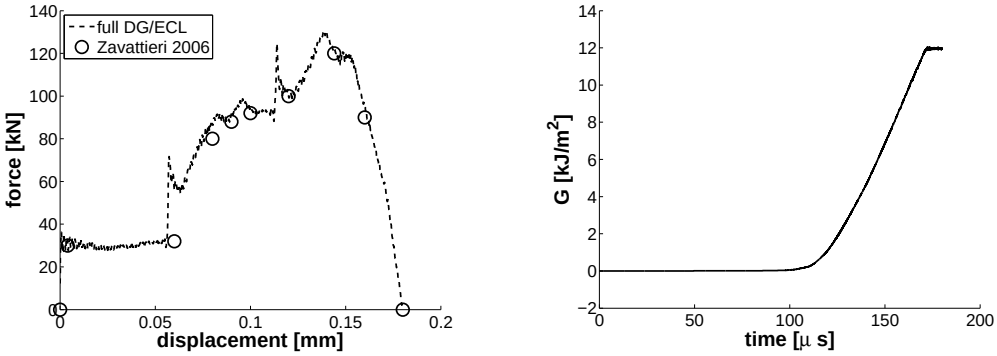

(a) Force *vs.* displacement. (b) Released energy.

Figure 5.6: Results of single-edge notched specimen for a structured mesh are in agreement with [269].

proximately 900 elements and a fine mesh of 2600 elements. Two simulations are performed with the coarse mesh, one without numerical dissipation and the other one with a low numerical damping (spectral radius of 0.9). Crack paths obtained with these unstructured meshes are illustrated on Fig. 5.7. It can be seen, that for the coarse mesh, a crack bifurcation appears if numerical damping is not introduced Fig. 5.7(a), while the use of numerical damping prevents this behavior, Fig. 5.7(b). The crack path obtained with the finer mesh and a spectral radius of 0.9 is illustrated on Fig. 5.7(c). In the three cases some elements blew up during the simulation. This phenomenon is purely numerical and occurs due to the combination of the fracture criterion and of the Gauss integration performed on the interface. The fracture is introduced at a Gauss point when a effective stress is larger than the characteristic material strength (*cfr.* Eq. (5.17)). Thus, the criterion can be satisfied at two Gauss points of adjacent edges at the same time step (see Fig. 5.9 for quadratic triangles). This is particularly true for small elements as the integration points on two different edges can be close. This eventually can lead to the blow up of an element. One way of avoiding this is to reduce the time step, or to give a statistical distribution of critical stress for the interface elements [276].

When analyzing the curve force *vs.* displacement illustrated on Fig. 5.8 it is observed that the results for the different meshes are in agreement. All curves are similar, which demonstrates that the unstructured meshes predict an excellent global result even if they don't reproduce the exact crack path. In particular, the finer mesh, shows a relative error of 2.7 % on maximal force, and of 4.3 % on the time where the force vanishes to zero.

Three-point bending impacted plate

This benchmark focuses on the simply supported notched plate presented above which is dynamically impacted in its center by a rigid cylinder with a prescribed velocity of 1 [m/s]. The setup of this benchmark, including the dimensions, is depicted on Fig. 5.10(a) and the material values are reported in Tab. 5.2. In fact, the crack propagation was previously reported

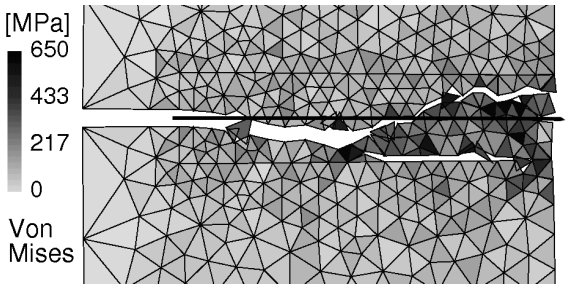

(a) Coarse mesh without dissipation.

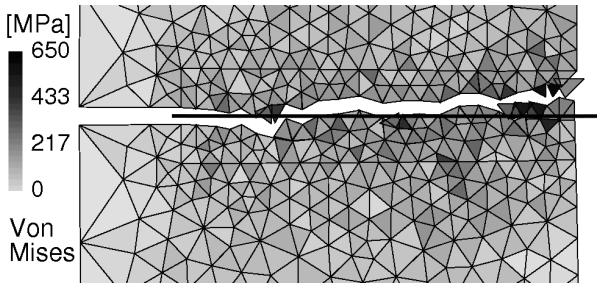

(b) Coarse mesh with numerical damping.

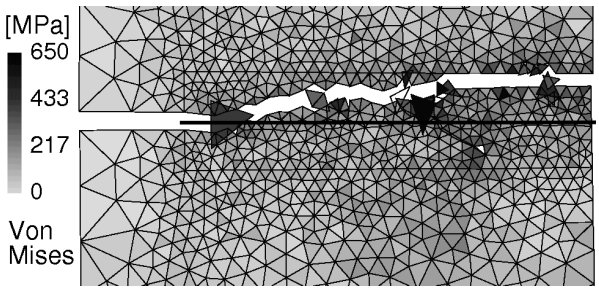

(c) Fine mesh with numerical damping.

Figure 5.7: Crack path obtained with unstructured meshes for the tensile test. The black line draws the reference crack path. The displacements are magnified 10 times.

in the literature by P. Zavattierri [269], who used shell elements combined with an intrinsic cohesive law for which cohesive elements are pre-inserted along the crack path. Furthermore he used a fracture criterion based on a maximal bending momentum, which is transformed herein to a criterion on the stress (*cfr.* Section 5.1.3). The mesh used, Fig. 5.10(b), has 40×80 cubic quadrangle elements. Finally, although the crack path is well defined for this case, due to the loading conditions, in our framework the crack can propagate along any interface elements. This shows that the stress wave propagation is not modified by the DG/ECL framework.

The simulation is performed on four CPUs using the Hulbert-Chung [123] time-integration algorithm, and without numerical dissipation. The crack propagation over time is displayed on Fig. 5.11 which also shows the results obtained by [269]. In both cases the crack propagation

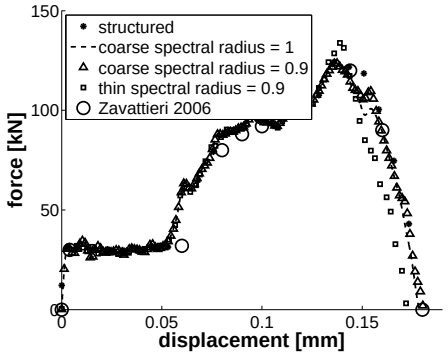

Figure 5.8: Small variations of the force-displacement relation are observed with different meshes for the tensile test.

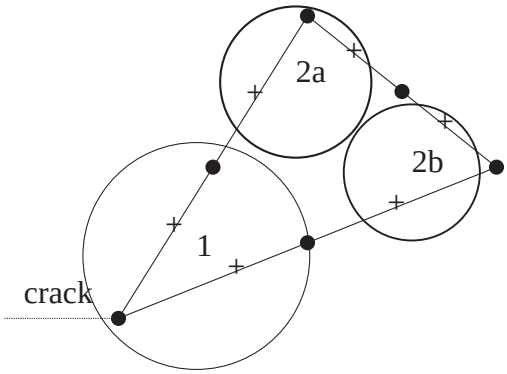

Figure 5.9: Activation of fracture at two Gauss points (+) on different edges. The initiation can occur simultaneously at both Gauss points of group 1 if the rupture criterion is reached at both points. The criterion can also be met later on for groups 2a and 2b independently. If all integration points are broken the element can blow up.

is initiated at the same time and the plate is broken at the same time. This example demonstrates that our fracture framework models with good accuracy the bending, in combination with contact.

Blast of a notched pressurized cylinder

A cylinder, with a diameter of 1.2 [m], a length of 1 [m] and with a thickness of 1 [mm], is blasted. It exhibits an initial crack of 56 [mm] centered on its height. It is made of Al2024-T3 aluminum alloy, which has the properties given in the Tab. 5.3. This example suggested by

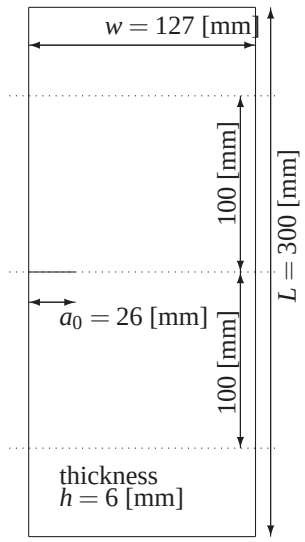

(a) Dimensions of the plate. The dotted lines represent the axes of the cylinders.

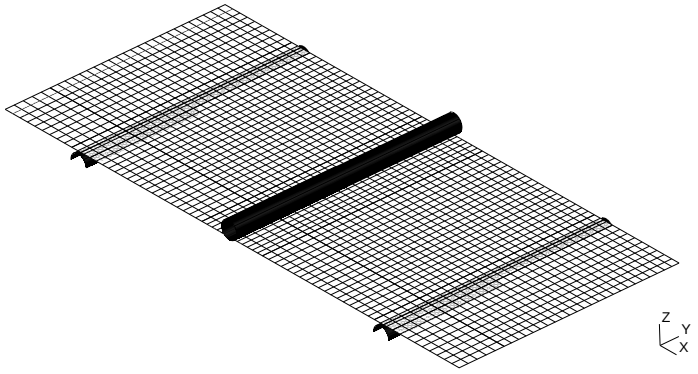

(b) Mesh.

Figure 5.10: Setup of the 3-point bending plate as previously presented by [269].

Property	Value
Young modulus [GPa]	200
Poisson ratio [-]	0.3
Density [kg/m^3]	7850
Fracture energy [J/m^2]	12250
Fracture stress [MPa]	2170
Coupling parameter [-]	1
Frictional coefficient [-]	0.

Table 5.2: Material properties for the single-edge notched test in bending.

R. Larsson *et al.* [133] is studied with two constitutive behaviors: a Hooke law and and a J_2-flow elasto-plastic law. Indeed, the obtained results with an elastic material law were not in correlation with experiments, as mentioned by R. Larsson *et al.* [133], who suggested to introduce an elasto-plastic finite deformation model to study the problem in a more realistic way.

Note that, contrarily to the elastic cases were the fracture energy is artificially increased to 67 [kJ/m^2], as suggested by R. Larsson *et al.* [133], to take into account the plastic work,

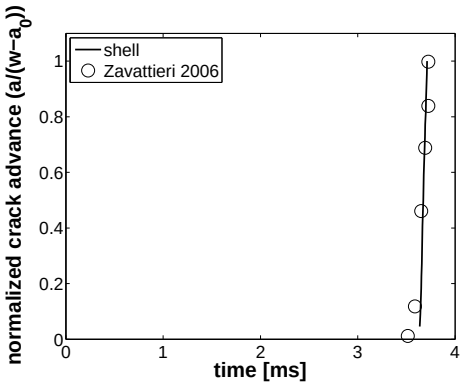

Figure 5.11: Crack propagation for the 3-point bending plate. Results are in agreement with [269].

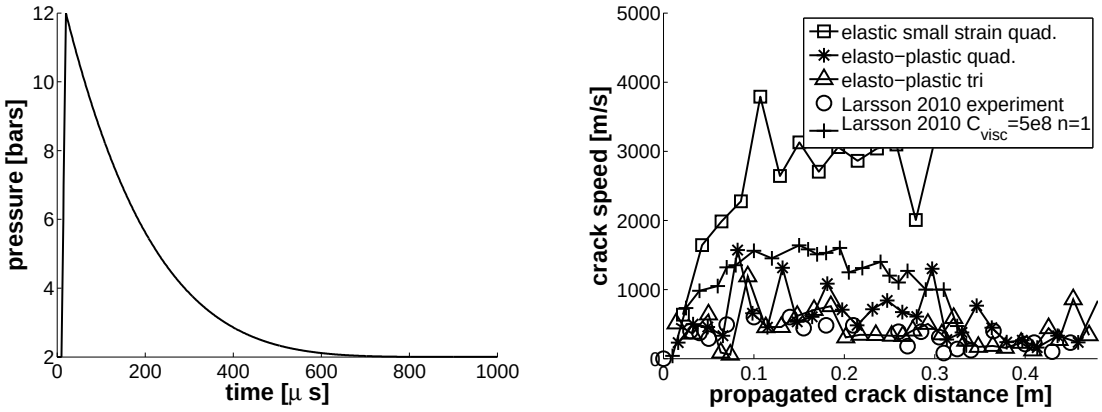

(a) Applied pressure.

(b) Crack speed.

Figure 5.12: Improvement of crack speed computation due to the consideration of elasto-plastic finite deformations.

the elasto-plastic behavior allows to use the real material values given R. Larsson *et al.* [133]. Furthermore, in order to avoid unphysical blow up of elements during crack propagation, the idea suggested by F. Zhou *et al.* [276], who used statistical distributions for the fracture strength σ_c, is considered. This strength can vary in a range around its nominal value (10% for the presented application) at each Gauss point of the interface elements which is physically justified by the material imperfections.

This notched cylinder is loaded by a blast wave, which is simulated using the internal pressure evolution depicted on Fig. 5.12(a). The cylinder is initially pressurized at $p_0 = 2$ [bars]. This initial pressure is applied in a quasi-static way. As the use of an implicit scheme is prohibitive due to the very thin mesh used to capture the crack path, the dynamic relaxation presented by M. Papadrakakis [195], which allows to perform a quasi-static analysis with an

Property	Value
Young modulus [GPa]	73.1
Poisson ratio [-]	0.33
Density [kg/m^3]	2780
Yield stress [MPa]	350
Hardening modulus [MPa]	800
Fracture strength [MPa]	650 ± 65
Fracture energy [kJ/m^2]	19 or 67

Table 5.3: Material properties of the Al2024-T3 alloy used to study the blast of a notched pressurized cylinder.

explicit dynamic scheme, is used to initiate the pressure in the cylinder, see Section 4.5 for a description of the method, before shifting to a classical explicit time integration.

Taking advantage of the problem symmetry, only the top side of the cylinder is modeled, successively, with 5500 bi-cubic quadrilateral elements and with an unstructured mesh of 18536 cubic triangles. These meshes ensure a mesh size smaller than the cohesive size (2.2), which is equal to 6 [mm] in this case. The simulations are performed on height processors using the explicit Hulbert-Chung scheme [123] including a low numerical dissipation (spectral radius of 0.9).

The speeds of crack propagation, measured experimentally and obtained by XFEM method by R. Larsson *et al.* [133], is also obtained with the presented DG/ECL framework for linear small strains and for elasto-plastic finite deformations. These speeds of crack propagation are shown in Fig. 5.12(b). As predicted by R. Larsson *et al.* [133], the introduction of plasticity allows to obtain results in agreement with experiments even if the speed at the beginning of the crack propagation seems faster in our model. After a propagation of 0.18 [m] the model matches well the experimental data. The crack path predicted by the simulations is shown on Figs. 5.13 and 5.14, respectively for triangular and quadrangle elements. A straight propagation is observed with quadrangle elements, so only the final crack path is depicted. With the unstructured triangular mesh, due to the heterogeneity in the mesh, the crack initially deviates but afterward it propagates straight before bifurcation when reaching the clamped part, as observed in the experimental data Fig. 5.13(h). As expected, an unstructured mesh converges toward the solution, but the structured mesh was used as comparison.

5.2.2 Dynamic fragmentations

The results previously presented demonstrate the ability of the full discontinuous Galerkin / extrinsic cohesive law framework to propagate an initial crack. Hereafter, we investigate the ability of such a model to initiate cracks. An interesting case of multiple crack initiations is the case of fragmentation. Recently, several authors investigate such a problem with 3D elements (in place of shell elements). On one hand, R. Radovitzky *et al.* [211] studied the fragmentation of a thick plate due to the impact of a rigid sphere. On the other hand, S. Levy [137] applied

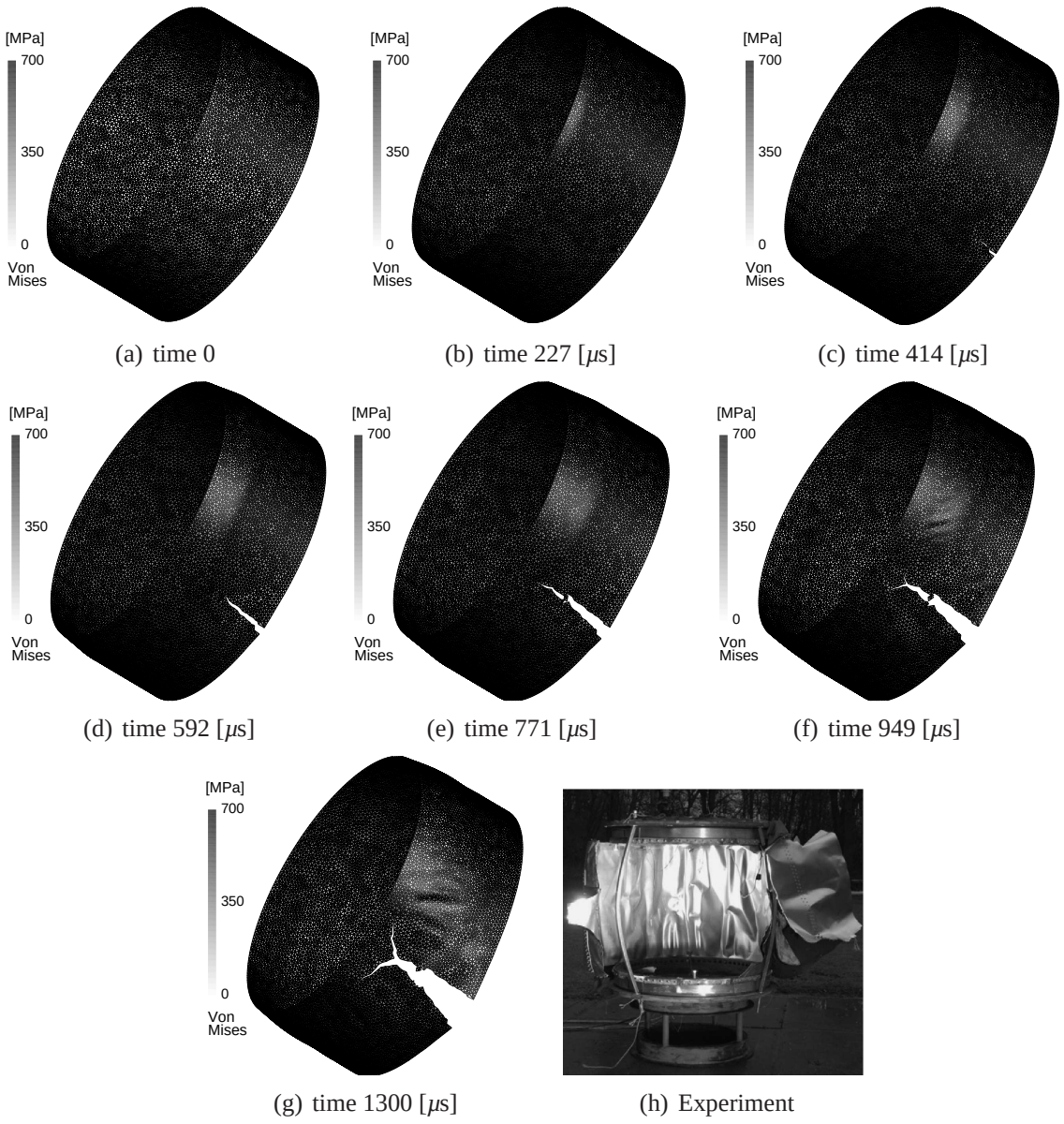

(a) time 0 (b) time 227 [μs] (c) time 414 [μs]

(d) time 592 [μs] (e) time 771 [μs] (f) time 949 [μs]

(g) time 1300 [μs] (h) Experiment

Figure 5.13: Crack propagation with the triangular mesh. Picture (h) comes from [133].

the same framework to the uniform expansion of a hollow sphere. This last case, can be solved with the linear shell formulation (4.148) when the thickness is small enough (the thickness of the sphere is 0.1 [mm] for an external radius of 10 [mm], which allows modelling the sphere as a thin body. Furthermore, the literature reports other fragmentation studies as, among others, the one presented by F. Zhou *et al.* [275]. In this reference the fragmentation of a plate ring under radial uniform expansion is studied with a classical extrinsic cohesive law for 2D elements. As they used a continuous formulation only serial computations were performed with a high computational time. The DG/ECL framework presented in this thesis allows using

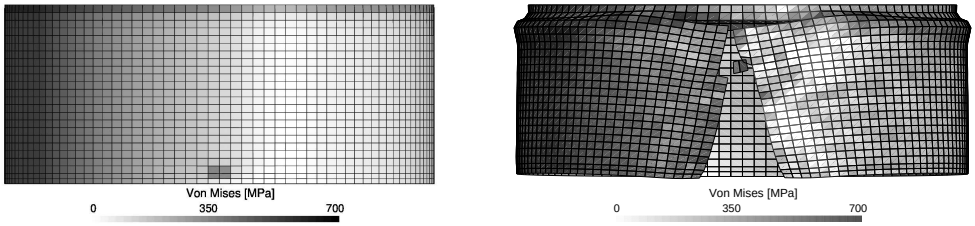

(a) Cylinder at the beginning of the simulation.

(b) Cylinder at the end of the simulation.

Figure 5.14: Straight crack path with the quadrangular mesh.

a parallel implementation and leads to a reduced computational time.

In the following, through the study of two benchmarks, a successful comparison between the 3D formulations of the literature and the shell framework presented herein is carried on.

Defect model: Weibull distribution

The mechanism of fragmentation is mainly controlled by the distribution of the defects in the specimen. Indeed, for a specimen made of a perfect material and uniformly loaded the fracture takes place in each point at the same time. Thus, the number of fragments obtained by a finite element analysis is equal to the number of elements contained in the mesh. On the contrary, in a component made of a non perfect material the fracture initiations of multiple cracks take place near the defects, which are the locations of stress concentration in the microstructure. Obviously, fracture occurs earlier at these stress concentrations and forms fragments composed of several elements. Thus the model of these defects is not straightforward in a finite element analysis as they cannot be represented by simple parameters. So a statistical distribution of the cohesive strength is commonly used as suggested by [80, 136, 137, 275].

In this section we consider a statistical distribution of the strength σ_c to be consistent with the fragmentation data of the literature based on the work of W. Weibull [255]. He performed some experiments which demonstrated that the tensile loading leading to fracture can vary for specimens of the same material and of the same geometry. Based on these experiments he suggested an empirical formula for the probability of fracture, accounting for the heterogeneity of the material,

$$P_f(\sigma, V) \;=\; 1 - \exp^{-N(\sigma,V)}, \tag{5.35}$$

where σ is the value of the equivalent stress and where V is the volume of the specimen. The function $N(\sigma, V)$ increases necessarily monotonically with σ and, therefore, [255] suggested, based on his experimental data, to employ a power law,

$$N(\sigma, V) \;=\; \begin{cases} \frac{V}{V_0}\left(\frac{\sigma-\sigma_{\min}}{\sigma_0}\right)^m & \text{if } \sigma \geq \sigma_{\min} \\ 0 & \text{otherwise} \end{cases}, \tag{5.36}$$

where V_0 is an arbitrary normalizing volume. Furthermore the other parameters σ_0, $\sigma_{\min}$ and m, representing respectively a stress scale factor, the minimal value for which the fracture can occur and the Weibull modulus, are all characteristics of the material.

The work of Weibull can be applied on the cohesive strength, which is then computed from

$$F(\sigma_c) = 1 - \exp^{-\left(\frac{\sigma_c - \sigma_{c,\min}}{\sigma_0}\right)^m} . \tag{5.37}$$

In practice it is easier to generate a uniform distribution between zero and one, from which a Weibull distribution can be easily obtained,

$$\sigma_{cs} = \sigma_0 \left(-\log(xrand)\right)^{\frac{1}{m}} + \sigma_{c,\min} , \tag{5.38}$$

where σ_{cs} is the value of the cohesive strength for the interface s and with *xrand* a random value coming from a uniform distribution between zero and one.

Therefore in this following, the simulations are performed with the linear full discontinuous Galerkin Kirchhoff-Love shell formulation presented in the Chapter 4. The fracture initiation is modeled by cohesive interface elements as described in Section 5.1. The cohesive strength of these elements follows a Weibull distribution, see Eq. (5.38).

Fragmentation of a plate ring

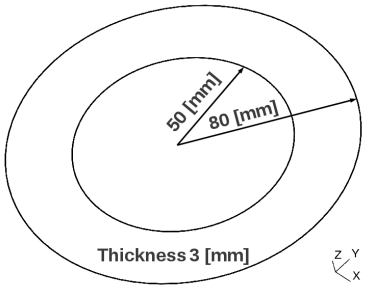

Figure 5.15: Geometry of the plate ring fragmentation.

The first example of fragmentation presented herein focuses on a thin plate ring under radial expansion, as shown on Fig. 5.15, and with the material properties given in Tab. 5.4. The fragmentation is consequent to a centrifugal force that is simulated, as suggested by F. Zhou *et al.* [275], by prescribing on each mass point i a body force computed as,

$$\boldsymbol{f}_i(\boldsymbol{r}) = m_i w^2 \boldsymbol{r} , \tag{5.39}$$

where m_i is the nodal mass, $\boldsymbol{r}$ is the radial vector of node i and where w is the angular velocity given by,

$$w = \begin{cases} \frac{w_0 t}{2\pi t_0} & \text{if } t \leq t_0 \\ \frac{w_0}{2\pi} & \text{if } t > t_0 \end{cases} . \tag{5.40}$$

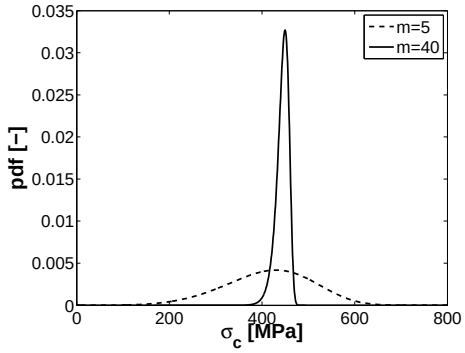

Figure 5.16: Weibull distribution: the more a material is homogeneous, the more the Weibull modulus is high and the more the pdf (probability density function) is concentrated around the peak value.

Property	Value
Young modulus [GPa]	320
Poisson ratio [-]	0.3
Density [kg/m^3]	3300
Fracture energy [J/m^2]	200
Minimal fracture strength [MPa]	0
Weibull modulus [-]	5 or 40
fracture strength scale factor [MPa]	450
Coupling parameter [-]	1
Frictional coefficient [-]	0.

Table 5.4: Material properties of the plate ring fragmentation.

Values $w_0 = 60000$ [rps] and $t_0 = 75$ [μs] are considered for the presented simulations.

The ring is meshed with 32380 quadratic triangles to obtain more or less the same number of interfaces than in the reference [275]. The simulation is performed on 16 CPUs for different Weibull moduli (5 and 40) with the explicit [123] time-integration algorithm associated to low numerical dissipation (spectral radius = 0.95). The stability parameters used are $\beta_1 = \beta_2 = 10$. In this case, as the out-of-plane displacement is prescribed, the value of β_3 has no influence on the results. Two Weibull moduli are successively considered, which give the strength distributions reported in Fig. 5.16.

For both Weibull moduli, the fragmentation processes, displayed on the Fig. 5.17 for $m = 5$ and Fig. 5.18 for $m = 40$, are coherent with the results provided by [275]. For $m = 5$, cracks initiate at the inner radius at approximately 28 [μs] and propagate more or less radially (with crack branching) toward the outer radius. With a Weibull modulus of 40, more cracks (*i.e.* smaller fragments) are generated and they appear later than for $m = 5$. This observation is in

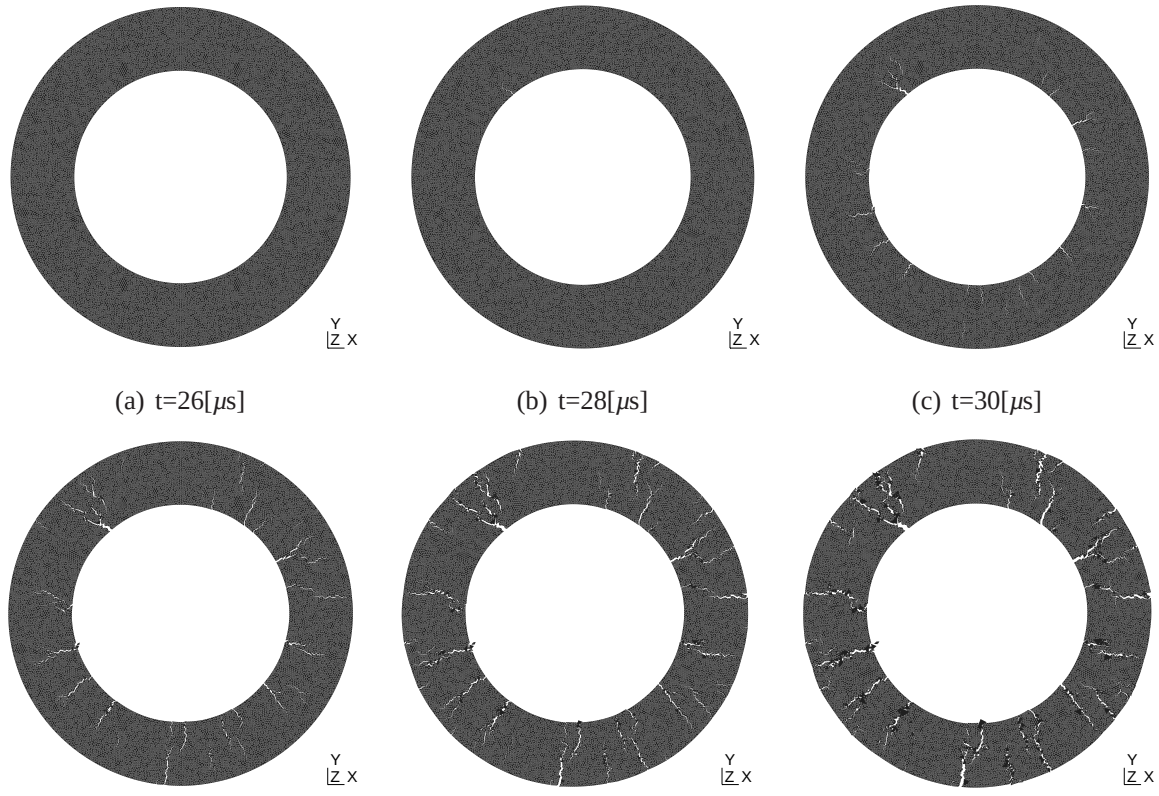

(a) t=26[μs] (b) t=28[μs] (c) t=30[μs]

(d) t=32[μs] (e) t=34[μs] (f) t=36[μs]

Figure 5.17: Fragmentation process of the plate ring with a Weibull modulus $m = 5$. Results are in agreement with [275].

agreement with [275] who noticed that "*a high Weibull modulus implies a fairly homogeneous material, it is not surprising that under sufficient loading conditions, crack initiation occurs at more locations [...] the ring rotation speed at crack initiation should be an increasing function of the Weibull modulus*". However in our simulations, for $m = 40$ the cracks reach the outer side after 44 [μs] instead of the 36 [μs] reported by [275].

Fragmentation of a sphere

The second fragmentation test considers a thin sphere under uniform expansion, as previously analyzed by S. Levy [137] with 3D elements. The material parameters of the ceramic sphere are reported in Tab. 5.5. The symmetry of the sphere is taken into account and only $1/8^{\text{th}}$ of the sphere is meshed with 144528 quadratic triangles. As the mesh corresponds to the mid-plane of the sphere, its radius is equal to $9.95[mm]$ for a thickness of $0.1[mm]$.

Note that the very thin mesh used to discretize the sphere leads to consider a problem with approximately 2.6 millions of unknowns. This large number of degrees of freedom

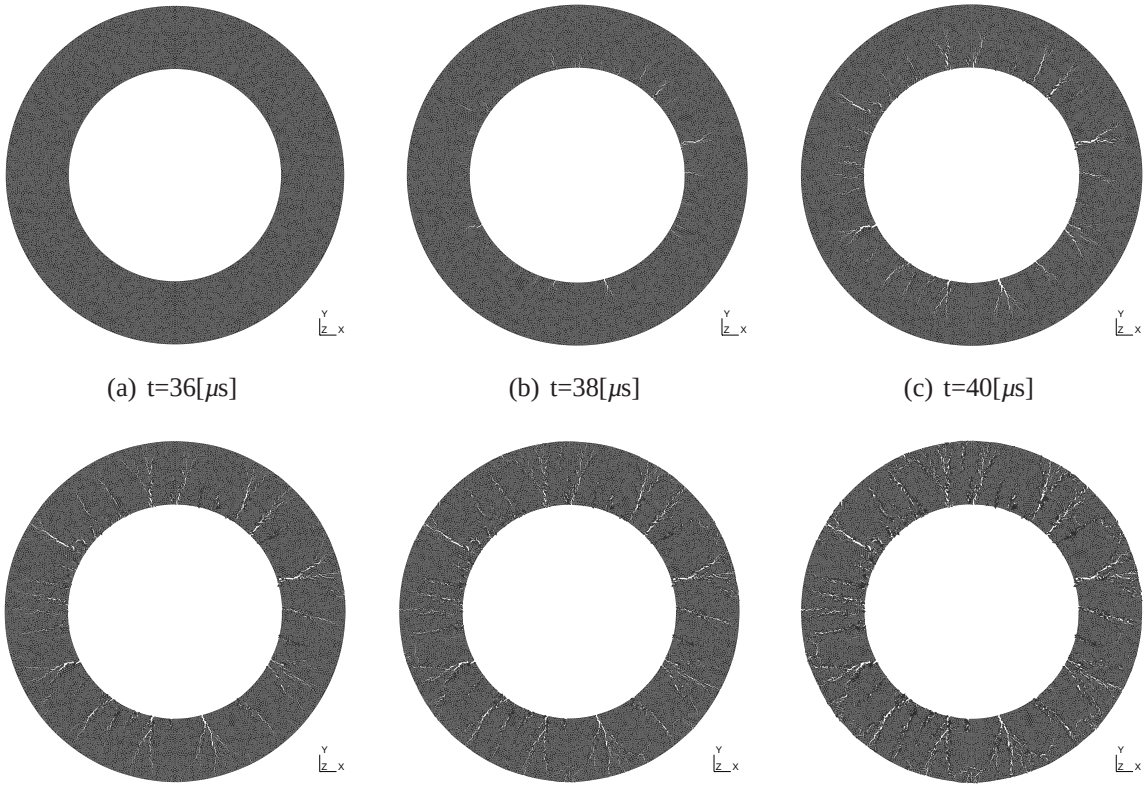

(a) t=36[μs] (b) t=38[μs] (c) t=40[μs]

(d) t=42[μs] (e) t=44[μs] (f) t=46[μs]

Figure 5.18: Fragmentation process of the plate ring with a Weibull modulus $m = 40$. Results are in agreement with [275].

can be treated by the parallel implementation presented in Section 4.5, and an acceptable computational time is obtained using 32 CPUs (about height hours). The stability parameters are set, to 10, 10 and 0.0001 respectively for β_1, β_2 and β_3. The uniform expansion of the sphere (centered in $(0,0,0)$) is simulated by prescribing an initial velocity profile following,

$$v_x(x,y,z) = \dot{\varepsilon}x, \tag{5.41}$$
$$v_y(x,y,z) = \dot{\varepsilon}y, \text{ and,} \tag{5.42}$$
$$v_z(x,y,z) = \dot{\varepsilon}z, \tag{5.43}$$

where $\dot{\varepsilon}$ is the strain rate. Three different strain rates are successively considered: $1e^4$, $2e^4$ and $1e^5[\mathrm{s}^{-1}]$.

Fig. 5.19 represents the time evolutions of the kinetic and potential energy of the sphere loaded with a strain rate of $1e^5\left[\mathrm{s}^{-1}\right]$. As an initial velocity is prescribed the kinetic energy is initially different from zero and decreases with the increase of the potential energy. This one reaches a peak value at time t_{peak} when part of the potential energy is released during the fracture process which occurs at that time. Afterward, the kinetic and potential energies

Property	Value
Young modulus [GPa]	370
Poisson ratio [-]	0.22
Density [kg/m^3]	3900
Fracture energy [J/m^2]	50
Minimal fracture strength [MPa]	264
Weibull modulus [-]	2
fracture strength scale factor [MPa]	50
Coupling parameter [-]	1
Frictional coefficient [-]	0

Table 5.5: Material properties for the fragmentation of a sphere.

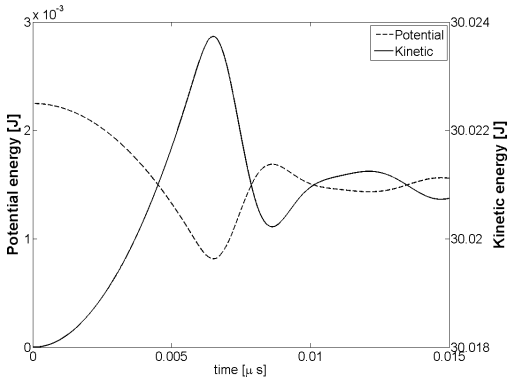

Figure 5.19: Kinetic and potential energy over time for the fragmentation of a sphere with a strain rate of $1e^5\left[\mathrm{s}^{-1}\right]$.

stabilize. The final time of our simulation is chosen as twice the value of t_{peak}, which differs for the different strain rates. Furthermore, the final configuration of the sphere is displayed on Fig. 5.20 in the case of a strain rate $\dot{\varepsilon} = 1e^4[\mathrm{s}^{-1}]$.

Fig. 5.21 represents the mass distribution and the number of fragments obtained in terms of the loading strain rate $\dot{\varepsilon}$. In the presented results, the dust-like fragments (*i.e.* the fragments composed of only one or two elements) are neglected as suggested by S. Levy [137]. The pictures show that the results obtained by the framework presented in this thesis are in agreement with the mass distribution and the number of fragments predicted by the work of [137], at the exception of the largest strain rate for which the shell formulation predicts less fragments. This difference is due to the small number of elements per fragment obtained with our mesh. Indeed, the mean value is around seven elements by fragment, which may cause a mesh dependency. Overall, our shell formulation is showed to be an efficient tool to predict fragmentation in brittle materials.

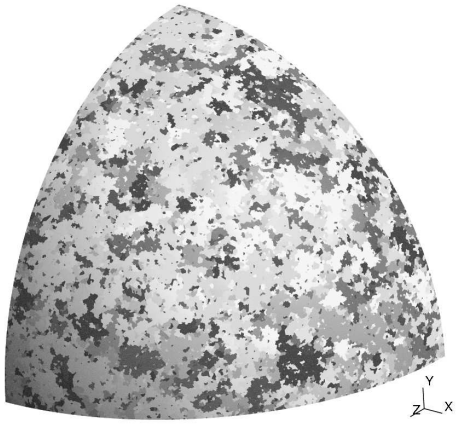

Figure 5.20: Final configuration of the fragmentation of a sphere with a strain rate of $1e^4\left[\mathrm{s}^{-1}\right]$.

5.3 Conclusions on the DG/ECL framework for thin bodies

In this chapter we have presented an original framework to simulate fracture mechanics problems in thin bodies. This framework is based on the combination between a DG discretization of the structure combined with an extrinsic cohesive law. The main advantage of the method is its ability to insert cohesive elements on the fly during the simulation without any topological mesh modifications. This simplicity leads to a straightforward parallel implementation which allows to simulate large problems (more than 10^6 dofs) within an acceptable computational time (few hours/days).

Furthermore, the cohesive zone approach is applied on reduced stresses in an original way leading to a fracture model which respects the energetic balance. Such an approach avoids the complex implementation of the neutral axis moving during the simulation required by the difference of fracture behavior in tension and compression. The ability of the model is demonstrated on several numerical benchmarks coming from literature by comparing our results with numerical and experimental data. In particular, the versatility of the framework is proved as different fracture phenomena (crack propagation, impact and fragmentation) are simulated with success. We restrict the applications to (explicit) dynamic cases where the XFEM method is less developed. Indeed, for quasi-static cases and linear elastic fracture, XFEM is very suitable and we don't think that our method can be an efficient alternative in this case, however a combination between our method and the XFEM could be envisaged in the case of parallel simulations. Indeed, the C^0/DG method could be used on each processor in combination with the full-DG formulation at interfaces of partitions to obtain an efficient parallel scheme. The fracture could be modeled by having recourse to the XFEM.

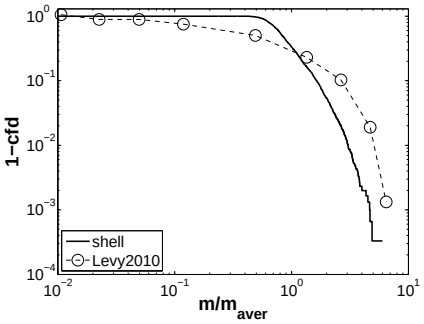

(a) Mass distribution of fragments $\dot{\varepsilon} = 1e4$ [s^{-1}].

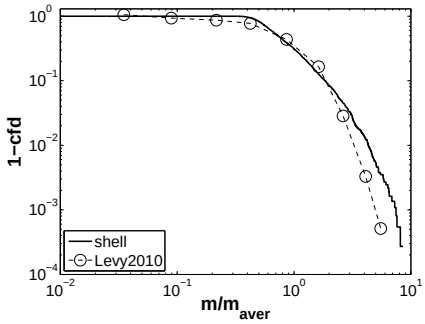

(b) Mass distribution of fragments $\dot{\varepsilon} = 2e4$ [s^{-1}].

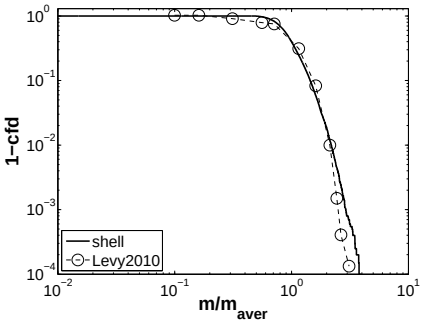

(c) Mass distribution of fragments $\dot{\varepsilon} = 1e5$ [s^{-1}].

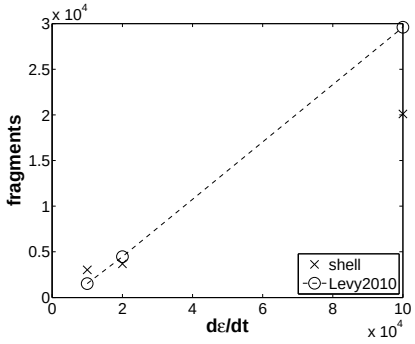

(d) Number of fragments.

Figure 5.21: Results for the fragmentation of a sphere with different strain rates. Results obtained with the DG/ECL shell framework are compared to 3D fragmentation results obtained by [137].

Chapter 6

Prospective of extension of the full-DG/ ECL framework to damage

The cohesive law introduced in Section 5.1 is suitable for brittle fracture but it is not applicable to ductile fracture although an elasto-plastic law can be used to account for the small scale yielding. Indeed, even if the elasto-plastic behavior of the material can be modeled thanks to the bulk constitutive behavior, the mechanisms of brittle and ductile fracture are too different to be treated with the same approach. In fact, in case of ductile fracture, cracks initiate in the material due to nucleation, growth and coalescence of micro-cavities and a continuum damage model is generally considered to model them [110, 135]. Nevertheless, the initiation of a crack is by nature a discontinuous phenomenon which explains the interest to develop a criterion to switch from the continuum damage theory to the fracture mechanics (*i.e.* to switch from a continuum to a discontinuous model). Among the different works presented on this subject in the literature, we focus on the work presented by J. Oliver *et al.* [187, 189, 188, 222, 121]. It has to be mentioned that a review of this work and its applicability to linear damage theory presented herein was part of the master thesis of G. Vo Thi [254] (the student that I supervised). The main idea of J. Oliver *et al.* is to model the damage with a continuum model until the lost of ellipticity of equations (Hadamard criterion [113]) and to introduce a strong discontinuity (crack) at this time. This idea is quite general and can be applied whatever the damage and crack models. In fact in their works J. Oliver *et al.* [121] used a modified Gurson model (see reference [110] for a presentation of this model) combined with the introduction of a strong embedded discontinuity (see Section 2.4 for a brief review) to model the crack. Notice that, as highlighted by F. Scheyvaerts *et al.* [226], the use of Hadamard criterion to insert a crack is reserved for low stress triaxiality cases. Indeed, it is experimentally observed that if cracks appear immediately after the maximal stress for low stress triaxiality, moderate and high stress triaxiality specimen exhibited a not negligible softening behavior before the apparition of a crack. The modeling of this softening behavior requires a non-local approach as suggested by several authors [30, 65, 102, 203, 202, 201].

Hereafter, we suggest to use this idea in the context of our full-DG/ECL framework. Indeed, we can model the damage thanks to the bulk material law as our formulation can be used with any constitutive behavior and we can activate a cohesive element when a criterion

is reached at an integration point. The major drawback compared with the work of J. Oliver *et al.* [187, 189, 188, 222, 121] is that with our approach the crack has to follow element boundaries. In fact, J. Oliver *et al.* [187, 189, 188, 222, 121], as they introduce a strong embedded discontinuity, can choose the direction of the crack based on a criterion [121]. Nevertheless, with our method we ensure, on one hand, a continuity of the crack during its propagation, and, on the other hand, an easy parallel implementation. Indeed, to investigate such problems, only three few adaptations are required in our full-DG/ECL implementation:

(i) Implementation of a damage constitutive model;

(ii) Change the fracture criterion (5.17) based on an effective stress by a criterion based on damage as *e.g.* the Hadamard criterion;

(iii) Define the shape of the cohesive law from the damage theory;

As a starting point to achieve this goal, in the following we discuss these adaptations through a simplified case. In fact we consider a membrane (no bending contribution) with a linear damage model and small displacements. Furthermore, although the value of the cohesive energy will be discussed, it will be assumed that the shape of the cohesive law remains linear and monotonically decreasing.

6.1 Linear damage model

The damage theory models the creation, growth and coalescence of micro-cavities and micro-cracks. Although these phenomena are discrete (and therefore discontinuous in the material) they can be modeled by a continuum variable, called D, if their sizes are small compared with a representative volume element (RVE) of the material. This variable D is defined for an isotropic damage in a section of surface S as the ratio between the surface of voids included in this section and S. Due to this void surface, at the continuum level, the stresses are exerted on a smaller surface, and so they are higher than if they were exerted on the surface S, leading to the definition of the effective stress as,

$$\tilde{\sigma}_{ij} = \frac{\sigma_{ij}}{1-D}. \tag{6.1}$$

This definition of the stress tensor allows writing the Hooke constitutive law as,

$$\boldsymbol{\sigma} = (1-D)\mathcal{H} : \boldsymbol{\varepsilon}, \tag{6.2}$$

thus the Hooke law can still be used if its tensor is multiplied by $(1-D)$.

The evolution of D is governed by a damage law, which can be written in the case of linear damage as,

$$f = (1-D)Y^{\frac{m}{2}} - Y_c^{\frac{m}{2}} \leq 0, \tag{6.3}$$

$$f\dot{D} = 0. \tag{6.4}$$

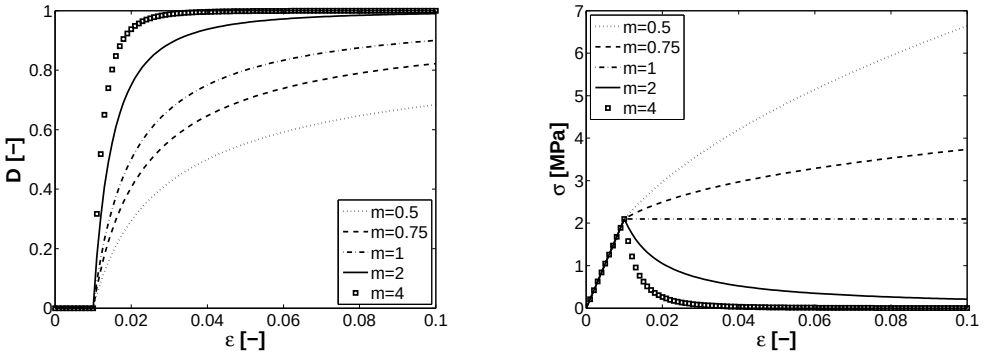

(a) Damage evolution. (b) Constitutive behavior.

Figure 6.1: There is no lost of ellipticity of acoustic tensor for the linear damage theory if $m < 1$. If $m > 1$, there is a lost of ellipticity as soon as $D > 0$.

where m is an exponent (material parameter), where Y is the damage energy release rate defined as,

$$Y = -\frac{\boldsymbol{\varepsilon} : \mathcal{H} : \boldsymbol{\varepsilon}}{2}, \tag{6.5}$$

and where Y_c is the energy of deformation required to initiate the damage (material parameter). When damage increases, Eq.(6.3) governs the damage evolution as,

$$D = 1 - \left(\frac{Y_c}{Y}\right)^{\frac{m}{2}}. \tag{6.6}$$

Such a law is drawn on Fig. 6.1 for the 1D case with different values of the parameter m. Unfortunately, it appears clearly from this picture that the Hadamard criterion cannot be used with this law. Indeed, this criterion inserts the crack when the acoustic (or localization) tensor loses its ellipticity. In 1D, if $m > 1$, this corresponds to the point of the maximal stress, as after this point the softening effect leads to the lost of the uniqueness of the solution for local formulation. If $m < 1$ the stress increases with the deformation without reaching a maximum. The case $m = 1$ corresponds to a degenerate case where the stress is constant with no unique maximum. Furthermore, this behavior was demonstrated mathematically by G. Vo Thi [254] for the general case of a linear plane stress law. Therefore the Hadamard criterion bifurcation cannot be applied with the linear damage constitutive behavior.

Keeping in mind that the main objective of this section is to illustrate the concept, we fix this issue by substitute to the Hadamard criterion a criterion based on a critical damage value D_c. Indeed, with a more realistic damage model as *e.g.* Lemaitre-Chaboche [135] or Gurson [110] the lost of ellipticity occurs for a damage value $\in]0;1[$ and we can simulate this effect by fixing the value to a given one. Therefore, in the following, the fracture criterion (5.17) based on an effective stress is replaced by a criterion on a critical damage value. This one is evaluated at each Gauss point of interface elements and a cohesive element is inserted where the criterion is reached. Finally, to keep uniqueness of the solution we consider $m < 1$.

6.2 Cohesive law for damage theory

If we assume a linear monotonically decreasing shape for the cohesive law, the values of (reduced) stresses being known at fracture initiation, the only parameter that has to be defined is the fracture energy. We suggest to compute this one following the work of J. Mazars *et al.* [155]. In this work they demonstrated, based on thermodynamic considerations, that an equivalence between the continuum damage theory and the fracture mechanics can be formulated as,

$$\int_V -Y\dot{D}dV \quad = \quad -G\dot{A}, \tag{6.7}$$

where V is the total volume of the considered body and where $\dot{A}$ is the variation of the cracked surface area. This equation allows to transform a given damage zone into an equivalent crack or conversely. Using this formula, M. Seabra *et al.* [227] suggested to define G_c of the cohesive zone as the energy which would be dissipated by the continuum damage model if this model was used to model the entire fracture process. Indeed, given D_f the final damage value (which can differ from one depending on the damage model) an amount of energy is dissipated between a damage value D_c, at which we insert a cohesive element, and D_f. This energy should be dissipated by the cohesive zone, which can be mathematically formulated as,

$$G_c dA = B\int_{D_c}^{D_f} Y dD, \tag{6.8}$$

with B is the width of the damage localization band. This one, supposed to be a material parameter, is introduced to take into account the accumulation of damage in a narrow band due to the softening effect. For the linear damage model used herein, using Eq. (6.3) we have,

$$Y \quad = \quad \frac{Y_c}{(1-D)^{\frac{2}{m}}}. \tag{6.9}$$

Inserting this last relation in Eq. (6.8) it comes,

$$\begin{aligned} G_c \quad &= \quad -BY_c\int_{D_c}^{D_f} \frac{1}{(1-D)^{\frac{2}{m}}} d(1-D), \\ &= \quad \begin{cases} \frac{BY_c}{\left(1-\frac{2}{m}\right)}\left[(1-D_c)^{1-\frac{2}{m}} - \left(1-D_f\right)^{1-\frac{2}{m}}\right] \text{ if } m \neq 2, \\ BY_c \log\frac{1-D_c}{1-D_f} \text{ if } m = 2. \end{cases} \end{aligned} \tag{6.10}$$

It has to be mentioned that to avoid the definition of the parameter B, a model of void coalescence by internal necking could be used as suggested by F. Scheyvaerts *et al.* [226]. In fact, their model is able to predict the unloading slope of the cohesive zone and thus it could be used to determine G_c without the recourse to a damage bandwidth.

6.3 Numerical benchmark

The fracture model combining the damage theory and the extrinsic cohesive zone as presented in Sections 6.1 and 6.2 is illustrated by considering a plate radially notched, as depicted on Fig. 6.2(a). The parameters of (fictitious) damage and cohesive materials are given in Tab. 6.1. The parameters of the material law are set to illustrate the developed model with an acceptable computational time on a personal computer.

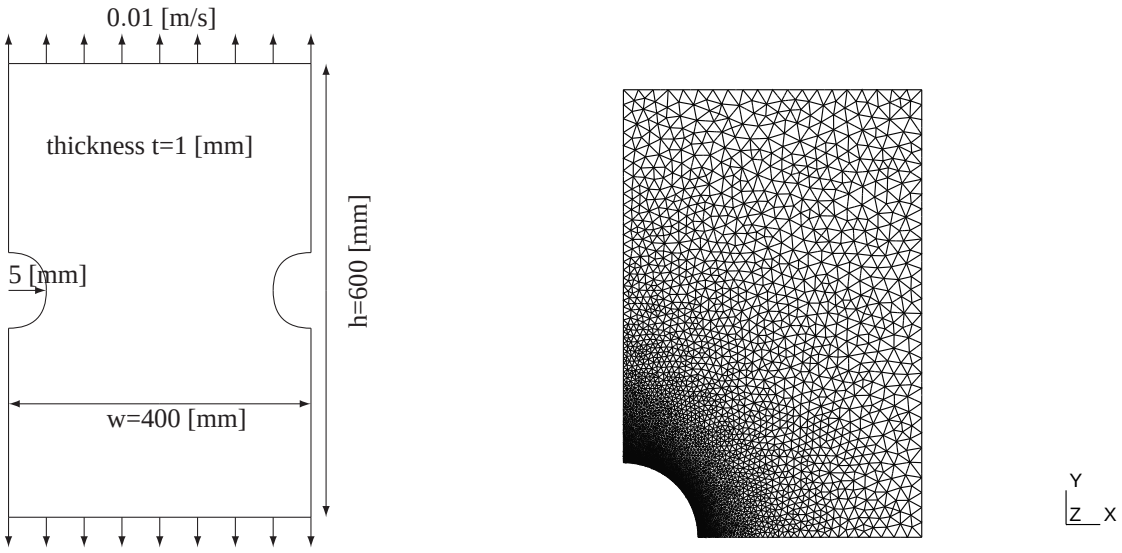

(a) Geometry. (b) Quadratic triangles mesh.

Figure 6.2: Configuration of the plate used to illustrate the transition from damage to crack.

Property	Value
Young modulus [GPa]	200
Poisson ratio [-]	0.3
Density [kg/m^3]	7850
Fracture energy [J/m^2]	13.26
Damage threshold $[\sqrt{\text{Pa}}]$	225
Critical damage [-]	$0.4 \pm 15\%$
Final damage [-]	0.8
Damage law exponent [-]	0.75
Coupling parameter [-]	1
Frictional coefficient [-]	0

Table 6.1: Material properties for the notched plate with damage.

Moreover, as the insertion of a cohesive element leads to convergence problem of the quasi-static scheme, we use the dynamic relaxation technique (see Section 4.5) to simulate in parallel (on six processors) the tensile loading. Moreover, to avoid spurious dynamic effects at computation initializing, an initial velocity along y-axis is prescribed. This one is zero at the edge near the hole and increases linearly to the pulling speed (0.01 [m/s]) at the opposite edge. One quarter of the plate is meshed (taking into account the symmetries) with quadratic triangles and with a refinement of the mesh near the hole, as depicted on Fig. 6.2(b). The plate is fixed along z-axis. The value of the last stability parameter β_2 (the only one remaining due to the boundary conditions) is set to 10.

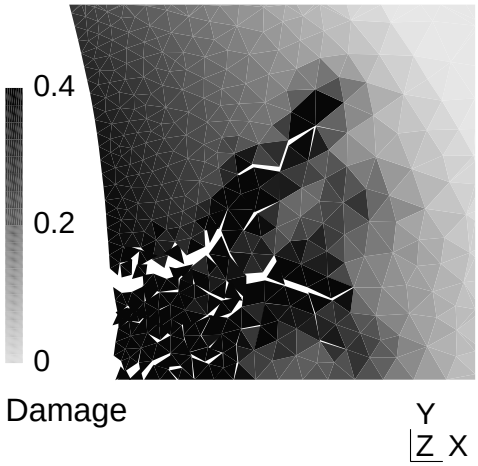

Figure 6.3: Blow-up of elements near the hole a few (pseudo)-times step after reaching the fracture criterion. Displacement are magnified 50 times.

Furthermore, with the aim of reducing the blow up of elements we prescribe a statistical distribution of D_c, which can vary from 15% around its nominal value from one interface to another one, although this strategy seems not as efficient as for crack propagation as illustrated on Fig. 6.3. Indeed, as expected the damage is concentrated near the hole (see also Fig. 6.4) but all interfaces in this area reach the fracture criterion more or less at the same time, leading to the blow up of elements in this region. A strategy to solve this spurious behavior should be develop in the future. One idea is notably to have recourse to a non local fracture criterion. Nevertheless, we can see from the different captures depicted on Fig. 6.4 that finally only one macro-crack propagates from this region to the other side of the specimen. Furthermore, during the whole propagation, the damage remains concentrated in a narrow band around the crack. Therefore this simple example demonstrates the ability of the suggested framework to produce qualitative results although improvements are still required to obtain quantitative results.

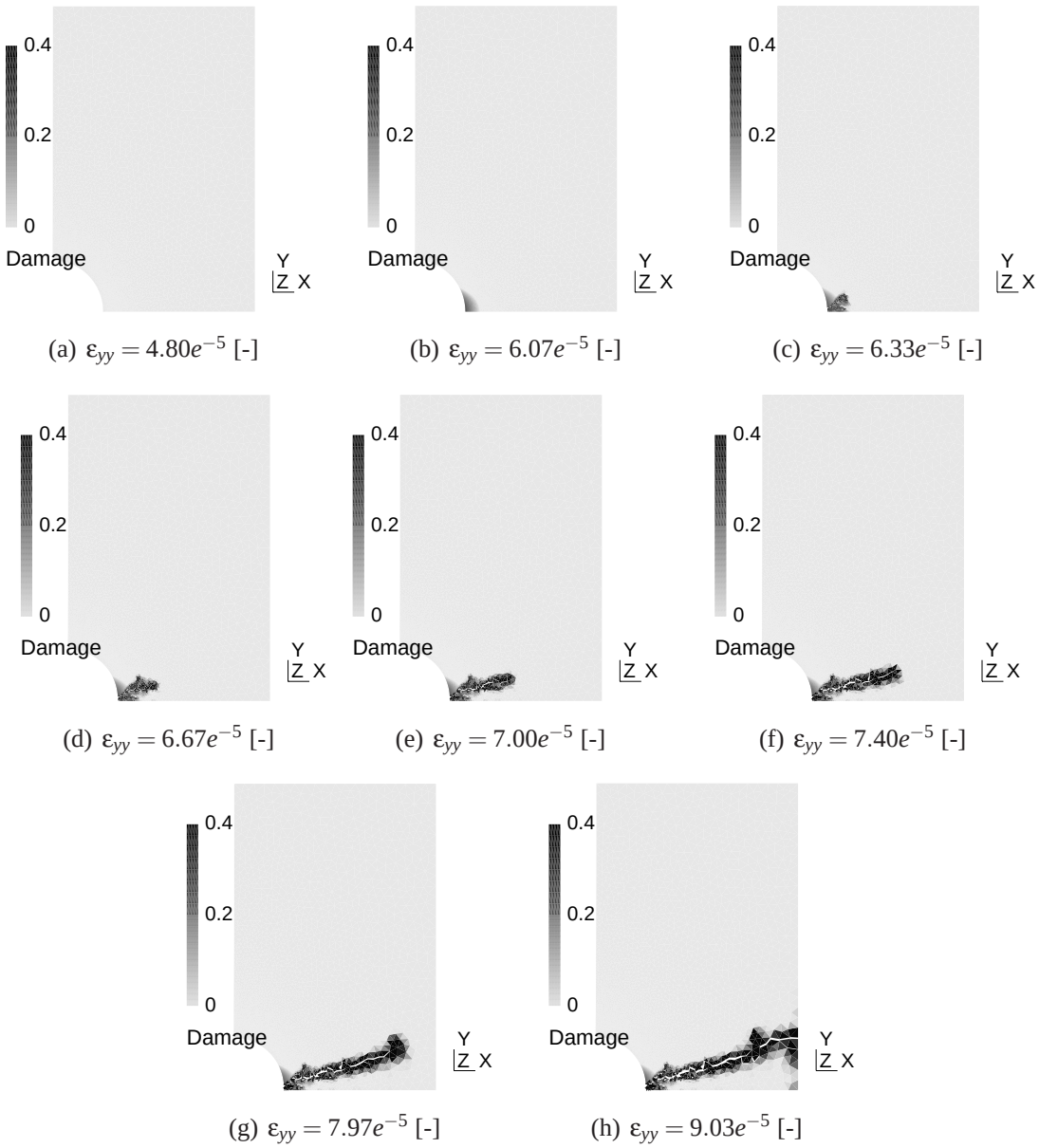

(a) $\varepsilon_{yy} = 4.80e^{-5}$ [-] (b) $\varepsilon_{yy} = 6.07e^{-5}$ [-] (c) $\varepsilon_{yy} = 6.33e^{-5}$ [-]

(d) $\varepsilon_{yy} = 6.67e^{-5}$ [-] (e) $\varepsilon_{yy} = 7.00e^{-5}$ [-] (f) $\varepsilon_{yy} = 7.40e^{-5}$ [-]

(g) $\varepsilon_{yy} = 7.97e^{-5}$ [-] (h) $\varepsilon_{yy} = 9.03e^{-5}$ [-]

Figure 6.4: The crack propagates due to damage which remains in a narrow band around the crack. The displacements are magnified 25 times and $\varepsilon_{yy} = \frac{u_y}{h/2}$ with u_y the value of the prescribed displacement.

6.4 Conclusions on the applicability of the DG/ECL framework to ductile fracture

As perspective to this thesis, we have illustrated on a very simple example the extension to the damage to crack transition of our framework. On this benchmark we demonstrate the capacity of our DG/ECL framework to model the damage thanks to a damage law and then to insert a cohesive element to model a crack when a criterion is reached to reproduce a phenomenon observed experimentally. Obviously, this part of the work should be improved (with a more complex damage model as *e.g.* the extension to shell of a non local damage model to capture the softening) to solve practical applications and this should be part of a future research project.

Chapter 7

General conclusions & perspectives

An original framework to model fracture in thin bodies is the main achievement of this work. Starting from a review of the literature in Chapter 2, it appeared that there are several methods which allow modeling such phenomena. Among them, the XFEM method, seems to be very efficient to study the quasi-static crack propagation in the context of linear fracture mechanics. Nevertheless, the efficiency of XFEM to study non-linear dynamic of large problems has still to be proved and thus our DG/ECL framework focuses with success on such problems.

Toward this end, we developed a framework similar to the one suggested by on one hand, J. Mergheim *et al.* [157] and on the other hand R. Radovitzky *et al.* [211] who presented a method combining DG formulation and ECL for 3D elements. The two main advantages to recourse to a DG formulation (compared with a classical CG one) are, on one hand, an easy parallel implementation, and, on the other hand, an easy insertion of cohesive elements at onset of fracture. We adapted this framework to thin bodies formulations in an original way by developing a novel full-DG formulation of Euler-Bernoulli beams and Kirchhoff-Love shells. Furthermore, an original cohesive model based on reduced stresses was also presented.

In Chapter 3, we focused on the Euler-Bernoulli beams case to demonstrate on a very simple example how the DG formulation leads to a straightforward insertion of a cohesive element for thin bodies. In fact, as the insertion of the cohesive elements at the beginning of the simulation generates numerical problems, such an element should only be inserted when a fracture criterion is reached. As a DG method ensures weakly the continuity between bulk elements thanks to interface terms, a cohesive element can very easily substitute to these terms at onset of fracture. Nevertheless, in the specific case of thin body formulations, the equilibrium equations are integrated separately on the thickness and are therefore formulated in term of reduced stresses. Furthermore, the propagation of a crack through-the-thickness requires the moving of the neutral axis during the through-the-thickness propagation with a classical cohesive law (*i.e.* a cohesive law based on stresses). For these two reasons we developed an original cohesive model based on reduced stresses. In our cohesive model different contributions of membrane and bending (there is no other contribution in the case of beams) are combined to respect the energetic balance. Indeed, it is well known that the energy released during the whole fracture process is a characteristic of the material. Therefore, at the end of

the fracture process the dissipated energy has to be identical to this quantity. We proved at the end of Chapter 3, that our suggested cohesive model verifies this identity.

These developments were then extended to Kirchhoff-Love shells. In a first time we presented an original full-DG formulation of non-linear Kirchhoff-Love shells in Chapter 4. We demonstrated that our new method has the same numerical properties as other shell methods suggested in the literature. In particular it is demonstrated through several numerical continuum mechanics problems that our method provides results as accurate as other (continuous) methods. The main advantages of our method in continuum mechanics are: a one-field locking-free formulation for shells and its easily parallel implementation. Indeed, as the mesh is discontinuous by nature, its partitioning between the different processors is straightforward and the interface terms can be used to ensure the continuity between the partitions. Toward this end, we suggested an original efficient manner to perform the integration at interfaces between two partitions. In fact, we used ghost elements which allow communicating (through MPI) only the degrees of freedom of these ghost elements. Proceeding this way, allows, on one hand, reducing the cost of communication, and, on the other hand, being independent of the material law. This advantage is demonstrated through numerical benchmarks.

Afterward in Chapter 5, we coupled this full-DG framework of non-linear shells with a cohesive law to model fracture mechanics problems. For the same reasons as the ones presented in the case of beams, we suggested an original cohesive law based on reduced stresses which respects the energetic balance. The differences with the law for beams are that, on one hand, the accounting for mixed fracture mode, and on the other hand, the accounting for non-linear material behaviors. Then we illustrated the ability of the framework to simulate crack propagation as well as fragmentation through several benchmarks, including non-linear plasticity and a large number of degrees of freedoms. This large number is required to capture the crack path and highlights the interest of the development of a parallel implementation. Furthermore, the comparison with the numerical and experimental results from the literature proved the ability of the framework to model different fracture phenomena.

Finally, as a preview to the future works, we present the application of the framework to the damage to crack transition problem in Chapter 6. We demonstrated that we can easily model the damage in the bulk material law and that a crack can be inserted through a cohesive zone when a criterion is reached. In the future, the damage constitutive behavior as well as the transition criterion will be improved notably by the recourse to the non local damage theory. Furthermore, although the stress triaxility plays a key role in ductile fracture, we neglected its effect which should be taken into account in our next development.

Moreover, the out-of-plane shearing is neglected in this work. Therefore, our framework cannot model a fracture mode III. The remove of this limitation requires the model of the out-of-plane shearing which necessitates some developments to integrate it in a Kirchhoff-Love formulation.

Bibliography

[1] ABEDI, R., HABER, R., AND ALIX, O. Spacetime damage-delay cohesive model for elastodynamic fracture with riemann contact conditions. In *IV European Conference on Computational Mechanics (ECCM2010)* (2010).

[2] ABEDI, R., HAWKER, M., HABER, R., AND MATOUSCARON, K. An adaptive space-time discontinuous galerkin method for cohesive models of elastodynamic fracture. *International Journal for Numerical Methods in Engineering 81*, 10 (2010), 1207–1241.

[3] ABEDI, R., PETRACOVICI, B., AND HABER, R. A space-time discontinuous galerkin method for linearized elastodynamics with element-wise momentum balance. *Computer Methods in Applied Mechanics and Engineering 195*, 25-28 (2006), 3247–3273.

[4] ACARY, V., AND MONERIE, Y. Nonsmooth fracture dynamics using a cohesive zone approach. Tech. rep., INRIA, 2006.

[5] ANVARI, M., LIU, J., AND THAULOW, C. Dynamic ductile fracture in aluminum round bars: experiments and simulations. *International Journal of Fracture 143*, 4 (2007), 317–332.

[6] ANVARI, M., SCHEIDER, I., AND THAULOW, C. Simulation of dynamic ductile crack growth using strain-rate and triaxiality-dependent cohesive elements. *Engineering Fracture Mechanics 73*, 15 (2006), 2210–2228.

[7] AREIAS, P. M. A., AND BELYTSCHKO, T. Analysis of three-dimensional crack initiation and propagation using the extended finite element method. *International Journal for Numerical Methods in Engineering 63*, 5 (2005), 760–788.

[8] AREIAS, P. M. A., AND BELYTSCHKO, T. Non-linear analysis of shells with arbitrary evolving cracks using xfem. *International Journal for Numerical Methods in Engineering 62*, 3 (2005), 384–415.

[9] AREIAS, P. M. A., SONG, J.-H., AND BELYTSCHKO, T. A finite-strain quadrilateral shell element based on discrete kirchhoff-love constraints. *International Journal for Numerical Methods in Engineering 64*, 9 (2005), 1166–1206.

[10] AREIAS, P. M. A., SONG, J. H., AND BELYTSCHKO, T. Analysis of fracture in thin shells by overlapping paired elements. *Computer Methods in Applied Mechanics and Engineering 195*, 41-43 (2006), 5343–5360.

[11] ARIAS, I., KNAP, J., CHALIVENDRA, V. B., HONG, S., ORTIZ, M., AND ROSAKIS, A. J. Numerical modelling and experimental validation of dynamic fracture events along weak planes. *Computer Methods in Applied Mechanics and Engineering 196*, 37-40 (2007), 3833 – 3840.

[12] ARMERO, F., AND GARIKIPATI, K. An analysis of strong discontinuities in multiplicative finite strain plasticity and their relation with the numerical simulation of strain localization in solids. *International Journal of Solids and Structures 33*, 20-22 (1996), 2863 – 2885.

[13] ARMERO, F., AND LINDER, C. New finite elements with embedded strong discontinuities in the finite deformation range. *Computer Methods in Applied Mechanics and Engineering 197*, 33-40 (2008), 3138 – 3170.

[14] ARMERO, F., AND LINDER, C. Numerical simulation of dynamic fracture using finite elements with embedded discontinuities. *International Journal of Fracture 160* (2009), 119–141.

[15] ARNOLD, D. N. An interior penalty finite element method with discontinuous elements. *SIAM Journal on Numerical Analysis 19*, 4 (1982), pp. 742–760.

[16] ARNOLD, D. N., BREZZI, F., COCKBURN, B., AND MARINI, L. D. Unified analysis of discontinuous galerkin methods for elliptic problems. *SIAM Journal on Numerical Analysis 39*, 5 (2002), 1749–1779.

[17] ARNOLD, D. N., BREZZI, F., AND MARINI, L. D. A family of discontinuous galerkin finite elements for the reissner-mindlin plate. *Journal of Scientific Computing 22-23* (2005), 25–45.

[18] ASADPOURE, A., AND MOHAMMADI, S. Developing new enrichment functions for crack simulation in orthotropic media by the extended finite element method. *International Journal for Numerical Methods in Engineering 69*, 10 (2007), 2150–2172.

[19] ATLURI, S. N., AND SHEN, S. The meshless local petrov-galerkin (mlpg) method: A simple & less-costly alternative to the finite element and boundary element methods. *Computer Modeling in Engineering & Sciences 3* (2002), 11–52.

[20] BAKER, G. Finite element methods for elliptic equations using nonconforming elements. *Mathematics of Computation 31* (1977), 45–59.

[21] BALAY, S., BROWN, J., , BUSCHELMAN, K., EIJKHOUT, V., GROPP, W. D., KAUSHIK, D., KNEPLEY, M. G., MCINNES, L. C., SMITH, B. F., AND ZHANG,

H. PETSc users manual. Tech. Rep. ANL-95/11 - Revision 3.1, Argonne National Laboratory, 2010.

[22] BALAY, S., BROWN, J., BUSCHELMAN, K., GROPP, W. D., KAUSHIK, D., KNEPLEY, M. G., MCINNES, L. C., SMITH, B. F., AND ZHANG, H. PETSc Web page, 2011. http://www.mcs.anl.gov/petsc.

[23] BALAY, S., GROPP, W. D., MCINNES, L. C., AND SMITH, B. F. Efficient management of parallelism in object oriented numerical software libraries. In *Modern Software Tools in Scientific Computing* (1997), E. Arge, A. M. Bruaset, and H. P. Langtangen, Eds., Birkhäuser Press, pp. 163–202.

[24] BARENBLATT, G. The mathematical theory of equilibrium cracks in brittle fracture. vol. 7. Elsevier, 1962, pp. 55–129.

[25] BARSOUM, R. S. On the use of isoparametric finite elements in linear fracture mechanics. *International Journal for Numerical Methods in Engineering 10*, 1 (1976), 25–37.

[26] BASAR, Y., AND DING, Y. Finite-rotation shell elements for the analysis of finite-rotation shell problems. *International Journal for Numerical Methods in Engineering 34*, 1 (1992), 165–169.

[27] BASSI, F., AND REBAY, S. High-order accurate discontinuous finite element solution of the 2d euler equations. *Journal of Computational Physics 138*, 2 (1997), 251 – 285.

[28] BATHE, K.-J., AND DVORKIN, E. N. A four-node plate bending element based on mindlin/reissner plate theory and a mixed interpolation. *International Journal for Numerical Methods in Engineering 21*, 2 (1985), 367–383.

[29] BATHE, K.-J., AND DVORKIN, E. N. A formulation of general shell elements - the use of mixed interpolation of tensorial components. *International Journal for Numerical Methods in Engineering 22*, 3 (1986), 697–722.

[30] BAZANT, Z. P., BELYTSCHKO, T. B., AND CHANG, T.-P. Continuum theory for strain-softening. *Journal of Engineering Mechanics 110*, 12 (1984), 1666–1692.

[31] BECKER, G., GEUZAINE, C., AND NOELS, L. A one field full discontinuous galerkin method for kirchhoff-love shells applied to fracture mechanics. *Computer Methods in Applied Mechanics and Engineering 200*, 45-46 (2011), 3223 – 3241.

[32] BECKER, G., AND NOELS, L. A fracture framework for euler-bernoulli beams based on a full discontinuous galerkin formulation/extrinsic cohesive law combination. *International Journal for Numerical Methods in Engineering 85*, 10 (2011), 1227–1251.

[33] BECKER, G., AND NOELS, L. A full discontinuous galerkin formulation of nonlinear kirchhoff-love shells: elasto-plastic finite deformations, parallel computation & fracture applications. *International Journal for Numerical Methods in Engineering submitted* (2012).

[34] BECKER, G., AND NOELS, L. Validation tests of the full discontinuous galerkin / extrinsic cohesive law framework of kirchhoff-love shell. *International Journal of Fracture CFRAC2011, submitted* (2012).

[35] BELTZ, G., AND RICE, J. Dislocation nucleation versus cleavage decohesion at crack tips. *Modeling and Deformation of Crystalline Solids* (1991), 457.

[36] BELYTSCHKO, T., AND BLACK, T. Elastic crack growth in finite elements with minimal remeshing. *International Journal for Numerical Methods in Engineering 45*, 5 (1999), 601–620.

[37] BELYTSCHKO, T., DANIEL, W. J. T., AND VENTURA, G. A monolithic smoothing-gap algorithm for contact-impact based on the signed distance function. *International Journal for Numerical Methods in Engineering 55*, 1 (2002), 101–125.

[38] BELYTSCHKO, T., AND LEVIATHAN, I. Physical stabilization of the 4-node shell element with one point quadrature. *Computer Methods in Applied Mechanics and Engineering 113*, 3-4 (1994), 321 – 350.

[39] BELYTSCHKO, T., LIN, J. I., AND CHEN-SHYH, T. Explicit algorithms for the nonlinear dynamics of shells. *Computer Methods in Applied Mechanics and Engineering 42*, 2 (1984), 225 – 251.

[40] BELYTSCHKO, T., LU, Y., AND GU, L. Crack propagation by element-free galerkin methods. *Engineering Fracture Mechanics 51*, 2 (1995), 295 – 315.

[41] BELYTSCHKO, T., LU, Y., GU, L., AND TABBARA, M. Element-free galerkin methods for static and dynamic fracture. *International Journal of Solids and Structures 32*, 17-18 (1995), 2547 – 2570.

[42] BELYTSCHKO, T., LU, Y. Y., AND GU, L. Element-free galerkin methods. *International Journal for Numerical Methods in Engineering 37*, 2 (1994), 229–256.

[43] BELYTSCHKO, T., MOËS, N., USUI, S., AND PARIMI, C. Arbitrary discontinuities in finite elements. *International Journal for Numerical Methods in Engineering 50*, 4 (2001), 993–1013.

[44] BELYTSCHKO, T., AND TABBARA, M. Dynamic fracture using element-free galerkin methods. *International Journal for Numerical Methods in Engineering 39*, 6 (1996), 923–938.

[45] BELYTSCHKO, T., WONG, B. L., AND PLASKACZ, E. J. Fission-fusion adaptivity in finite elements for nonlinear dynamics of shells. *Computers & Structures 33*, 5 (1989), 1307 – 1323.

[46] BERNARDI, C. A new nonconforming approach to domain decomposition : The mortar element method. *Nonliner Partial Differential Equations and Their Applications* (1994).

[47] BERNARDI, C., DEBIT, N., AND MADAY, Y. Coupling finite element and spectral methods: First results. *Mathematics of Computation 54*, 189 (1990), pp. 21–39.

[48] BETSCH, P., AND STEIN, E. Numerical implementation of multiplicative elastoplasticity into assumed strain elements with application to shells at large strains. *Computer Methods in Applied Mechanics and Engineering 179*, 3-4 (1999), 215 – 245.

[49] BEY, K. S., AND ODEN, J. T. hp-version discontinuous galerkin methods for hyperbolic conservation laws. *Computer Methods in Applied Mechanics and Engineering 133*, 3-4 (1996), 259 – 286.

[50] BISCHOFF, M., AND RAMM, E. Shear deformable shell elements for large strains and rotations. *International Journal for Numerical Methods in Engineering 40*, 23 (1997), 4427–4449.

[51] BITTENCOURT, T., WAWRZYNEK, P., INGRAFFEA, A., AND SOUSA, J. Quasi-automatic simulation of crack propagation for 2d lefm problems. *Engineering Fracture Mechanics 55*, 2 (1996), 321 – 334.

[52] BLACKFORD, L., DEMMEL, J., DONGARRA, J., DUFF, I., HAMMARLING, S., HENRY, G., HEROUX, M., KAUFMAN, L., LUMSDAINE, A., AND PETITET, A. An updated set of basic linear algebra subprograms (blas). *ACM Transactions on Mathematical Software 28* (2002), 135–151.

[53] BONET, J., AND KULASEGARAM, S. Correction and stabilization of smooth particle hydrodynamics methods with applications in metal forming simulations. *International Journal for Numerical Methods in Engineering 47*, 6 (2000), 1189–1214.

[54] BORST, R. D., GUTIÉRREZ, M. A., WELLS, G. N., REMMERS, J. J. C., AND ASKES, H. Cohesive-zone models, higher-order continuum theories and reliability methods for computational failure analysis. *International Journal for Numerical Methods in Engineering 60*, 1 (2004), 289–315.

[55] BORST, R. D., REMMERS, J. J. C., NEEDLEMAN, A., AND ABELLAN, M.-A. Discrete vs smeared crack models for concrete fracture: bridging the gap. *International Journal for Numerical and Analytical Methods in Geomechanics 28*, 7-8 (2004), 583–607.

[56] BOUCHARD, P., BAY, F., AND CHASTEL, Y. Numerical modelling of crack propagation: automatic remeshing and comparison of different criteria. *Computer Methods in Applied Mechanics and Engineering 192*, 35-36 (2003), 3887 – 3908.

[57] BOZZOLO, G., FERRANTE, J., AND SMITH, J. R. Universal behavior in ideal slip. *Scripta Metallurgica et Materialia 25*, 8 (1991), 1927 – 1931.

[58] BREZZI, F., AND FORTIN, M. *Mixed and hybrid finite element methods*. Springer-Verlag New York, Inc., New York, NY, USA, 1991.

[59] BUDIANSKY, B., AND RICE, J. R. Conservation laws and energy-release rates. *Journal of Applied Mechanics 40*, 1 (1973), 201–203.

[60] BUECHTER, N., AND RAMM, E. Shell theory versus degeneration-a comparison in large rotation finite element analysis. *International Journal for Numerical Methods in Engineering 34*, 1 (1992), 39–59.

[61] CALEYRON, F., COMBESCURE, A., FAUCHER, V., AND POTAPOV, S. Une méthode sans maillage pour la modélisation des interactions fluide-structure: Application Ã la rupture dún réservoir sous impact. In *10e Colloque National en Calcul des Structures (CSMA2011)* (2011).

[62] CAMACHO, G. *Computational modelling of impact damage and penetration of brittle and ductile solids*. Providance, 1996.

[63] CAMACHO, G. T., AND ORTIZ, M. Computational modelling of impact damage in brittle materials. *International Journal of Solids and Structures 33*, 20-22 (1996), 2899–2938.

[64] CARPENTER, W. C., READ, D. T., AND DODDS, R. H. Comparison of several path independent integrals including plasticity effects. *International Journal of Fracture 31* (1986), 303–323.

[65] CASTAÑEDA, P. Exact second-order estimates for the effective mechanical properties of nonlinear composite materials. *Journal of the Mechanics and Physics of Solids 44*, 6 (1996), 827 – 862.

[66] CELIKER, F., AND COCKBURN, B. Element-by-element post-processing of discontinuous galerkin methods for timoshenko beams. *Journal of Scientific Computing 27*, 1 (2006), 177–187.

[67] CELIKER, F., COCKBURN, B., AND STOLARSKI, H. K. Locking-free optimal discontinuous galerkin methods for timoshenko beams. *SIAM Journal on Numerical Analysis 44*, 6 (2006), 2297–2325.

[68] CHAN, S., TUBA, I., AND WILSON, W. On the finite element method in linear fracture mechanics. *Engineering Fracture Mechanics 2*, 1 (1970), 1 – 17.

[69] CIRAK, F., DEITERDING, R., AND MAUCH, S. P. Large-scale fluid-structure interaction simulation of viscoplastic and fracturing thin-shells subjected to shocks and detonations. *Computers & Structures 85*, 11-14 (2007), 1049–1065.

[70] CIRAK, F., ORTIZ, M., AND PANDOLFI, A. A cohesive approach to thin-shell fracture and fragmentation. *Computer Methods in Applied Mechanics and Engineering 194*, 21-24 (2005), 2604–2618.

[71] COCKBURN, B. Discontinuous galerkin methods. *ZAMM - Journal of Applied Mathematics and Mechanics / Zeitschrift far Angewandte Mathematik und Mechanik 83*, 11 (2003), 731–754.

[72] COCKBURN, B., AND SHU, C.-W. Runge-kutta discontinuous galerkin methods for convection-dominated problems. *Journal of Scientific Computing 16* (2001), 173–261.

[73] CORIGLIANO, A., CACCHIONE, F., FRANGI, A., AND ZERBINI, S. Numerical modelling of impact rupture in polysilicon microsystems. *Computational Mechanics 42* (2008), 251–259.

[74] CUITINO, A., AND ORTIZ, M. A material-independent method for extending stress update algorithms from small-strain plasticity to finite plasticity with multiplicative kinematics. *Engineering Computations 9* (1992), 437–451.

[75] DAUX, C., MOËS, N., DOLBOW, J., SUKUMAR, N., AND BELYTSCHKO, T. Arbitrary branched and intersecting cracks with the extended finite element method. *International Journal for Numerical Methods in Engineering 48*, 12 (2000), 1741–1760.

[76] DEITERDING, R., RADOVITZKY, R., MAUCH, S., NOELS, L., CUMMINGS, J., AND MEIRON, D. A virtual test facility for the efficient simulation of solid material response under strong shock and detonation wave loading. *Engineering with Computers 22*, 3 (2006), 325–347.

[77] DELORENZI, H. G. On the energy release rate and the j-integral for 3-d crack configurations. *International Journal of Fracture 19* (1982), 183–193.

[78] DELORENZI, H. G. Energy release rate calculations by the finite element method. *Engineering Fracture Mechanics 21*, 1 (1985), 129 – 143.

[79] DIAS-DA COSTA, D., ALFAIATE, J., SLUYS, L., AND JULIO, E. A comparative study on the modelling of discontinuous fracture by means of enriched nodal and element techniques and interface elements. *International Journal of Fracture 161* (2010), 97–119.

[80] DICKENS, S. H., AND CHO, B. H. Interpretation of bond failure through conversion and residual solvent measurements and weibull analyses of flexural and microtensile bond strengths of bonding agents. *Dental Materials 21*, 4 (2005), 354 – 364.

[81] DODDS, R., AND VARGAS, P. Numerical evaluation of domain and contour integrals for nonlinear fracture mechanics: Formulation and implementation aspects. Civil Engineering Studies SRS-542, University of Illinois Engineering Experiment Station. College of Engineering. University of Illinois at Urbana-Champaign., 1988.

[82] DOLBOW, J., AND NADEAU, J. On the use of effective properties for the fracture analysis of microstructured materials. *Engineering Fracture Mechanics 69*, 14-16 (2002), 1607 – 1634.

[83] DONGARRA, J. J., DU CROZ, J., HAMMARLING, S., AND DUFF, I. S. A set of level 3 basic linear algebra subprograms. *ACM Transactions on Mathematical Software 16* (1990), 1–17.

[84] DOUGLAS, J. H1-galerkin methods for a nonlinear dirichlet problem. In *Mathematical Aspects of Finite Element Methods*, I. Galligani and E. Magenes, Eds., vol. 606 of *Lecture Notes in Mathematics*. Springer Berlin / Heidelberg, 1977, pp. 64–86.

[85] DOUGLAS, J., AND DUPONT, T. Interior penalty procedures for elliptic and parabolic galerkin methods. In *Computing Methods in Applied Sciences*, R. Glowinski and J. Lions, Eds., vol. 58 of *Lecture Notes in Physics*. Springer Berlin / Heidelberg, 1976, pp. 207–216.

[86] DUFLOT, M. A meshless method with enriched weight functions for three-dimensional crack propagation. *International Journal for Numerical Methods in Engineering 65*, 12 (2006), 1970–2006.

[87] DUFLOT, M., AND NGUYEN-DANG, H. A meshless method with enriched weight functions for fatigue crack growth. *International Journal for Numerical Methods in Engineering 59*, 14 (2004), 1945–1961.

[88] DUFLOT, M., WYART, E., LANI, F., MARTINY, P., AND SAGNIER, S. Application of xfem to multi-site crack propagation. *Engineering Fracture Mechanics submitted* (2011).

[89] DUGDALE, D. S. Yielding of steel sheets containing slits. *Journal of the Mechanics and Physics of Solids 8*, 2 (1960), 100–104.

[90] ELGUEDJ, T., GRAVOUIL, A., AND COMBESCURE, A. Appropriate extended functions for x-fem simulation of plastic fracture mechanics. *Computer Methods in Applied Mechanics and Engineering 195*, 7-8 (2006), 501–515.

[91] ENGEL, G., GARIKIPATI, K., HUGHES, T. J. R., LARSON, M. G., MAZZEI, L., AND TAYLOR, R. L. Continuous/discontinuous finite element approximations of fourth-order elliptic problems in structural and continuum mechanics with applications to thin beams and plates, and strain gradient elasticity. *Computer Methods in Applied Mechanics and Engineering 191*, 34 (2002), 3669–3750.

[92] ERDOGAN, F., AND SIH, G. On the crack extension in plates under plane loading and transverse shear. *Journal of Basic Engineering 85D* (1963), 519–525.

[93] ESPINOSA, H., DWIVEDI, S., AND LU, H.-C. Modeling impact induced delamination of woven fiber reinforced composites with contact/cohesive laws. *Computer Methods in Applied Mechanics and Engineering 183*, 3-4 (2000), 259 – 290.

[94] ESPINOSA, H. D., AND ZAVATTIERI, P. D. A grain level model for the study of failure initiation and evolution in polycrystalline brittle materials. part i: Theory and numerical implementation. *Mechanics of Materials 35*, 3-6 (2003), 333 – 364.

[95] ESPINOSA, H. D., AND ZAVATTIERI, P. D. A grain level model for the study of failure initiation and evolution in polycrystalline brittle materials. part ii: Numerical examples. *Mechanics of Materials 35*, 3-6 (2003), 365 – 394.

[96] ESPINOSA, H. D., ZAVATTIERI, P. D., AND DWIVEDI, S. K. A finite deformation continuum-discrete model for the description of fragmentation and damage in brittle materials. *Journal of the Mechanics and Physics of Solids 46*, 10 (1998), 1909 – 1942.

[97] EYCK, A. T., AND LEW, A. Discontinuous galerkin methods for non-linear elasticity. *International Journal for Numerical Methods in Engineering 67*, 9 (2006), 1204–1243.

[98] FAGERSTRÖM, M., AND LARSSON, R. Theory and numerics for finite deformation fracture modelling using strong discontinuities. *International Journal for Numerical Methods in Engineering 66*, 6 (2006), 911–948.

[99] FERRANTE, J., AND SMITH, J. R. Theory of the bimetallic interface. *Phys. Rev. B 31* (1985), 3427–3434.

[100] FIELD, J. Investigation of the inmpact performance of various glass and ceramic systems. Tech. Rep. A344202, cambridge University, 1988.

[101] FISH, J., AND YUAN, Z. Multiscale enrichment based on partition of unity. *International Journal for Numerical Methods in Engineering 62*, 10 (2005), 1341–1359.

[102] GEERS, M. *Experimental analysis and computational modelling of damage and fracture*. PhD thesis, Technische Universiteit Eindhoven, 1997.

[103] GÉRADIN, M., AND RIXEN, D. *Théorie des vibrations: application à la dynamique des structures*, 2ème ed. Masson, 1996.

[104] GEUBELLE, P. H., AND BAYLOR, J. S. Impact-induced delamination of composites: a 2d simulation. *Composites Part B: Engineering 29*, 5 (1998), 589 – 602.

[105] GEUZAINE, C., AND REMACLE, J.-F. Gmsh: A 3-d finite element mesh generator with built-in pre- and post-processing facilities. *International Journal for Numerical Methods in Engineering 79*, 11 (2009), 1309–1331.

[106] GINGOLD, R. A., AND MONAGHAN, J. J. Smoothed particle hydrodynamics - theory and application to non-spherical stars. *Monthly Notices of the Royal Astronomical Society 181* (1977), 375–389.

[107] GRADY, D., AND BENSON, D. Fragmentation of metal rings by electromagnetic loading. *Experimental Mechanics 23* (1983), 393–400.

[108] GRADY, D., AND KIPP, M. The micromechanics of impact fracture of rock. *International Journal of Rock Mechanics and Mining Sciences & Geomechanics Abstracts 16*, 5 (1979), 293 – 302.

[109] GRIFFITH, A. A. The phenomena of rupture and flow in solids. *Philosophical Transactions of the Royal Society of London. Series A, Containing Papers of a Mathematical or Physical Character 221* (1921), 163–198.

[110] GURSON, A. L. Continuum theory of ductile rupture by void nucleation and growth: Part i—yield criteria and flow rules for porous ductile media. *Journal of Engineering Materials and Technology 99*, 1 (1977), 2–15.

[111] GÜZEY, S., COCKBURN, B., AND STOLARSKI, H. K. The embedded discontinuous galerkin method: application to linear shell problems. *International Journal for Numerical Methods in Engineering 70*, 7 (2007), 757–790.

[112] GÜZEY, S., STOLARSKI, H. K., COCKBURN, B., AND TAMMA, K. K. Design and development of a discontinuous galerkin method for shells. *Computer Methods in Applied Mechanics and Engineering 195*, 25-28 (2006), 3528–3548.

[113] HADAMARD, J. *Leçons sur la propagation des ondes et les eq́uations de l'hydrodynamique*. Librairie Scientifique A. Hermann et Fils, Paris., 1903.

[114] HALLQUIST, J. *LS-DYNA Theoretical Manual*. Livermore Software Technology Corporation, 1998.

[115] HANSBO, P., AND LARSON, M. G. A discontinuous galerkin method for the plate equation. *Calcolo 39*, 1 (2002), 41–59.

[116] HANSBO, P., AND LARSON, M. G. Discontinuous galerkin methods for incompressible and nearly incompressible elasticity by nitsche's method. *Computer Methods in Applied Mechanics and Engineering 191*, 17-18 (2002), 1895–1908.

[117] HILLERBORG, A., MODÉER, M., AND PETERSSON, P.-E. Analysis of crack formation and crack growth in concrete by means of fracture mechanics and finite elements. *Cement and Concrete Research 6*, 6 (1976), 773 – 781.

[118] HOUSTON, P., SCHÖTZAU, D., AND WIHLER, T. P. An hp-adaptive mixed discontinuous galerkin fem for nearly incompressible linear elasticity. *Computer Methods in Applied Mechanics and Engineering 195*, 25-28 (2006), 3224 – 3246.

[119] HOUSTON, P., SCHWAB, C., AND SULI, E. Stabilized hp-finite element methods for first-order hyperbolic problems. *SIAM Journal on Numerical Analysis 37*, 5 (2000), pp. 1618–1643.

[120] HU, H., CHAMBON, L., CROZES, D., FRANGI, A., AND BONNET, M. Symmetric fem-driven bem-fem coupling for 3d linear fracture mechanics. In *European Conference on Computational Mechanics (ECCM 2010)* (2010).

[121] HUESPE, A., NEEDLEMAN, A., OLIVER, J., AND SÃ¡NCHEZ, P. A finite thickness band method for ductile fracture analysis. *International Journal of Plasticity 25*, 12 (2009), 2349–2365.

[122] HUGHES, T. J., AND LIU, W. K. Nonlinear finite element analysis of shells: Part i. three-dimensional shells. *Computer Methods in Applied Mechanics and Engineering 26*, 3 (1981), 331 – 362.

[123] HULBERT, G. M., AND CHUNG, J. Explicit time integration algorithms for structural dynamics with optimal numerical dissipation. *Computer Methods in Applied Mechanics and Engineering 137*, 2 (1996), 175 – 188.

[124] HUSSAIN, M. A., PU, S. L., AND UNDERWOOD, J. H. Strain energy release rate for a crack under combined mode i and mode ii. Tech. rep., Defense Technical Information Center OAI-PMH Repository [http://stinet.dtic.mil/oai/oai] (United States), 1998.

[125] HUTCHINSON, J. Singular behaviour at the end of a tensile crack in a hardening material. *Journal of the Mechanics and Physics of Solids 16*, 1 (1968), 13 – 31.

[126] IRWIN, G. Analysis of stresses and strains near the end of a crack traversing a plate. *Journal of Applied Mechanics 24* (1957), 361–364.

[127] KARYPIS, G., AND KUMAR, V. A fast and high quality multilevel scheme for partitioning irregular graphs. *SIAM Journal on Scientific Computing 20*, 1 (1998), 359–392.

[128] KHOEI, A., SHAMLOO, A., AND AZAMI, A. Extended finite element method in plasticity forming of powder compaction with contact friction. *International Journal of Solids and Structures 43*, 18-19 (2006), 5421 – 5448.

[129] KIPP, M. E., GRADY, D. E., AND CHEN, E. P. Strain-rate dependent fracture initiation. *International Journal of Fracture 16* (1980), 471–478.

[130] KRYSL, P., AND BELYTSCHKO, T. The element free galerkin method for dynamic propagation of arbitrary 3-d cracks. *International Journal for Numerical Methods in Engineering 44*, 6 (1999), 767–800.

[131] LANKFORD, J. Compressive strength and microplasticity in polycrystalline alumina. *Journal of Materials Science 12* (1977), 791–796.

[132] LANKFORD, J. The role of subcritical tensile microfracture processes in compression failure of ceramics. *Fracture Mechanics of Ceramics 5*, 4 (1981), 625.

[133] LARSSON, R., MEDIAVILLA, J., AND FAGERSTRÖM, M. Dynamic fracture modeling in shell structures based on xfem. *International Journal for Numerical Methods in Engineering 86*, 4-5 (2011), 499–527.

[134] LAWSON, C. L., HANSON, R. J., KINCAID, D. R., AND KROGH, F. T. Basic linear algebra subprograms for fortran usage. *ACM Transactions on Mathematical Software 5* (1979), 308–323.

[135] LEMAITRE, J., AND DESMORAT, R. *Engineering damage mechanics: ductile, creep, fatigue and brittle failures*. Springer-Verlag, Berlin, 2005.

[136] LETERRIER, Y., ANDERSONS, J., PITTON, Y., AND MANSON, J.-A. E. Adhesion of silicon oxide layers on poly(ethylene terephthalate). ii: Effect of coating thickness on adhesive and cohesive strengths. *Journal of Polymer Science Part B: Polymer Physics 35*, 9 (1997), 1463–1472.

[137] LEVY, S. *Exploring the Physics behind Dynamic Fragmentation through Parallel Simulations*. PhD thesis, Ecole Polytechnique Fédérale de Lausanne, Lausanne, 2010.

[138] LEVY, S., MOLINARI, J. F., VICARI, I., AND DAVISON, A. C. Dynamic fragmentation of a ring: Predictable fragment mass distributions. *Physical Review E 82* (2010), 066105.

[139] LEW, A., EYCK, A., AND RANGARAJAN, R. Some applications of discontinuous galerkin methods in solid mechanics. *IUTAM Symposium on Theoretical, Computational and Modelling Aspects of Inelastic Media* (2008), 227–236.

[140] LEW, A., NEFF, P., SULSKY, D., AND ORTIZ, M. Optimal bv estimates for a discontinuous galerkin method for linear elasticity. *Appl Math Res Express 2004*, 3 (2004), 73–106.

[141] LI, F., SHIH, C., AND NEEDLEMAN, A. A comparison of methods for calculating energy release rates. *Engineering Fracture Mechanics 21*, 2 (1985), 405 – 421.

[142] LI, H., AND CHANDRA, N. Analysis of crack growth and crack-tip plasticity in ductile materials using cohesive zone models. *International Journal of Plasticity 19*, 6 (2003), 849–882–.

[143] LI, S., MEAR, M., AND XIAO, L. Symmetric weak-form integral equation method for three-dimensional fracture analysis. *Computer Methods in Applied Mechanics and Engineering 151*, 3-4 (1998), 435 – 459.

[144] LIBERSKY, L. D., PETSCHEK, A. G., CARNEY, T. C., HIPP, J. R., AND ALLAHDADI, F. A. High strain lagrangian hydrodynamics: A three-dimensional sph code for dynamic material response. *Journal of Computational Physics 109*, 1 (1993), 67 – 75.

[145] LINDER, C., AND ARMERO, F. Finite elements with embedded strong discontinuities for the modeling of failure in solids. *International Journal for Numerical Methods in Engineering 72*, 12 (2007), 1391–1433.

[146] LINDER, C., AND ARMERO, F. Finite elements with embedded branching. *Finite Elements in Analysis and Design 45*, 4 (2009), 280 – 293.

[147] LIONS, J., AND MAGENES, E. Problèmes aux limites non homogènes (vi). *Journal d'Analyse Mathématique 11*, 1 (1963), 165–188.

[148] LIU, J. Meshless study of dynamic failure in shells. *Journal of Engineering Mathematics* (2010), 1–18.

[149] LIU, W. K., JUN, S., AND ZHANG, Y. F. Reproducing kernel particle methods. *International Journal for Numerical Methods in Fluids 20*, 8-9 (1995), 1081–1106.

[150] LU, Y., BELYTSCHKO, T., AND TABBARA, M. Element-free galerkin method for wave propagation and dynamic fracture. *Computer Methods in Applied Mechanics and Engineering 126*, 1-2 (1995), 131 – 153.

[151] LUCY, L. B. A numerical approach to the testing of the fission hypothesis. *Astronomical Journal 82* (1977), 1013–1024.

[152] MACNEAL, R. H., AND HARDER, R. L. A proposed standard set of problems to test finite element accuracy. *Finite Elements in Analysis and Design 1*, 1 (1985), 3 – 20.

[153] MASSONNET, C., AND CESCOTTO, S. *Mécanique des matériaux*, 3 ed. De Boeck, 1994.

[154] MAUREL, B., AND COMBESCURE, A. An sph shell formulation for plasticity and fracture analysis in explicit dynamics. *International Journal for Numerical Methods in Engineering 76*, 7 (2008), 949–971.

[155] MAZARS, J., AND PIJAUDIER-CABOT, G. From damage to fracture mechanics and conversely: A combined approach. *International Journal of Solids and Structures 33*, 20-22 (1996), 3327 – 3342.

[156] MENOUILLARD, T., RÉTHORÉ, J., COMBESCURE, A., AND BUNG, H. Efficient explicit time stepping for the extended finite element method (x-fem). *International Journal for Numerical Methods in Engineering 68*, 9 (2006), 911–939.

[157] MERGHEIM, J., KUHL, E., AND STEINMANN, P. A hybrid discontinuous galerkin/interface method for the computational modelling of failure. *Communications in Numerical Methods in Engineering 20*, 7 (2004), 511–519.

[158] MERGHEIM, J., KUHL, E., AND STEINMANN, P. A finite element method for the computational modelling of cohesive cracks. *International Journal for Numerical Methods in Engineering 63*, 2 (2005), 276–289.

[159] MERGHEIM, J., AND STEINMANN, P. A geometrically nonlinear fe approach for the simulation of strong and weak discontinuities. *Computer Methods in Applied Mechanics and Engineering 195*, 37-40 (2006), 5037 – 5052.

[160] MILLER, O., FREUND, L., AND NEEDLEMAN, A. Modeling and simulation of dynamic fragmentation in brittle materials. *International Journal of Fracture 96* (1999), 101–125.

[161] MILLER, O., FREUND, L. B., AND NEEDLEMAN, A. Energy dissipation in dynamic fracture of brittle materials. *Modelling and Simulation in Materials Science and Engineering 7* (1999), 573–586.

[162] MOËS, N., BÉCHET, E., AND TOURBIER, M. Imposing dirichlet boundary conditions in the extended finite element method. *International Journal for Numerical Methods in Engineering 67*, 12 (2006), 1641–1669.

[163] MOËS, N., AND BELYTSCHKO, T. Extended finite element method for cohesive crack growth. *Engineering Fracture Mechanics 69*, 7 (2002), 813–833.

[164] MOËS, N., CLOIREC, M., CARTRAUD, P., AND REMACLE, J.-F. A computational approach to handle complex microstructure geometries. *Computer Methods in Applied Mechanics and Engineering 192*, 28-30 (2003), 3163 – 3177.

[165] MOËS, N., DOLBOW, J., AND BELYTSCHKO, T. A finite element method for crack growth without remeshing. *International Journal for Numerical Methods in Engineering 46*, 1 (1999), 131–150.

[166] MOËS, N., STOLZ, C., BERNARD, P.-E., AND CHEVAUGEON, N. A level set based model for damage growth: The thick level set approach. *International Journal for Numerical Methods in Engineering 86*, 3 (2011), 358–380.

[167] MOLARI, L., WELLS, G. N., GARIKIPATI, K., AND UBERTINI, F. A discontinuous galerkin method for strain gradient-dependent damage: Study of interpolations and convergence. *Computer Methods in Applied Mechanics and Engineering 195*, 13-16 (2006), 1480 – 1498.

[168] MOLINARI, J.-F., GAZONAS, G., RAGHUPATHY, R., RUSINEK, A., AND ZHOU, F. The cohesive element approach to dynamic fragmentation: the question of energy convergence. *International Journal for Numerical Methods in Engineering 69*, 3 (2007), 484–503.

[169] MONAGHAN, J. An introduction to sph. *Computer Physics Communications 48*, 1 (1988), 89 – 96.

[170] MONAGHAN, J. J. Why particle methods work. *Journal on Scientific and Statistical Computing 3*, 4 (1982), 422–433.

[171] MORAN, B., AND SHIH, C. A general treatment of crack tip contour integrals. *International Journal of Fracture 35* (1987), 295–310.

[172] MOTA, A., KLUG, W. S., ORTIZ, M., AND PANDOLFI, A. Finite-element simulation of firearm injury to the human cranium. *Computational Mechanics 31* (2003), 115–121.

[173] MOTA, A., KNAP, J., AND ORTIZ, M. Fracture and fragmentation of simplicial finite element meshes using graphs. *International Journal for Numerical Methods in Engineering 73*, 11 (2008), 1547–1570.

[174] NAGASHIMA, T., AND SUEMASU, H. Application of extended finite element method to fracture of composite materials. In *European Congress on Computational Methods in Applied Sciences and Engineering (ECCOMAS 2004)* (2004).

[175] NEEDLEMAN, A. A continuum model for void nucleation by inclusion debonding. *Journal of Applied Mechanics 54* (1987), 525–531.

[176] NEEDLEMAN, A. An analysis of decohesion along an imperfect interface. *International Journal of Fracture 42* (1990), 21–40.

[177] NEEDLEMAN, A. An analysis of tensile decohesion along an interface. *Journal of the Mechanics and Physics of Solids 38*, 3 (1990), 289 – 324.

[178] NEEDLEMAN, A. Numerical modeling of crack growth under dynamic loading conditions. *Computational Mechanics 19* (1997), 463–469.

[179] NGUYEN, O., REPETTO, E., ORTIZ, M., AND RADOVITZKY, R. A cohesive model of fatigue crack growth. *International Journal of Fracture 110* (2001), 351–369.

[180] NITSCHE, J. Über ein Variationsprinzip zur Lösung von Dirichlet-Problemen bei Verwendung von Teilräumen, die keinen Randbedingungen unterworfen sind. *Abh. Math. Sem. Univ. Hamburg 36* (1971), 9–15.

[181] NOELS, L. A discontinuous galerkin formulation of non-linear kirchhoff-love shells. *International Journal for Numerical Methods in Engineering 78*, 3 (2009), 296–323.

[182] NOELS, L., AND RADOVITZKY, R. A general discontinuous galerkin method for finite hyperelasticity. formulation and numerical applications. *International Journal for Numerical Methods in Engineering 68*, 1 (2006), 64–97.

[183] NOELS, L., AND RADOVITZKY, R. Alternative approaches for the derivation of discontinuous galerkin methods for nonlinear mechanics. *Journal of Applied Mechanics 74*, 5 (2007), 1031–1036.

[184] NOELS, L., AND RADOVITZKY, R. An explicit discontinuous galerkin method for non-linear solid dynamics: Formulation, parallel implementation and scalability properties. *International Journal for Numerical Methods in Engineering 74*, 9 (2008), 1393–1420.

[185] NOELS, L., AND RADOVITZKY, R. A new discontinuous galerkin method for kirchhoff-love shells. *Computer Methods in Applied Mechanics and Engineering 197*, 33-40 (2008), 2901–2929.

[186] OAKLEY, D. R., AND KNIGHT, N. F. Adaptive dynamic relaxation algorithm for non-linear hyperelastic structures part i. formulation. *Computer Methods in Applied Mechanics and Engineering 126*, 1-2 (1995), 67 – 89.

[187] OLIVER, J. On the discrete constitutive models induced by strong discontinuity kinematics and continuum constitutive equations. *International Journal of Solids and Structures 37*, 48-50 (2000), 7207 – 7229.

[188] OLIVER, J., AND HUESPE, A. Theoretical and computational issues in modelling material failure in strong discontinuity scenarios. *Computer Methods in Applied Mechanics and Engineering 193*, 27-29 (2004), 2987 – 3014.

[189] OLIVER, J., HUESPE, A., PULIDO, M., AND CHAVES, E. From continuum mechanics to fracture mechanics: the strong discontinuity approach. *Engineering Fracture Mechanics 69*, 2 (2002), 113 – 136.

[190] OLIVER, J., HUESPE, A., AND SÁNCHEZ, P. A comparative study on finite elements for capturing strong discontinuities: E-fem vs x-fem. *Computer Methods in Applied Mechanics and Engineering 195*, 37-40 (2006), 4732 – 4752.

[191] ORTIZ, M., AND PANDOLFI, A. Finite-deformation irreversible cohesive elements for three-dimensional crack propagation analysis. *International Journal for Numerical Methods in Engineering 44* (2000), 44–1267.

[192] PANDOLFI, A., GUDURU, P., ORTIZ, M., AND ROSAKIS, A. Three dimensional cohesive-element analysis and experiments of dynamic fracture in c300 steel. *International Journal of Solids and Structures 37*, 27 (2000), 3733 – 3760.

[193] PANDOLFI, A., KRYSL, P., AND ORTIZ, M. Finite element simulation of ring expansion and fragmentation: The capturing of length and time scales through cohesive models of fracture. *International Journal of Fracture 95*, 1 (1999), 279–297.

[194] PANDOLFI, A., AND ORTIZ, M. An efficient adaptive procedure for three-dimensional fragmentation simulations. *Engineering with Computers 18*, 2 (2002), 148–159.

[195] PAPADRAKAKIS, M. A method for the automatic evaluation of the dynamic relaxation parameters. *Computer Methods in Applied Mechanics and Engineering 25*, 1 (1981), 35 – 48.

[196] PAPOULIA, K. D., SAM, C.-H., AND VAVASIS, S. A. Time continuity in cohesive finite element modeling. *International Journal for Numerical Methods in Engineering 58*, 5 (2003), 679–701.

[197] PAPOULIA, K. D., VAVASIS, S. A., AND GANGULY, P. Spatial convergence of crack nucleation using a cohesive finite-element model on a pinwheel-based mesh. *International Journal for Numerical Methods in Engineering 67*, 1 (2006), 1–16.

[198] PARKS, D. The virtual crack extension method for nonlinear material behavior. *Computer Methods in Applied Mechanics and Engineering 12*, 3 (1977), 353 – 364.

[199] PARKS, D. M. A stiffness derivative finite element technique for determination of crack tip stress intensity factors. *International Journal of Fracture 10* (1974), 487–502.

[200] PAULINO, G., CELES, W., ESPINHA, R., AND ZHANG, Z. A general topology-based framework for adaptive insertion of cohesive elements in finite element meshes. *Engineering with Computers 24* (2008), 59–78.

[201] PEERLINGS, R., DEÂ BORST, R., BREKELMANS, W., AND GEERS, M. Localisation issues in local and nonlocal continuum approaches to fracture. *European Journal of Mechanics - A/Solids 21*, 2 (2002), 175 – 189.

[202] PEERLINGS, R., GEERS, M., DE BORST, R., AND BREKELMANS, W. A critical comparison of nonlocal and gradient-enhanced softening continua. *International Journal of Solids and Structures 38* (2001), 7723 – 7746.

[203] PEERLINGS, R. H. J., DE BORST, R., BREKELMANS, W. A. M., AND GEERS, M. G. D. Gradient-enhanced damage modelling of concrete fracture. *Mechanics of Cohesive-frictional Materials 3*, 4 (1998), 323–342.

[204] PERALES, F., BOURGEOIS, S., CHRYSOCHOOS, A., AND MONERIE, Y. Two field multibody method for periodic homogenization in fracture mechanics of nonlinear heterogeneous materials. *Engineering Fracture Mechanics 75*, 11 (2008), 3378–3398.

[205] PERCELL, P., AND WHEELER, M. F. A local residual finite element procedure for elliptic equations. *SIAM Journal on Numerical Analysis 15*, 4 (1978), 705–714.

[206] PIAN, T. H. H., AND TONG, P. Basis of finite element methods for solid continua. *International Journal for Numerical Methods in Engineering 1*, 1 (1969), 3–28.

[207] PONTHOT, J.-P., AND BELYTSCHKO, T. Arbitrary lagrangian-eulerian formulation for element-free galerkin method. *Computer Methods in Applied Mechanics and Engineering 152*, 1-2 (1998), 19 – 46.

[208] PRABEL, B., COMBESCURE, A., GRAVOUIL, A., AND MARIE, S. Level set x-fem non-matching meshes: application to dynamic crack propagation in elastic-plastic media. *International Journal for Numerical Methods in Engineering 69*, 8 (2007), 1553–1569.

[209] PRECHTEL, M., LEUGERING, G., STEINMANN, P., AND STINGL, M. Towards optimization of crack resistance of composite materials by adjustment of fiber shapes. *Engineering Fracture Mechanics 78*, 6 (2011), 944 – 960.

[210] PRECHTEL, M., RONDA, P., JANISCH, R., HARTMAIER, A., LEUGERING, G., STEINMANN, P., AND STINGL, M. Simulation of fracture in heterogeneous elastic materials with cohesive zone models. *International Journal of Fracture 168* (2011), 15–29.

[211] RADOVITZKY, R., SEAGRAVES, A., TUPEK, M., AND NOELS, L. A scalable 3d fracture and fragmentation algorithm based on a hybrid, discontinuous galerkin, cohesive element method. *Computer Methods in Applied Mechanics and Engineering 200*, 1-4 (2011), 326 – 344.

[212] RADULOVIC, R., BRUHNS, O. T., AND MOSLER, J. Effective 3d failure simulations by combining the advantages of embedded strong discontinuity approaches and classical interface elements. *Engineering Fracture Mechanics 78*, 12 (2011), 2470 – 2485.

[213] REED, W., AND HILL, T. Triangular mesh methods for the neutron transport equation. In *Conference: National topical meeting on mathematical models and computational techniques for analysis of nuclear systems, Ann Arbor, Michigan, USA, 8 Apr 1973; Other Information: Orig. Receipt Date: 31-DEC-73* (1973).

[214] REPETTO, E., RADOVITZKY, R., AND ORTIZ, M. Finite element simulation of dynamic fracture and fragmentation of glass rods. *Computer Methods in Applied Mechanics and Engineering 183*, 1-2 (2000), 3 – 14.

[215] RICE, J. *Mathematical analysis in the mechanics of fracture*, vol. 2. H. Liebotwitz, Editor, Fracture: An Advanced Treatise, 1968.

[216] RICE, J., AND ROSENGREN, G. Plane strain deformation near a crack tip in a power-law hardening material. *Journal of the Mechanics and Physics of Solids 16*, 1 (1968), 1 – 12.

[217] RICE, J. R., AND TRACEY, D. M. Computational fracture mechanics. *Interface*, January (1973), 1–22.

[218] ROSE, J. H., FERRANTE, J., AND SMITH, J. R. Universal binding energy curves for metals and bimetallic interfaces. *Physical Review Letters 47* (1981), 675–678.

[219] ROSE, J. H., SMITH, J. R., AND FERRANTE, J. Universal features of bonding in metals. *Physical Review B 28* (1983), 1835–1845.

[220] RUIZ, G., ORTIZ, M., AND PANDOLFI, A. Three-dimensional finite-element simulation of the dynamic brazilian tests on concrete cylinders. *International Journal for Numerical Methods in Engineering 48*, 7 (2000), 963–994.

[221] RUIZ, G., PANDOLFI, A., AND ORTIZ, M. Three-dimensional cohesive modeling of dynamic mixed-mode fracture. *International Journal for Numerical Methods in Engineering 52*, 1-2 (2001), 97–120.

[222] SANCHEZ, P., HUESPE, A., AND OLIVER, J. On some topics for the numerical simulation of ductile fracture. *International Journal of Plasticity 24*, 6 (2008), 1008 – 1038.

[223] SANSOUR, C., AND BOCKO, J. On hybrid stress, hybrid strain and enhanced strain finite element formulations for a geometrically exact shell theory with drilling degrees of freedom. *International Journal for Numerical Methods in Engineering 43*, 1 (1998), 175–192.

[224] SANSOUR, C., AND KOLLMANN, F. G. Families of 4-node and 9-node finite elements for a finite deformation shell theory. an assesment of hybrid stress, hybrid strain and enhanced strain elements. *Computational Mechanics 24* (2000), 435–447.

[225] SCHEIDER, I., AND BROCKS, W. Simulation of cup-cone fracture using the cohesive model. *Engineering Fracture Mechanics 70*, 14 (2003), 1943–1961.

[226] SCHEYVAERTS, F., PARDOEN, T., AND ONCK, P. A new model for void coalescence by internal necking. *International Journal of Damage Mechanics 19*, 1 (2010), 95–126.

[227] SEABRA, M., DE SA, J., ANDRADE, F., AND PIRES, F. Continuous-discontinuous formulation for ductile fracture. *International Journal of Material Forming 4* (2011), 271–281.

[228] SEAGRAVES, A., AND RADOVITZKY, R. Advances in cohesive zone modeling of dynamic fracture. In *Dynamic Failure of Materials and Structures*, A. Shukla, G. Ravichandran, and Y. D. Rajapakse, Eds. Springer US, 2010, pp. 349–405.

[229] SHIH, C. F., MORAN, B., AND NAKAMURA, T. Energy release rate along a three-dimensional crack front in a thermally stressed body. *International Journal of Fracture 30* (1986), 79–102.

[230] SIEGMUND, T., AND BROCKS, W. Prediction of the work of separation and implications to modeling. *International Journal of Fracture 99*, 1 (1999), 97–116.

[231] SIEGMUND, T., AND NEEDLEMAN, A. A numerical study of dynamic crack growth in elastic-viscoplastic solids. *International Journal of Solids and Structures 34*, 7 (1997), 769 – 787.

[232] SILVANI, C., DÉSOYER, T., AND BONELLI, S. Discrete modelling of time-dependent rockfill behaviour. *International Journal for Numerical and Analytical Methods in Geomechanics 33*, 5 (2009), 665–685.

[233] SIMO, J., AND FOX, D. On stress resultant geometrically exact shell model. part i: formulation and optimal parametrization. *Computer Methods in Applied Mechanics and Engineering 72*, 3 (1989), 267–304.

[234] SIMO, J., FOX, D., AND RIFAI, M. On a stress resultant geometrically exact shell model. part ii: the linear theory; computational aspects. *Computer Methods in Applied Mechanics and Engineering 73*, 1 (1989), 53–92.

[235] SIMO, J., FOX, D., AND RIFAI, M. On a stress resultant geometrically exact shell model. part iii: Computational aspects of the nonlinear theory. *Computer Methods in Applied Mechanics and Engineering 79*, 1 (1990), 21 – 70.

[236] SIMO, J., AND KENNEDY, J. On a stress resultant geometrically exact shell model. part v. nonlinear plasticity: formulation and integration algorithms. *Computer Methods in Applied Mechanics and Engineering 96*, 2 (1992), 133 – 171.

[237] SIMO, J., RIFAI, M., AND FOX, D. On a stress resultant geometrically exact shell model. part iv: Variable thickness shells with through-the-thickness stretching. *Computer Methods in Applied Mechanics and Engineering 81*, 1 (1990), 91 – 126.

[238] SIMO, J., RIFAI, M., AND FOX, D. On a stress resultant geometrically exact shell model. part vi: Conserving algorithms for non-linear dynamics. *International Journal for Numerical Methods in Engineering 34*, 1 (1992), 117–164.

[239] SONG, J.-H., AREIAS, P. M. A., AND BELYTSCHKO, T. A method for dynamic crack and shear band propagation with phantom nodes. *International Journal for Numerical Methods in Engineering 67*, 6 (2006), 868–893.

[240] SONG, J.-H., AND BELYTSCHKO, T. Cracking node method for dynamic fracture with finite elements. *International Journal for Numerical Methods in Engineering 77*, 3 (2009), 360–385.

[241] SUBHASH, G., MAITI, S., GEUBELLE, P. H., AND GHOSH, D. Recent advances in dynamic indentation fracture, impact damage and fragmentation of ceramics. *Journal of the American Ceramic Society 91*, 9 (2008), 2777–2791.

[242] SUKUMAR, N., MOËS, N., MORAN, B., AND BELYTSCHKO, T. Extended finite element method for three-dimensional crack modelling. *International Journal for Numerical Methods in Engineering 48*, 11 (2000), 1549–1570.

[243] SWADDIWUDHIPONG, S., AND LIU, Z. S. Dynamic response of large strain elasto-plastic plate and shell structures. *Thin-Walled Structures 26*, 4 (1996), 223 – 239.

[244] TOLEDO, S., CHEN, D., AND ROTKIN, V. Taucs: A library of sparse linear solvers. Tech. Rep. version 2.2, Tel-Aviv University, 2003.

[245] TOLEDO, S., CHEN, D., AND ROTKIN, V. TAUCS Web page, 2003. http://www.tau.ac.il/ stoledo/taucs/.

[246] TRACEY, D. M. Finite elements for determination of crack tip elastic stress intensity factors. *Engineering Fracture Mechanics 3*, 3 (1971), 255 – 265.

[247] TVERGAARD, V. Effect of fibre debonding in a whisker-reinforced metal. *Materials Science and Engineering: A 125*, 2 (1990), 203 – 213.

[248] TVERGAARD, V. Crack growth predictions by cohesive zone model for ductile fracture. *Journal of the Mechanics and Physics of Solids 49*, 9 (2001), 2191–2207.

[249] TVERGAARD, V., AND HUTCHINSON, J. W. The relation between crack growth resistance and fracture process parameters in elastic-plastic solids. *Journal of the Mechanics and Physics of Solids 40*, 6 (1992), 1377 – 1397.

[250] TVERGAARD, V., AND HUTCHINSON, J. W. The influence of plasticity on mixed mode interface toughness. *Journal of the Mechanics and Physics of Solids 41*, 6 (1993), 1119 – 1135.

[251] TVERGAARD, V., AND HUTCHINSON, J. W. Effect of strain-dependent cohesive zone model on predictions of crack growth resistance. *International Journal of Solids and Structures 33*, 20-22 (1996), 3297–3308.

[252] TVERGAARD, V., AND NEEDLEMAN, A. An analysis of the brittle-ductile transition in dynamic crack growth. *International Journal of Fracture 59* (1993), 53–67.

[253] VAN VROONHOVEN, J., AND DE BORST, R. Combination of fracture and damage mechanics for numerical failure analysis. *International Journal of Solids and Structures 36*, 8 (1999), 1169 – 1191.

[254] VO THI, G. Modélisation de la rupture ductile par la methode de dg/czm. Travail de fin d'étude, Ulg, Liège, june 2011. In French.

[255] WEIBULL, W. A statistical theory of strength of materials. vol. Proceedings of the Ingeniors Vetenskapsakad, p. 151.

[256] WELLS, G., AND SLUYS, L. Three-dimensional embedded discontinuity model for brittle fracture. *International Journal of Solids and Structures 38*, 5 (2000), 897 – 913.

[257] WELLS, G. N., AND DUNG, N. T. A c0 discontinuous galerkin formulation for kirchhoff plates. *Computer Methods in Applied Mechanics and Engineering 196*, 35-36 (2007), 3370–3380.

[258] WELLS, G. N., GARIKIPATI, K., AND MOLARI, L. A discontinuous galerkin formulation for a strain gradient-dependent damage model. *Computer Methods in Applied Mechanics and Engineering 193*, 33-35 (2004), 3633 – 3645.

[259] WHEELER, M. F. An elliptic collocation-finite element method with interior penalties. *SIAM Journal on Numerical Analysis 15*, 1 (1978), 152–161.

[260] WYART, E., COULON, D., DUFLOT, M., PARDOEN, T., REMACLE, J.-F., AND LANI, F. A substructured fe-shell/xfe-3d method for crack analysis in thin-walled structures. *International Journal for Numerical Methods in Engineering 72*, 7 (2007), 757–779.

[261] XU, X.-P., AND NEEDLEMAN, A. Void nucleation by inclusion debonding in a crystal matrix. *Modelling and Simulation in Materials Science and Engineering 1* (1993), 111–132.

[262] XU, X.-P., AND NEEDLEMAN, A. Numerical simulations of fast crack growth in brittle solids. *Journal of the Mechanics and Physics of Solids 42*, 9 (1994), 1397 – 1434.

[263] XU, X.-P., AND NEEDLEMAN, A. Numerical simulations of dynamic interfacial crack growth allowing for crack growth away from the bond line. *International Journal of Fracture 74* (1995), 253–275.

[264] XU, X.-P., AND NEEDLEMAN, A. Numerical simulations of dynamic crack growth along an interface. *International Journal of Fracture 74* (1996), 289–324.

[265] YU, C., ORTIZ, M., AND ROSAKIS, A. 3d modelling of impact failure in sandwich structures. In *Fracture of Polymers, Composites and Adhesives II*, A. P. B.R.K. Blackman and J. Williams, Eds., vol. 32 of *European Structural Integrity Society*. Elsevier, 2003, pp. 527 – 537.

[266] YU, C., PANDOLFI, A., ORTIZ, M., COKER, D., AND ROSAKIS, A. Three-dimensional modeling of intersonic shear-crack growth in asymmetrically loaded unidirectional composite plates. *International Journal of Solids and Structures 39*, 25 (2002), 6135 – 6157.

[267] YU, R. C., RUIZ, G., AND PANDOLFI, A. Numerical investigation on the dynamic behavior of advanced ceramics. *Engineering Fracture Mechanics 71*, 4-6 (2004), 897 – 911.

[268] ZAVATTIERI, P. Modeling of crack propagation in thin-walled structures. *Mecanica Computacional XXIII* (2004), 209–228.

[269] ZAVATTIERI, P. Modeling of crack propagation in thin-walled structures using a cohesive model for shell elements. *Journal of Applied Mechanics 73*, 6 (2006), 948–958.

[270] ZAVATTIERI, P., AND ESPINOSA, H. Grain level analysis of crack initiation and propagation in brittle materials. *Acta Materialia 49*, 20 (2001), 4291 – 4311.

[271] ZENG, Q., AND COMBESCURE, A. A new one-point quadrature, general non-linear quadrilateral shell element with physical stabilization. *International Journal for Numerical Methods in Engineering 42*, 7 (1998), 1307–1338.

[272] ZHANG, L., KADKHODAYAN, M., AND MAI, Y.-W. Development of the madr method. *Computers & Structures 52*, 1 (1994), 1 – 8.

[273] ZHANG, Z. J., AND PAULINO, G. H. Cohesive zone modeling of dynamic failure in homogeneous and functionally graded materials. *International Journal of Plasticity 21*, 6 (2005), 1195 – 1254.

[274] ZHANG, Z. J., PAULINO, G. H., AND CELES, W. Extrinsic cohesive modelling of dynamic fracture and microbranching instability in brittle materials. *International Journal for Numerical Methods in Engineering 72*, 8 (2007), 893–923.

[275] ZHOU, F., AND MOLINARI, J.-F. Dynamic crack propagation with cohesive elements: a methodology to address mesh dependency. *International Journal for Numerical Methods in Engineering 59*, 1 (2004), 1–24.

[276] ZHOU, F., AND MOLINARI, J.-F. Stochastic fracture of ceramics under dynamic tensile loading. *International Journal of Solids and Structures 41*, 22-23 (2004), 6573 – 6596.

[277] ZI, G., AND BELYTSCHKO, T. New crack-tip elements for xfem and applications to cohesive cracks. *International Journal for Numerical Methods in Engineering 57*, 15 (2003), 2221–2240.

Appendix A

Annex to chapter 3

A.1 Euler-Bernoulli beams kinematics

The kinematics of thin bodies is previously established in Section 4.1.1 in the general case of Kirchhhoff-Love shells. These equations can be particularized to Euler-Bernoulli beams. Under the assumptions given in Chapter 3, which are,

(i) Linear small strains;

(ii) Initially straight beam;

(iii) The out-of-plane shearing is neglected;

(iv) Plane stress state.

First, for a straight beam with small strain the mapping of the mid-surface (4.3) $\boldsymbol{\varphi}$ can be written,

$$\boldsymbol{\varphi} = \boldsymbol{\varphi}_0 + u_1(\xi^1)\boldsymbol{E}_1 + u_3(\xi^1)\boldsymbol{E}_3 \tag{A.1}$$

as under this assumption, the mid-surface is subjected to the small displacement field $\boldsymbol{u}$ leading to,

$$\boldsymbol{\varphi} \;=\; \boldsymbol{\varphi}_0 + \boldsymbol{u}\,. \tag{A.2}$$

Furthermore, the calculation of the derivatives of $\boldsymbol{\varphi}$ are straightforward,

$$\boldsymbol{\varphi}_{,1} \;=\; \boldsymbol{\varphi}_{0,1} + u_{1,1}\boldsymbol{E}_1 + u_{3,1}\boldsymbol{E}_3 = (1+u_{1,1})\,\boldsymbol{E}_1 + u_{3,1}\boldsymbol{E}_3 \tag{A.3}$$

$$\boldsymbol{\varphi}_{,2} \;=\; \boldsymbol{E}_2 \tag{A.4}$$

as a straight beam is always included in the plane $\boldsymbol{E}_1, \boldsymbol{E}_3$.

The third assumption leads to neglect the out-of-plane shearing and so the cross section always remains perpendicular to the neutral axis. Therefore, $\boldsymbol{t}$ is always perpendicular to the neutral axis and it comes at first order,

$$\begin{aligned} \boldsymbol{t} &= \frac{\boldsymbol{\varphi}_{,1} \wedge \boldsymbol{\varphi}_{,2}}{||\boldsymbol{\varphi}_{,1} \wedge \boldsymbol{\varphi}_{,2}||} && \text{(A.5)} \\ &= \frac{(1+u_{1,1})\boldsymbol{E}_3 - u_{3,1}\boldsymbol{E}_1}{\sqrt{1+2u_{1,1}}} && \text{(A.6)} \\ &= \boldsymbol{E}_3 - u_{3,1}\boldsymbol{E}_1 \,. && \text{(A.7)} \end{aligned}$$

Then, following these developments, the use of relations (4.12) and (A.7) in the expression of $\nabla\Phi$ (4.8) gives at first order,

$$\begin{aligned} \nabla\Phi &= [(1+u_{1,1})\,\boldsymbol{E}_1 + u_{3,1}\boldsymbol{E}_3] \otimes \boldsymbol{E}^1 + \boldsymbol{E}_2 \otimes \boldsymbol{E}^2 - \left(\xi^3 u_{3,11}\boldsymbol{E}_1\right) \otimes \boldsymbol{E}^1 \\ &\quad + (\boldsymbol{E}_3 - u_{3,1}\boldsymbol{E}_1) \otimes \boldsymbol{E}_3 && \text{(A.8)} \\ &= \begin{pmatrix} 1+u_{1,1}-\xi^3 u_{3,11} & 0 & -u_{3,1} \\ 0 & 1 & 0 \\ u_{3,1} & 0 & 1 \end{pmatrix}. && \text{(A.9)} \end{aligned}$$

Moreover, as there is initially no deformation mapping, $\nabla\Phi_0 = \mathbf{I}$, and so $\nabla\Phi_0^{-T} = \mathbf{I}$. Therefore, using Eq. (4.7), the deformation gradient $\mathbf{F} = \nabla\Phi$ and as by definition of Cauchy strain tensor $\boldsymbol{\varepsilon} = \frac{1}{2}\left(\mathbf{F} + \mathbf{F}^T - 2\mathbf{I}\right)$, which leads to,

$$\boldsymbol{\varepsilon} = \begin{pmatrix} u_{1,1}-\xi^3 u_{3,11} & 0 & 0 \\ 0 & 0 & 0 \\ 0 & 0 & \lambda_h \end{pmatrix} \qquad \text{(A.10)}$$

A.2 Governing equations of Euler-Bernoulli beams

The governing equations of shells previoulsy obtained in Section 4.1.2 are now particularized to Euler-Bernoulli beams. The set of Eqs. (4.30) and (4.50) can be written with the stress tensor related to the particular case of Euler-Bernoulli beams,

$$\boldsymbol{\sigma} = \begin{pmatrix} \sigma^{11} & 0 & \sigma^{31} \\ 0 & 0 & 0 \\ \sigma^{31} & 0 & 0 \end{pmatrix}. \qquad \text{(A.11)}$$

with $\sigma^{11} = E\varepsilon_{11}$ as plane stress is assumed. Normally, as out-of-plane shearing is neglected by assumption, $\sigma^{31} \approx 0$, but this term is kept as it will be used to obtain the full discontinuous Galerkin formulation.

Furthermore, the initial deformation mapping of a straight beam reads, $\boldsymbol{g}_0^I = \boldsymbol{E}_I$, the expression of resultant quantities (other values are equal to zero) are,

$$n^{11} = \frac{1}{j}\int_{h_{\min}}^{h_{\max}} j\sigma^{11} d\xi^3 \tag{A.12}$$

$$\tilde{m}^{11} = \frac{1}{j}\int_{h_{\min}}^{h_{\max}} j\sigma^{11}\xi^3 d\xi^3 \tag{A.13}$$

$$l^1 = \frac{1}{j}\int_{h_{\min}}^{h_{\max}} j\sigma^{31} d\xi^3 \tag{A.14}$$

Finally, as there are no external effort by assumption, the balance of linear (4.30) and angular momentum (4.50) become respectively,

$$n^{11}_{,1} = \overline{\rho}\ddot{u}_1\,, \tag{A.15}$$

$$\tilde{m}^{11}_{,1} - l^1 = 0 \text{ and,} \tag{A.16}$$

$$l^1_{,1} = \overline{\rho}\ddot{u}_3\,. \tag{A.17}$$

Notice that the Jacobian of $\nabla\Phi$ can be determined from Eq. (A.8) with a first order approximation,

$$j = 1 + u_{1,1} - \xi^3 u_{3,11}\,. \tag{A.18}$$

(A.19)

At neutral axis ($\xi^3 = 0$) and the Jacobian reads,

$$\overline{j} = 1 + u_{1,1}\,. \tag{A.20}$$

Since we have the following identities,

$$\overline{\rho}_B = \overline{\rho}\,, \tag{A.21}$$

$$n^{11} = n_B^{11}\,, \tag{A.22}$$

$$\tilde{m_B}^{11} = \tilde{m}^{11} \text{ and,} \tag{A.23}$$

$$l_B^1 = l^1\,, \tag{A.24}$$

the set of Eqs. (A.15) - (A.17) corresponds to the set of Eqs. (3.8) and (3.14)

A.3 Numerical properties of the full-DG formulation

In Chapter 3 we enumerated the numerical properties of the suggested DG formulation of Euler-Bernoulli beams. To be concise some demonstrations were omitted. They are reported here below.

A.3.1 Upper bound of the bilinear form

To obtain an upper bound of the bilinear form each term of (3.34) is bounded separately as suggested in [185]. First, the membrane and bending terms are considered. The use of Cauchy-Schwartz inequality[1] leads to,

$$\left|\sum_e \int_{l_e} Ehu_{1,1}\delta u_{1,1}dx\right| \leq \sum_e \left|\left|\sqrt{Eh}u_{1,1}\right|\right|_{\mathbf{L}^2(l_e)} \left|\left|\sqrt{Eh}\delta u_{1,1}\right|\right|_{\mathbf{L}^2(l_e)} \text{and,} \tag{A.25}$$

$$\left|\sum_e \int_{l_e} \frac{Eh^3}{12}(-u_{3,11})\delta(-u_{3,11})dx\right| \leq \sum_e \left|\left|\sqrt{\frac{Eh^3}{12}}u_{3,11}\right|\right|_{\mathbf{L}^2(l_e)} \left|\left|\sqrt{\frac{Eh^3}{12}}\delta u_{3,11}\right|\right|_{\mathbf{L}^2(l_e)}. \tag{A.26}$$

Now the interface terms can be bounded. As all terms are bounded by the same way, only the first membrane interface term of consistency is developed. The results for the others terms will be extended. First, the sum on the interface elements are replaced by a sum of elements's integral of contour. In doing this, the contribution of each interface term is taken twice which is valid because it is a upper bound,

$$\begin{aligned}\left|\sum_s \left\langle {n_B}^{11}\right\rangle [\![\delta u_1]\!]\right| &= \left|\sum_s \langle Ehu_{1,1}\rangle [\![\delta u_1]\!]\right| \\ &\leq \sum_s |\langle Ehu_{1,1}\rangle [\![\delta u_1]\!]| \\ &\leq \sum_e |Ehu_{1,1}[\![\delta u_1]\!]|. \end{aligned} \tag{A.27}$$

Then,

$$\begin{aligned}\left|\sum_s \left\langle {n_B}^{11}\right\rangle [\![\delta u_1]\!]\right| &\leq \sum_e \left|\left|\sqrt{Eh}u_{1,1}\right|\right|_{\mathbf{L}^2(\partial l_e)} \left|\left|\sqrt{Eh}[\![\delta u_1]\!]\right|\right|_{\mathbf{L}^2(\partial l_e)} \\ &\leq 2\sum_e \left|\left|\sqrt{Eh}u_{1,1}\right|\right|_{\mathbf{L}^2(\partial l_e)} \left|\left|\sqrt{Eh}[\![\delta u_1]\!]\right|\right|_{\mathbf{L}^2(\partial l_e)}. \end{aligned} \tag{A.28}$$

Finally, to have a norm over $\mathbf{L}^2(l_e)$ the scaling property[2] demonstrated by P. Hansbo *et al.* in [116] is used,

$$\left|\sum_s \left\langle {n_B}^{11}\right\rangle [\![\delta u_1]\!]\right| \leq \frac{C_2^k}{\sqrt{\beta_2}} \sum_e \left|\left|\sqrt{Eh}u_{1,1}\right|\right|_{\mathbf{L}^2(l_e)} \left|\left|\sqrt{\frac{Eh\beta_2}{h^s}}[\![\delta u_1]\!]\right|\right|_{\mathbf{L}^2(\partial l_e)}. \tag{A.29}$$

The same procedure applied to the others terms gives successively[3]:

[1] $|ab| \leq \sqrt{a^2}\sqrt{b^2}$

[2] For an element e $h^s \left|\left|\sqrt{\mathcal{H}}a\right|\right|^2_{\mathbf{L}^2(\partial l_e)} \leq C^k \left|\left|\sqrt{\mathcal{H}}a\right|\right|^2_{\mathbf{L}^2(l_e)}$ with $h^s = \frac{|l_e|}{|\partial l_e|}$ and with $C^k = \sup_{a\in\mathcal{P}^k(l_e)} \frac{|l_e|\int_s a^2 d\partial l_e}{|s|\int_{l_e} a^2 dl} \geq 0$ depends only on the polynomial degree k

[3] Note that the scaling property is not applied for the terms of stabilization

- for the symmetrization term of membrane part,

$$\left|\sum_s \langle Eh\delta u_{1,1}\rangle [\![u_1]\!]\right| \leq \frac{C_2^k}{\sqrt{\beta_2}} \sum_e \left|\left|\sqrt{Eh}\delta u_{1,1}\right|\right|_{\mathbf{L}^2(l_e)} \left|\left|\sqrt{\frac{Eh\beta_2}{h^s}}[\![u_1]\!]\right|\right|_{\mathbf{L}^2(\partial l_e)},$$

- for the stabilization term of membrane part,

$$\left|\sum_s [\![u_1]\!] \left\langle \frac{\beta_2 Eh}{h^s} \right\rangle [\![\delta u_1]\!]\right| \leq \sum_e \left|\left|\sqrt{\frac{\beta_2 Eh}{h^s}}[\![u_1]\!]\right|\right|_{\mathbf{L}^2(\partial l_e)} \left|\left|\sqrt{\frac{\beta_2 Eh}{h^s}}[\![\delta u_1]\!]\right|\right|_{\mathbf{L}^2(\partial l_e)},$$

- for the consistency term of bending part,

$$\begin{aligned}\left|\sum_s \langle \tilde{m_B}^{11}\rangle [\![\delta(-u_{3,1})]\!]\right| \leq & \frac{C_1^k}{\sqrt{\beta_1}} \sum_e \left|\left|\sqrt{\frac{Eh^3}{12}}u_{3,11}\right|\right|_{\mathbf{L}^2(l_e)} \\ & \times \left|\left|\sqrt{\frac{\beta_1 Eh^3}{12h^s}}[\![\delta u_{3,1}]\!]\right|\right|_{\mathbf{L}^2(\partial l_e)},\end{aligned}$$

- for the symmetrization term of bending part,

$$\begin{aligned}\left|\sum_s \left\langle \frac{Eh^3}{12}\delta(-u_{3,11}) \right\rangle [\![(-u_{3,1})]\!]\right| \leq & \frac{C_1^k}{\sqrt{\beta_1}} \sum_e \left|\left|\sqrt{\frac{Eh^3}{12}}\delta u_{3,11}\right|\right|_{\mathbf{L}^2(l_e)} \\ & \times \left|\left|\sqrt{\frac{\beta_1 Eh^3}{12h^s}}[\![u_{3,1}]\!]\right|\right|_{\mathbf{L}^2(\partial l_e)},\end{aligned}$$

- for the stabilization term of bending part,

$$\begin{aligned}\left|\sum_s [\![u_{3,1}]\!] \left\langle \frac{\beta_1 Eh^3}{12h^s} \right\rangle [\![\delta u_{3,1}]\!]\right| \leq & \sum_e \left|\left|\sqrt{\frac{\beta_1 Eh^3}{12h^s}}[\![u_{3,1}]\!]\right|\right|_{\mathbf{L}^2(\partial l_e)} \\ & \times \left|\left|\sqrt{\frac{\beta_1 Eh^3}{12h^s}}[\![\delta u_{3,1}]\!]\right|\right|_{\mathbf{L}^2(\partial l_e)},\end{aligned}$$

- and for the stabilization term of the "shearing" part,

$$\left|\sum_s [\![u_3]\!]\left\langle \frac{\beta_3 Eh}{2(1+\nu)h^s}\right\rangle [\![\delta u_3]\!]\right| \leq \sum_e \left|\left|\sqrt{\frac{\beta_3 Eh}{2(1+\nu)h^s}}\,[\![u_3]\!]\right|\right|_{\mathbf{L}^2(\partial l_e)} \times \left|\left|\sqrt{\frac{\beta_3 Eh}{2(1+\nu)h^s}}\,[\![\delta u_3]\!]\right|\right|_{\mathbf{L}^2(\partial l_e)}.$$

The summation of these different expressions with Eqs. (A.25-A.26) gives the inequality,

$$\begin{aligned}
|a(\boldsymbol{u},\delta\boldsymbol{u})| \leq \sum_e \Bigg\{ & \left|\left|\sqrt{Eh}u_{1,1}\right|\right|_{\mathbf{L}^2(l_e)} \left|\left|\sqrt{Eh}\delta u_{1,1}\right|\right|_{\mathbf{L}^2(l_e)} \\
& + \left|\left|\sqrt{\frac{Eh^3}{12}}u_{3,11}\right|\right|_{\mathbf{L}^2(l_e)} \left|\left|\sqrt{\frac{Eh^3}{12}}\delta u_{3,11}\right|\right|_{\mathbf{L}^2(l_e)} \\
& + \frac{C_2^k}{\sqrt{\beta_2}} \left|\left|\sqrt{Eh}u_{1,1}\right|\right|_{\mathbf{L}^2(l_e)} \left|\left|\sqrt{\frac{Eh\beta_2}{h^s}}\,[\![\delta u_1]\!]\right|\right|_{\mathbf{L}^2(\partial l_e)} \\
& + \frac{C_2^k}{\sqrt{\beta_2}} \left|\left|\sqrt{Eh}\delta u_{1,1}\right|\right|_{\mathbf{L}^2(l_e)} \left|\left|\sqrt{\frac{Eh\beta_2}{h^s}}\,[\![u_1]\!]\right|\right|_{\mathbf{L}^2(\partial l_e)} \\
& + \left|\left|\sqrt{\frac{\beta_2 Eh}{h^s}}\,[\![u_1]\!]\right|\right|_{\mathbf{L}^2(\partial l_e)} \left|\left|\sqrt{\frac{\beta_2 Eh}{h^s}}\,[\![\delta u_1]\!]\right|\right|_{\mathbf{L}^2(\partial l_e)} \\
& + \frac{C_1^k}{\sqrt{\beta_1}} \left|\left|\sqrt{\frac{Eh^3}{12}}u_{3,11}\right|\right|_{\mathbf{L}^2(l_e)} \left|\left|\sqrt{\frac{\beta_1 Eh^3}{12h^s}}\,[\![\delta u_{3,1}]\!]\right|\right|_{\mathbf{L}^2(\partial l_e)} \\
& + \frac{C_1^k}{\sqrt{\beta_1}} \left|\left|\sqrt{\frac{Eh^3}{12}}\delta u_{3,11}\right|\right|_{\mathbf{L}^2(l_e)} \left|\left|\sqrt{\frac{\beta_1 Eh^3}{12h^s}}\,[\![u_{3,1}]\!]\right|\right|_{\mathbf{L}^2(\partial l_e)} \\
& + \left|\left|\sqrt{\frac{\beta_1 Eh^3}{12h^s}}\,[\![u_{3,1}]\!]\right|\right|_{\mathbf{L}^2(\partial l_e)} \left|\left|\sqrt{\frac{\beta_1 Eh^3}{12h^s}}\,[\![\delta u_{3,1}]\!]\right|\right|_{\mathbf{L}^2(\partial l_e)} \\
& + \left|\left|\sqrt{\frac{\beta_3 Eh}{2(1+\nu)h^s}}\,[\![u_3]\!]\right|\right|_{\mathbf{L}^2(\partial l_e)} \left|\left|\sqrt{\frac{\beta_3 Eh}{2(1+\nu)h^s}}\,[\![\delta u_3]\!]\right|\right|_{\mathbf{L}^2(\partial l_e)} \Bigg\}. \qquad \text{(A.30)}
\end{aligned}$$

Then, a constant defines by $C'^k(\beta_1,\beta_2) = \max\left(1, \frac{C_1^k}{\sqrt{\beta_1}}, \frac{C_2^k}{\sqrt{\beta_2}}\right)$ is put in evidence. Indeed, as the equation (A.30) is an inequality, it is possible to replace $\frac{C_1^k}{\sqrt{\beta_1}}$ and $\frac{C_2^k}{\sqrt{\beta_2}}$ by C'^k and to multiply the two first terms by C'^k. Moreover, the terms five, eight and nine of right member

of (A.30) can be multiply by $\frac{C^k(\beta)}{\sqrt{2}}$ with $C^k(\beta_1,\beta_2) = \max\left(2, \sqrt{2}C'^k(\beta_1,\beta_2)\right)$ and $C'^k(\beta_1,\beta_2)$ can be replaced by $C^k(\beta_1,\beta_2)$ in the others terms, which gives,

$$
\begin{aligned}
\frac{|a(\boldsymbol{u},\delta\boldsymbol{u})|}{C^k(\beta_1,\beta_2)} \leq \sum_e \Bigg\{ & \left|\left|\sqrt{Eh}u_{1,1}\right|\right|_{\mathbf{L}^2(l_e)} \left|\left|\sqrt{Eh}\delta u_{1,1}\right|\right|_{\mathbf{L}^2(l_e)} \\
& + \left|\left|\sqrt{\frac{Eh^3}{12}}u_{3,11}\right|\right|_{\mathbf{L}^2(l_e)} \left|\left|\sqrt{\frac{Eh^3}{12}}\delta u_{3,11}\right|\right|_{\mathbf{L}^2(l_e)} \\
& + \left|\left|\sqrt{Eh}u_{1,1}\right|\right|_{\mathbf{L}^2(l_e)} \left|\left|\sqrt{\frac{Eh\beta_2}{h^s}}[\![\delta u_1]\!]\right|\right|_{\mathbf{L}^2(\partial l_e)} \\
& + \left|\left|\sqrt{Eh}\delta u_{1,1}\right|\right|_{\mathbf{L}^2(l_e)} \left|\left|\sqrt{\frac{Eh\beta_2}{h^s}}[\![u_1]\!]\right|\right|_{\mathbf{L}^2(\partial l_e)} \\
& + \left|\left|\sqrt{\frac{\beta_2 Eh}{h^s}}[\![u_1]\!]\right|\right|_{\mathbf{L}^2(\partial l_e)} \left|\left|\sqrt{\frac{\beta_2 Eh}{h^s}}[\![\delta u_1]\!]\right|\right|_{\mathbf{L}^2(\partial l_e)} \\
& + \left|\left|\sqrt{\frac{Eh^3}{12}}u_{3,11}\right|\right|_{\mathbf{L}^2(l_e)} \left|\left|\sqrt{\frac{\beta_1 Eh^3}{12h^s}}[\![\delta u_{3,1}]\!]\right|\right|_{\mathbf{L}^2(\partial l_e)} \\
& + \left|\left|\sqrt{\frac{Eh^3}{12}}\delta u_{3,11}\right|\right|_{\mathbf{L}^2(l_e)} \left|\left|\sqrt{\frac{\beta_1 Eh^3}{12h^s}}[\![u_{3,1}]\!]\right|\right|_{\mathbf{L}^2(\partial l_e)} \\
& + \left|\left|\sqrt{\frac{\beta_1 Eh^3}{12h^s}}[\![u_{3,1}]\!]\right|\right|_{\mathbf{L}^2(\partial l_e)} \left|\left|\sqrt{\frac{\beta_1 Eh^3}{12h^s}}[\![\delta u_{3,1}]\!]\right|\right|_{\mathbf{L}^2(\partial l_e)} \\
& + \left|\left|\sqrt{\frac{\beta_3 Eh}{2(1+\nu)h^s}}[\![u_3]\!]\right|\right|_{\mathbf{L}^2(\partial l_e)} \left|\left|\sqrt{\frac{\beta_3 Eh}{2(1+\nu)h^s}}[\![\delta u_3]\!]\right|\right|_{\mathbf{L}^2(\partial l_e)} \Bigg\} . \quad \text{(A.31)}
\end{aligned}
$$

Then the terms can be rearranged to write [4],

$$\begin{aligned}
\frac{|a(\boldsymbol{u},\delta\boldsymbol{u})|}{C^k(\beta_1,\beta_2)} \leq \sum_e \Bigg\{ & \Bigg[\left|\left| \sqrt{Eh} u_{1,1} \right|\right|_{\mathbf{L}^2(l_e)} + \left|\left| \sqrt{\frac{Eh^3}{12}} u_{3,11} \right|\right|_{\mathbf{L}^2(l_e)} \\
& + \left|\left| \sqrt{\frac{\beta_1 Eh^3}{2*12h^s}} [\![u_{3,1}]\!] \right|\right|_{\mathbf{L}^2(\partial l_e)} + \left|\left| \sqrt{\frac{\beta_2 Eh}{2h^s}} [\![u_1]\!] \right|\right|_{\mathbf{L}^2(\partial l_e)} \\
& + \left|\left| \sqrt{\frac{\beta_3 Eh}{2*2(1+\nu)h^s}} [\![u_3]\!] \right|\right|_{\mathbf{L}^2(\partial l_e)} \Bigg] \times \\
& + \Bigg[\left|\left| \sqrt{Eh} \delta u_{1,1} \right|\right|_{\mathbf{L}^2(l_e)} + \left|\left| \sqrt{\frac{Eh^3}{12}} \delta u_{3,11} \right|\right|_{\mathbf{L}^2(l_e)} \\
& + \left|\left| \sqrt{\frac{\beta_1 Eh^3}{2*12h^s}} [\![\delta u_{3,1}]\!] \right|\right|_{\mathbf{L}^2(\partial l_e)} + \left|\left| \sqrt{\frac{\beta_2 Eh}{2h^s}} [\![\delta u_1]\!] \right|\right|_{\mathbf{L}^2(\partial l_e)} \\
& + \left|\left| \sqrt{\frac{\beta_3 Eh}{2*2(1+\nu)h^s}} [\![\delta u_3]\!] \right|\right|_{\mathbf{L}^2(\partial l_e)} \Bigg] \Bigg\} . \qquad \text{(A.32)}
\end{aligned}$$

Now using the Cauchy-Schwartz inequality, the relation (A.32) becomes,

$$\begin{aligned}
\frac{|a(\boldsymbol{u},\delta\boldsymbol{u})|^2}{C'^k(\beta_1,\beta_2)} \leq \sum_e \Bigg\{ & \Bigg[\left|\left| \sqrt{Eh} u_{1,1} \right|\right|^2_{\mathbf{L}^2(l_e)} + \left|\left| \sqrt{\frac{Eh^3}{12}} u_{3,11} \right|\right|^2_{\mathbf{L}^2(l_e)} \\
& + \frac{1}{2} \left|\left| \sqrt{\frac{\beta_1 Eh^3}{12h^s}} [\![u_{3,1}]\!] \right|\right|^2_{\mathbf{L}^2(\partial l_e)} + \frac{1}{2} \left|\left| \sqrt{\frac{\beta_2 Eh}{h^s}} [\![u_1]\!] \right|\right|^2_{\mathbf{L}^2(\partial l_e)} \\
& + \frac{1}{2} \left|\left| \sqrt{\frac{\beta_3 Eh}{2(1+\nu)h^s}} [\![u_3]\!] \right|\right|^2_{\mathbf{L}^2(\partial l_e)} \Bigg] \times \\
& + \Bigg[\left|\left| \sqrt{Eh} \delta u_{1,1} \right|\right|^2_{\mathbf{L}^2(l_e)} + \left|\left| \sqrt{\frac{Eh^3}{12}} \delta u_{3,11} \right|\right|^2_{\mathbf{L}^2(l_e)} \\
& + \frac{1}{2} \left|\left| \sqrt{\frac{\beta_1 Eh^3}{12h^s}} [\![\delta u_{3,1}]\!] \right|\right|^2_{\mathbf{L}^2(\partial l_e)} + \frac{1}{2} \left|\left| \sqrt{\frac{\beta_2 Eh}{h^s}} [\![\delta u_1]\!] \right|\right|^2_{\mathbf{L}^2(\partial l_e)} \\
& + \frac{1}{2} \left|\left| \sqrt{\frac{\beta_3 Eh}{2(1+\nu)h^s}} [\![\delta u_3]\!] \right|\right|^2_{\mathbf{L}^2(\partial l_e)} \Bigg] \Bigg\} , \qquad \text{(A.33)}
\end{aligned}$$

[4] If the product of the right member of (A.32) is developed the nine terms of right members of (A.30) are found back with sixteen other terms (≥ 0) added which is possible as it is a upper bound.

with $C''^k(\beta_1,\beta_2) = (C^k(\beta_1,\beta_2))^2$. Finally using (3.45) and the definition of energy norm (3.43) the relation (A.33) can be rewritten,

$$|a(\boldsymbol{u},\delta\boldsymbol{u})|^2 \;\leq\; C''^k(\beta_1,\beta_2)\,|||\boldsymbol{u}|||^2\,|||\delta\boldsymbol{u}|||^2\,, \tag{A.34}$$

which is identical to the relation (3.46).

A.3.2 Lower bound of the bilinear form

The lower bound of the bilinear form is found following the developments suggested in [185]. By definition of $a(\boldsymbol{u},\boldsymbol{u})$ (see equation (3.34)),

$$\begin{aligned} a(\boldsymbol{u},\boldsymbol{u}) \;=\; & \sum_e \left|\left|\sqrt{Eh}u_{1,1}\right|\right|^2_{\mathbf{L}^2(l_e)} + \sum_e \left|\left|\sqrt{\frac{Eh^3}{12}}u_{3,11}\right|\right|^2_{\mathbf{L}^2(l_e)} + 2\sum_s \langle u_{1,1}\rangle\, Eh\,[\![u_1]\!] \\ & + 2\sum_s \left\langle \frac{Eh^3}{12}u_{3,11}\right\rangle [\![u_{3,1}]\!] + \sum_s \left|\left|\sqrt{\frac{\beta_1 Eh^3}{12h^s}}\,[\![u_{3,1}]\!]\right|\right|^2_{\mathbf{L}^2(s)} \\ & + \sum_s \left|\left|\sqrt{\frac{\beta_2 Eh}{h^s}}\,[\![u_1]\!]\right|\right|^2_{\mathbf{L}^2(s)} + \sum_s \left|\left|\sqrt{\frac{\beta_3 Eh}{2(1+\nu)h^s}}\,[\![u_3]\!]\right|\right|^2_{\mathbf{L}^2(s)}\,. \end{aligned} \tag{A.35}$$

First to have a lower bound of $a(\boldsymbol{u},\boldsymbol{u})$, the two terms of the form $2\sum_s \langle a\rangle\, \mathcal{H}\, [\![a]\!]$ in (A.35) are bounded by a sum of integrals on the boundary of elements,

$$\begin{aligned} 2\sum_s \langle a\rangle\, \mathcal{H}\, [\![a]\!] \;&\leq\; 2\left|\sum_s \langle a\rangle\, \mathcal{H}\, [\![a]\!]\right| \\ &\leq\; 2\sum_s \left|\langle a\rangle\, \mathcal{H}\, [\![a]\!]\right| \\ &\leq\; 2\sum_e \left|\langle a\rangle\, \mathcal{H}\, [\![a]\!]\right|_{\partial l_e}\,. \end{aligned} \tag{A.36}$$

and,

$$2\sum_e \left|\langle a\rangle\, \mathcal{H}\, [\![a]\!]\right|_{\partial l_e} \;\leq\; 2\sum_e \left|a\mathcal{H}\, [\![a]\!]\right|_{\partial l_e}\,, \tag{A.37}$$

using the Cauchy-Schwartz inequality in the right member of this inequality, and introducing $\sqrt{h^s}$,

$$2\sum_s \langle a\rangle\, \mathcal{H}\, [\![a]\!] \leq 2\sqrt{h^s}\sum_e \left|\left|\sqrt{\mathcal{H}}\,a\right|\right|_{\mathbf{L}^2(\partial l_e)} \left|\left|\sqrt{\frac{\mathcal{H}}{h^s}}\,[\![a]\!]\right|\right|_{\mathbf{L}^2(\partial l_e)}\,. \tag{A.38}$$

Afterwards the scaling property can be applied to equation (A.38) which leads to,

$$2\sum_s \langle a\rangle\, \mathcal{H}\, [\![a]\!] \;\leq\; \frac{2\sqrt{2}C^k(\beta)}{\sqrt{\beta}}\sum_e \left|\left|\sqrt{\mathcal{H}}\,a\right|\right|_{\mathbf{L}^2(l_e)} \left|\left|\sqrt{\frac{\mathcal{H}\beta}{2h^s}}\,[\![a]\!]\right|\right|_{\mathbf{L}^2(\partial l_e)}\,. \tag{A.39}$$

Finally this equation can be multiply by -1 to reverse the inequality,

$$-2\sum_s \langle a\rangle\, \mathcal{H}\, [\![a]\!] \;\geq\; \frac{-2\sqrt{2}C^k(\beta)}{\sqrt{\beta}} \sum_e \left|\left| \sqrt{\mathcal{H}}\, a \right|\right|_{\mathbf{L}^2(l_e)} \left|\left| \sqrt{\frac{\mathcal{H}\,\beta}{2h^s}}\, [\![a]\!] \right|\right|_{\mathbf{L}^2(\partial l_e)} . \quad \text{(A.40)}$$

This relation (A.40) can be used to replace the terms of the form $2\sum_s \langle a\rangle\, \mathcal{H}\, [\![a]\!]$ in the equation (A.35),

$$\begin{aligned} a(\boldsymbol{u},\boldsymbol{u}) \;\geq\; & \sum_e \left|\left| \sqrt{Eh} u_{1,1} \right|\right|^2_{\mathbf{L}^2(l_e)} + \sum_e \left|\left| \sqrt{\frac{Eh^3}{12}} u_{3,11} \right|\right|^2_{\mathbf{L}^2(l_e)} \\ & - \frac{2\sqrt{2}C_2^k(\beta_2)}{\sqrt{\beta_2}} \sum_e \left|\left| \sqrt{Eh} u_{1,1} \right|\right|_{\mathbf{L}^2(l_e)} \left|\left| \sqrt{\frac{Eh\beta_2}{2h^s}} [\![u_1]\!] \right|\right|_{\mathbf{L}^2(\partial l_e)} \\ & - \frac{2\sqrt{2}C_1^k(\beta_1)}{\sqrt{\beta_1}} \sum_e \left|\left| \sqrt{\frac{Eh^3}{12}} u_{3,11} \right|\right|_{\mathbf{L}^2(l_e)} \left|\left| \sqrt{\frac{Eh^3\beta_1}{24h^s}} [\![u_{3,1}]\!] \right|\right|_{\mathbf{L}^2(\partial l_e)} \\ & + \sum_s \left|\left| \sqrt{\frac{\beta_1 Eh^3}{12h^s}} [\![u_{3,1}]\!] \right|\right|^2_{\mathbf{L}^2(s)} \\ & + \sum_s \left|\left| \sqrt{\frac{\beta_2 Eh}{h^s}} [\![u_1]\!] \right|\right|^2_{\mathbf{L}^2(s)} + \sum_s \left|\left| \sqrt{\frac{\beta_3 Eh}{2(1+\nu)h^s}} [\![u_3]\!] \right|\right|^2_{\mathbf{L}^2(s)} . \end{aligned} \quad \text{(A.41)}$$

Then, the ε-inequality[5] can be applied to the two terms of the form :
$\sum_e \left|\left| \sqrt{\mathcal{H}}\, a \right|\right|_{\mathbf{L}^2(l_e)} \left|\left| \sqrt{\frac{\mathcal{H}\beta}{2h^s}}\, [\![a]\!] \right|\right|_{\mathbf{L}^2(\partial l_e)}$ to have,

$$\begin{aligned} & \frac{2\sqrt{2}C_2^k(\beta_2)}{\sqrt{\beta_2}} \sum_e \left(\left|\left| \sqrt{Eh} u_{1,1} \right|\right|_{\mathbf{L}^2(l_e)} \left|\left| \sqrt{\frac{Eh\beta_2}{2h^s}} [\![u_1]\!] \right|\right|_{\mathbf{L}^2(\partial l_e)} \right) \leq \\ & \left(\varepsilon_2 \sum_e \left|\left| \sqrt{Eh} u_{1,1} \right|\right|^2_{\mathbf{L}^2(l_e)} + \frac{2(C_2^k)^2}{\beta_2\varepsilon_2} \sum_e \left|\left| \sqrt{\frac{Eh\beta_2}{2h^s}} [\![u_1]\!] \right|\right|^2_{\mathbf{L}^2(\partial l_e)} \right) , \end{aligned} \quad \text{(A.42)}$$

which multiplied by -1 leads to,

$$\begin{aligned} & -\frac{2\sqrt{2}C_2^k(\beta_2)}{\sqrt{\beta_2}} \sum_e \left(\left|\left| \sqrt{Eh} u_{1,1} \right|\right|_{\mathbf{L}^2(l_e)} \left|\left| \sqrt{\frac{Eh\beta_2}{2h^s}} [\![u_1]\!] \right|\right|_{\mathbf{L}^2(\partial l_e)} \right) \geq \\ & - \left(\varepsilon_2 \sum_e \left|\left| \sqrt{Eh} u_{1,1} \right|\right|^2_{\mathbf{L}^2(l_e)} + \frac{2(C_2^k)^2}{\beta_2\varepsilon_2} \sum_e \left|\left| \sqrt{\frac{Eh\beta_2}{2h^s}} [\![u_1]\!] \right|\right|^2_{\mathbf{L}^2(\partial l_e)} \right) . \end{aligned} \quad \text{(A.43)}$$

[5] $\forall \varepsilon > 0 : |ab| \leq \frac{\varepsilon}{2}a^2 + \frac{1}{2\varepsilon}b^2$ or $|ab| \leq \varepsilon a^2 + \frac{1}{4\varepsilon}b^2$

Similarly for the bending term one has,

$$-\frac{2\sqrt{2}\beta_1}{\sqrt{\beta_1}}\sum_e\left(\left|\left|\sqrt{\frac{Eh^3}{12}}u_{3,11}\right|\right|_{\mathbf{L}^2(l_e)}\left|\left|\sqrt{\frac{Eh^3\beta_1}{24h^s}}[\![u_{3,1}]\!]\right|\right|_{\mathbf{L}^2(\partial l_e)}\right)\geq$$
$$-\left(\varepsilon_1\sum_e\left|\left|\sqrt{\frac{Eh^3}{12}}u_{3,11}\right|\right|^2_{\mathbf{L}^2(l_e)}+\frac{2(C_1^k)^2}{\beta_1\varepsilon_1}\sum_e\left|\left|\sqrt{\frac{Eh^3\beta_1}{24h^s}}[\![u_{3,1}]\!]\right|\right|^2_{\mathbf{L}^2(\partial l_e)}\right). \quad \text{(A.44)}$$

Furtermore, for the term $\sum_s\left|\left|\sqrt{\frac{\beta_3 Eh}{2(1+\nu)h^s}}[\![u_3]\!]\right|\right|^2_{\mathbf{L}^2(s)}$ of equation (A.35) it is possible to write,

$$\begin{aligned}\sum_s\left|\left|\sqrt{\frac{\beta_3 Eh}{2(1+\nu)h^s}}[\![u_3]\!]\right|\right|^2_{\mathbf{L}^2(s)} &= \frac{1}{2}\sum_e\left|\left|\sqrt{\frac{\beta_3 Eh}{2(1+\nu)h^s}}[\![u_3]\!]\right|\right|^2_{\mathbf{L}^2(\partial l_e)}\\ &\geq \frac{1}{2}\sum_e\left|\left|\sqrt{\frac{\beta_3 Eh}{2*2(1+\nu)h^s}}[\![u_3]\!]\right|\right|^2_{\mathbf{L}^2(\partial l_e)} \quad \text{(A.45)}\end{aligned}$$

Then the final form of the lower bound of $a(\boldsymbol{u},\boldsymbol{u})$ is obtained by injecting the relations (A.43), (A.44) and (A.45) in the relation (A.41),

$$\begin{aligned}a(\boldsymbol{u},\boldsymbol{u}) \geq\ & (1-\varepsilon_2)\sum_e\left|\left|\sqrt{Eh}u_{1,1}\right|\right|^2_{\mathbf{L}^2(l_e)}+(1-\varepsilon_1)\sum_e\left|\left|\sqrt{\frac{Eh^3}{12}}u_{3,11}\right|\right|^2_{\mathbf{L}^2(l_e)}\\ &+\left(1-\frac{2(C_2^k(\beta_2))^2}{\varepsilon_2\beta_2}\right)\sum_e\left|\left|\sqrt{\frac{Eh\beta_2}{2h^s}}[\![u_1]\!]\right|\right|^2_{\mathbf{L}^2(\partial l_e)}\\ &+\left(1-\frac{2(C_1^k(\beta_1))^2}{\varepsilon_1\beta_1}\right)\sum_e\left|\left|\sqrt{\frac{Eh^3\beta_1}{24h^s}}[\![u_{3,1}]\!]\right|\right|^2_{\mathbf{L}^2(\partial l_e)}\\ &+\frac{1}{2}\sum_e\left|\left|\sqrt{\frac{\beta_3 Eh}{2*2(1+\nu)h^s}}[\![u_3]\!]\right|\right|^2_{\mathbf{L}^2(\partial l_e)}, \quad \text{(A.46)}\end{aligned}$$

which is identical to the lower bound given by (3.47).

A.3.3 Proof of convergence rate in the energy-norm

The convergence rate in the energy norm of the full-DG formulation is derived by following [185] under a quasi static assumption. To achieve this the error between the FE solution and the interpolation of the exact solution with the same polynomial degree is calculated. First, some definitions and assumptions are given. Consider $\boldsymbol{u}$ is the exact solution of the problem where displacement and derivative are constraint to zero on the boundary and $\boldsymbol{u}^k$

its interpolation of degree k in each element defined by $\int_{A_h}(\boldsymbol{u}-\boldsymbol{u}^k)\delta\boldsymbol{u}dA=0$, satisfying the essential boundary conditions. Then the error is defined by $\boldsymbol{e}=\boldsymbol{u}_h-\boldsymbol{u}$, and the error with the interpolation of the exact solution is given by $\boldsymbol{e}^k=\boldsymbol{u}_h-\boldsymbol{u}^k$.

To show the convergence rate in the energy norm the bilinear expression $a(\boldsymbol{u},\delta\boldsymbol{u})$ is considered. This expression includes only linear terms by definition so,

$$a(\boldsymbol{u}_h-\boldsymbol{u}^k,\boldsymbol{u}_h-\boldsymbol{u}^k) \;=\; a(\boldsymbol{u}_h-\boldsymbol{u},\boldsymbol{u}_h-\boldsymbol{u}^k)+a(\boldsymbol{u}-\boldsymbol{u}^k,\boldsymbol{u}_h-\boldsymbol{u}^k)\,. \tag{A.47}$$

The term $a(\boldsymbol{u}_h-\boldsymbol{u},\boldsymbol{u}_h-\boldsymbol{u}^k)$ is equal to zero (see the orthogonality property (3.42)). Furthermore, using the expression of the lower bound of the bilinear form (3.49) leads to,

$$a(\boldsymbol{u}_h-\boldsymbol{u}^k,\boldsymbol{u}_h-\boldsymbol{u}^k) \;\geq\; C(\beta_1,\beta_2)\left|\left|\left|\boldsymbol{u}_h-\boldsymbol{u}^k\right|\right|\right|^2, \tag{A.48}$$

or, using the error definition,

$$a(\boldsymbol{u}_h-\boldsymbol{u}^k,\boldsymbol{u}_h-\boldsymbol{u}^k) \;\geq\; C(\beta_1,\beta_2)\left|\left|\left|\boldsymbol{e}^k\right|\right|\right|^2. \tag{A.49}$$

Then the Eq. (A.47) can be replaced by an upper bound given by expression (3.46),

$$C_1(\beta_1,\beta_2,\beta_3)\left|\left|\left|\boldsymbol{u}-\boldsymbol{u}^k\right|\right|\right|\left|\left|\left|\boldsymbol{e}^k\right|\right|\right| \;\geq\; C(\beta_1,\beta_2)\left|\left|\left|\boldsymbol{e}^k\right|\right|\right|^2. \tag{A.50}$$

Then, an upper bound of $\left|\left|\boldsymbol{e}^k\right|\right|$ can be obtained by bounding the term $\left|\left|\left|\boldsymbol{u}-\boldsymbol{u}^k\right|\right|\right|$. To achieve this, the terms of the energetic norm are bounded. First the membrane and the bending terms are considered. The framework is the same for the two terms so the calculations are only presented for the membrane term.

$$\left|\left|\sqrt{Eh}(u_{1,1}-u^k_{1,1})\right|\right|^2_{\mathbf{L}^2(l_e)} \;\leq\; C_{n1}\left|\left|\sqrt{1}(u_{1,1}-u^k_{1,1})\right|\right|^2_{\mathbf{L}^2(l_e)}, \tag{A.51}$$

where C_{n1} is a constant sufficiently large to bound Eh. Using the definition of the notation $\left|\left|\sqrt{\mathcal{H}}\,a\right|\right|^2_{\mathbf{L}^2(l_e)}$ (see equation (3.44)),

$$\begin{aligned}\left|\left|\sqrt{Eh}(u_{1,1}-u^k_{1,1})\right|\right|^2_{\mathbf{L}^2(l_e)} &\leq C_{n1}\int_{l_e}(u_{1,1}-u^k_{1,1})(u_{1,1}-u^k_{1,1})dl\\ &\leq C_{n1}\int_{l_e}(u_1-u^k_1)_{,1}(u_1-u^k_1)_{,1}dl\\ &\leq C_{n1}\left|\left|\sqrt{1}(u_1-u^k_1)_{,1}\right|\right|^2_{\mathbf{L}^2(l_e)}.\end{aligned} \tag{A.52}$$

Afterward, the definition of the Sobolev[6] space is used,

$$\left|\left|\sqrt{Eh}(u_{1,1}-u^k_{1,1})\right|\right|^2_{\mathbf{L}^2(l_e)} \;\leq\; C_{n1}\left|\left|\sqrt{1}u_1-u^k_1\right|\right|^2_{\mathbf{H}^1(l_e)}. \tag{A.53}$$

[6] A property of Sobolev space is the inequality $\left|\left|\sqrt{1}a_{,\alpha}\right|\right|_{H^0(l_e)}\leq\left|\left|\sqrt{1}a\right|\right|_{H^1(l_e)}$.

Furthermore, the basic error estimates of interpolation theory[7] is applied,

$$\left|\left|\sqrt{Eh}(u_{1,1}-u^k_{1,1})\right|\right|^2_{\mathbf{L}^2(l_e)} \leq C_n(h^s)^{2k}\,|\boldsymbol{u}|^2_{\mathbf{H}^{k+1}(l_e)}\,. \tag{A.54}$$

Similarly, using the same framework, the bending term is bounded by,

$$\left|\left|\sqrt{\frac{Eh^3}{12}}(u_{3,11}-u^k_{3,11})\right|\right|^2_{\mathbf{L}^2(l_e)} \leq C_m(h^s)^{2k-2}\,|u_3|^2_{\mathbf{H}^{k+1}(l_e)}\,. \tag{A.55}$$

Moreover, the interface terms can be bounded. As the framework is again the same for the three terms, the calculations are only presented in the case of the membrane term. Given C_{nI1} a constant such as $C_{nI1} > Eh$ one has,

$$\frac{1}{2}\sum_e \left|\left|\sqrt{\frac{\beta_2 Eh}{h^s}}\left[\!\left[u_1-u^k_1\right]\!\right]\right|\right|^2_{\mathbf{L}^2(\partial l_e)} \leq \frac{C_{nI1}\beta_2}{h^s}\sum_e \left|\left|\sqrt{1}(u_1-u^k_1)\right|\right|^2_{\mathbf{L}^2(\partial l_e)}, \tag{A.56}$$

Furthermore, using the scaling property leads to,

$$\frac{1}{2}\sum_e \left|\left|\sqrt{\frac{\beta_2 Eh}{h^s}}\left[\!\left[u_1-u^k_1\right]\!\right]\right|\right|^2_{\mathbf{L}^2(\partial l_e)} \leq \frac{C_{nI2}\beta_2}{h^{s^2}}\sum_e \left|\left|\sqrt{1}(u_1-u^k_1)\right|\right|^2_{\mathbf{L}^2(l_e)}. \tag{A.57}$$

Using the Sobolev space's definition yields,

$$\frac{1}{2}\sum_e \left|\left|\sqrt{\frac{\beta_2 Eh}{h^s}}\left[\!\left[u_1-u^k_1\right]\!\right]\right|\right|^2_{\mathbf{L}^2(\partial l_e)} \leq \frac{C_{nI2}\beta_2}{h^{s^2}}\sum_e \left|\left|\sqrt{1}(u_1-u^k_1)\right|\right|^2_{\mathbf{H}^0(l_e)}. \tag{A.58}$$

Using the basic error estimates of interpolation theory one has,

$$\frac{1}{2}\sum_e \left|\left|\sqrt{\frac{\beta_2 Eh}{h^s}}\left[\!\left[u_1-u^k_1\right]\!\right]\right|\right|^2_{\mathbf{L}^2(\partial l_e)} \leq \sum_e C_{nI}\beta_2 h^{s2k}\,|u_1|^2_{\mathbf{H}^{k+1}(l_e)}\,. \tag{A.59}$$

Similarly for the bending interface term,

$$\frac{1}{2}\sum_e \left|\left|\sqrt{\frac{\beta_1 Eh^3}{12h^s}}\left[\!\left[u_{3,1}-u^k_{3,1}\right]\!\right]\right|\right|^2_{\mathbf{L}^2(\partial l_e)} \leq \sum_e C_{mI}\beta_1 h^{s2k-2}\,|u_3|^2_{\mathbf{H}^{k+1}(l_e)}\,, \tag{A.60}$$

and for the "shearing" interface term,

$$\frac{1}{2}\sum_e \left|\left|\sqrt{\frac{\beta_3 Eh}{2(1+\nu)h^s}}\left[\!\left[u_3-u^k_3\right]\!\right]\right|\right|^2_{\mathbf{L}^2(\partial l_e)} \leq \sum_e C_{II}\beta_3 h^{s2k}\,|u_3|^2_{\mathbf{H}^{k+1}(l_e)} \tag{A.61}$$

[7] Given a mapping $\boldsymbol{u} \in \boldsymbol{H}^{k+1}(l_e)$, then $\forall \boldsymbol{u}^k \in \mathcal{P}^k$ interpolating $\boldsymbol{u} \in l_e$: $\left|\left|\sqrt{1}\boldsymbol{u}-\boldsymbol{u}^k\right|\right|_{\mathbf{H}^q(l_e)} \leq C_1 h^{sk+1-q}\,|\boldsymbol{u}|_{\mathbf{H}^{k+1}(l_e)}\,\forall 0 \leq q \leq k+1$ with C_1 independent of h^s, the size of l_e [140].

Finally, as there is no coupling between the different variables u_1, u_3 these quantities can be replaced by $\boldsymbol{u}$ in the right hand terms equations (A.54),(A.55),(A.59),(A.60) and (A.61). Moreover, these inequalities are upper bounds of the right terms of the energy norm's definition (3.43) so they can be used to bound the quantity $\left|\left|\left|\boldsymbol{u}-\boldsymbol{u}^k\right|\right|\right|$,

$$\begin{aligned}\left|\left|\left|\boldsymbol{u}-\boldsymbol{u}^k\right|\right|\right| \;\leq\; & \sum_e C_n h^{sk} |\boldsymbol{u}|_{\mathbf{H}^{k+1}(l_e)} + \sum_e C_m h^{sk-1} |\boldsymbol{u}|_{\mathbf{H}^{k+1}(l_e)} + \sum_e C_{mI}\beta_1 h^{sk-1} |\boldsymbol{u}|_{\mathbf{H}^{k+1}(l_e)} \\ & + \sum_e C_{nI}\beta_2 h^{sk} |\boldsymbol{u}|_{\mathbf{H}^{k+1}(l_e)} + \sum_e C_{lI}\beta_3 h^{sk} |\boldsymbol{u}|_{\mathbf{H}^{k+1}(l_e)} \end{aligned} \tag{A.62}$$

Giving $C(\beta_1,\beta_2,\beta_3) = \max(C_m, C_n, C_{mI}\beta_1, C_{nI}\beta_2, C_{lI}\beta_3)$ this last equation is rewritten,

$$\left|\left|\left|\boldsymbol{u}-\boldsymbol{u}^k\right|\right|\right| \;\leq\; C(\beta_1,\beta_2,\beta_3)\sum_e h^{sk-1} |\boldsymbol{u}|_{\mathbf{H}^{k+1}(l_e)}\,. \tag{A.63}$$

This equation (A.63) can be injected in the relation (A.50) leading to,

$$\left|\left|\left|\boldsymbol{e}^k\right|\right|\right| \;\leq\; C(\beta_1,\beta_2,\beta_3)\sum_e h^{sk-1} |\boldsymbol{u}|_{\mathbf{H}^{k+1}(l_e)}\,, \tag{A.64}$$

which corresponds to the Eq. (3.50).

A.3.4 Proof of the convergence rate in the $\mathbf{L}^2$-norm

The convergence rate in the $\mathbf{L}^2$-norm of the full-DG formulation is derived by following [185] and under the three assumptions :

1. Cubic approximation;
2. Proper elliptic regularity of the problem;
3. Pure Dirichlet boundary conditions (ie $\boldsymbol{u} = \boldsymbol{t} = 0$ on ∂L_h).

Given $\boldsymbol{u}_d$ the exact solution of a problem governed by the external loading $\boldsymbol{b}(\delta\boldsymbol{u})$ such that $\boldsymbol{u}_d$ satisfies the essential boundary conditions. This solution satisfies the equation $a(\boldsymbol{u}_d, \delta\boldsymbol{u}) = \boldsymbol{b}(\delta\boldsymbol{u})$. So considering the particular case $\boldsymbol{e}$ satisfying the essential boundary conditions as virtual displacements field,

$$\boldsymbol{b}(\boldsymbol{e}) \;=\; a(\boldsymbol{u}_d, \boldsymbol{e})\,. \tag{A.65}$$

Defining $\boldsymbol{u}_d^k$ the interpolation of $\boldsymbol{u}_d$ satisfying the essential boundary conditions, the bilinear form allows writing,

$$\boldsymbol{b}(\boldsymbol{e}) \;=\; a(\boldsymbol{u}_d, \boldsymbol{e}) = a(\boldsymbol{u}_d - \boldsymbol{u}_d^k, \boldsymbol{e}) + a(\boldsymbol{u}_d^k, \boldsymbol{e})\,. \tag{A.66}$$

Furthermore $a(\boldsymbol{u}, \delta\boldsymbol{u})$ is symmetric so,

$$\boldsymbol{e} \;=\; a(\boldsymbol{u}_d - \boldsymbol{u}_d^k, \boldsymbol{e}) + a(\boldsymbol{e}, \boldsymbol{u}_d^k)\,. \tag{A.67}$$

Then by definition of the error $a(\boldsymbol{e},\boldsymbol{u}_d^k)=a(\boldsymbol{u}_h-\boldsymbol{u},\boldsymbol{u}_d^k)=0$ from orthogonality relation (3.42) and Eq. (A.66) becomes,

$$\boldsymbol{b}(\boldsymbol{e}) \;=\; a(\boldsymbol{u}_d-\boldsymbol{u}_d^k,\boldsymbol{u}_h-\boldsymbol{u})\,. \tag{A.68}$$

Afterward, as $a(\boldsymbol{u},\delta\boldsymbol{u})$ is a bilinear form, one has

$$\boldsymbol{b}(\boldsymbol{e}) \;=\; a(\boldsymbol{u}_d-\boldsymbol{u}_d^k,\boldsymbol{u}_h-\boldsymbol{u}^k)+a(\boldsymbol{u}_d-\boldsymbol{u}_d^k,\boldsymbol{u}^k-\boldsymbol{u})\,. \tag{A.69}$$

Now the external loading is particularized such that $\boldsymbol{b}(\boldsymbol{e})=||\boldsymbol{e}||^2_{\mathbf{L}^2(L_h)}$ leading to,

$$\boldsymbol{e} \;=\; a(\boldsymbol{u}_d-\boldsymbol{u}_d^k,\boldsymbol{u}_h-\boldsymbol{u}^k)+a(\boldsymbol{u}_d-\boldsymbol{u}_d^k,\boldsymbol{u}^k-\boldsymbol{u})\,. \tag{A.70}$$

Then, an upper bound of $\boldsymbol{e}$ is obtained by applying the upper bound of energy (3.46),

$$\begin{aligned}
||\boldsymbol{e}||^2_{\mathbf{L}^2(L_h)} &\leq C_1^k\left|\left|\left|\boldsymbol{u}_d-\boldsymbol{u}_d^k\right|\right|\right|\left|\left|\left|\boldsymbol{u}_h-\boldsymbol{u}^k\right|\right|\right|+C_2^k\left|\left|\left|\boldsymbol{u}_d-\boldsymbol{u}_d^k\right|\right|\right|\left|\left|\left|\boldsymbol{u}^k-\boldsymbol{u}\right|\right|\right| \\
&\leq \left|\left|\left|\boldsymbol{u}_d-\boldsymbol{u}_d^k\right|\right|\right|\left(C_1^k\left|\left|\left|\boldsymbol{e}^k\right|\right|\right|+C_2^k\left|\left|\left|\boldsymbol{u}^k-\boldsymbol{u}\right|\right|\right|\right) \\
&\leq C^k\left|\left|\left|\boldsymbol{u}_d-\boldsymbol{u}_d^k\right|\right|\right|\left(\left|\left|\left|\boldsymbol{e}^k\right|\right|\right|+\left|\left|\left|\boldsymbol{u}^k-\boldsymbol{u}\right|\right|\right|\right)\,,
\end{aligned} \tag{A.71}$$

with $C^k=\max(C_1^k,C_2^k)$. The error will be bounded if the term $\left|\left|\left|\boldsymbol{u}_d-\boldsymbol{u}_d^k\right|\right|\right|$ is bounded. To prove this, we use the theorem 5.1 and 5.4 demonstrated by J. Lions *et al.* [147]. The result of the theorems under proper ellipticity is,

$$||\boldsymbol{u}||_{\mathbf{H}^p(L)}\leq C^p\left\{||\mathbf{A}\cdot\boldsymbol{u}||_{\mathbf{H}^{p-2m}(L)}+\sum_i||\boldsymbol{B}\cdot\boldsymbol{u}||_{\mathbf{H}^{p-i-1/2}(\partial L)}\right\}\,, \tag{A.72}$$

$\forall p\geq 2m$. As by assumption pure Dirichlet boundary conditions are assumed the last term of (A.72) is equal to zeros so,

$$||\boldsymbol{u}||_{\mathbf{H}^p(L)}\leq C^p\left\{||\boldsymbol{L}\cdot\boldsymbol{u}||_{\mathbf{H}^{p-2m}(L)}\right\} \tag{A.73}$$

Moreover the application of equation (A.63) to $\left|\left|\left|\boldsymbol{u}_d-\boldsymbol{u}_d^k\right|\right|\right|$ gives,

$$\left|\left|\left|\boldsymbol{u}_d-\boldsymbol{u}_d^k\right|\right|\right| \;\leq\; \begin{cases} \sum_e Ch^{s2}\,|\boldsymbol{u}_d|_{\mathbf{H}^4(l_e)} \text{ if } k>2 \\ \sum_e Ch^{s}\,|\boldsymbol{u}_d|_{\mathbf{H}^4(l_e)} \text{ if } k=2 \end{cases} \tag{A.74}$$

where the case $k=2$ is obtained by following the work of G. Wells *et al.* [257]. Then the result of the theorems (A.73) can be applied to the relation (A.74) with $m=2$, $p=4\geq 2m$ which gives,

$$\left|\left|\left|\boldsymbol{u}_d-\boldsymbol{u}_d^k\right|\right|\right| \;\leq\; \begin{cases} \sum_e Ch^{s2}\,||\boldsymbol{e}||_{\mathbf{L}^2(l_e)} \text{ if } k>2 \\ \sum_e Ch^{s}\,||\boldsymbol{e}||_{\mathbf{L}^2(l_e)} \text{ if } k=2 \end{cases}\,. \tag{A.75}$$

To finish and to have a bound of the error, using the triangle inequality $||e||_{\mathbf{L}^2(l_e)} < \left|\left|e^k\right|\right|_{\mathbf{L}^2(l_e)}$ (see G. Wells *et al.* [257] for details), and injecting the Eqs. (A.64) and (A.75) into the Eq. (A.71) it comes,

$$||e||_{\mathbf{L}^2(l_e)} \leq \begin{cases} \sum_e Ch^{sk+1} |u|_{\mathbf{H}^{k+1}(l_e)} \text{ if } k > 2 \\ \sum_e Ch_s^2 |u|_{\mathbf{H}^3(l_e)} \text{ if } k = 2 \end{cases}, \tag{A.76}$$

which proves that the method has a optimal convergence if at least cubic element are used as presented in Chapter 3 Eq. (3.51). Note that for a pure membrane problem,

$$\left|\left|\left| u_d - u_d^k \right|\right|\right| \leq \sum_e Ch^s |u_d|_{\mathbf{H}^2(l_e)}, \tag{A.77}$$

which leads to (in applying the theorems with $m = 1$ and $p = 2$),

$$||e||_{\mathbf{L}^2(l_e)} \leq \sum_e Ch^{sk+1} |u|_{\mathbf{H}^{k+1}(l_e)} \text{ if } k \geq 1, \tag{A.78}$$

which shows that if only the membrane term is present, the convergence of the method is optimal in $\mathbf{L}^2$-norm even for second order interpolation. This is consistent with the fact that as the membrane terms include only the first derivative, the continuity is (weakly) enforced by second order shape functions.

A.4 Difference of internal energy in a DCB at fracture initiation

In this section we demonstrate formula (3.126) and (3.127). We demonstrate first the expression of internal energy for the two configurations: (i) DCB (unfractured) and (ii) 2 SCB (full broken) and afterward the formula are obtained by a subtraction.

First we investigate the case of a DCB, which force-displacement relation is given by,

$$P = \frac{16Eh^3}{L_{DCB}^3} u_3, \tag{A.79}$$

with u_3 the vertical displacement at the center of the beam, P the punctual loading at the middle of the beam and L_{DCB} the beam length. It has to be mentioned that in the following a unit width is considered.

Secondly for a SCB the relation force-displacement is expressed by,

$$u_3 = \frac{4PL_{SCB}^3}{Eh^3} = \frac{PL_{DCB}^3}{2Eh^3}, \tag{A.80}$$

or,

$$P = \frac{2Eh^3}{L_{DCB}^3} u_3, \tag{A.81}$$

where L_{SCB} is the length of a SCB. As the fracture occurs at center of DCB this one becomes 2 SCB, which have both the same length (*i.e.* $L_{DCB} = 2L_{SCB}$).

Furthermore, the relation between the maximal bending stress (*i.e.* the stress at lower or upper skin) and the force P is given by,

$$\sigma = \frac{M_{\text{bending}} h}{2I}, \tag{A.82}$$

with $M_{\text{bending}} = \frac{PL_{DCB}}{8}$ for a DCB, the bending moment and $I = \frac{1*h^3}{12}$ the inertia of the beam. Therefore for a DCB,

$$u_3 = \frac{L_{DCB}\sigma}{12Eh}. \tag{A.83}$$

Similarly for a SCB, $M_{\text{bending}} = PL_{SCB} = \frac{PL_{DCB}}{2}$, and Eq. (A.81) becomes

$$u_3 = \frac{L_{DCB}^3}{12Eh}\sigma. \tag{A.84}$$

From these developments the internal energy is given by (linear elasticity),

$$W_{int} = \frac{1}{2}Pu_3. \tag{A.85}$$

The application of this formula to the particular case of DCB (A.79) gives,

$$W_{int\,DCB} = \frac{8Eh^3}{L_{DCB}^3}u_3^2, \tag{A.86}$$

and for a SCB (A.81),

$$W_{int\,SCB} = \frac{Eh^3}{L_{DCB}^3}u_3^2. \tag{A.87}$$

Afterward, the energy can be expressed with respect to the stress. For the DCB case the Eq. (A.83) allows writing,

$$W_{int\,DCB} = \frac{8Eh^3}{L_{DCB}^3}\left(\frac{L_{DCB}\sigma}{12Eh}\right)^2 = \frac{hL_{DCB}}{18E}\sigma^2, \tag{A.88}$$

similarly, for SCBcase using Eq. (A.84) it comes,

$$W_{int\,SCB} = \frac{Eh^3}{L_{DCB}^3}\left(\frac{L_{DCB}^2}{12Eh}\right)^2\sigma^2 = \frac{hL_{DCB}}{144E}\sigma^2. \tag{A.89}$$

Finally the difference of internal energy at fracture initiation is given by,

$$\Delta W_{int\,\text{bending}} = W_{int\,DCB} - 2W_{int\,SCB} = \frac{hL_{DCB}}{18E}\sigma^2 - 2\frac{hL_{DCB}}{144E}\sigma^2 = \frac{hL_{DCB}}{24E}\sigma^2.$$

Moreover as the fracture occurs when the stress reaches σ_c (fracture criterion), the difference of internal energy at fracture initiation is given by,

$$\Delta W_{int\,\text{bending}} = \frac{hL_{DCB}}{24E}\sigma_c^2\,, \tag{A.90}$$

which is identical to Eq. (3.126). It appears from this equation than the geometry of the beam has an influence on the fracture stability. Indeed the fracture will be unstable if $L_{DCB} \geq \frac{24EG_c}{\sigma_c^2}$.

Eq. (A.90) is valid for a pure bending loading and for a combined membrane/bending case the energy of the membrane mode has to be considered. Nevertheless, we assume that the membrane energy after fracture is equal to zero. This hypothesis restricts the validity of formula to tension loading and to compressive loading with no interpenetration (*i.e.* there is no contact forces between crack lips after fracture).

The energy of membrane mode can be computed in linear elasticity by,

$$\begin{aligned} W_{int\,\text{membrane}} &= \frac{1}{2}P_{\text{membrane}}u_1 \\ &= \frac{hL_{DCB}}{2E}\sigma^2_{\text{membrane}}\,, \end{aligned} \tag{A.91}$$

as $u_1 = \frac{\sigma_{\text{membrane}}L_{DCB}}{E}$ and $\sigma_{\text{membrane}} = \frac{P_{\text{membrane}}}{h}$. The total internal energy of the DCB configuration can be obtained by linear superposition using Eqs. (A.91) and (A.88) with the part of the stress in bending,

$$W_{int\,DCB\,combined} = \frac{hL_{DCB}}{2E}\left(\frac{1}{9}\sigma^2_{\text{bending}} + \sigma^2_{\text{membrane}}\right)\,. \tag{A.92}$$

The difference of internal energy at fracture initialization can be obtained as previously by,

$$\begin{aligned} \Delta W_{int\,\text{combined}} &= W_{int\,DCB\,combined} - 2W_{int\,SCB}\,, \\ &= \frac{hL_{DCB}}{2E}\left(\frac{1}{12}\sigma^2_{\text{bending}} + \sigma^2_{\text{membrane}}\right)\,. \end{aligned} \tag{A.93}$$

Finally this formula can be expressed with respect of η_I. Indeed,

$$\eta_I = \frac{6/hM_{coh0}}{N_{coh0} + 6/hM_{coh0}} = \frac{\sigma_{\text{bending}\,0}}{\sigma_{\text{membrane}\,0} + \sigma_{\text{bending}\,0}}\,, \tag{A.94}$$

as $M_{coh0} = \frac{h}{6}\sigma_{\text{bending}\,0}$ and $N_{coh0} = h\sigma_{\text{membrane}\,0}$ in linear elasticity by definition. Furthermore at fracture initialization the identity $\sigma_c = \sigma_{\text{bending}\,0} + \sigma_{\text{membrane}\,0}$ is verified which leads to,

$$\begin{aligned} \Delta W_{int\,\text{combined}} &= \frac{hL_{DCB}}{2E}\left(\frac{1}{12}\frac{\sigma^2_{\text{bending}\,0}}{\sigma_c^2} + \frac{\sigma^2_{\text{membrane}\,0}}{\sigma_c^2}\right)\sigma_c^2 \\ &= \frac{hL_{DCB}}{2E}\left(\frac{1}{12}\eta_I^2 + (1-\eta_I)^2\right)\sigma_c^2 \\ &= \frac{hL_{DCB}}{2E}\left(\frac{13}{12}\eta_I^2 - 2\eta_I + 1\right)\sigma_c^2\,, \end{aligned} \tag{A.95}$$

which is the relation Eq. (3.127). Furthermore for the pure bending case, $\eta_I = 1$, which gives the relation (A.90). As previously the fracture stability is governed by the beam's length but also by the ratio between the membrane and bending stresses.

Appendix B

Annex to chapter 4

B.1 Linearization of compatibility terms

The derivation of the full discontinuous Galerkin formulation of shells is realized by introducing compatibilty interface terms that are linearized. The development of this linearization is written herein. The linearized expression of $\delta(\bar{j}\bar{\lambda}_h\tilde{\boldsymbol{m}}^\alpha)$ is suggested by L. Noels *et al.* [185] and is summarized in this work. Afterwards, the same argumentation is applied on $\delta(\bar{j}\boldsymbol{n}^\alpha)$.

B.1.1 Bending compatibility term

The expression of the bending compatibility term is presented by L. Noels [181], who develops $\delta(\bar{j}\bar{\lambda}_h\tilde{\boldsymbol{m}}^\alpha)$. First, $\bar{j}\bar{\lambda}_h\tilde{\boldsymbol{m}}^\alpha$ is decomposed into the mid-plane convected basis,

$$\delta(\bar{j}\bar{\lambda}_h\tilde{\boldsymbol{m}}^\alpha) = \delta\left(\bar{j}\bar{\lambda}_h\tilde{m}^{\alpha\beta}\boldsymbol{\varphi}_{,\beta} + \bar{j}\bar{\lambda}_h^2\tilde{m}^{3\alpha}\boldsymbol{t}\right). \tag{B.1}$$

Then this equation reads, separating the material and geometric parts,

$$\delta(\bar{j}\bar{\lambda}_h\tilde{\boldsymbol{m}}^\alpha) = \delta\left(\bar{j}\bar{\lambda}_h\tilde{m}^{\alpha\beta}\right)\boldsymbol{\varphi}_{,\beta} + \bar{j}\bar{\lambda}_h\tilde{m}^{\alpha\beta}\delta\boldsymbol{\varphi}_{,\beta} + \delta\left(\bar{j}\bar{\lambda}_h^2\tilde{m}^{3\alpha}\right)\boldsymbol{t} + \bar{j}\bar{\lambda}_h^2\tilde{m}^{3\alpha}\delta\boldsymbol{t}. \tag{B.2}$$

The material part can then be computed using the linear expression of $\tilde{m}^{\alpha\beta}$ and $\tilde{m}^{3\alpha}$ given by [237], for elasticity with finite deformations,

$$\tilde{m}^{\alpha\beta} = \frac{\bar{j}_0}{\bar{j}\bar{\lambda}_h}\mathcal{H}_m^{\alpha\beta\gamma\delta}\left(\boldsymbol{\varphi}_{,\gamma}\cdot\boldsymbol{t}_{,\delta} - \boldsymbol{\varphi}_{0,\gamma}\cdot\boldsymbol{t}_{0,\delta}\right) \text{ and,} \tag{B.3}$$

$$\tilde{m}^{3\alpha} = \frac{\bar{j}_0}{\bar{j}\bar{\lambda}_h^2}\frac{jE\left(h_{\max}-h_{\min}\right)^3}{240\left(1+\nu\right)}\boldsymbol{\varphi}_0^{,\alpha}\cdot\boldsymbol{\varphi}_0^{,\beta}\left(\log\lambda_h\right)_{,\beta}. \tag{B.4}$$

Thus,

$$\delta\left(\bar{j}\lambda_h\tilde{m}^{\alpha\beta}\right) = \bar{j}_0\mathcal{H}_m^{\alpha\beta\gamma\delta}\left(\delta\boldsymbol{\varphi}_{,\gamma}\cdot\boldsymbol{t}_{,\delta}+\boldsymbol{\varphi}_{,\gamma}\cdot\delta\boldsymbol{t}_{\delta}\right) \text{ and,} \tag{B.5}$$

$$\begin{aligned}\delta\left(\bar{j}\lambda_h^2\tilde{m}^{3\alpha}\right) &= \bar{j}_0\frac{jE\left(h_{\max}-h_{\min}\right)^3}{240\left(1+\nu\right)}\boldsymbol{\varphi}_0^{,\alpha}\cdot\boldsymbol{\varphi}_0^{,\beta}\delta\left(\log\lambda_h\right)_{,\beta}\\ &= \bar{j}_0\frac{jE\left(h_{\max}-h_{\min}\right)^3}{240\left(1+\nu\right)}\boldsymbol{\varphi}_0^{,\alpha}\cdot\boldsymbol{\varphi}_0^{,\beta}\left(\frac{\delta\lambda_h}{\lambda_h}\right)_{,\beta}.\end{aligned} \tag{B.6}$$

Finally, using these two linearizations and using $\tilde{m}^{\alpha\beta}=\tilde{m}^{\alpha\gamma}\boldsymbol{\varphi}_{,\gamma}\cdot\boldsymbol{\varphi}^{,\beta}=\tilde{\boldsymbol{m}}^{\alpha}\cdot\boldsymbol{\varphi}^{,\beta}$, as $\boldsymbol{\varphi}_{,\gamma}\cdot\boldsymbol{\varphi}^{,\beta}=\delta_{\gamma\beta}$

$$\begin{aligned}\delta\left(\bar{j}\lambda_h\tilde{\boldsymbol{m}}^{\alpha}\right) &= \bar{j}_0\mathcal{H}_m^{\alpha\beta\gamma\delta}\left(\delta\boldsymbol{\varphi}_{,\gamma}\cdot\boldsymbol{t}_{,\delta}+\boldsymbol{\varphi}_{,\gamma}\cdot\delta\boldsymbol{t}_{,\delta}\right)\boldsymbol{\varphi}_{,\beta}+\bar{j}\lambda_h\tilde{\boldsymbol{m}}^{\alpha}\cdot\boldsymbol{\varphi}^{,\beta}\delta\boldsymbol{\varphi}_{,\beta}\\ &\quad+\frac{\bar{j}_0}{\bar{j}\lambda_h^2}\frac{jE\left(h_{\max}-h_{\min}\right)^3}{240\left(1+\nu\right)}\boldsymbol{\varphi}_0^{,\alpha}\cdot\boldsymbol{\varphi}_0^{,\beta}\delta\left(\log\lambda_h\right)_{,\beta}\boldsymbol{t}+j\lambda_h^2\tilde{m}^{3\alpha}\delta\boldsymbol{t},\end{aligned} \tag{B.7}$$

furthermore, as the terms in $\delta\lambda_h$ or λ_h^2 are of the same order than the out of plane shearing which is neglected the final form of the bending compatibility term is,

$$\delta\left(\bar{j}\lambda_h\tilde{\boldsymbol{m}}^{\alpha}\right) = \bar{j}_0\mathcal{H}_m^{\alpha\beta\gamma\delta}\left(\delta\boldsymbol{\varphi}_{,\gamma}\cdot\boldsymbol{t}_{,\delta}+\boldsymbol{\varphi}_{,\gamma}\cdot\delta\boldsymbol{t}_{,\delta}\right)\boldsymbol{\varphi}_{,\beta}+\bar{j}\lambda_h\tilde{\boldsymbol{m}}^{\alpha}\cdot\boldsymbol{\varphi}^{,\beta}\delta\boldsymbol{\varphi}_{,\beta}, \tag{B.8}$$

which is identical to the Eq. (4.83).

B.1.2 Membrane compatibility term

We describe here the derivation of $\delta\left(\bar{j}\boldsymbol{n}^{\alpha}\right)$ which appears in the compatibility membrane term (see equation (4.87)). As the shearing is neglected for Kirchhoff-Love shells,

$$\boldsymbol{n}^{\alpha} = \left(\tilde{n}^{\alpha\beta}+\lambda_{\mu}^{\beta}\tilde{m}^{\alpha\mu}\right)\boldsymbol{\varphi}_{,\beta}, \tag{B.9}$$

with,

$$\lambda_{\mu}^{\beta} = \lambda_h\boldsymbol{t}_{,\mu}\cdot\boldsymbol{\varphi}^{,\beta}. \tag{B.10}$$

The virtual form can therefore be computed as,

$$\begin{aligned}\delta\left(\bar{j}\boldsymbol{n}^{\alpha}\right) &= \delta\left[\bar{j}\left(\tilde{n}^{\alpha\beta}+\lambda_{\mu}^{\beta}\tilde{m}^{\alpha\mu}\right)\boldsymbol{\varphi}_{,\beta}\right]\\ &= \delta\left(\bar{j}\tilde{n}^{\alpha\beta}+\bar{j}\lambda_{\mu}^{\beta}\tilde{m}^{\alpha\mu}\right)\boldsymbol{\varphi}_{,\beta}+\bar{j}\left(\tilde{n}^{\alpha\beta}+\lambda_{\mu}^{\beta}\tilde{m}^{\alpha\mu}\right)\delta\boldsymbol{\varphi}_{,\beta}\\ &= \delta\left(\bar{j}\tilde{n}^{\alpha\beta}\right)\boldsymbol{\varphi}_{,\beta}+\bar{j}\tilde{m}^{\alpha\mu}\delta\lambda_{\mu}^{\beta}\boldsymbol{\varphi}_{,\beta}+\lambda_{\mu}^{\beta}\delta\left(\bar{j}\tilde{m}^{\alpha\mu}\right)\boldsymbol{\varphi}_{,\beta}+\\ &\quad\bar{j}\left(\tilde{n}^{\alpha\beta}+\lambda_{\mu}^{\beta}\tilde{m}^{\alpha\mu}\right)\boldsymbol{\varphi}_{,\beta}\cdot\boldsymbol{\varphi}^{,\gamma}\delta\boldsymbol{\varphi}_{,\gamma},\end{aligned} \tag{B.11}$$

with the introduction of the identity $\boldsymbol{\varphi}_{,\beta}\cdot\boldsymbol{\varphi}^{,\gamma}=\delta_{\beta\gamma}$ in the last term. Then, the values of $\delta(\bar{j}\tilde{m}^{\alpha\mu})=\frac{\delta(\bar{j}\tilde{m}^{\alpha\mu}\lambda_h)}{\lambda_h}-\bar{j}\tilde{m}^{\alpha\mu}\frac{\delta\lambda_h}{\lambda_h}$ is provided by Eq. (B.3) and the one of $\delta\tilde{n}^{\alpha\beta}$ can be computed from,

$$\tilde{n}^{\alpha\beta} = \frac{\bar{j}_0}{2\bar{j}}\mathcal{H}_n^{\alpha\beta\gamma\delta}\left(\boldsymbol{\varphi}_{,\gamma}\cdot\boldsymbol{\varphi}_{,\delta}-\boldsymbol{\varphi}_{0,\gamma}\cdot\boldsymbol{\varphi}_{0,\delta}\right), \tag{B.12}$$

and Eq. (B.11) is rewritten when neglecting $\delta\lambda_h$ (as always did),

$$\begin{aligned}\delta(\bar{j}\boldsymbol{n}^{\alpha}) &= \frac{\bar{j}_0}{2}\mathcal{H}_n^{\alpha\beta\gamma\delta}\left(\delta\boldsymbol{\varphi}_{,\gamma}\cdot\boldsymbol{\varphi}_{,\delta}+\boldsymbol{\varphi}_{,\gamma}\cdot\delta\boldsymbol{\varphi}_{,\delta}\right)\boldsymbol{\varphi}_{,\beta}+\bar{j}\boldsymbol{n}^{\alpha}\cdot\boldsymbol{\varphi}^{,\beta}\delta\boldsymbol{\varphi}_{,\beta}\\ &+ \frac{\bar{j}_0}{\lambda_h}\lambda_\mu^\beta\mathcal{H}_m^{\alpha\mu\gamma\delta}\left(\delta\boldsymbol{\varphi}_{,\gamma}\cdot\boldsymbol{t}_{,\delta}+\boldsymbol{\varphi}_{,\gamma}\cdot\delta\boldsymbol{t}_{,\delta}\right)\boldsymbol{\varphi}_{,\beta}+\bar{j}\tilde{m}^{\alpha\mu}\delta\lambda_\mu^\beta\boldsymbol{\varphi}_{,\beta}.\end{aligned} \tag{B.13}$$

Moreover using equation (B.10) and neglecting $\delta\lambda_h$,

$$\delta\lambda_\mu^\beta = \lambda_h\left(\delta\boldsymbol{t}_{,\mu}\cdot\boldsymbol{\varphi}^{,\beta}+\boldsymbol{t}_{,\mu}\cdot\delta\boldsymbol{\varphi}^{,\beta}\right). \tag{B.14}$$

The second member of this equation can be rewritten (to remove $\delta\boldsymbol{\varphi}^{,\beta}$) using successively

$$\delta\left(\boldsymbol{\varphi}^{,\alpha}\cdot\boldsymbol{\varphi}_{,\beta}\right) = 0, \tag{B.15}$$

$$\delta\boldsymbol{\varphi}^{,\alpha}\cdot\boldsymbol{\varphi}_{,\beta} = -\boldsymbol{\varphi}^{,\alpha}\cdot\delta\boldsymbol{\varphi}_{,\beta}, \tag{B.16}$$

and from Eq. (B.10),

$$\boldsymbol{t}_{,\alpha}\cdot\delta\boldsymbol{\varphi}^{,\beta} = \frac{\lambda_\alpha^\mu}{\lambda_h}\boldsymbol{\varphi}_{,\mu}\cdot\delta\boldsymbol{\varphi}^{,\beta}=-\frac{\lambda_\alpha^\mu}{\lambda_h}\boldsymbol{\varphi}^{,\beta}\delta\boldsymbol{\varphi}_{,\mu}, \tag{B.17}$$

leading to

$$\delta\lambda_\mu^\beta = \lambda_h\left(\delta\boldsymbol{t}_{,\mu}\cdot\boldsymbol{\varphi}^{,\beta}-\frac{\lambda_\mu^\zeta}{\lambda_h}\boldsymbol{\varphi}^{,\beta}\cdot\delta\boldsymbol{\varphi}_{,\zeta}\right). \tag{B.18}$$

Finally (B.13) becomes

$$\begin{aligned}\delta(\bar{j}\boldsymbol{n}^{\alpha}) &= \frac{\bar{j}_0}{2}\mathcal{H}_n^{\alpha\beta\gamma\delta}\left(\delta\boldsymbol{\varphi}_{,\gamma}\cdot\boldsymbol{\varphi}_{,\delta}+\boldsymbol{\varphi}_{,\gamma}\cdot\delta\boldsymbol{\varphi}_{,\delta}\right)\boldsymbol{\varphi}_{,\beta}+\bar{j}\boldsymbol{n}^{\alpha}\cdot\boldsymbol{\varphi}^{,\beta}\delta\boldsymbol{\varphi}_{,\beta}\\ &+ \frac{\bar{j}_0}{\lambda_h}\lambda_\mu^\beta\mathcal{H}_m^{\alpha\mu\gamma\delta}\left(\delta\boldsymbol{\varphi}_{,\gamma}\cdot\boldsymbol{t}_{,\delta}+\boldsymbol{\varphi}_{,\gamma}\cdot\delta\boldsymbol{t}_{,\delta}\right)\boldsymbol{\varphi}_{,\beta}\\ &+ \bar{j}\lambda_h\tilde{m}^{\alpha\mu}\left(\delta\boldsymbol{t}_{,\mu}\cdot\boldsymbol{\varphi}^{,\beta}-\frac{\lambda_\mu^\zeta}{\lambda_h}\boldsymbol{\varphi}^{,\beta}\cdot\delta\boldsymbol{\varphi}_{,\zeta}\right)\boldsymbol{\varphi}_{,\beta},\end{aligned} \tag{B.19}$$

with $\tilde{m}^{\alpha\mu}=\tilde{\boldsymbol{m}}^{\alpha}\cdot\boldsymbol{\varphi}^{,\mu}$. This expression can be used for the implementation of $a_{nI2}^s(\boldsymbol{\varphi}_h,\delta\boldsymbol{\varphi})$ (4.87).

B.2 Development of the stability shearing term

We present here the developments leading to the expression of the stability shearing term $a^s_{sI3}(\boldsymbol{\varphi}_h, \delta\boldsymbol{\varphi})$ (4.92) suggested in Chapter 4. Toward this end, we first reduce our analysis to the linear case and then we show that a linearization of the non-linear term (4.92) is identical to the linear form suggested.

Following the developments presented in Section 4.4.2 it is possible to give the linear form of the consistency shearing $a^s_{lsI1}(\boldsymbol{u}_h, \delta\boldsymbol{u})$ as well as of the compatibility shearing $a^s_{lsI2}(\boldsymbol{u}_h, \delta\boldsymbol{u})$ terms,

$$a^s_{lsI1}(\boldsymbol{u}_h, \delta\boldsymbol{u}) = \int_s \langle \bar{j_0}\boldsymbol{l}\rangle \cdot \left[\!\!\left[\int_\alpha \delta\Delta t_\beta \boldsymbol{\varphi}_0^{,\beta} d\alpha' \right]\!\!\right] \nu^-_\alpha d\partial\mathcal{A}_e \approx 0 \text{ and,} \tag{B.20}$$

$$a^s_{lsI2}(\boldsymbol{u}_h, \delta\boldsymbol{u}) = \int_s \left[\!\!\left[\int_\alpha \Delta t_\beta \boldsymbol{\varphi}_0^{,\beta} d\alpha' \right]\!\!\right] \cdot \left\langle \boldsymbol{\varphi}_{0,\gamma} \mathcal{H}_s^{\gamma\delta} \delta\gamma_\delta \bar{j_0} \right\rangle \nu^-_\alpha d\partial\mathcal{A}_e \approx 0\,. \tag{B.21}$$

Therefore, by inspection of these two relations the quadratic stability term is formulated as,

$$\begin{aligned} a^s_{lsI3}(\boldsymbol{u}_h, \delta\boldsymbol{u}) = \int_s \Bigg\{ & \left[\!\!\left[\int_\mu \Delta t_\gamma \boldsymbol{\varphi}_0^{,\gamma} d\mu' \right]\!\!\right] \cdot \boldsymbol{\varphi}_{0,\alpha} \nu^-_\mu \left\langle \frac{\beta_3 \mathcal{H}_s^{\alpha\beta} \bar{j_0}}{h^s} \right\rangle \\ & \boldsymbol{\varphi}_{0,\beta} \cdot \left[\!\!\left[\int_\nu \delta\Delta t_\delta \boldsymbol{\varphi}_0^{,\delta} d\nu' \right]\!\!\right] \nu^-_\nu \Bigg\} d\partial\mathcal{A}_e\,, \end{aligned} \tag{B.22}$$

which weakly ensures the compatibility of the deflection normal to the mid-surface. However, in order to implement it in an efficient way, it is necessary to find an expression for the primitive of $\boldsymbol{\Delta t}$ and $\delta\boldsymbol{\Delta t}$. Using the definition of the shearing strain component (4.112) it comes $\boldsymbol{u}_{h,\alpha} \cdot \boldsymbol{t}_0 \approx -\boldsymbol{\Delta t} \cdot \boldsymbol{\varphi}_{0,\alpha}$ which yields

$$\int_\mu \Delta t_\gamma \boldsymbol{\varphi}_0^{,\gamma} d\mu' \approx -\int_\mu \boldsymbol{u}_{h,\gamma} \cdot \boldsymbol{t}_0 \boldsymbol{\varphi}_0^{,\gamma} d\mu'\,. \tag{B.23}$$

As the unique purpose of the stability shearing term is to weakly enforce the stability, it can be approximated without damaging the accuracy of the method (consistency is preserved). Therefore, the relation (B.23) can be approximated by assuming a surface with a curvature radius large compared to the sizes, thus leading for a planar assumption to

$$\left[\!\!\left[\int_\mu \Delta t_\gamma \boldsymbol{\varphi}_0^{,\gamma} d\mu' \right]\!\!\right] \cdot \boldsymbol{\varphi}_{0,\alpha} = -\left[\!\!\left[\int_\mu \boldsymbol{u}_{h,\gamma} \cdot \boldsymbol{t}_0 \boldsymbol{\varphi}_0^{,\gamma} d\mu' \right]\!\!\right] \cdot \boldsymbol{\varphi}_{0,\alpha} \rightarrow -[\![\boldsymbol{u}_h]\!] \cdot \boldsymbol{t}_0 \delta_{\alpha\mu}\,. \tag{B.24}$$

Finally, using this last approximation in Eq. (B.22) it comes,

$$a^s_{lsI3}(\boldsymbol{u}_h, \delta\boldsymbol{u}) = \int_s [\![\boldsymbol{u}_h]\!] \cdot \boldsymbol{t}_0 \nu^-_\beta \left\langle \frac{\beta_3 \mathcal{H}_q^{\alpha\beta} \bar{j_0}}{h^s} \right\rangle [\![\delta\boldsymbol{u}]\!] \cdot \boldsymbol{t}_0 \nu^-_\alpha d\partial\mathcal{A}_e\,, \tag{B.25}$$

which is identical to the Eq. (4.147).

Then we discuss the non-linear form of $a^s_{sI3}(\boldsymbol{\varphi}_h, \delta\boldsymbol{\varphi})$ (4.92). As the unique purpose of this term is to ensure the stability and the compatibility of the displacement normal to the mid-surface, any consistent expression can be used. Therefore, in a similar way for the other compatibility and stability terms we derive an expression of $a^s_{sI3}(\boldsymbol{\varphi}_h, \delta\boldsymbol{\varphi})$ which after linearization leads to the linear form $a^s_{lsI3}(\boldsymbol{u}_h, \delta\boldsymbol{u})$ (B.25). Toward this end, we suggest the expression:

$$a^s_{sI3}(\boldsymbol{\varphi}_h, \delta\boldsymbol{\varphi}) \;=\; \int_s [\![\boldsymbol{\varphi}_h]\!]\cdot\boldsymbol{t}\,(\boldsymbol{\varphi}_h)\,\nu^-_\beta \left\langle \frac{\beta_3 \mathcal{H}_s^{\alpha\beta}\,\bar{j}_0}{h^s} \right\rangle [\![\delta\boldsymbol{\varphi}]\!]\cdot\boldsymbol{t}\,(\boldsymbol{\varphi}_h)\,\nu^-_\alpha\, d\partial\mathcal{A}_e\,, \tag{B.26}$$

whose linearization leads to Eq. (B.25). Indeed, using (4.101-4.102),

$$[\![\boldsymbol{\varphi}_h]\!]\cdot\boldsymbol{t} \;=\; [\![\boldsymbol{\varphi}_{h0}+\boldsymbol{u}_h]\!]\cdot(\boldsymbol{t}_0+\boldsymbol{\Delta t}) \approx [\![\boldsymbol{u}_h]\!]\cdot(\boldsymbol{t}_0+\boldsymbol{\Delta t})\,, \tag{B.27}$$

as $[\![\boldsymbol{\varphi}_{h0}]\!] \approx 0$ and, with a first order approximation, Eq. (B.27) reads,

$$[\![\boldsymbol{\varphi}_h]\!]\cdot\boldsymbol{t} \;\approx\; [\![\boldsymbol{u}_h]\!]\cdot\boldsymbol{t}_0\,. \tag{B.28}$$

Similarly,

$$[\![\delta\boldsymbol{\varphi}]\!]\cdot\boldsymbol{t} \;\approx\; [\![\delta\boldsymbol{u}]\!]\cdot\boldsymbol{t}_0\,. \tag{B.29}$$

Finally, using Eqs. (B.28-B.29) to linearize the shearing stability terms $a^s_{sI3}(\boldsymbol{\varphi}_h, \delta\boldsymbol{\varphi})$ (B.26) it provides its linear counterpart $a^s_{lsI3}(\boldsymbol{u}_h, \delta\boldsymbol{u})$ (B.25).

B.3 Implication of the symmetry of σ

To satisfy Eq. (4.47), the symmetry of the effective membrane stress tensor can be enforced. This tensor is defined, in the convected basis, as

$$\tilde{\mathbf{n}} \;=\; \tilde{n}^{\alpha\beta}\boldsymbol{\varphi}_{,\alpha}\otimes\boldsymbol{\varphi}_{,\beta} = \boldsymbol{n}^\alpha\otimes\boldsymbol{\varphi}_{,\alpha} + \boldsymbol{l}\otimes\lambda_h\boldsymbol{t} - (\lambda_h\boldsymbol{t})_{,\alpha}\otimes\tilde{\boldsymbol{m}}^\alpha = \tilde{n}^{\alpha\beta}\boldsymbol{\varphi}_{,\beta}\otimes\boldsymbol{\varphi}_{,\alpha}\,. \tag{B.30}$$

From this definition, the components $\tilde{n}^{\alpha 3} = (\tilde{\mathbf{n}}\cdot\boldsymbol{\varphi}^{,\alpha})\cdot\lambda_h\boldsymbol{t}$ and $\tilde{n}^{3\alpha}$ read,

$$\tilde{n}^{\alpha 3} \;=\; l^\alpha - \lambda^\alpha_\gamma\tilde{m}^{3\gamma} = \tilde{l}^\alpha \text{ and,} \tag{B.31}$$

$$\tilde{n}^{3\alpha} \;=\; q^\alpha - \lambda^3_\gamma\tilde{m}^{\alpha\gamma}, \tag{B.32}$$

where $\lambda^\beta_\mu = \lambda_h\boldsymbol{t}_{,\mu}\cdot\boldsymbol{\varphi}^{,\beta}$. Moreover as we neglect by assumption $\lambda_{h,\alpha}$ and taking into account the relation $\boldsymbol{t}_{,\alpha}\cdot\boldsymbol{t} = 0$ we have $\lambda^3_\alpha = 0$. Finally, as $\tilde{\boldsymbol{m}}^3$ vanishes fore thin bodies the Eqs. (B.31-B.32) can be written as,

$$\tilde{n}^{\alpha 3} \;=\; l^\alpha = \tilde{l}^\alpha \text{ and,} \tag{B.33}$$

$$\tilde{n}^{3\alpha} \;=\; q^\alpha\,. \tag{B.34}$$

But as Eq. (4.47) is satisfied by enforcing the symmetry of the effective membrane stress resultant tensor it leads to $\tilde{n}^{\alpha 3} = \tilde{n}^{3\alpha}$ and thus,

$$q^\alpha = \tilde{l}^\alpha \tag{B.35}$$

Finally, from the definition of $\tilde{\mathbf{n}}$ (B.30), we have also,

$$\tilde{n}^{\alpha\beta} \;=\; n^{\alpha\beta} - \lambda^\beta_\mu\tilde{m}^{\alpha\beta}\,. \tag{B.36}$$

B.4 Numerical properties

In Chapter 4 we enumerated the numerical properties of the suggested DG formulation of Kirchhoff-Love shells. To be concise some demonstrations were omitted. They are a generalization to shells of the different demonstrations made in Appendix A.3 in the case of Euler-Bernoulli beams. Notice that all the demonstrations reported here below are made under a linear assumption as discussed in Section 4.4.

B.4.1 Upper bound of the bilinear form

The upper bound of $|a(\boldsymbol{u},\delta\boldsymbol{u})|^2$, is derived by first using the Cauchy-Schwartz inequality ($\left|a^{\alpha\beta}b^{\alpha\beta}\right| \leq \sqrt{a^{\alpha\beta}a^{\alpha\beta}}\sqrt{b^{\alpha\beta}b^{\alpha\beta}}$) in the membrane and bending parts of the bilinear form (4.148) which gives,

$$\begin{aligned}
\left|\sum_e a_n^e(\boldsymbol{u},\delta\boldsymbol{u})\right| &\leq \sum_e \left\| \sqrt{\mathcal{H}_n \bar{j}_0}^{\alpha\beta} \frac{1}{2}\left(\boldsymbol{\varphi}_{0,\alpha}\cdot\boldsymbol{u}_{,\beta}+\boldsymbol{u}_{,\alpha}\cdot\boldsymbol{\varphi}_{0,\beta}\right)\right\|_{\mathrm{L}^2(\mathcal{A}_e)} \\
&\quad \times \left\| \sqrt{\mathcal{H}_n \bar{j}_0}^{\gamma\delta} \frac{1}{2}\left(\boldsymbol{\varphi}_{0,\gamma}\cdot\delta\boldsymbol{u}_{,\delta}+\delta\boldsymbol{u}_{,\gamma}\cdot\boldsymbol{\varphi}_{0,\delta}\right)\right\|_{\mathrm{L}^2(\mathcal{A}_e)} \quad \text{and,} \qquad \text{(B.37)} \\
\left|\sum_e a_m^e(\boldsymbol{u},\delta\boldsymbol{u})\right| &\leq \sum_e \left\| \sqrt{\mathcal{H}_m \bar{j}_0}^{\alpha\beta} \left(\boldsymbol{\varphi}_{0,\alpha}\cdot\boldsymbol{\Delta t}_{,\beta}+\boldsymbol{u}_{,\alpha}\cdot\boldsymbol{t}_{0,\beta}\right)\right\|_{\mathrm{L}^2(\mathcal{A}_e)} \\
&\quad \times \left\| \sqrt{\mathcal{H}_m \bar{j}_0}^{\gamma\delta} \left(\boldsymbol{\varphi}_{0,\gamma}\cdot\delta\boldsymbol{\Delta t}_{,\delta}+\delta\boldsymbol{u}_{,\gamma}\cdot\boldsymbol{t}_{0,\delta}\right)\right\|_{\mathrm{L}^2(\mathcal{A}_e)} , \qquad \text{(B.38)}
\end{aligned}$$

where the notation,

$$\left\| \sqrt{\mathcal{H}}^{\alpha\beta} a_{\alpha\beta} \right\|^2_{\mathrm{L}^2(\mathcal{A}_e)} = \int_{\mathcal{A}_e} a_{\alpha\beta}\mathcal{H}^{\alpha\beta\gamma\delta}a_{\gamma\delta}\,d\mathcal{A}\,, \qquad \text{(B.39)}$$

is used. Then, the recourse to the property $\|\langle\bullet\rangle\|^2_{\mathrm{L}^2(s)} \leq \|\bullet^+\|^2_{\mathrm{L}^2(s)} + \|\bullet^-\|^2_{\mathrm{L}^2(s)}$ allows bounding the consistent membrane interface term,

$$\begin{aligned}
\left|\sum_s a^s_{lnI1}(\boldsymbol{u}_h,\delta\boldsymbol{u})\right| &\leq \sum_e \left| \int_{\partial\mathcal{A}_e} a^s_{lnI1}(\boldsymbol{u}_h,\delta\boldsymbol{u}) \right| \\
&\leq 2\sum_e \left\| \sqrt{h^s\mathcal{H}_n \bar{j}_0}^{\alpha\beta} \left(\boldsymbol{\varphi}_{0,\alpha}\cdot\boldsymbol{u}_{,\beta}+\boldsymbol{u}_{,\alpha}\cdot\boldsymbol{\varphi}_{0,\beta}\right)\right\|_{\mathrm{L}^2(\partial\mathcal{A}_e)} \\
&\quad \times \left\| \sqrt{\frac{\mathcal{H}_n \bar{j}_0}{h^s}}^{\gamma\delta} [\![\delta\boldsymbol{u}]\!]\cdot\boldsymbol{\varphi}_{0,\delta}\nu^-_\gamma \right\|_{\mathrm{L}^2(\partial\mathcal{A}_e)} , \qquad \text{(B.40)}
\end{aligned}$$

which becomes using the scaling property[1],

$$\left|\sum_s a^s_{lnI1}(\boldsymbol{u}_h,\delta\boldsymbol{u})\right| \leq \frac{C_2^k}{\sqrt{\beta_2}}\sum_e \left\|\sqrt{\mathcal{H}_n\bar{j}_0}^{\alpha\beta}\left(\boldsymbol{\varphi}_{0,\alpha}\cdot\boldsymbol{u}_{,\beta}+\boldsymbol{u}_{,\alpha}\cdot\boldsymbol{\varphi}_{0,\beta}\right)\right\|_{\mathrm{L}^2(\mathcal{A}_e)} \times\left\|\sqrt{\frac{\beta_2\mathcal{H}_n\bar{j}_0}{h^s}}^{\gamma\delta}[\![\delta\boldsymbol{u}]\!]\cdot\boldsymbol{\varphi}_{0,\delta}\nu^-_\gamma\right\|_{\mathrm{L}^2(\partial\mathcal{A}_e)}, \tag{B.41}$$

where C_2^k depends only on the degree of $\boldsymbol{u}$. Note that this one is *a priori* unknown, but applying the bounds to the discretization $\boldsymbol{u}_h$ satisfying the essential boundary conditions, the degree of $\boldsymbol{u}$, corresponds to the degree of the polynomial approximation. The other interface terms can be bounded in a similar ways[2]:

- Compatibility membrane term,

$$\left|\sum_s a^s_{lnI2}(\boldsymbol{u}_h,\delta\boldsymbol{u})\right| \leq \frac{C_2^k}{\sqrt{\beta_2}}\sum_e \left\|\sqrt{\mathcal{H}_n\bar{j}_0}^{\alpha\beta}\left(\boldsymbol{\varphi}_{0,\alpha}\cdot\delta\boldsymbol{u}_{,\beta}+\delta\boldsymbol{u}_{,\alpha}\cdot\boldsymbol{\varphi}_{0,\beta}\right)\right\|_{\mathrm{L}^2(\mathcal{A}_e)} \times\left\|\sqrt{\frac{\beta_2\mathcal{H}_n\bar{j}_0}{h^s}}^{\gamma\delta}[\![\boldsymbol{u}]\!]\cdot\boldsymbol{\varphi}_{0,\delta}\nu^-_\gamma\right\|_{\mathrm{L}^2(\partial\mathcal{A}_e)}, \tag{B.42}$$

- Stability membrane term,

$$\left|\sum_s a^s_{lnI3}(\boldsymbol{u}_h,\delta\boldsymbol{u})\right| \leq \sum_e \left\|\sqrt{\frac{\beta_2\mathcal{H}_n\bar{j}_0}{h^s}}^{\alpha\beta}[\![\delta\boldsymbol{u}]\!]\cdot\boldsymbol{\varphi}_{0,\beta}\nu^-_\alpha\right\|_{\mathrm{L}^2(\partial\mathcal{A}_e)} \times\left\|\sqrt{\frac{\beta_2\mathcal{H}_n\bar{j}_0}{h^s}}^{\gamma\delta}[\![\boldsymbol{u}]\!]\cdot\boldsymbol{\varphi}_{0,\delta}\nu^-_\gamma\right\|_{\mathrm{L}^2(\partial\mathcal{A}_e)} \tag{B.43}$$

- Consistency bending term,

$$\left|\sum_s a^s_{lmI1}(\boldsymbol{u}_h,\delta\boldsymbol{u})\right| \leq \frac{C_1^k}{\sqrt{\beta_1}}\sum_e \left\|\sqrt{\mathcal{H}_m\bar{j}_0}^{\alpha\beta}\left(\boldsymbol{\varphi}_{0,\alpha}\cdot\boldsymbol{\Delta t}_{,\beta}+\boldsymbol{u}_{,\alpha}\cdot\boldsymbol{t}_{0,\beta}\right)\right\|_{\mathrm{L}^2(\mathcal{A}_e)} \times\left\|\sqrt{\frac{\beta_1\mathcal{H}_m\bar{j}_0}{h^s}}^{\gamma\delta}[\![\boldsymbol{\Delta t}(\delta\boldsymbol{u})]\!]\cdot\boldsymbol{\varphi}_{0,\delta}\nu^-_\gamma\right\|_{\mathrm{L}^2(\partial\mathcal{A}_e)}, \tag{B.44}$$

[1] Hansbo *et al.* [115] demonstrate that for an element e one has the property $h^s\|a\|^2_{\mathrm{L}^2(\partial\mathcal{A}_e)} \leq C^k\|a\|^2_{\mathrm{L}^2(\mathcal{A}_e)}$ with $C^k>0$ independent of the element geometry and with $h^s=\frac{|\mathcal{A}_e|}{|\partial\mathcal{A}_e|}$. Constant $C^k=\sup_{a^{\alpha\beta}\in\mathbb{P}^k(\mathcal{A}_e)}\frac{|\mathcal{A}_e|\int_s\{a^{\alpha\beta}:a^{\alpha\beta}\}d\partial\mathcal{A}}{|s|\int_{\mathcal{A}_e}\{a^{\alpha\beta}:a^{\alpha\beta}\}d\mathcal{A}}$ depends only on the polynomial degree k.

[2] Note that the scaling property is not applied for the terms of stabilization

- Compatibility bending term,

$$\left|\sum_s a^s_{lmI2}(\boldsymbol{u}_h,\delta\boldsymbol{u})\right| \leq \frac{C_1^k}{\sqrt{\beta_1}}\sum_e \left\|\sqrt{\mathcal{H}_m \bar{j}_0}^{\alpha\beta}\left(\boldsymbol{\varphi}_{0,\alpha}\cdot\delta\boldsymbol{\Delta t}_{,\beta}+\delta\boldsymbol{u}_{,\alpha}\cdot\boldsymbol{t}_{0,\beta}\right)\right\|_{\mathrm{L}^2(\mathcal{A}_e)} \times\left\|\sqrt{\frac{\beta_1\mathcal{H}_m\bar{j}_0}{h^s}}^{\gamma\delta}[\![\boldsymbol{\Delta t}]\!]\cdot\boldsymbol{\varphi}_{0,\delta}\nu^-_\gamma\right\|_{\mathrm{L}^2(\partial\mathcal{A}_e)}, \tag{B.45}$$

- Stability bending term,

$$\left|\sum_s a^s_{lmI3}(\boldsymbol{u}_h,\delta\boldsymbol{u})\right| \leq \sum_e \left\|\sqrt{\frac{\beta_1\mathcal{H}_m\bar{j}_0}{h^s}}^{\alpha\beta}[\![\delta\boldsymbol{\Delta t}]\!]\cdot\boldsymbol{\varphi}_{0,\beta}\nu^-_\alpha\right\|_{\mathrm{L}^2(\partial\mathcal{A}_e)} \times\left\|\sqrt{\frac{\beta_1\mathcal{H}_m\bar{j}_0}{h^s}}^{\gamma\delta}[\![\boldsymbol{\Delta t}]\!]\cdot\boldsymbol{\varphi}_{0,\delta}\nu^-_\gamma\right\|_{\mathrm{L}^2(\partial\mathcal{A}_e)}, \tag{B.46}$$

- Stability shearing term,

$$\left|\sum_s a^s_{lsI3}(\boldsymbol{u}_h,\delta\boldsymbol{u})\right| \leq \sum_e \left\|\sqrt{\frac{\beta_3\mathcal{H}_q\bar{j}_0}{h^s}}^{\alpha}[\![\delta\boldsymbol{u}]\!]\cdot\boldsymbol{t}_0\nu^-_\alpha\right\|_{\mathrm{L}^2(\partial\mathcal{A}_e)} \times\left\|\sqrt{\frac{\beta_3\mathcal{H}_q\bar{j}_0}{h^s}}^{\gamma}[\![\boldsymbol{u}]\!]\cdot\boldsymbol{t}_0\nu^-_\gamma\right\|_{\mathrm{L}^2(\partial\mathcal{A}_e)}. \tag{B.47}$$

Then, completing the form to obtain the complete binomial terms, the summation of Eqs. (B.37-B.47) gives,

$$
\begin{aligned}
\frac{|a_l(\boldsymbol{u}_h,\delta\boldsymbol{u})|}{C^k(\beta)} \leq \sum_e \; & \left[\left\| \sqrt{\mathcal{H}_n \bar{j}_0}^{\alpha\beta} \frac{1}{2}\left(\boldsymbol{\varphi}_{0,\alpha}\cdot\boldsymbol{u}_{,\beta}+\boldsymbol{u}_{,\alpha}\cdot\boldsymbol{\varphi}_{0,\beta}\right)\right\|_{\mathrm{L}^2(\mathcal{A}_e)} + \right. \\
& \left\| \sqrt{\mathcal{H}_m \bar{j}_0}^{\alpha\beta} \left(\boldsymbol{\varphi}_{0,\alpha}\cdot\boldsymbol{\Delta t}_{,\beta}+\boldsymbol{u}_{,\alpha}\cdot\boldsymbol{t}_{0,\beta}\right)\right\|_{\mathrm{L}^2(\mathcal{A}_e)} + \\
& \left\| \sqrt{\frac{\beta_2\mathcal{H}_n \bar{j}_0}{2h^s}}^{\alpha\beta} [\![\boldsymbol{u}]\!]\cdot\boldsymbol{\varphi}_{0,\beta}\nu_\alpha^-\right\|_{\mathrm{L}^2(\partial\mathcal{A}_e)} + \\
& \left\| \sqrt{\frac{\beta_1\mathcal{H}_m \bar{j}_0}{2h^s}}^{\alpha\beta} [\![\boldsymbol{\Delta t}]\!]\cdot\boldsymbol{\varphi}_{0,\beta}\nu_\alpha^-\right\|_{\mathrm{L}^2(\partial\mathcal{A}_e)} + \\
& \left. \left\| \sqrt{\frac{\beta_3\mathcal{H}_q \bar{j}_0}{2h^s}}^{\alpha} [\![\boldsymbol{u}]\!]\cdot\boldsymbol{t}_0\nu_\alpha^-\right\|_{\mathrm{L}^2(\partial\mathcal{A}_e)}\right] \times \\
& \left[\left\| \sqrt{\mathcal{H}_n \bar{j}_0}^{\gamma\delta} \frac{1}{2}\left(\boldsymbol{\varphi}_{0,\gamma}\cdot\delta\boldsymbol{u}_{,\delta}+\delta\boldsymbol{u}_{,\gamma}\cdot\boldsymbol{\varphi}_{0,\delta}\right)\right\|_{\mathrm{L}^2(\mathcal{A}_e)} + \right. \\
& \left\| \sqrt{\mathcal{H}_m \bar{j}_0}^{\gamma\delta} \left(\boldsymbol{\varphi}_{0,\gamma}\cdot\delta\boldsymbol{\Delta t}_{,\delta}+\delta\boldsymbol{u}_{,\gamma}\cdot\boldsymbol{t}_{0,\delta}\right)\right\|_{\mathrm{L}^2(\mathcal{A}_e)} + \\
& \left\| \sqrt{\frac{\beta_2\mathcal{H}_n \bar{j}_0}{2h^s}}^{\gamma\delta} [\![\delta\boldsymbol{u}]\!]\cdot\boldsymbol{\varphi}_{0,\delta}\nu_\gamma^-\right\|_{\mathrm{L}^2(\partial\mathcal{A}_e)} + \\
& \left\| \sqrt{\frac{\beta_1\mathcal{H}_m \bar{j}_0}{2h^s}}^{\gamma\delta} [\![\delta\boldsymbol{\Delta t}]\!]\cdot\boldsymbol{\varphi}_{0,\delta}\nu_\gamma^-\right\|_{\mathrm{L}^2(\partial\mathcal{A}_e)} + \\
& \left. \left\| \sqrt{\frac{\beta_3\mathcal{H}_q \bar{j}_0}{2h^s}}^{\gamma} [\![\delta\boldsymbol{u}]\!]\cdot\boldsymbol{t}_0\nu_\gamma^-\right\|_{\mathrm{L}^2(\partial\mathcal{A}_e)}\right], \qquad \text{(B.48)}
\end{aligned}
$$

with $C^k(\beta_i) = \max\left(2, C_1^k\sqrt{2/\beta_1}, C_2^k\sqrt{2/\beta_2}\right)$. Finally, using the property $2ab \leq a^2 + b^2$ and the Cauchy-Schwartz inequality ($\left|\sum_i a_i b_i\right| \leq \sqrt{\sum_i a_i^2 \sum_j b_j^2}$) is Eq. (B.48), this last one reads,

$$
\begin{aligned}
\frac{|a_l(\boldsymbol{u}_h, \delta\boldsymbol{u})|^2}{C^{k'}(\beta_i)} \leq \sum_e & \left[\left\| \sqrt{\mathcal{H}_n \bar{j}_0}^{\alpha\beta} \frac{1}{2}\left(\boldsymbol{\varphi}_{0,\alpha}\cdot\boldsymbol{u}_{,\beta} + \boldsymbol{u}_{,\alpha}\cdot\boldsymbol{\varphi}_{0,\beta}\right)\right\|^2_{\mathrm{L}^2(\mathcal{A}_e)} + \right. \\
& \left\| \sqrt{\mathcal{H}_m \bar{j}_0}^{\alpha\beta} \left(\boldsymbol{\varphi}_{0,\alpha}\cdot\boldsymbol{\Delta t}_{,\beta} + \boldsymbol{u}_{,\alpha}\cdot\boldsymbol{t}_{0,\beta}\right)\right\|^2_{\mathrm{L}^2(\mathcal{A}_e)} + \\
& \frac{1}{2}\left\| \sqrt{\frac{\beta_2 \mathcal{H}_n \bar{j}_0}{h^s}}^{\alpha\beta} [\![\boldsymbol{u}]\!]\cdot\boldsymbol{\varphi}_{0,\beta}\nu_\alpha^-\right\|^2_{\mathrm{L}^2(\partial\mathcal{A}_e)} + \\
& \frac{1}{2}\left\| \sqrt{\frac{\beta_1 \mathcal{H}_m \bar{j}_0}{h^s}}^{\alpha\beta} [\![\boldsymbol{\Delta t}]\!]\cdot\boldsymbol{\varphi}_{0,\beta}\nu_\alpha^-\right\|^2_{\mathrm{L}^2(\partial\mathcal{A}_e)} + \\
& \left. \frac{1}{2}\left\| \sqrt{\frac{\beta_3 \mathcal{H}_q \bar{j}_0}{h^s}}^{\alpha} [\![\boldsymbol{u}]\!]\cdot\boldsymbol{t}_0\nu_\alpha^-\right\|^2_{\mathrm{L}^2(\partial\mathcal{A}_e)}\right] \times \\
\sum_{e'} & \left[\left\| \sqrt{\mathcal{H}_n \bar{j}_0}^{\gamma\delta} \frac{1}{2}\left(\boldsymbol{\varphi}_{0,\gamma}\cdot\delta\boldsymbol{u}_{,\delta} + \delta\boldsymbol{u}_{,\gamma}\cdot\boldsymbol{\varphi}_{0,\delta}\right)\right\|^2_{\mathrm{L}^2(\partial\mathcal{A}_{e'})} + \right. \\
& \left\| \sqrt{\mathcal{H}_m \bar{j}_0}^{\gamma\delta} \left(\boldsymbol{\varphi}_{0,\gamma}\cdot\delta\boldsymbol{\Delta t}_{,\delta} + \delta\boldsymbol{u}_{,\gamma}\cdot\boldsymbol{t}_{0,\delta}\right)\right\|^2_{\mathrm{L}^2(\partial\mathcal{A}_{e'})} + \\
& \frac{1}{2}\left\| \sqrt{\frac{\beta_2 \mathcal{H}_n \bar{j}_0}{h^s}}^{\gamma\delta} [\![\delta\boldsymbol{u}]\!]\cdot\boldsymbol{\varphi}_{0,\delta}\nu_\gamma^-\right\|^2_{\mathrm{L}^2(\partial\mathcal{A}_{e'})} + \\
& \frac{1}{2}\left\| \sqrt{\frac{\beta_1 \mathcal{H}_m \bar{j}_0}{h^s}}^{\gamma\delta} [\![\delta\boldsymbol{\Delta t}]\!]\cdot\boldsymbol{\varphi}_{0,\delta}\nu_\gamma^-\right\|^2_{\mathrm{L}^2(\partial\mathcal{A}_{e'})} + \\
& \left. \frac{1}{2}\left\| \sqrt{\frac{\beta_3 \mathcal{H}_q \bar{j}_0}{h^s}}^{\gamma} [\![\delta\boldsymbol{u}]\!]\cdot\boldsymbol{t}_0\nu_\gamma^-\right\|^2_{\mathrm{L}^2(\partial\mathcal{A}_{e'})}\right], \qquad \text{(B.49)}
\end{aligned}
$$

which can be written as,

$$
|a_l(\boldsymbol{u}_h, \delta\boldsymbol{u})|^2 \leq C^k(\beta)\,|||\boldsymbol{u}|||^2\,|||\delta\boldsymbol{u}|||^2\,, \qquad \text{(B.50)}
$$

for all $\boldsymbol{u}$ satisfying the essential boundary conditions and where C^k depends only on the degree of $\boldsymbol{u}$. The Eq. (B.50) corresponds to the upper bound given by the Eq. (4.156)

B.4.2 Lower bound of the bilinear form

The following relation is used in order to obtain a lower bound of the bilinear form,

$$
\begin{aligned}
a_l(\boldsymbol{u},\boldsymbol{u}) = &\sum_e \left\| \sqrt{\mathcal{H}_n \bar{j}_0}^{\alpha\beta} \tfrac{1}{2}\left(\boldsymbol{\varphi}_{0,\alpha}\cdot\boldsymbol{u}_{,\beta}+\boldsymbol{u}_{,\alpha}\cdot\boldsymbol{\varphi}_{0,\beta}\right)\right\|^2_{\mathrm{L}^2(\mathcal{A}_e)} + \\
&\sum_e \left\| \sqrt{\mathcal{H}_m \bar{j}_0}^{\alpha\beta} \left(\boldsymbol{\varphi}_{0,\alpha}\cdot\boldsymbol{\Delta t}_{,\beta}+\boldsymbol{u}_{,\alpha}\cdot\boldsymbol{t}_{0,\beta}\right)\right\|^2_{\mathrm{L}^2(\mathcal{A}_e)} + \\
&2\sum_s \int_s [\![\boldsymbol{u}]\!]\cdot\boldsymbol{\varphi}_{0,\gamma}\left\langle \left(\boldsymbol{\varphi}_{0,\alpha}\cdot\boldsymbol{u}_{,\beta}+\boldsymbol{u}_{,\alpha}\cdot\boldsymbol{\varphi}_{0,\beta}\right)\mathcal{H}_n^{\alpha\beta\gamma\delta}\bar{j}_0\right\rangle \nu^-_\delta\, d\partial\mathcal{A} \\
&+\sum_s \left\| \sqrt{\frac{\beta_2 \mathcal{H}_n \bar{j}_0}{h^s}}^{\gamma\delta} \boldsymbol{\varphi}_{0,\gamma}\cdot[\![\boldsymbol{u}]\!]\nu^-_\delta \right\|^2_{\mathrm{L}^2(s)} + \\
&2\sum_s \int_s [\![\boldsymbol{\Delta t}]\!]\cdot\boldsymbol{\varphi}_{0,\gamma}\left\langle \left(\boldsymbol{\varphi}_{0,\alpha}\cdot\boldsymbol{\Delta t}(\boldsymbol{u})_{,\beta}+\boldsymbol{u}_{,\alpha}\cdot\boldsymbol{t}_{0,\beta}\right)\mathcal{H}_m^{\alpha\beta\gamma\delta}\bar{j}_0\right\rangle \nu^-_\delta\, d\partial\mathcal{A} \\
&+\sum_s \left\| \sqrt{\frac{\beta_1 \mathcal{H}_m \bar{j}_0}{h^s}}^{\gamma\delta} \boldsymbol{\varphi}_{0,\gamma}\cdot[\![\boldsymbol{\Delta t}(\boldsymbol{u})]\!]\nu^-_\delta \right\|^2_{\mathrm{L}^2(s)} + \\
&+\sum_s \left\| \sqrt{\frac{\beta_3 \mathcal{H}_q \bar{j}_0}{h^s}}^{\gamma\delta} \boldsymbol{t}_0\cdot[\![\boldsymbol{u}]\!]\nu^-_\delta \right\|^2_{\mathrm{L}^2(s)} .
\end{aligned}
\tag{B.51}
$$

Then, the product of $\mathbf{L}^2$-norms with constants C_1^k and C_2^k depending on the degree of $\boldsymbol{u}$ is used to bound the remaining interface integral (see Eq. (B.42)), which gives,

$$
\begin{aligned}
a_l(\boldsymbol{u},\boldsymbol{u}) \geq \quad & \sum_e \left\| \sqrt{\mathcal{H}_n \bar{j}_0}^{\alpha\beta} \frac{1}{2}\left(\boldsymbol{\varphi}_{0,\alpha}\cdot\boldsymbol{u}_{,\beta}+\boldsymbol{u}_{,\alpha}\cdot\boldsymbol{\varphi}_{0,\beta}\right)\right\|^2_{\mathrm{L}^2(\mathcal{A}_e)} + \\
& \sum_e \left\| \sqrt{\mathcal{H}_m \bar{j}_0}^{\alpha\beta} \left(\boldsymbol{\varphi}_{0,\alpha}\cdot\boldsymbol{\Delta t}_{,\beta}+\boldsymbol{u}_{,\alpha}\cdot\boldsymbol{t}_{0,\beta}\right)\right\|^2_{\mathrm{L}^2(\mathcal{A}_e)} - \\
& \frac{2\sqrt{2}C_n^k}{\sqrt{\beta_2}} \sum_e \left\| \sqrt{\mathcal{H}_n \bar{j}_0}^{\alpha\beta} \frac{1}{2}\left(\boldsymbol{\varphi}_{0,\alpha}\cdot\boldsymbol{u}_{,\beta}+\boldsymbol{u}_{,\alpha}\cdot\boldsymbol{\varphi}_{0,\beta}\right)\right\|_{\mathrm{L}^2(\mathcal{A}_e)} \\
& \qquad \times \left\| \sqrt{\frac{\beta_2 \mathcal{H}_n \bar{j}_0}{2h^s}}^{\gamma\delta} [\![\boldsymbol{u}]\!]\cdot\boldsymbol{\varphi}_{0,\delta}\nu_\gamma^- \right\|_{\mathrm{L}^2(\partial\mathcal{A}_e)} - \\
& \frac{2\sqrt{2}C_m^k}{\sqrt{\beta_1}} \sum_e \left\| \sqrt{\mathcal{H}_m \bar{j}_0}^{\alpha\beta} \left(\boldsymbol{\varphi}_{0,\alpha}\cdot\boldsymbol{\Delta t}_{,\beta}+\boldsymbol{u}_{,\alpha}\cdot\boldsymbol{t}_{0,\beta}\right)\right\|_{\mathrm{L}^2(\mathcal{A}_e)} \\
& \qquad \times \left\| \sqrt{\frac{\beta_1 \mathcal{H}_m \bar{j}_0}{2h^s}}^{\gamma\delta} [\![\boldsymbol{\Delta t}]\!]\cdot\boldsymbol{\varphi}_{0,\delta}\nu_\gamma^- \right\|_{\mathrm{L}^2(\partial\mathcal{A}_e)} + \\
& \sum_e \left\| \sqrt{\frac{\beta_2 \mathcal{H}_n \bar{j}_0}{2h^s}}^{\gamma\delta} \boldsymbol{\varphi}_{0,\gamma}\cdot[\![\boldsymbol{u}]\!]\nu_\delta^- \right\|^2_{\mathrm{L}^2(\partial\mathcal{A}_e)} + \\
& \sum_e \left\| \sqrt{\frac{\beta_1 \mathcal{H}_m \bar{j}_0}{2h^s}}^{\gamma\delta} \boldsymbol{\varphi}_{0,\gamma}\cdot[\![\boldsymbol{\Delta t}(\boldsymbol{u})]\!]\nu_\delta^- \right\|^2_{\mathrm{L}^2(\partial\mathcal{A}_e)} + \\
& \sum_s \left\| \sqrt{\frac{\beta_3 \mathcal{H}_q \bar{j}_0}{2h^s}}^{\gamma} \boldsymbol{t}_0\cdot[\![\boldsymbol{u}]\!]\nu_\gamma^- \right\|^2_{\mathrm{L}^2(s)} .
\end{aligned}
\tag{B.52}
$$

Finally, the recourse to the ε-inequality[3] applied to Eq. (B.52) provides the lower bound

[3] $\forall\varepsilon>0 : |ab| \leq \frac{\varepsilon}{2}a^2 + \frac{1}{2\varepsilon}b^2$ or $\forall\varepsilon>0 : |ab| \leq \varepsilon a^2 + \frac{1}{4\varepsilon}b^2$.

of the bilinear form,

$$
\begin{aligned}
a(\boldsymbol{u},\boldsymbol{u}) \;\geq\; & (1-\varepsilon_n)\sum_e \left\| \sqrt{\mathcal{H}_n \bar{j}_0}^{\alpha\beta} \frac{1}{2}\left(\boldsymbol{\varphi}_{0,\alpha}\cdot\boldsymbol{u}_{,\beta}+\boldsymbol{u}_{,\alpha}\cdot\boldsymbol{\varphi}_{0,\beta}\right)\right\|^2_{\mathrm{L}^2(\mathcal{A}_e)} + \\
& (1-\varepsilon_m)\sum_e \left\| \sqrt{\mathcal{H}_m \bar{j}_0}^{\alpha\beta} \left(\boldsymbol{\varphi}_{0,\alpha}\cdot\boldsymbol{\Delta t}_{,\beta}+\boldsymbol{u}_{,\alpha}\cdot\boldsymbol{t}_{0,\beta}\right)\right\|^2_{\mathrm{L}^2(\mathcal{A}_e)} + \\
& \left(1-2\frac{C_n^{k\,2}}{\varepsilon_n\beta_2}\right)\sum_e \left\| \sqrt{\frac{\beta_2\mathcal{H}_n\bar{j}_0}{2h^s}}^{\gamma\delta} \boldsymbol{\varphi}_{0,\gamma}\cdot[\![\boldsymbol{u}]\!]\,\nu^-_\delta\right\|^2_{\mathrm{L}^2(\partial\mathcal{A}_e)} + \\
& \left(1-2\frac{C_m^{k\,2}}{\varepsilon_m\beta_1}\right)\sum_e \left\| \sqrt{\frac{\beta_1\mathcal{H}_m\bar{j}_0}{2h^s}}^{\gamma\delta} \boldsymbol{\varphi}_{0,\gamma}\cdot[\![\boldsymbol{\Delta t}(\boldsymbol{u})]\!]\,\nu^-_\delta\right\|^2_{\mathrm{L}^2(\partial\mathcal{A}_e)} + \\
& \sum_e \left\| \sqrt{\frac{\beta_3\mathcal{H}_s\bar{j}_0}{2h^s}}^{\gamma} \boldsymbol{t}_0\cdot[\![\boldsymbol{u}]\!]\,\nu^-_\gamma\right\|^2_{\mathrm{L}^2(\partial\mathcal{A}_e)}, \qquad \text{(B.53)}
\end{aligned}
$$

for all $\boldsymbol{u}$ satisfying the essential boundary conditions. The lower bound (B.53) corresponds to the definition given in Section 4.4 by the Eq. (4.157)

B.4.3 Proof of the convergence in the energy-norm

The convergence rate of the problem is established by calculating the error between the finite element solution and the interpolant $\boldsymbol{u}^k$ of the exact solution $\boldsymbol{u}$ in the same space of functions of polynomial degree k. If both $\boldsymbol{u}$ and $\boldsymbol{u}^k$ satisfy the essential boundary conditions, the definition of $\boldsymbol{u}^k$ is,

$$
\int_{\mathcal{A}_h}\left(\boldsymbol{u}-\boldsymbol{u}^k\right)\cdot\delta\boldsymbol{u}\,\bar{j}_0 d\mathcal{A} = 0 \;\;\forall\delta\boldsymbol{u}\,, \qquad \text{(B.54)}
$$

for all $\delta\boldsymbol{u}$ satisfying the essential boundary conditions. The definition of the error is,

$$
\boldsymbol{e} \;=\; \boldsymbol{u}_h-\boldsymbol{u}\,, \qquad \text{(B.55)}
$$

where the prescribed displacement on $\partial_U\mathcal{A}$ and the prescribed normal director on $\partial_T\mathcal{A}$ are strictly equal to zero. Furthermore, the error on the exact solution interpolant reads,

$$
\boldsymbol{e}^k = \boldsymbol{u}_h-\boldsymbol{u}^k \qquad \text{(B.56)}
$$

As the terms (4.148) are by definition linear, having recourse to Eqs. (4.156) and (4.158) it comes, using the orthogonality relation (4.152) ,

$$
\begin{aligned}
C_2\left|\left|\left|\boldsymbol{e}^k\right|\right|\right|^2 &\leq a\left(\boldsymbol{u}_h-\boldsymbol{u}^k,\boldsymbol{u}_h-\boldsymbol{u}^k\right)\\
&\leq a\left(\boldsymbol{u}_h-\boldsymbol{u},\boldsymbol{u}_h-\boldsymbol{u}^k\right)+a\left(\boldsymbol{u}-\boldsymbol{u}^k,\boldsymbol{u}_h-\boldsymbol{u}^k\right)\\
&\leq C_1\left|\left|\left|\boldsymbol{u}-\boldsymbol{u}^k\right|\right|\right|\left|\left|\left|\boldsymbol{u}_h-\boldsymbol{u}^k\right|\right|\right| = C_1\left|\left|\left|\boldsymbol{u}-\boldsymbol{u}^k\right|\right|\right|\left|\left|\left|\boldsymbol{e}^k\right|\right|\right|, \qquad \text{(B.57)}
\end{aligned}
$$

Afterward, the error resulting from the discontinuous Galerkin method is calculated by bounding the terms of $\left|\left|\left|\boldsymbol{u}-\boldsymbol{u}^k\right|\right|\right|$. Giving ${}_I{}^{\alpha\beta\gamma\delta}$ the unit forth order tensor, a bound of the membrane energy term is,

$$\begin{aligned}
&\left\| \sqrt{\mathcal{H}_n \underline{j_0}}^{\alpha\beta} \tfrac{1}{2} \left(\boldsymbol{\varphi}_{0,\alpha} \cdot \left(\boldsymbol{u}_{,\beta} - \boldsymbol{u}^k_{,\beta} \right) + \left(\boldsymbol{u}_{,\alpha} - \boldsymbol{u}^k_{,\alpha} \right) \cdot \boldsymbol{\varphi}_{0,\beta} \right) \right\|^2_{\mathrm{L}^2(\mathcal{A}_e)} \leq \\
&C_{n1} \left\| \sqrt{I}^{\alpha\beta} \boldsymbol{\varphi}_{0,\alpha} \cdot \left(\boldsymbol{u}_{,\beta} - \boldsymbol{u}^k_{,\beta} \right) \right\|^2_{\mathrm{L}^2(\mathcal{A}_e)} \leq \\
&2C_{n1} \left[\left\| \sqrt{I}^{\alpha\beta} \left(\boldsymbol{\varphi}_{0,\alpha} \cdot \left(\boldsymbol{u} - \boldsymbol{u}^k \right) \right)_{,\beta} \right\|^2_{\mathrm{L}^2(\mathcal{A}_e)} + \left\| \sqrt{I}^{\alpha\beta} \boldsymbol{\varphi}_{0,\alpha\beta} \cdot \left(\boldsymbol{u} - \boldsymbol{u}^k \right) \right\|^2_{\mathrm{L}^2(\mathcal{A}_e)} \right] \\
&\leq 2C_{n2} \left\| \sqrt{\mathrm{I}}^{\alpha} \boldsymbol{\varphi}_{0,\alpha} \cdot \left(\boldsymbol{u} - \boldsymbol{u}^k \right) \right\|^2_{\mathrm{H}^1(\mathcal{A}_e)} + 2C_{n1} \left\| \sqrt{I}^{\alpha\beta} \boldsymbol{\varphi}_{0,\alpha\beta} \cdot \left(\boldsymbol{u} - \boldsymbol{u}^k \right) \right\|^2_{\mathrm{L}^2(\mathcal{A}_e)} \\
&\leq C_{n3} \left(\left\| \boldsymbol{u} - \boldsymbol{u}^k \right\|^2_{\mathbf{H}^1(\mathcal{A}_e)} + \left\| \boldsymbol{u} - \boldsymbol{u}^k \right\|^2_{\mathbf{L}^2(\mathcal{A}_e)} \right) \leq \\
&C_{n4} h^{s2k} \left| \boldsymbol{u} \right|^2_{\mathbf{H}^{k+1}(\mathcal{A}_e)} + C_{n5} h^{s2k+2} \left| \boldsymbol{u} \right|^2_{\mathbf{H}^{k+1}(\mathcal{A}_e)} \leq C_n h^{s2k} \left| \boldsymbol{u} \right|^2_{\mathbf{H}^{k+1}(\mathcal{A}_e)} ,
\end{aligned} \tag{B.58}$$

as $\mathcal{H}_n$ is positive and symmetric by nature and where in Eq. (B.58) the derivation by part, the property $(a+b)^2 < 2a^2 + 2b^2$, the definition of the Sobolev space ($\|a_{,\alpha}\|_{\mathrm{H}^0(\mathcal{A}_e)} \leq \|a\|_{\mathrm{H}^1(\mathcal{A}_e)}$), the property $\|\boldsymbol{a} \cdot \boldsymbol{b}\| \leq \|\boldsymbol{a}\| \, \|\boldsymbol{b}\|$, the basic error estimates of interpolation theory[4] as well as the assumption $h^s < 1$ are used. Therefore these assumptions lead to considers that the surface is continuous and regular (no singular point).

The same argumentation holds to bound the bending term which reads,

$$\begin{aligned}
&\left\| \sqrt{\mathcal{H}_m \underline{j_0}}^{\alpha\beta} \left(\boldsymbol{\varphi}_{0,\alpha} \cdot \boldsymbol{\Delta t}_{,\beta} \left(\boldsymbol{u} - \boldsymbol{u}^k \right) + \left(\boldsymbol{u}_{,\alpha} - \boldsymbol{u}^k_{,\alpha} \right) \cdot \boldsymbol{t}_{0,\beta} \right) \right\|^2_{\mathrm{L}^2(\mathcal{A}_e)} \leq \\
&C_{m1} \left\| \boldsymbol{u} - \boldsymbol{u}^k \right\|^2_{\mathrm{H}^2(\mathcal{A}_e)} + C_{m2} \left\| \boldsymbol{u} - \boldsymbol{u}^k \right\|^2_{\mathrm{H}^1(\mathcal{A}_e)} + C_{m3} \left\| \boldsymbol{u} - \boldsymbol{u}^k \right\|^2_{\mathrm{L}^2(\mathcal{A}_e)}
\end{aligned} \tag{B.59}$$

where the definition (4.104) of $\boldsymbol{\Delta t}_{,\gamma}$ is used. Having recourse to the error estimates from interpolation theory and the fact that $h^s < 1$, Eq. (B.59) becomes,

$$\begin{aligned}
&\left\| \sqrt{\mathcal{H}_m \underline{j_0}}^{\alpha\beta} \left(\boldsymbol{\varphi}_{0,\alpha} \cdot \boldsymbol{\Delta t}_{,\beta} \left(\boldsymbol{u} - \boldsymbol{u}^k \right) + \left(\boldsymbol{u}_{,\alpha} - \boldsymbol{u}^k_{,\alpha} \right) \cdot \boldsymbol{t}_{0,\beta} \right) \right\|^2_{\mathrm{L}^2(\mathcal{A}_e)} \leq \\
&C_m h^{s2k-2} \left| \boldsymbol{u} \right|^2_{\mathbf{H}^{k+1}(\mathcal{A}_e)} .
\end{aligned} \tag{B.60}$$

Now the bound of the different interface terms are investigated. For the membrane inter-

[4] Given a mapping $\boldsymbol{u} \in \mathbf{H}^{k+1}(\mathcal{A}_e)$, then $\forall \boldsymbol{u}^k \in \mathbb{P}^k$ interpolating $\boldsymbol{u}$ in $\mathcal{A}_e$: $\left\| \boldsymbol{u} - \boldsymbol{u}^k \right\|_{\mathbf{H}^q(\mathcal{A}_e)} \leq C_i h^{sk+1-q} \left| \boldsymbol{u} \right|_{\mathbf{H}^{k+1}(\mathcal{A}_e)} \; \forall 0 \leq q \leq k+1$, with C_i independent of h^s, the size of $\mathcal{A}_e$ [140].

face terms one has,

$$\begin{gathered}
\tfrac{1}{2}\sum_e \left\| \sqrt{\frac{\beta_2 \mathcal{H}_n \bar{j}_0}{h^s}}^{\alpha\beta} \boldsymbol{\varphi}_{0,\alpha} \cdot [\![\boldsymbol{u} - \boldsymbol{u}^k]\!] \, \nu_\beta^- \right\|^2_{\mathbf{L}^2(\partial\mathcal{A}_e)} \leq \\
\sum_e \left\| \sqrt{\frac{\beta_2 \mathcal{H}_n \bar{j}_0}{h^s}}^{\alpha\beta} \boldsymbol{\varphi}_{0,\alpha} \cdot \left(\boldsymbol{u} - \boldsymbol{u}^k \right) \nu_\beta^- \right\|^2_{\mathbf{L}^2(\partial\mathcal{A}_e)} \leq \\
\sum_e \tfrac{C_{nI1}\beta_2}{h^s} \left\| \sqrt{\mathrm{I}}^\alpha \left(\boldsymbol{u} - \boldsymbol{u}^k \right) \right\|^2_{\mathbf{L}^2(\partial\mathcal{A}_e)} \leq \\
\sum_e \tfrac{C_{nI2}\beta_2}{h^{s4}} \left\| \boldsymbol{u} - \boldsymbol{u}^k \right\|^2_{\mathbf{L}^2(\mathcal{A}_e)} \leq \\
\sum_e C_{nI} \beta_2 h^{s2k} \left| \boldsymbol{u} \right|^2_{\mathbf{H}^{k+1}(\mathcal{A}_e)} ,
\end{gathered} \tag{B.61}$$

as $\mathcal{H}_n$ is positive and symmetric by nature, and where the property $\|\boldsymbol{a}\cdot\boldsymbol{b}\| \leq \|\boldsymbol{a}\|\|\boldsymbol{b}\|$, the trace inequality[5], the definition of Sobolev spaces (*i.e.* $\|\boldsymbol{\nabla}\boldsymbol{x}\|_{\mathbf{H}^0(\mathcal{A}_e)} \leq \|\boldsymbol{x}\|_{\mathbf{H}^1(\mathcal{A}_e)}$), the inverse inequality[6] as well as the the interpolation theory are used. Notice that h^s is assumed to be constant in this development. Similarly, for the bending interface terms the Eqs. (4.12) and (4.103) imply, $[\![\boldsymbol{\Delta t}]\!] \cdot \boldsymbol{\varphi}_{0,\alpha} = -[\![\boldsymbol{u}_{,\alpha}]\!] \cdot \boldsymbol{t}_0$, and

$$\begin{gathered}
\tfrac{1}{2}\sum_e \left\| \sqrt{\frac{\beta_1 \mathcal{H}_m \bar{j}_0}{h^s}}^{\alpha\beta} \boldsymbol{\varphi}_{0,\alpha} \cdot [\![\boldsymbol{\Delta t} \left(\boldsymbol{u} - \boldsymbol{u}^k \right)]\!] \, \nu_\beta^- \right\|^2_{\mathrm{L}^2(\partial\mathcal{A}_e)} \leq \\
\sum_e \left\| \sqrt{\frac{\beta_1 \mathcal{H}_m \bar{j}_0}{h^s}}^{\alpha\beta} \boldsymbol{t}_0 \cdot \left(\boldsymbol{u}_{,\alpha} - \boldsymbol{u}^k_{,\alpha} \right) \nu_\beta^- \right\|^2_{\mathrm{L}^2(\partial\mathcal{A}_e)} \leq \\
\sum_e \tfrac{C_{mI1}\beta_1}{h^s} \left\| \sqrt{\mathrm{I}}^\alpha \left(\boldsymbol{u}_{,\alpha} - \boldsymbol{u}^k_{,\alpha} \right) \right\|^2_{\mathbf{L}^2(\partial\mathcal{A}_e)} \leq \\
\sum_e \tfrac{C_{mI2}\beta_1}{h^{s2}} \left\| \sqrt{\mathrm{I}}^\alpha \left(\boldsymbol{u}_{,\alpha} - \boldsymbol{u}^k_{,\alpha} \right) \right\|^2_{\mathbf{L}^2(\mathcal{A}_e)} + \sum_e C_{mI3}\beta_1 \left\| \sqrt{I}^{\alpha\beta} \left(\boldsymbol{u}_{,\alpha\beta} - \boldsymbol{u}^k_{,\alpha\beta} \right) \right\|^2_{\mathbf{L}^2(\mathcal{A}_e)} \leq \\
\sum_e \tfrac{C_{mI2}\beta_1}{h^{s2}} \left\| \boldsymbol{u} - \boldsymbol{u}^k \right\|^2_{\mathbf{H}^1(\mathcal{A}_e)} + \sum_e C_{mI3}\beta_1 \left\| \boldsymbol{u} - \boldsymbol{u}^k \right\|^2_{\mathbf{H}^2(\mathcal{A}_e)} \leq \\
\sum_e \tfrac{C_{mI4}\beta_1}{h^{s4}} \left\| \boldsymbol{u} - \boldsymbol{u}^k \right\|^2_{\mathbf{L}^2(\mathcal{A}_e)} \leq \\
\sum_e C_{mI} \beta_1 h^{s2k-2} \left| \boldsymbol{u} \right|^2_{\mathbf{H}^{k+1}(\mathcal{A}_e)} ,
\end{gathered} \tag{B.62}$$

and finally, for the shearing interface term it comes,

$$\frac{1}{2}\sum_e \left\| \sqrt{\frac{\beta_3 \mathcal{H}_q \bar{j}_0}{h^s}}^{\alpha} \boldsymbol{t}_0 \cdot [\![\boldsymbol{u}]\!] \, \nu_\beta^- \right\|^2_{\mathrm{L}^2(\partial\mathcal{A}_e)} \leq \sum_e C_{lI} \beta_3 h^{s2k} \left| \boldsymbol{u} \right|^2_{\mathbf{H}^{k+1}(\mathcal{A}_e)} . \tag{B.63}$$

[5] $\forall \boldsymbol{v} \in \mathrm{H}^1(\mathcal{A}_e) \;\; \exists C_T > 0 : \|\boldsymbol{v}\|^2_{\mathbf{L}^2(\partial\mathcal{A}_e)} \leq \frac{C_T}{h^s} \|\boldsymbol{v}\|^2_{\mathbf{L}^2(\mathcal{A}_e)} + C_T h^s \|\boldsymbol{v}_{,\alpha}\|^2_{\mathbf{L}^2(\mathcal{A}_e)}$.

[6] $\forall m \geq l \;\; \exists C_I > 0 : \;\; \|\boldsymbol{v}\|_{\mathbf{H}^m(\mathcal{A}_e)} \leq C_I h^{sl-m} \|\boldsymbol{v}\|_{\mathbf{H}^l(\mathcal{A}_e)}$.

Combining the results of Eqs. (B.58-B.63) the Eq. (B.57) is formulated as,

$$\left|\left|\left| e^k \right|\right|\right| \leq \sum_e C h^{sk-1} \left| \boldsymbol{u} \right|_{\mathbf{H}^{k+1}(\mathcal{A}_e)} . \tag{B.64}$$

The governing equation involving high order derivatives leading, as expected, to an order of convergence lower than the degree of the polynomial approximation and thus implies to have recourse to at least quadratic interpolation.

B.4.4 Proof of the convergence in the $\mathbf{L}^2$-norm

A proper elliptic regularity, a cubic approximation of the problem, as well as pure Dirichlet boundary conditions are assumed to prove the optimal-convergence rate in the $\mathbf{L}^2$-norm. First, the notations are simplified by formulating the linear dependency of vector $\boldsymbol{\Delta t}$ with $\boldsymbol{u}_{,\alpha}$ explicitly from Eq. (4.103), which gives

$$\boldsymbol{\Delta t} = \tilde{\boldsymbol{\Delta}}\mathbf{t}_\alpha \boldsymbol{u}_{,\alpha} \text{ with,} \tag{B.65}$$

$$\tilde{\boldsymbol{\Delta}}\mathbf{t}_\alpha = \frac{e_{\beta\alpha 3}}{j_0}\left[\tilde{\boldsymbol{\varphi}}_{0,\beta} - \boldsymbol{t}_0 \otimes \left(\boldsymbol{t}_0 \wedge \boldsymbol{\varphi}_{0,\beta}\right)\right] , \tag{B.66}$$

where $\tilde{\boldsymbol{\Delta}}\mathbf{t}_\alpha$ is a second-order tensor and $\tilde{\boldsymbol{\varphi}}_{0,\beta}$ is the skew rotation matrix associated to $\boldsymbol{\varphi}_{0,\beta}$. The assumption of pure Dirichlet boundary conditions leads to,

$$\partial_U \mathcal{A}_h = \partial_T \mathcal{A}_h = \partial \mathcal{A}_h \text{ and } \partial_N \mathcal{A}_h = \partial_M \mathcal{A}_h = \emptyset , \tag{B.67}$$

$$\boldsymbol{u} = \boldsymbol{\Delta t} = \mathbf{0} \text{ on } \partial \mathcal{A}_h . \tag{B.68}$$

The demonstration of the consistency of the formulation in Section 4.4.1 leads to the fact that the exact deformation fields $\boldsymbol{u}$, satisfying the essential boundary conditions, satisfies the bilinear form (4.148). Furthermore, under pure Dirichlet boundary conditions, $b(\delta\boldsymbol{u}) = b_{\text{ext}}(\delta\boldsymbol{u}) + b_{\text{bound}}(\delta\boldsymbol{u})$ can be formulated using (B.65) and (B.68),

$$b^{\boldsymbol{n}^{\mathcal{A}}, \tilde{\boldsymbol{m}}^{\mathcal{A}}}(\delta\boldsymbol{u}) = \int_{\mathcal{A}_h} \left[\bar{j}_0 \boldsymbol{n}^{\mathcal{A}} - \left(\bar{j}_0 \tilde{\boldsymbol{\Delta}}\mathbf{t}_\mu^T \tilde{\boldsymbol{m}}^{\mathcal{A}} \right)_{,\mu} \right] \cdot \delta\boldsymbol{u} d\mathcal{A} . \tag{B.69}$$

Let $\boldsymbol{u}_d$, satisfying the essential boundary conditions, be the exact solution of a problem governed by the system (4.148) for a given pair $\left(\boldsymbol{n}_d^{\mathcal{A}}, \tilde{\boldsymbol{m}}_d^{\mathcal{A}}\right)$. Therefore, considering the error $\boldsymbol{e}$ (B.55), satisfying also the essential boundary conditions, as the virtual displacements yields

$$\begin{aligned} b^{\boldsymbol{n}^{\mathcal{A}}, \tilde{\boldsymbol{m}}^{\mathcal{A}}}(\boldsymbol{e}) &= a(\boldsymbol{u}_d, \boldsymbol{e}) = a\left(\boldsymbol{u}_d - \boldsymbol{u}_d^k, \boldsymbol{e}\right) + a\left(\boldsymbol{u}_d^k, \boldsymbol{e}\right) \\ &= a\left(\boldsymbol{u}_d - \boldsymbol{u}_d^k, \boldsymbol{e}\right) + a\left(\boldsymbol{e}, \boldsymbol{u}_d^k\right) \\ &= a\left(\boldsymbol{u}_d - \boldsymbol{u}_d^k, \boldsymbol{e}\right) + a\left(\boldsymbol{u}_h - \boldsymbol{u}, \boldsymbol{u}_d^k\right) = a\left(\boldsymbol{u}_d - \boldsymbol{u}_d^k, \boldsymbol{e}\right) \\ &= a\left(\boldsymbol{u}_d - \boldsymbol{u}_d^k, \boldsymbol{u}_h - \boldsymbol{u}^k\right) + a\left(\boldsymbol{u}_d - \boldsymbol{u}_d^k, \boldsymbol{u}^k - \boldsymbol{u}\right) \end{aligned} \tag{B.70}$$

where the $\boldsymbol{u}_d^k$ is the interpolation of $\boldsymbol{u}_d$ satisfies the essential boundary conditions, and where the recourse to the symmetric nature of $a(,)$ as well as the orthogonality relation (4.152) are used. Using the Eq. (4.156) with the particular choice of the adjoint problem such that,

$$\bar{j}_0 \boldsymbol{n}^{\mathcal{A}} - \left(\bar{j}_0 \tilde{\boldsymbol{\Delta}}\mathbf{t}_\mu^T \tilde{\boldsymbol{m}}^{\mathcal{A}} \right)_{,\mu} = \boldsymbol{e}\,, \tag{B.71}$$

enables rewriting (B.70) as

$$\|\boldsymbol{e}\|^2_{\mathbf{L}^2(\mathcal{A}_h)} \;\leq\; C^k(\beta) \left|\!\left|\!\left| \boldsymbol{u}_d - \boldsymbol{u}_d^k \right|\!\right|\!\right| \left[\;\left|\!\left|\!\left| \boldsymbol{e}^k \right|\!\right|\!\right| + \left|\!\left|\!\left| \boldsymbol{u}^k - \boldsymbol{u} \right|\!\right|\!\right| \;\right], \tag{B.72}$$

as all the terms involved satisfy the essential boundary conditions.

The theorems 5.1 and 5.4 presented in [147] allows establishing the convergence rate by bounding the term $\left|\!\left|\!\left| \boldsymbol{u}_d - \boldsymbol{u}_d^k \right|\!\right|\!\right|$. Toward this end, these theorems are particularized to a problem under pure Dirichlet boundary conditions, and thus summarized as:

Theorem 1 *Consider the problem*

$$\mathbf{A}\cdot\boldsymbol{u} \;=\; \boldsymbol{f} \in \mathcal{A}\,, \tag{B.73}$$

$$\mathbf{B}_i\cdot\boldsymbol{u} \;=\; \boldsymbol{g}_i \text{ on } \partial\mathcal{A} \qquad \text{for } i = 0,1,...,m-1\,, \tag{B.74}$$

with the proper elliptic operator $\mathbf{A} \;:\; \mathcal{C}^\infty(\mathcal{A}) \to \mathbf{H}^{s-2m}(\mathcal{A})$ *and the operator* $\mathbf{B}_i \;:\; \mathcal{C}^\infty(\partial\mathcal{A}) \to \mathbf{H}^{s-i-1/2}(\partial\mathcal{A})$ *which respectively take the expression*

$$\mathbf{A}\cdot\boldsymbol{u} \;=\; \sum_{0\leq p,q\leq m} (-1)^p D^p \left(\mathbf{a}_{pq}(\xi^\alpha) D^q \boldsymbol{u} \right), \tag{B.75}$$

$$\mathbf{B}_i\cdot\boldsymbol{u} \;=\; \frac{\partial^i}{\partial\zeta^i}\boldsymbol{u}\,, \tag{B.76}$$

with ζ *the outer normal of* $\partial\mathcal{A}$*, and with*

$$D^p \;=\; \frac{\partial^{p_1+p_2}}{\partial\xi^{1p_1}\partial\xi^{2p_2}}\,, \quad p_1+p_2 = p\,. \tag{B.77}$$

Therefore, if $\boldsymbol{u} \in \mathbf{H}^{2m}(\mathcal{A})$ *and if* $\mathbf{A}\cdot\boldsymbol{u} \in \mathbf{H}^{p-2m}(\mathcal{A})$, $\mathbf{B}_i\cdot\boldsymbol{u} \in \mathbf{H}^{p-i-1/2}(\partial\mathcal{A})$*, one has* $\forall p \geq 2m$

$$\|\boldsymbol{u}\|_{\mathbf{H}^p(\mathcal{A})} \leq C^p \left\{ \|\mathbf{A}\cdot\boldsymbol{u}\|_{\mathbf{H}^{p-2m}(\mathcal{A})} + \sum_i \|\mathbf{B}_i\cdot\boldsymbol{u}\|_{\mathbf{H}^{p-i-1/2}(\partial\mathcal{A})} \right\}. \tag{B.78}$$

Notice that the use of this theorem limits the demonstration to a problem with a proper elliptic regularity, which can be easily proved only for particular cases like pure bending.

Then using Eq. (B.64) it comes,

$$\left|\!\left|\!\left| \boldsymbol{u}_d - \boldsymbol{u}_d^k \right|\!\right|\!\right| \leq \left\{ \begin{array}{ll} Ch^{s2} \left|\boldsymbol{u}_d\right|_{\mathbf{H}^4(\mathcal{A}_h)} & \text{if } k > 2 \\ Ch^s \left|\boldsymbol{u}_d\right|_{\mathbf{H}^4(\mathcal{A}_h)} & \text{if } k = 2 \end{array} \right., \tag{B.79}$$

where the result for $k=2$ is obtained following the argumentation of G. Wells *et al.* [257]. Thus, if the theorem 1 is applied to Eq. (B.79) with $m=2$, $p=4\geq 2m$, $\boldsymbol{f}=\boldsymbol{e}$ and $\boldsymbol{g}_i=0$, it comes

$$\left|\left|\left|\boldsymbol{u}_d-\boldsymbol{u}_d^k\right|\right|\right| \leq \begin{cases} C^r h^{s2}\left\|\boldsymbol{e}\right\|_{\mathbf{L}^2(\mathcal{A}_h)} & \text{if } k>2 \\ C^r h^{s}\left\|\boldsymbol{e}\right\|_{\mathbf{L}^2(\mathcal{A}_h)} & \text{if } k=2 \end{cases}. \tag{B.80}$$

Combining this last results with (B.64), the Eq. (B.72) reads

$$\left\|\boldsymbol{e}^k\right\|_{\mathbf{L}^2(\mathcal{A}_h)} \leq \begin{cases} \sum\limits_e C h^{sk+1}\left|\boldsymbol{u}\right|_{\mathbf{H}^{k+1}(\mathcal{A}_e)} & \text{if } k>2 \\ \sum\limits_e C h^{s2}\left|\boldsymbol{u}\right|_{\mathbf{H}^{3}(\mathcal{A}_e)} & \text{if } k=2 \end{cases} \tag{B.81}$$

Finally, using the triangular inequality one has $\left\|\boldsymbol{e}\right\|_{\mathbf{L}^2(\mathcal{A}_h)} \leq \left\|\boldsymbol{e}^k\right\|_{\mathbf{L}^2(\mathcal{A}_h)}$ (see G. Wells *et al.* [257] for details) and thus,

$$\left\|\boldsymbol{e}\right\|_{\mathbf{L}^2(\mathcal{A}_h)} \leq \begin{cases} \sum\limits_e C h^{sk+1}\left|\boldsymbol{u}\right|_{\mathbf{H}^{k+1}(\mathcal{A}_e)} & \text{if } k>2 \\ \sum\limits_e C h^{s2}\left|\boldsymbol{u}\right|_{\mathbf{H}^{3}(\mathcal{A}_e)} & \text{if } k=2 \end{cases} \tag{B.82}$$

Therefore the full-DG shell formulation is proved to have an optimal-convergence in the $\mathbf{L}^2$-norm if at least cubic elements are used. Nevertheless, it is shown in a numerical example of Section 4.6.1 that the optimal convergence rate is also observed for quadratic elements.

B.5 Expression of the elementary force vectors

In this section we provide the expression of the elementary force vectors of the non linear full-DG formulation of Kirchhoff-Love shells.

B.5.1 Bulk terms

We first present the vectors related to the bulk terms. In these ones, the integration on the surface is performed through a Gauss quadrature rule with (ξ_g^1,ξ_g^2) the coordinates of the Gauss points and w_g the corresponding weight. Using the developments provided in Section 4.5.1 the expressions of the elementary force vectors of the non-linear shell formulation are successively:

- Membrane term:

$$\begin{aligned} \sum_e \int_{\mathcal{A}_e} \bar{j}\boldsymbol{n}^\alpha \cdot \delta\boldsymbol{\varphi}_{,\alpha} d\mathcal{A} &= \sum_e \left[\int_{\mathcal{A}_e} \bar{j}\boldsymbol{n}^\alpha N^{\boldsymbol{\mu}}_{,\xi^\alpha}\left(\xi^1,\xi^2\right) d\mathcal{A}\right]\cdot \delta\boldsymbol{\varphi}^{\boldsymbol{\mu}} \\ &= \sum_e \boldsymbol{F}^e_{int\,n}{}^{\boldsymbol{\mu}} \cdot \delta\boldsymbol{\varphi}^{\boldsymbol{\mu}}, \end{aligned} \tag{B.83}$$

where,

$$\boldsymbol{F}^{e}_{int\,n}{}^{\boldsymbol{\mu}} = \sum_{g} w_g \bar{j}\left(\xi^1_g,\xi^2_g\right)\boldsymbol{n}^{\alpha}(\xi^1_g,\xi^2_g)N^{\boldsymbol{\mu}}_{,\xi^{\alpha}}\left(\xi^1_g,\xi^2_g\right), \tag{B.84}$$

is the elementary membrane internal forces vector.

- Bending term:

$$\int_{\bar{\mathcal{A}}_e} \bar{j}\tilde{\boldsymbol{m}}^{\alpha}(\boldsymbol{\varphi}_h)\cdot(\delta\boldsymbol{t}\lambda_h)_{,\alpha}\,d\mathcal{A} = \int_{\bar{\mathcal{A}}_e}\left[\bar{j}\lambda_h\left[\tilde{\boldsymbol{\Delta}}\mathbf{t}^{\boldsymbol{\mu}}_{,\alpha}\right]^T\cdot\tilde{\boldsymbol{m}}^{\alpha}d\mathcal{A}\right]\cdot\delta\boldsymbol{\varphi}^{\boldsymbol{\mu}}, \tag{B.85}$$

where,

$$\boldsymbol{F}^{e}_{int\,b}{}^{\boldsymbol{\mu}} = \sum_{g} w_g \bar{j}\left(\xi^1_g,\xi^2_g\right)\left[\tilde{\boldsymbol{\Delta}}\mathbf{t}^{\boldsymbol{\mu}}_{,\alpha}\left(\xi^1_g,\xi^2_g\right)\right]^T\cdot\tilde{\boldsymbol{m}}^{\alpha}\left(\xi^1_g,\xi^2_g\right) \tag{B.86}$$

Notice that in these expressions it has been supposed that the resultant membrane and bending stresses are computed thanks to the material law and that the variation of the normal vector in terms of nodal displacements is computed from,

$$\delta\boldsymbol{t} = \tilde{\boldsymbol{\Delta}}\mathbf{t}^{\boldsymbol{\mu}}\cdot\delta\boldsymbol{\varphi}^{\boldsymbol{\mu}}, \tag{B.87}$$

where $\tilde{\boldsymbol{\Delta}}\mathbf{t}^{\boldsymbol{\mu}}$ is a 3×3 matrix defined by,

$$\tilde{\boldsymbol{\Delta}}\mathbf{t}^{\boldsymbol{\mu}} = \frac{\varepsilon_{\alpha\beta 3}}{j}\left[\tilde{\boldsymbol{\varphi}}_{h,\alpha}-\boldsymbol{t}\otimes\left(\boldsymbol{t}\wedge\boldsymbol{\varphi}_{h,\alpha}\right)\right]N^{\boldsymbol{\mu}}_{,\xi^{\beta}}\left(\xi^1,\xi^2\right), \tag{B.88}$$

and where $\tilde{\boldsymbol{\varphi}}_{h,\alpha}$ is the skew rotation matrix[7] associated to $\boldsymbol{\varphi}_{h,\alpha}$. From these definitions the variation of the derivative of the normal unit vector in terms of displacements reads,

$$\delta\boldsymbol{t}_{,\alpha} = \tilde{\boldsymbol{\Delta}}\mathbf{t}^{\boldsymbol{\mu}}_{,\alpha}\cdot\delta\boldsymbol{\varphi}^{\boldsymbol{\mu}}, \tag{B.89}$$

where $\tilde{\boldsymbol{\Delta}}\mathbf{t}^{\boldsymbol{\mu}}_{,\alpha}$ is a 3×3 matrix defined as,

$$\begin{aligned}
\tilde{\boldsymbol{\Delta}}\mathbf{t}^{\boldsymbol{\mu}}_{,\alpha} = \frac{1}{j}\Big\{&\Big[\tilde{\boldsymbol{\varphi}}_{h,1\alpha}N^{\boldsymbol{\mu}}_{,\xi^2}\left(\xi^1,\xi^2\right)-\tilde{\boldsymbol{\varphi}}_{h,2}N^{\boldsymbol{\mu}}_{,\xi^1\xi^{\alpha}}\left(\xi^1,\xi^2\right)+\tilde{\boldsymbol{\varphi}}_{h,1}N^{\boldsymbol{\mu}}_{,\xi^2\xi^{\alpha}}\left(\xi^1,\xi^2\right)-\\
&\tilde{\boldsymbol{\varphi}}_{h,2\alpha}N^{\boldsymbol{\mu}}_{,\xi^1}\left(\xi^1,\xi^2\right)\Big]-\tilde{\boldsymbol{\Delta}}\mathbf{t}^{\boldsymbol{\mu}}\cdot\left[\boldsymbol{\varphi}_{h,1\alpha}\cdot\left(\boldsymbol{\varphi}_{h,2}\wedge\boldsymbol{t}\right)-\boldsymbol{\varphi}_{h,2\alpha}\cdot\left(\boldsymbol{\varphi}_{h,1}\wedge\boldsymbol{t}\right)\right]\\
&+\boldsymbol{t}\otimes\Big[-\left(\boldsymbol{\varphi}_{h,2}\wedge\boldsymbol{t}\right)N^{\boldsymbol{\mu}}_{,\xi^1\xi^{\alpha}}\left(\xi^1,\xi^2\right)+\left(\boldsymbol{\varphi}_{h,1}\wedge\boldsymbol{t}\right)N^{\boldsymbol{\mu}}_{,\xi^2\xi^{\alpha}}\left(\xi^1,\xi^2\right)-\\
&\left(\boldsymbol{t}\wedge\boldsymbol{\varphi}_{h,1\alpha}\right)N^{\boldsymbol{\mu}}_{,\xi^2}\left(\xi^1,\xi^2\right)+\left(\boldsymbol{t}\wedge\boldsymbol{\varphi}_{h,2\alpha}\right)N^{\boldsymbol{\mu}}_{,\xi^1}\left(\xi^1,\xi^2\right)\Big]\\
&+\boldsymbol{t}\otimes\left[\left[\tilde{\boldsymbol{\Delta}}\mathbf{t}^{\boldsymbol{\mu}}\right]^T\cdot\left[-\left(\boldsymbol{\varphi}_{h,1\alpha}\wedge\boldsymbol{\varphi}_{h,2}\right)+\left(\boldsymbol{\varphi}_{h,21}\wedge\boldsymbol{\varphi}_{h,1}\right)\right]\right]\\
&+\boldsymbol{t}_{,\alpha}\otimes\left[-\left(\boldsymbol{t}\wedge\boldsymbol{\varphi}_{h,1}\right)N^{\boldsymbol{\mu}}_{,\xi^2}\left(\xi^1,\xi^2\right)+\left(\boldsymbol{t}\wedge\boldsymbol{\varphi}_{h,2}\right)N^{\boldsymbol{\mu}}_{,\xi^1}\left(\xi^1,\xi^2\right)\right]\Big\}.
\end{aligned} \tag{B.90}$$

[7] Given $\boldsymbol{a}$ a 3-components vector, its associated 3×3 skew rotation matrix is $\begin{bmatrix} 0 & -a_3 & a_2 \\ a_3 & 0 & -a_1 \\ -a_2 & a_1 & 0 \end{bmatrix}$.

B.5.2 Interface terms

We discuss the implementation of the different interface elementary force vectors of the full-DG formulation of non-linear Kirchhoff-Love shells. In these ones, the integration on the curve is performed through a Gauss quadrature rule with (ξ_g^{s1}) the coordinate of the Gauss points and w_g the corresponding weight. Nevertheless, some quantities are computed on the corresponding point of the elements as depicted on Fig. B.1. Therefore at each coordinate

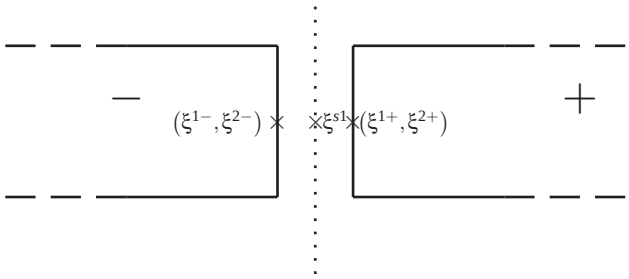

Figure B.1: Gauss integration on the interface is performed on a curve of coordinate ξ^{s1} but the different quantities are computed on (minus and plus) elements edges of coordinates $\left(\xi^{1\pm},\xi^{2\pm}\right)$. The symbol $\times$ marks a Gauss integration point of the interface. With a continuous method the three $\times$ are congruent and with a discontinuous method, they are very close.

(ξ_g^{s1}) of the interface it corresponds a point of coordinates $\left(\xi_g^{1-},\xi_g^{2-}\right)$ of the minus element and another one of coordinates $\left(\xi_g^{1+},\xi_g^{2+}\right)$ of the plus element. In the following we write $N^{\mu-}\left(\xi_g^{s1}\right)$ and $N^{\mu+}\left(\xi_g^{s1}\right)$ respectively the shape functions of minus and plus element of coordinates $\left(\xi^{1\pm},\xi^{2\pm}\right)$ evaluated at the point ξ_g^{s1}. Thus, these shape functions can be derived with respect to both coordinates ξ^1 and ξ^2. Once computed on elements, the quantities $\bullet$ are formulated in the interface convected basis using the push-forward tensor, defined by Eq. (4.181), and are then written $\widehat{\bullet}$. Furthermore, the Jacobian $\bar{j}$ is computed on the interface following Eq. (4.180). Defining $\delta\boldsymbol{\varphi}^s = \begin{bmatrix} \delta\boldsymbol{\varphi}^- \\ \delta\boldsymbol{\varphi}^+ \end{bmatrix}$ and using the developments provided in Section 4.5.1, the expressions of the interface elementary force vectors of the non-linear shell formulation are successively:

- Consistency membrane term:

$$\sum_s \int_s \langle \bar{j}\boldsymbol{n}^\alpha \rangle \cdot [\![\delta\boldsymbol{\varphi}]\!]\, \nu_\alpha^- d\partial\mathcal{A}_e \;=\; \sum_s \boldsymbol{F}^s_{int\,consn}{}^{\mu} \cdot \delta\boldsymbol{\varphi}^{s\mu}, \tag{B.91}$$

  where,

$$\boldsymbol{F}^s_{int\,consn}{}^{\mu} \;=\; \sum_g w_g \bar{j}\left(\xi_g^{s1}\right) \nu_\alpha^- \begin{bmatrix} -\left\langle \widehat{\boldsymbol{n}^\alpha} \right\rangle N^{\mu-}\left(\xi_g^{s1}\right) \\ \left\langle \widehat{\boldsymbol{n}^\alpha} \right\rangle N^{\mu+}\left(\xi_g^{s1}\right) \end{bmatrix}, \tag{B.92}$$

  is the elementary interface consistency membrane forces vector.

- Compatibility membrane term:

$$\sum_s \int_s [\![\boldsymbol{\varphi}_h]\!] \cdot \langle \delta(\bar{j}\boldsymbol{n}^\alpha)\rangle \nu_\alpha^- d\partial\mathcal{A}_e \;=\; \sum_s \boldsymbol{F}^s_{int\,compn}{}^{\boldsymbol{\mu}} \cdot \delta\boldsymbol{\varphi}^{s\boldsymbol{\mu}} \tag{B.93}$$

where,

$$\boldsymbol{F}^s_{int\,compn}{}^{\boldsymbol{\mu}} \;=\; \boldsymbol{F}^s_{int\,compn_1}{}^{\boldsymbol{\mu}} + \boldsymbol{F}^s_{int\,compn_2}{}^{\boldsymbol{\mu}} + \boldsymbol{F}^s_{int\,compn_3}{}^{\boldsymbol{\mu}} + \boldsymbol{F}^s_{int\,compn_4}{}^{\boldsymbol{\mu}}, \tag{B.94}$$

is the elementary interface compatibility membrane forces vector and where,

$$\boldsymbol{F}^s_{int\,compn_1}{}^{\boldsymbol{\mu}} \;=\; \sum_g w_g \frac{\bar{j}_0\left(\xi^{s1}_g\right)}{4} \nu_\alpha^- [\![\boldsymbol{\varphi}_h]\!] \cdot \boldsymbol{\varphi}_{h,\beta} \begin{bmatrix} \widehat{\mathcal{H}_n^{\alpha\beta\gamma\delta}}^- \widehat{N}^{\boldsymbol{\mu}-}_{,\xi^\gamma}\left(\xi^1_g\right)\boldsymbol{\varphi}_{h,\gamma} \\ \widehat{\mathcal{H}_n^{\alpha\beta\gamma\delta}}^+ \widehat{N}^{\boldsymbol{\mu}+}_{,\xi^\gamma}\left(\xi^1_g\right)\boldsymbol{\varphi}_{h,\gamma} \end{bmatrix}, \tag{B.95}$$

$$\boldsymbol{F}^s_{int\,compn_2}{}^{\boldsymbol{\mu}} \;=\; \sum_g w_g \bar{j}\left(\xi^{s1}_g\right) \nu_\alpha^- \langle \boldsymbol{n}^\alpha\rangle \cdot \boldsymbol{\varphi}_h{}^{,\beta} \begin{bmatrix} \widehat{N}^{\boldsymbol{\mu}-}_{,\xi^\beta}\left(\xi^1_g\right)[\![\boldsymbol{\varphi}_h]\!] \\ \widehat{N}^{\boldsymbol{\mu}+}_{,\xi^\beta}\left(\xi^1_g\right)[\![\boldsymbol{\varphi}_h]\!] \end{bmatrix}, \tag{B.96}$$

$$\boldsymbol{F}^s_{int\,compn_3}{}^{\boldsymbol{\mu}} = \sum_g w_g \frac{\bar{j}_0\left(\xi^{s1}_g\right)}{2} \nu_\alpha^- \begin{bmatrix} \left[\frac{\lambda_o^{\beta-}}{\lambda_h^-}\widehat{\mathcal{H}_m^{\alpha o\gamma\delta}}^-\left[\left(\boldsymbol{\varphi}_{h,\beta}\otimes\boldsymbol{t}_{,\delta}\right)\widehat{N}^{\boldsymbol{\mu}-}_{,\xi^\gamma}\left(\xi^1_g\right)+\left(\boldsymbol{\varphi}_{h,\beta}\otimes\boldsymbol{\varphi}_{h,\gamma}\right)\cdot\widehat{\tilde{\boldsymbol{\Delta}}\mathbf{t}^{\boldsymbol{\mu}-}_{,\delta}}\right]\right]^T\cdot[\![\boldsymbol{\varphi}_h]\!] \\ \left[\frac{\lambda_o^{\beta+}}{\lambda_h^+}\widehat{\mathcal{H}_m^{\alpha o\gamma\delta}}^+\left[\left(\boldsymbol{\varphi}_{h,\beta}\otimes\boldsymbol{t}_{,\delta}\right)\widehat{N}^{\boldsymbol{\mu}+}_{,\xi^\gamma}\left(\xi^1_g\right)+\left(\boldsymbol{\varphi}_{h,\beta}\otimes\boldsymbol{\varphi}_{h,\gamma}\right)\cdot\widehat{\tilde{\boldsymbol{\Delta}}\mathbf{t}^{\boldsymbol{\mu}+}_{,\delta}}\right]\right]^T\cdot[\![\boldsymbol{\varphi}_h]\!] \end{bmatrix}, \tag{B.97}$$

$$\boldsymbol{F}^s_{int\,compn_4}{}^{\boldsymbol{\mu}} = \sum_g w_g \frac{\bar{j}\left(\xi^{s1}_g\right)}{2} \nu_\alpha^- \begin{bmatrix} \left[\lambda_h{}^-\widehat{\tilde{m}^{\alpha o}}^-\left\{\left(\boldsymbol{\varphi}_{h,\beta}\otimes\boldsymbol{\varphi}_h{}^{,\beta}\right)\cdot\widehat{\tilde{\boldsymbol{\Delta}}\mathbf{t}^{\boldsymbol{\mu}-}_{,o}}-\frac{\lambda_o^{\zeta-}}{\lambda_h^-}\left(\boldsymbol{\varphi}_{h,\beta}\otimes\boldsymbol{\varphi}_h{}^{,\beta}\right)\widehat{N}^{\boldsymbol{\mu}-}_{,\xi^\zeta}\left(\xi^1_g\right)\right\}\right]^T\cdot[\![\boldsymbol{\varphi}_h]\!] \\ \left[\lambda_h{}^+\widehat{\tilde{m}^{\alpha o}}^+\left\{\left(\boldsymbol{\varphi}_{h,\beta}\otimes\boldsymbol{\varphi}_h{}^{,\beta}\right)\cdot\widehat{\tilde{\boldsymbol{\Delta}}\mathbf{t}^{\boldsymbol{\mu}+}_{,o}}-\frac{\lambda_o^{\zeta+}}{\lambda_h^+}\left(\boldsymbol{\varphi}_{h,\beta}\otimes\boldsymbol{\varphi}_h{}^{,\beta}\right)\widehat{N}^{\boldsymbol{\mu}+}_{,\xi^\zeta}\left(\xi^1_g\right)\right\}\right]^T\cdot[\![\boldsymbol{\varphi}_h]\!] \end{bmatrix}. \tag{B.98}$$

- Stability membrane term:

$$\sum_s \int_s [\![\boldsymbol{\varphi}_h]\!] \cdot \boldsymbol{\varphi}_{h,\gamma}\nu_\delta^- \left\langle \frac{\beta_2 \mathcal{H}_n^{\alpha\beta\gamma\delta}\bar{j}_0}{h^s}\right\rangle [\![\delta\boldsymbol{\varphi}]\!] \cdot \boldsymbol{\varphi}_{h,\beta}\nu_\alpha^- d\partial\mathcal{A}_e = \sum_s \boldsymbol{F}^s_{int\,stabn}{}^{\boldsymbol{\mu}} \cdot \delta\boldsymbol{\varphi}^{s\boldsymbol{\mu}}, \tag{B.99}$$

where,

$$\boldsymbol{F}^s_{int\,stabn}{}^{\boldsymbol{\mu}} \;=\; \sum_g w_g \bar{j}_0\left(\xi^{s1}_g\right)\nu_\alpha^-\nu_\delta^- [\![\boldsymbol{\varphi}_h]\!] \cdot \boldsymbol{\varphi}_{h,\gamma} \left\langle \frac{\beta_2\widehat{\mathcal{H}_n^{\alpha\beta\gamma\delta}}}{h^s}\right\rangle \begin{bmatrix} -N^{\boldsymbol{\mu}-}\left(\xi^{s1}_g\right)\boldsymbol{\varphi}_{h,\beta} \\ N^{\boldsymbol{\mu}+}\left(\xi^{s1}_g\right)\boldsymbol{\varphi}_{h,\beta} \end{bmatrix}, \tag{B.100}$$

is the elementary interface stability membrane forces vector. Note that as explained in Section 4.2 the two last term of $a^s_{nI3}(\boldsymbol{\varphi}_h, \delta\boldsymbol{\varphi})$ can be and are neglected.

- Consistency bending term:

$$\sum_s \int_s \langle \bar{j}\bar{\lambda}_h \tilde{\boldsymbol{m}}^\alpha \rangle \cdot [\![\delta \boldsymbol{t}]\!] \nu^-_\alpha d\partial\mathcal{A}_e \;=\; \sum_s \boldsymbol{F}^s_{int\,cons\,m}{}^{\boldsymbol{\mu}} \cdot \delta\boldsymbol{\varphi}^{s\boldsymbol{\mu}} \tag{B.101}$$

where,

$$\boldsymbol{F}^s_{int\,cons\,m}{}^{\boldsymbol{\mu}} \;=\; \sum_g w_g \bar{j}\left(\xi^{s1}_g\right) \nu^-_\alpha \begin{bmatrix} -\left[\widehat{\tilde{\boldsymbol{\Delta}}\mathbf{t}^{\mu-}}\right]^T \cdot \left\langle \lambda_h \widehat{\tilde{\boldsymbol{m}}^\alpha} \right\rangle \\ \left[\widehat{\tilde{\boldsymbol{\Delta}}\mathbf{t}^{\mu+}}\right]^T \cdot \left\langle \lambda_h \widehat{\tilde{\boldsymbol{m}}^\alpha} \right\rangle \end{bmatrix}, \tag{B.102}$$

is the elementary interface consistency bending forces vector.

- Compatibility bending term:

$$\sum_s \int_s [\![\boldsymbol{t}(\boldsymbol{\varphi}_h)]\!] \cdot \langle \delta(\bar{j}\bar{\lambda}_h \tilde{\boldsymbol{m}}^\alpha) \rangle \nu^-_\alpha d\partial\mathcal{A}_e \;=\; \sum_s \boldsymbol{F}^s_{int\,comp\,m}{}^{\boldsymbol{\mu}} \cdot \delta\boldsymbol{\varphi}^{s\boldsymbol{\mu}}, \tag{B.103}$$

where,

$$\boldsymbol{F}^s_{int\,comp\,m}{}^{\boldsymbol{\mu}} = \sum_g w_g \frac{\bar{j}_0\left(\xi^{s1}_g\right)}{2} \nu^-_\alpha$$
$$\begin{bmatrix} \left[\widehat{\mathcal{H}_m^{\alpha\beta\gamma\delta}}^-\left[\left(\boldsymbol{\varphi}_{h,\beta}\otimes\boldsymbol{t}_{,\delta}\right)\widehat{N}^{\mu-}_{,\xi^\gamma}\left(\xi^1_g\right) + \left(\boldsymbol{\varphi}_{h,\beta}\otimes\boldsymbol{\varphi}_{h,\gamma}\right)\cdot\widehat{\tilde{\boldsymbol{\Delta}}\mathbf{t}^{\mu-}_{,\delta}}\right]\right]^T \cdot [\![\boldsymbol{t}]\!] \\ \left[\widehat{\mathcal{H}_m^{\alpha\beta\gamma\delta}}^+\left[\left(\boldsymbol{\varphi}_{h,\beta}\otimes\boldsymbol{t}_{,\delta}\right)\widehat{N}^{\mu+}_{,\xi^\gamma}\left(\xi^1_g\right) + \left(\boldsymbol{\varphi}_{h,\beta}\otimes\boldsymbol{\varphi}_{h,\gamma}\right)\cdot\widehat{\tilde{\boldsymbol{\Delta}}\mathbf{t}^{\mu+}_{,\delta}}\right]\right]^T \cdot [\![\boldsymbol{t}]\!] \end{bmatrix}, \tag{B.104}$$

is the elementary interface compatibility bending forces vector.

- Stability bending term:

$$\sum_s \int_s [\![\boldsymbol{t}(\boldsymbol{\varphi}_h)]\!] \cdot \boldsymbol{\varphi}_{h,\gamma} \nu^-_\delta \left\langle \frac{\beta_1 \mathcal{H}_m^{\alpha\beta\gamma\delta} \bar{j}_0}{h^s} \right\rangle [\![\delta\boldsymbol{t}(\boldsymbol{\varphi}_h)]\!] \cdot \boldsymbol{\varphi}_{h,\beta} \nu^-_\alpha d\partial\mathcal{A}_e =$$
$$\sum_s \boldsymbol{F}^s_{int\,stab\,m}{}^{\boldsymbol{\mu}} \cdot \delta\boldsymbol{\varphi}^{s\boldsymbol{\mu}}, \tag{B.105}$$

where,

$$\boldsymbol{F}^s_{int\,stab\,m}{}^{\boldsymbol{\mu}} \;=\; \sum_g \bar{j}_0\left(\xi^{s1}_g\right) \nu^-_\alpha \nu^-_\delta [\![\boldsymbol{t}]\!] \cdot \boldsymbol{\varphi}_{h,\gamma} \left\langle \frac{\beta_1 \widehat{\mathcal{H}_m^{\alpha\beta\gamma\delta}}}{h^s} \right\rangle \begin{bmatrix} \left[-\widehat{\tilde{\boldsymbol{\Delta}}\mathbf{t}^{\mu-}}\right]^T \cdot \boldsymbol{\varphi}_{h,\beta} \\ \left[\widehat{\tilde{\boldsymbol{\Delta}}\mathbf{t}^{\mu+}}\right]^T \cdot \boldsymbol{\varphi}_{h,\beta} \end{bmatrix}, \tag{B.106}$$

is the elementary interface stability bending forces vector.

- Stability shearing term:

$$\sum_s \int_s [\![\boldsymbol{\varphi}_h]\!] \cdot \boldsymbol{t}(\boldsymbol{\varphi}_h) \nu_\beta^- \left\langle \frac{\beta_3 \mathcal{H}_q^{\alpha\beta} \bar{j}_0}{h^s} \right\rangle [\![\delta\boldsymbol{\varphi}]\!] \cdot \boldsymbol{t}(\boldsymbol{\varphi}_h) \nu_\alpha^- d\partial\mathcal{A}_e = \sum_s \boldsymbol{F}^s_{int\,stab\,a}{}^{\mu} \cdot \delta\boldsymbol{\varphi}^{s\mu}, \tag{B.107}$$

where,

$$\boldsymbol{F}^s_{int\,stab\,a}{}^{\mu} = \sum_g \bar{j}_0(\xi_g^{s1}) \nu_\alpha^- \nu_\beta^- [\![\boldsymbol{\varphi}_h]\!] \cdot \boldsymbol{t} \left\langle \widehat{\frac{\beta_3 \mathcal{H}_q^{\alpha\beta}}{h^s}} \right\rangle \begin{bmatrix} -N^{\mu-}(\xi_g^{s1})\boldsymbol{t} \\ N^{\mu+}(\xi_g^{s1})\boldsymbol{t} \end{bmatrix}, \tag{B.108}$$

is the elementary interface stability shearing forces vector.

B.6 Dynamic relaxation benchmark: SCB loaded at free extremity

The principle of dynamic relaxation is illustrated on a simply cantilever beam (SCB) loaded perpendicularly at its free extremity as depicted on Fig. B.2. Material properties are reported in Tab. B.1. The equilibrium displacement at the free extremity can be computed

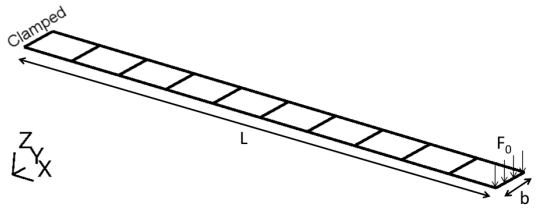

Figure B.2: Geometry of the simply cantilever beam benchmark.

with a quasi-static scheme or analytically by [153],

$$u_z\text{stat} = 4\frac{F_0 L^3}{E b h^3}, \tag{B.109}$$

with, F_0 the applied load, L, b and h respectively the length, the width and the thickness of the beam and E the young modulus (see Tab. B.1 for numerical values).

As this benchmark is elastic, the use of an explicit scheme leads to oscillations between 0 and $2u_z\text{stat}$ as depicted on Fig. B.3. However, if the simulation is performed with the dynamic relaxation presented above, the oscillations are annihilated and the displacement tends toward $u_z\text{stat}$ in just over one period. After one period the convergence is slower which justifies the limitation of e_{tol} to 10^{-3}. This benchmark demonstrates the ability of dynamic relaxation to prescribe a quasi-static load using an explicit scheme and without evaluation (and inversion) of the stiffness matrix.

Property	Value
Length [mm]	100
Width [mm]	10
Thickness [mm]	10
Young modulus [GPa]	100
Poisson ratio [-]	0.3
Density [kg/m^3]	7850
Applied force [N]	10000

Table B.1: Material properties of the simply cantilever beam benchmark.

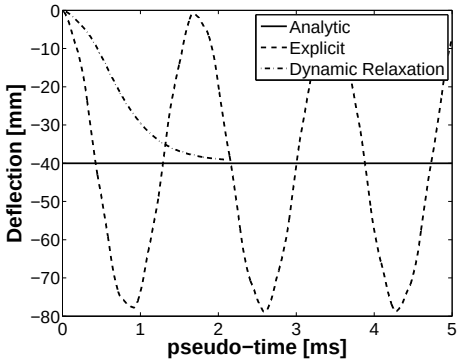

Figure B.3: Simply cantilever beam loaded with dynamic relaxation.